

ScholarWorks@GSU

Fundamental Properties of O and B Stars with Optical Interferometry

Authors	Gordon, Kathryn D
Citation	Gordon, Kathryn D. "Fundamental Properties of O and B Stars with Optical Interferometry." 2018. Dissertation, Georgia State University. https://doi.org/10.57709/12494145
DOI	https://doi.org/10.57709/12494145
Download date	2026-04-15 23:15:19
Link to Item	https://hdl.handle.net/20.500.14694/12247

FUNDAMENTAL PROPERTIES OF O AND B STARS WITH OPTICAL INTERFEROMETRY

by

KATHRYN DARE GORDON

Under the Direction of Douglas R. Gies, PhD

ABSTRACT

We obtained interferometric observations of 6 spectral type O stars and 25 spectral type B stars with the Precision Astronomical Visible Observations (PAVO) and the CLassic Interferometry with Multiple Baselines (CLIMB) beam combiners at the Center for High Angular Resolution Astronomy (CHARA) Array on Mt. Wilson, California. All luminosity classes were represented with 3 supergiants, 16 giants, and 12 dwarf stars. We directly measured the angular sizes of these stars with an average error of 10% for the O stars and 6% for the B stars. The stars range in size from 1.090 milliarcsec (mas) for β Tau down to 0.12 mas for 10 Lac, the smallest star yet resolved with the CHARA Array. These observations represent the first interferometric observations of O stars since 1974 (Hanbury Brown et al. 1974). We

collected ultraviolet to infrared spectrophotometry for these stars, and we derived angular diameters and reddening estimates that best fit the spectra when the effective temperature was set by published results from analysis of the line spectrum. We find that the model-based angular diameters slightly overestimate (by $\approx 4\%$) the observed angular diameters for our O-star and B-star samples. We also present estimates for the effective temperatures of these stars derived by setting the interferometric angular size and fitting the spectrophotometry. We find the spectroscopic based effective temperatures are smaller ($\approx 7\%$) than our interferometrically derived temperatures for all B-stars in our sample. Finally, we place our sample stars on an observational HR-diagram based on our measurements.

INDEX WORDS: techniques: interferometric, stars: early-type, stars: fundamental parameters

FUNDAMENTAL PROPERTIES OF O AND B STARS WITH OPTICAL INTERFEROMETRY

by

KATHRYN DARE GORDON

A Dissertation Submitted in Partial Fulfillment of the Requirements for the Degree of

Doctor of Philosophy

in the College of Arts and Sciences

Georgia State University

2018

Copyright by
Kathryn Gordon
2018

FUNDAMENTAL PROPERTIES OF O AND B STARS WITH OPTICAL INTERFEROMETRY

by

KATHRYN DARE GORDON

Committee Chair: Douglas R. Gies

Committee: Fabien Baron

Russel White

Vadym Apalkov

Gail Schaefer

Daniel Huber

Electronic Version Approved:

Office of Graduate Studies

College of Arts and Sciences

Georgia State University

August 2018

DEDICATION

I would like to dedicate this work to my husband who struggled with me through many hard years of graduate school and to my parents. My mother did not live to see me finish my degree but she would be so happy that I followed my passion and my father who has always been one of my biggest supporters.

ACKNOWLEDGMENTS

I would like to thank my advisor, Doug Gies, for all his help and support through the years. As this project, which started out sounding straight forward, became more and more complicated he provided invaluable help and insight into many areas from observing strategies to data analysis to writing. Over the course of this work, and thanks to Doug's help, I have become a better programmer, writer and scientist. I would also like to thank Doug for being understanding when life presented roadblocks and for doing all he could to help me get around them.

Next, I would like to thank all the people at CHARA who got it working (magic) and keep it working (still magic), including Hal McAlister, Theo ten Brummelaar, Judit and Laszlo Sturmann, and Nils Turner. A big thank you to all the CHARA Array operators who made my observing runs possible and helped troubleshoot the many issues that arose: Chris Farrington, Nic Scott, Olli Majoinen, and Norm Vargas.

I am deeply thankful for the immense amount of help Gail Schaefer provided on a wide variety of problems. She helped during PAVO observing runs when things weren't working and taught me how to use PAVO, she helped me understand and analyze both PAVO data and CLIMB data, and provided fixes to innumerable little programming bugs. She also helped me understand how to correct my data for companions, of which I have many!

I would like to thank Dan Huber for teaching me how to use the PAVO data reduction pipeline, for helping me to get it actually working, and for his insight into PAVO data

analysis.

Thank you to my thesis committee (Doug Gies, Russel White, Fabien Baron, Gail Schaefer, Dan Huber and Vadym Apalkov) for their help and feedback to improve this document.

I would like to express my thanks for the financial support of a NASA Georgia Space Grant Fellowship. This work is based upon observations obtained with the Georgia State University Center for High Angular Resolution Astronomy Array at Mount Wilson Observatory. The CHARA Array is supported by the National Science Foundation under Grant No. AST-1211929, AST-1411654, AST-1636624, and AST-1715788. Institutional support has been provided from the GSU College of Arts and Sciences and the GSU Office of the Vice President for Research and Economic Development.

I would like to thank all my fellow graduate students, but especially Michele Silverstein, Crystal Gnilka, and Ryan Norris, for keeping me sane and helping with myriad little IDL and Linux problems.

Finally, I would like to thank my family - my dad, my husband, and my mother- and father-in-law, for being so supportive, both emotionally and financially, while I spent many years as a student.

TABLE OF CONTENTS

ACKNOWLEDGMENTS	v
LIST OF TABLES	xii
LIST OF FIGURES	xv
1 INTRODUCTION	1
1.1 The O Stars	1
1.2 The B Stars	7
1.3 Importance of Directly Measured Parameters	9
1.4 Outline of Thesis Work	11
2 INTERFEROMETRY	12
2.1 A History of Interferometry	12
2.2 Interferometric Theory and Observables	14
2.3 Measuring Stellar Sizes with Interferometry	19
2.4 The CHARA Array	20
2.4.1 <i>The CLIMB Beam Combiner</i>	22
2.4.2 <i>The PAVO Beam Combiner</i>	24
3 STELLAR SAMPLE AND METHODS	28
3.1 Sample Selection	28
3.2 CHARA Array Observational Methods	30
3.2.1 <i>Interferometric Correction for Companion Flux</i>	34
3.2.2 <i>Calibrators</i>	34
3.3 Spectral Energy Distribution Modeling Methods	37
3.3.1 <i>Spectrophotometric Correction for Companion Flux</i>	39

3.3.2	<i>TLUSTY Models</i>	40
3.3.3	<i>ATLAS9 Models</i>	41
4	EFFECTIVE TEMPERATURES AND ANGULAR SIZES OF O STARS	42
4.1	CHARA Array Interferometry	42
4.1.1	<i>Angular Size Calibration Bias Correction</i>	49
4.2	Spectrophotometry	54
4.3	Results and Comparison to Models	69
4.4	Notes on Individual Stars	72
4.4.1	λ <i>Ori A</i>	72
4.4.2	ζ <i>Ori A</i>	72
4.4.3	ζ <i>Oph</i>	74
4.4.4	<i>10 Lac</i>	75
5	EFFECTIVE TEMPERATURES AND ANGULAR SIZES OF B STARS	77
5.1	CHARA Array Interferometry	77
5.1.1	<i>Comparing CLIMB and PAVO</i>	81
5.2	Spectrophotometry	85
5.3	Results and Comparison to Models	89
5.4	Notes on Individual Stars	93
5.4.1	<i>HD 3360</i>	93
5.4.2	<i>HD 11502</i>	94
5.4.3	<i>HD 23302</i>	94
5.4.4	<i>HD 23408</i>	95
5.4.5	<i>HD 23850</i>	95
5.4.6	<i>HD 29763</i>	96
5.4.7	<i>HD 35497</i>	97
5.4.8	<i>HD 36267</i>	97
5.4.9	<i>HD 155763</i>	98
5.4.10	<i>HD 176437</i>	98

5.4.11	<i>HD 198478</i>	99
5.4.12	<i>HD 205021</i>	101
5.4.13	<i>HD 218045</i>	101
6	SUMMARY	104
	Appendices	113
A	Observing logs and visibility curves	114
A.1	<i>HD 2772</i>	114
A.2	<i>HD 3360</i>	115
A.3	<i>HD 11502</i>	116
A.4	<i>HD 15318</i>	117
A.5	<i>HD 23302</i>	118
A.6	<i>HD 23408</i>	119
A.7	<i>HD 23850</i>	120
A.8	<i>HD 24912</i>	121
A.9	<i>HD 29763</i>	122
A.10	<i>HD 30614</i>	123
A.11	<i>HD 35497</i>	124
A.12	<i>HD 36267</i>	125
A.13	<i>HD 36861</i>	126
A.14	<i>HD 37742</i>	127
A.15	<i>HD 98664</i>	128
A.16	<i>HD 120315</i>	129
A.17	<i>HD 147394</i>	130
A.18	<i>HD 149757</i>	131
A.19	<i>HD 155763</i>	133
A.20	<i>HD 160762</i>	134
A.21	<i>HD 176437</i>	135
A.22	<i>HD 177756</i>	136
A.23	<i>HD 184930</i>	137

<i>A.24</i>	<i>HD 186882</i>	138
<i>A.25</i>	<i>HD 196867</i>	139
<i>A.26</i>	<i>HD 198478</i>	141
<i>A.27</i>	<i>HD 205021</i>	142
<i>A.28</i>	<i>HD 214680</i>	143
<i>A.29</i>	<i>HD 214923</i>	144
<i>A.30</i>	<i>HD 218045</i>	146
<i>A.31</i>	<i>HD 222661</i>	148
B	B Star Contours and SEDs	149
<i>B.1</i>	<i>HD 2772</i>	150
<i>B.2</i>	<i>HD 3360</i>	151
<i>B.3</i>	<i>HD 11502</i>	152
<i>B.4</i>	<i>HD 15318</i>	153
<i>B.5</i>	<i>HD 23302</i>	154
<i>B.6</i>	<i>HD 23408</i>	155
<i>B.7</i>	<i>HD 23850</i>	156
<i>B.8</i>	<i>HD 29763</i>	157
<i>B.9</i>	<i>HD 35497</i>	158
<i>B.10</i>	<i>HD 36267</i>	159
<i>B.11</i>	<i>HD 98664</i>	160
<i>B.12</i>	<i>HD 120315</i>	161
<i>B.13</i>	<i>HD 147394</i>	162
<i>B.14</i>	<i>HD 155763</i>	163
<i>B.15</i>	<i>HD 160762</i>	164
<i>B.16</i>	<i>HD 176437</i>	165
<i>B.17</i>	<i>HD 177756</i>	166
<i>B.18</i>	<i>HD 184930</i>	167
<i>B.19</i>	<i>HD 186882</i>	168
<i>B.20</i>	<i>HD 196867</i>	169
<i>B.21</i>	<i>HD 198478</i>	170

<i>B.22 HD 205021</i>	171
<i>B.23 HD 214923</i>	172
<i>B.24 HD 218045</i>	173
<i>B.25 HD 222661</i>	174
REFERENCES	175

LIST OF TABLES

Table 3.1	Parameters of target stars	29
Table 3.2	Companions to target stars	30
Table 3.3	Calibrated Visibilities	33
Table 3.4	Calibrators used for this study. Target ID is the star ID given in Table 3.1.	35
Table 4.1	Observations and measured angular diameters of O stars	45
Table 4.2	Comparison of measured O star angular diameters to literature values	47
Table 4.3	O Star Spectrophotometry Sources	55
Table 4.4	O Star Literature Temperatures (kK)	55
Table 4.5	Comparison of best fit and literature values for O stars	57
Table 4.6	O Star Distance and Radius Estimates	72
Table 5.1	Observations and measured angular diameters of sample B stars	80
Table 5.2	Comparison of measured B star angular diameters to literature values	81
Table 5.3	Comparison of measured angular diameters from PAVO and CLIMB .	82
Table 5.4	Comparison of best fit and literature values for B stars	89
Table 5.5	B Star Distance and Radius Estimates	91
Table 5.6	Fitted binary parameters for Atlas	96
Table A.1	HD 2772 Observing Log	114
Table A.2	HD 3360 Observing Log	115
Table A.3	HD 11502 Observing Log	116
Table A.4	HD 15318 Observing Log	117

Table A.5	HD 23302 Observing Log	118
Table A.6	HD 23408 Observing Log	119
Table A.7	HD 23850 Observing Log	120
Table A.8	HD 24912 Observing Log	121
Table A.9	HD 29763 Observing Log	122
Table A.10	HD 30614 Observing Log	123
Table A.11	HD 35497 Observing Log	124
Table A.12	HD 36267 Observing Log	125
Table A.13	HD 36861 Observing Log	126
Table A.14	HD 37742 Observing Log	127
Table A.15	HD 98664 Observing Log	128
Table A.16	HD 120315 Observing Log	129
Table A.17	HD 147394 Observing Log	130
Table A.18	HD 149757 Observing Log	131
Table A.19	HD 155763 Observing Log	133
Table A.20	HD 160762 Observing Log	134
Table A.21	HD 176437 Observing Log	135
Table A.22	HD 177756 Observing Log	136
Table A.23	HD 184930 Observing Log	137
Table A.24	HD 186882 Observing Log	138
Table A.25	HD 196867 Observing Log	139
Table A.26	HD 198478 Observing Log	141
Table A.27	HD 205021 Observing Log	142
Table A.28	HD 214680 Observing Log	143
Table A.29	HD 214923 Observing Log	144

Table A.30 HD 218045 Observing Log	146
Table A.31 HD 222661 Observing Log	148

LIST OF FIGURES

Figure 1.1 Stellar evolutionary tracks away from the ZAMS on an HR diagram for various masses at Galactic metallicity. Red tracks are non-rotating models and blue tracks are models with an initial rotation of about 550 km s^{-1} . Adopted from Brott et al. (2011).	3
Figure 1.2 Example model SED of an O star in black with an effective temperature of 40,000 K and a log gravity of 4.5 [units of cm s^{-2}]. Example model SED of a B star in blue with an effective temperature of 25,000 K and a log gravity of 4.5 [units of cm s^{-2}]. Made using the TLUSTY O and B star models.	6
Figure 2.1 A fringe packet of net intensity as a function of delay with maximum and minimum intensity of the packet labeled as I_{max} and I_{min} , respectively.	16
Figure 2.2 An example visibility curve for a star with a 1.0 mas diameter. The solid line shows a limb-darkened fit with a linear limb-darkening coefficient of 0.3. The dashed line shows a uniform disk fit.	17
Figure 2.3 A map of the CHARA Array at the Mt. Wilson Observatory.	21
Figure 2.4 Schematic of the optical layout of the CLIMB beam combiner. From ten Brummelaar et al. (2013).	23
Figure 2.5 Layout of the CLASSIC/CLIMB optics with optical paths drawn. The diagram shows both beam combiners in the CLIMB configuration along with the output optics that feed the beams into the detector. From ten Brummelaar et al. (2013).	24
Figure 2.6 An example of the fringes on one baseline during a scan of CLIMB data, also known as a waterfall plot. Example data for HD 23850.	25
Figure 2.7 A schematic of the PAVO combiner design. The beams are focused by sets of achromat lenses in an image plane and pass through a 3-hole mask. Next, the beams interfere to produce spatially modulated pupil-plane fringes, which are then formed on a lenslet array that separates the pupil into 16 segments. The fringes in each lenslet are dispersed by a prism into independent wavelength channels and are recorded on the detector. Image from Maestro et al. (2012).	26

- Figure 2.8 An example of a step in the PAVO data processing pipeline, *l0_l1_gui.pro*. This is showing a scan for HD 24912, or ξ Per and the plots are described in the text above. 27
- Figure 4.1 Squared visibility versus spatial frequency for ξ Per (HD 24912). The solid line indicates the best fit for a single star limb-darkened disk model. . . 42
- Figure 4.2 Squared visibility versus spatial frequency for α Cam (HD 30614). The solid line indicates the best fit for a single star limb-darkened disk model. . . 43
- Figure 4.3 Squared visibility versus spatial frequency for λ Ori A (HD 36861). The solid line indicates the best fit for a single star limb-darkened disk model. 44
- Figure 4.4 Squared visibility versus spatial frequency for ζ Ori A (HD 37742). The solid line indicates the best fit for a single star limb-darkened disk model. 45
- Figure 4.5 Squared visibility versus spatial frequency for ζ Oph (HD 149757). The solid line indicates the best fit for a single star limb-darkened disk model. 46
- Figure 4.6 Squared visibility versus spatial frequency for 10 Lac (HD 214680). The solid line indicates the best fit for a single star limb-darkened disk model. 47
- Figure 4.7 A simple ellipse fitted to our interferometric data for ζ Oph. Each symbol shows the derived angular size of a limb-darkened star whose visibility equals the observed value, and each is plotted at a position angle derived from the (u, v) spatial frequencies of the observation. The fit was made of the major and minor axes with the position angle of the minor axis set by published polarimetry. The dashed line shows the adopted rotational axis of the star at a position angle of 132.5° 48
- Figure 4.8 Top panel: An enlarged portion of the visibility curve for ξ Per together with fit from simple uncertainty weighting. Lower panel: The derived limb darkened angular diameter for each measurement plotted as a function of the fractional error in visibility. The linear fit of the trend is shown as a solid line and written as a formula above the plot. The diamond symbol on the left side of the fit shows the bias corrected angular diameter that we adopt. 51
- Figure 4.9 Top panel: An enlarged portion of the visibility curve for α Cam together with fit from simple uncertainty weighting. Lower panel: The derived limb darkened angular diameter for each measurement plotted as a function of the fractional error in visibility. The linear fit of the trend is shown as a solid line and written as a formula above the plot. The diamond symbol on the left side of the fit shows the bias corrected angular diameter that we adopt. 52

- Figure 4.10 Top panel: An enlarged portion of the visibility curve for ζ Ori A together with fit from simple uncertainty weighting. Lower panel: The derived limb darkened angular diameter for each measurement plotted as a function of the fractional error in visibility. The linear fit of the trend is shown as a solid line and written as a formula above the plot. The diamond symbol on the left side of the fit shows the bias corrected angular diameter that we adopt. 53
- Figure 4.11 Contour map of fitted TLUSTY O star model to observed spectra for ξ Per (HD 24912). Overplotted are vertical lines showing angular size obtained from our interferometry and horizontal lines showing the average literature temperature. Dotted lines show an error margin of 1σ for the angular size and temperature. The diamond indicates the best fit model temperature for our directly determined angular size. 56
- Figure 4.12 Contour map of fitted TLUSTY O star model to observed spectra for α Cam (HD 30614). Overplotted are vertical lines showing angular size obtained from our interferometry and horizontal lines showing the average literature temperature. Dotted lines show an error margin of 1σ for the angular size and temperature. The diamond indicates the best fit model temperature for our directly determined angular size. 58
- Figure 4.13 Contour map of fitted TLUSTY O star model to observed spectra for λ Ori A (HD 36861). Overplotted are vertical lines showing angular size obtained from our interferometry and horizontal lines showing the average literature temperature. Dotted lines show an error margin of 1σ for the angular size and temperature. The diamond indicates the best fit model temperature for our directly determined angular size. 59
- Figure 4.14 Contour map of fitted TLUSTY O star model to observed spectra for ζ Ori A (HD 37742). Overplotted are vertical lines showing angular size obtained from our interferometry and horizontal lines showing the average literature temperature. Dotted lines show an error margin of 1σ for the angular size and temperature. The diamond indicates the best fit model temperature for our directly determined angular size. 60
- Figure 4.15 Contour map of fitted TLUSTY O star model to observed spectra for ζ Oph (HD 149757). Overplotted are vertical lines showing angular size obtained from our interferometry and horizontal lines showing the average literature temperature. Dotted lines show an error margin of 1σ for the angular size and temperature. The diamond indicates the best fit model temperature for our directly determined angular size. 61

- Figure 4.16 Contour map of fitted TLUSTY O star model to observed spectra for 10 Lac (HD 214680). Overplotted are vertical lines showing angular size obtained from our interferometry and horizontal lines showing the average literature temperature. Dotted lines show an error margin of 1σ for the angular size and temperature. The diamond indicates the best fit model temperature for our directly determined angular size. 62
- Figure 4.17 Spectral energy distributions for ξ Per (HD 24912) with the best fit model shown in the solid green line. The best fit model was chosen using our observed angular diameter from interferometry combined with the best fit temperature and reddening value found from our contour map. The dashed line indicates the SED derived using the average published T_{eff} and the corresponding best fit angular size. 63
- Figure 4.18 Spectral energy distributions for α Cam (HD 30614) with the best fit model shown in the solid green line. The best fit model was chosen using our observed angular diameter from interferometry combined with the best fit temperature and reddening value found from our contour map. The dashed line indicates the SED derived using the average published T_{eff} and the corresponding best fit angular size. 64
- Figure 4.19 Spectral energy distributions for λ Ori A (HD 36861) with the best fit model shown in the solid green line. The best fit model was chosen using our observed angular diameter from interferometry combined with the best fit temperature and reddening value found from our contour map. The dashed line indicates the SED derived using the average published T_{eff} and the corresponding best fit angular size. 65
- Figure 4.20 Spectral energy distributions for ζ Ori A (HD 37742) with the best fit model shown in the solid green line. The best fit model was chosen using our observed angular diameter from interferometry combined with the best fit temperature and reddening value found from our contour map. The dashed line indicates the SED derived using the average published T_{eff} and the corresponding best fit angular size. 66
- Figure 4.21 Spectral energy distributions for ζ Oph (HD 149757) with the best fit model shown in the solid green line. The best fit model was chosen using our observed angular diameter from interferometry combined with the best fit temperature and reddening value found from our contour map. The dashed line indicates the SED derived using the average published T_{eff} and the corresponding best fit angular size. 67

- Figure 4.22 Spectral energy distributions for 10 Lac (HD 214680) with the best fit model shown in the solid green line. The best fit model was chosen using our observed angular diameter from interferometry combined with the best fit temperature and reddening value found from our contour map. The dashed line indicates the SED derived using the average published T_{eff} and the corresponding best fit angular size. 68
- Figure 4.23 Observed angular size θ_{LD} compared to the angular size $\theta_{LD}(T_{\text{eff}})$ derived from the published T_{eff} and fit to the SED. The mean of the small and large diameters is plotted for the oblate star ζ Oph. The solid line shows a line with a slope of unity for reference, and the dashed line shows the trend for the mean ratio of these diameters. Blue points indicate stars likely dominated by systematic errors due to only a single bracket of data, or an extremely small angular size in the case of 10 Lac. 70
- Figure 5.1 Visibility data for HD 98664 and HD 120315. PAVO data is shown to the left and H -band CLIMB data to the right. Solid line is the best fit linear limb-darkened single star disk model. 77
- Figure 5.2 Nightly variation in size (σ) plotted vs. measured angular diameter each night (θ) for each beam combiner. 78
- Figure 5.3 A comparison of PAVO and CLIMB measurements from Table 5.3. Red points represent CLIMB data reduced with the original CLIMB pipeline, blue points with the weighted mean CLIMB pipeline, and green points with John Monnier’s CLIMB pipeline. Solid line shown with a slope of one for reference. 83
- Figure 5.4 A comparison of a star near the cut-off temperature of 17kK fit with both the TLUSTY B star model (left) and the ATLAS9 model (right). For hotter stars the TLUSTY B star models appear to better fit observations. . . 85
- Figure 5.5 Contour map of a fitted ATLAS9 stellar atmosphere model to observed spectra for HD 98664. Overplotted are vertical lines showing angular size obtained from our interferometry and horizontal lines showing the average literature temperature. Dotted lines show an error margin of 1σ for the angular size and average literature temperature. The diamond symbol indicates the best fit model temperature for our directly determined angular size. . . . 86
- Figure 5.6 Spectral energy distribution for HD 98664. The solid green line shows the SED derived from our interferometric size and best fit temperature and reddening. The dashed line indicates the SED derived from the temperature and angular size predicted by the model. 88

- Figure 5.7 The left panel shows a comparison of our observed angular diameters to the predicted model size. The right panel shows a comparison of our derived temperatures to the average literature temperature. In both plots the solid line is a unit line for reference and the dotted line indicates the weighted mean of $\theta_{model}/\theta_{obs}$ and Literature $T_{eff}/\text{Fit } T_{eff}$, respectively. Square symbols indicate stars fit the TLUSTY B models, triangles indicate stars fit with ATLAS9 models, and filled triangles indicate stars with CLIMB data or CLIMB+PAVO data. 90
- Figure 5.8 Squared visibility versus spatial frequency of second lobe data for HD 218045. The dashed line indicates a fit with no limb-darkening and the solid line indicates a fit with a limb-darkening coefficient of $\mu = 0.34$ 102
- Figure 5.9 Squared visibility versus spatial frequency for individual brackets of second lobe data for HD 218045. The dashed line indicates a fit with no limb-darkening and the solid line indicates a fit with a limb-darkening coefficient of $\mu = 0.34$. Moving from left to right, the plots represent a chronological sequence during a single night of observation. 103
- Figure 6.1 Comparison of our measured θ_{LD} to previous work. Square = VEGA observations by Challouf et al. (2014), open triangle = PAVO observations by Maestro et al. (2013), filled triangle = PAVO observation by White et al. (2017), circle = NSII observations by Hanbury Brown et al. (1974). 109
- Figure 6.2 Observational HR diagram for our targets. The pink diamonds indicate B stars, blue circles O stars, and dark blue triangles are O stars with only upper effective temperature estimates. Symbols enclosed by squares indicate stars that are cluster members. Evolutionary tracks and isochrones from the MESA grid. 110
- Figure A.1 Squared visibility versus spatial frequency for HD 2772. The solid line indicates the best fit for a single star limb-darkened disk model. 114
- Figure A.2 Squared visibility versus spatial frequency for HD 3360. The solid line indicates the best fit for a single star limb-darkened disk model. 115
- Figure A.3 Squared visibility versus spatial frequency for HD 11502. The solid line indicates the best fit for a single star limb-darkened disk model. 116
- Figure A.4 Squared visibility versus spatial frequency for HD 15318. The solid line indicates the best fit for a single star limb-darkened disk model. 117
- Figure A.5 Squared visibility versus spatial frequency for HD 23302. The solid line indicates the best fit for a single star limb-darkened disk model. 118

Figure A.6 Squared visibility versus spatial frequency for HD 23408. The solid line indicates the best fit for a single star limb-darkened disk model.	119
Figure A.7 Squared visibility versus spatial frequency for HD 23850. The solid line indicates the best fit for a single star limb-darkened disk model.	120
Figure A.8 Squared visibility versus spatial frequency for HD 24912. The solid line indicates the best fit for a single star limb-darkened disk model.	121
Figure A.9 Squared visibility versus spatial frequency for HD 29763. The solid line indicates the best fit for a single star limb-darkened disk model.	122
Figure A.10 Squared visibility versus spatial frequency for HD 30614. The solid line indicates the best fit for a single star limb-darkened disk model.	123
Figure A.11 Squared visibility versus spatial frequency for HD 35497. The solid line indicates the best fit for a single star limb-darkened disk model.	124
Figure A.12 Squared visibility versus spatial frequency for HD 36267. The solid line indicates the best fit for a single star limb-darkened disk model.	125
Figure A.13 Squared visibility versus spatial frequency for HD 36861. The solid line indicates the best fit for a single star limb-darkened disk model.	126
Figure A.14 Squared visibility versus spatial frequency for HD 37742. The solid line indicates the best fit for a single star limb-darkened disk model.	127
Figure A.15 Squared visibility versus spatial frequency for HD 98664. The solid line indicates the best fit for a single star limb-darkened disk model.	128
Figure A.16 Squared visibility versus spatial frequency for HD 120315, <i>H</i> -band data only. The solid line indicates the best fit for a single star limb-darkened disk model.	129
Figure A.17 Squared visibility versus spatial frequency for HD 147394. The solid line indicates the best fit for a single star limb-darkened disk model.	130
Figure A.18 Squared visibility versus spatial frequency for HD 149757 (w1S2). The solid line indicates the best fit for a single star limb-darkened disk model. . .	131
Figure A.19 Squared visibility versus spatial frequency for HD 149757 (E2S2). The solid line indicates the best fit for a single star limb-darkened disk model. . .	132
Figure A.20 Squared visibility versus spatial frequency for HD 155763. The solid line indicates the best fit for a single star limb-darkened disk model.	133

Figure A.21 Squared visibility versus spatial frequency for HD 160762. The solid line indicates the best fit for a single star limb-darkened disk model.	134
Figure A.22 Squared visibility versus spatial frequency for HD 176437. The solid line indicates the best fit for a single star limb-darkened disk model.	135
Figure A.23 Squared visibility versus spatial frequency for HD 177756. The solid line indicates the best fit for a single star limb-darkened disk model.	136
Figure A.24 Squared visibility versus spatial frequency for HD 184930. The solid line indicates the best fit for a single star limb-darkened disk model.	137
Figure A.25 Squared visibility versus spatial frequency for HD 186882. The solid line indicates the best fit for a single star limb-darkened disk model.	138
Figure A.26 Squared visibility versus spatial frequency for HD 196867 (PAVO). The solid line indicates the best fit for a single star limb-darkened disk model. . .	139
Figure A.27 Squared visibility versus spatial frequency for HD 196867 (CLIMB). The solid line indicates the best fit for a single star limb-darkened disk model.	140
Figure A.28 Squared visibility versus spatial frequency for HD 198478. The solid line indicates the best fit for a single star limb-darkened disk model.	141
Figure A.29 Squared visibility versus spatial frequency for HD 205021. The solid line indicates the best fit for a single star limb-darkened disk model.	142
Figure A.30 Squared visibility versus spatial frequency for HD 214680. The solid line indicates the best fit for a single star limb-darkened disk model.	143
Figure A.31 Squared visibility versus spatial frequency for HD 214923 (PAVO). The solid line indicates the best fit for a single star limb-darkened disk model. . .	144
Figure A.32 Squared visibility versus spatial frequency for HD 214923 (CLIMB). The solid line indicates the best fit for a single star limb-darkened disk model.	145
Figure A.33 Squared visibility versus spatial frequency for HD 218045 (PAVO). The solid line indicates the best fit for a single star limb-darkened disk model. . .	146
Figure A.34 Squared visibility versus spatial frequency for HD 218045 (CLIMB). The solid line indicates the best fit for a single star limb-darkened disk model.	147
Figure A.35 Squared visibility versus spatial frequency for HD 222661. The solid line indicates the best fit for a single star limb-darkened disk model.	148
Figure B.1 Contour (top) and SED (bottom) plots for HD 2772. Fit with the ATLAS9 model.	150

Figure B.2 Contour (top) and SED (bottom) plots for HD 3360. Fit with the TLUSTY B star model.	151
Figure B.3 Contour (top) and SED (bottom) plots for HD 11502. Fit with the ATLAS9 model.	152
Figure B.4 Contour (top) and SED (bottom) plots for HD 15318. Fit with the ATLAS9 model.	153
Figure B.5 Contour (top) and SED (bottom) plots for HD 23302. Fit with the ATLAS9 model.	154
Figure B.6 Contour (top) and SED (bottom) plots for HD 23408. Fit with the ATLAS9 model.	155
Figure B.7 Contour (top) and SED (bottom) plots for HD 23850. Fit with the ATLAS9 model.	156
Figure B.8 Contour (top) and SED (bottom) plots for HD 29763. Fit with the TLUSTY B star model.	157
Figure B.9 Contour (top) and SED (bottom) plots for HD 35497. Fit with the ATLAS9 model.	158
Figure B.10 Contour (top) and SED (bottom) plots for HD 36267. Fit with the TLUSTY B star model.	159
Figure B.11 Contour (top) and SED (bottom) plots for HD 98664. Fit with the ATLAS9 model.	160
Figure B.12 Contour (top) and SED (bottom) plots for HD 120315. Fit with the TLUSTY B star model.	161
Figure B.13 Contour (top) and SED (bottom) plots for HD 147394. Fit with the ATLAS9 model.	162
Figure B.14 Contour (top) and SED (bottom) plots for HD 155763. Fit with the ATLAS9 model.	163
Figure B.15 Contour (top) and SED (bottom) plots for HD 160762. Fit with the TLUSTY B star model.	164
Figure B.16 Contour (top) and SED (bottom) plots for HD 176437. Fit with the ATLAS9 model.	165
Figure B.17 Contour (top) and SED (bottom) plots for HD 177756. Fit with the ATLAS9 model.	166

Figure B.18 Contour (top) and SED (bottom) plots for HD 184930. Fit with the ATLAS9 model.	167
Figure B.19 Contour (top) and SED (bottom) plots for HD 186882. Fit with the ATLAS9 model.	168
Figure B.20 Contour (top) and SED (bottom) plots for HD 196867. Fit with the ATLAS9 model.	169
Figure B.21 Contour (top) and SED (bottom) plots for HD 198478. Fit with the ATLAS9 model.	170
Figure B.22 Contour (top) and SED (bottom) plots for HD 205021. Fit with the TLUSTY B star model.	171
Figure B.23 Contour (top) and SED (bottom) plots for HD 214923. Fit with the ATLAS9 model.	172
Figure B.24 Contour (top) and SED (bottom) plots for HD 218045. Fit with the ATLAS9 model.	173
Figure B.25 Contour (top) and SED (bottom) plots for HD 222661. Fit with the ATLAS9 model.	174

CHAPTER 1

INTRODUCTION

Spectral type O and B stars, also known as ‘early-type stars’, are among the hottest and most massive stars in the universe. They anchor the upper end of the Hertzsprung-Russell diagram of luminosity as a function of temperature and they are very important in the production of heavy elements and enrichment of the interstellar medium. This chapter will provide a background on O- and B-type stars and discuss their importance in understanding stellar parameters.

1.1 The O Stars

O stars range in mass from $16M_{\odot}$ to $200M_{\odot}$ and have an effective temperature range of about 30,000 K to 55,000 K. Due to their large masses and temperatures, O stars can range from 100,000 times to several million times more luminous than the Sun depending on the luminosity class of the star (Weidner & Vink 2010). This incredible luminosity causes O stars to have very short lives compared to other spectral types because the energy radiated depletes the nuclear-burning gas in the core so quickly. The least massive O stars will remain on the main sequence for only 10 million years and then cool, expand and become a supergiant B type star (Maeder & Meynet 2000). O-type stars were originally defined as stars that showed absorption lines of He II in blue-violet part of their spectra. O stars only make up 0.00001% of all stars by number but are some of the brightest objects in the sky and can be seen at great distances (Roberts 1957; Ledrew 2001).

The stellar life-cycle is often described in terms of a star’s position on the Hertzsprung-

Russell (HR) diagram shown in Figure 1.1. This plot shows temperature or color of a star vs. its luminosity or magnitude. Stars will spend the majority of their life on the main sequence, moving off of it as they enter the last stages of their life. As O stars are the most massive and hottest stars, they will burn through their fuel faster than other stars and will only spend a few million years on the main sequence. O stars will start their life as other stars do, contracting from a cloud of gas and dust (Mottram et al. 2011). Once the gas has contracted enough to produce high enough temperatures for hydrogen fusion, the star is formed and takes its place on the main sequence.

Due to the extremely high temperatures in the cores of O stars ($T_c \sim 2 \times 10^7$ K) hydrogen fusion via the CNO cycle dominates energy production over the proton-proton chain (Hansen et al. 2004). This cycle uses carbon, nitrogen and oxygen as catalysts to fuse four protons into a helium nucleus and each reaction will produce 26.7 MeV of energy. A massive star with the CNO cycle as its main source of energy production will burn through its fuel much faster than less massive stars using the proton-proton chain.

After a few million years an O star will run out of hydrogen fuel in its core and hydrogen fusion will stop. The lack of heating and pressure from the fusion to counter balance the force of gravity will cause the star's core to contract. This will heat the core and start a new nuclear reaction of He burning in the core surrounded by H burning in a shell. For massive stars this burning of successively heavier atoms will happen many times, and the resulting star will have a structure of many shells burning elements from hydrogen to silicon with inert iron at the core. This heats the outer layers of the star causing them to expand. As

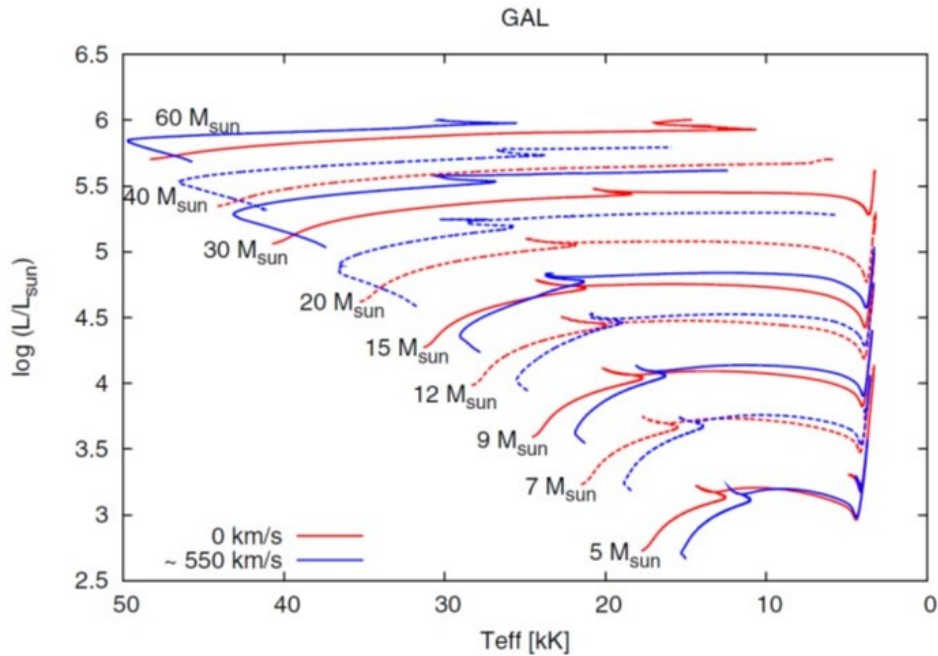


Figure 1.1 Stellar evolutionary tracks away from the ZAMS on an HR diagram for various masses at Galactic metallicity. Red tracks are non-rotating models and blue tracks are models with an initial rotation of about 550 km s^{-1} . Adopted from Brott et al. (2011).

the layers expand they will cool, becoming redder in color. This stage of the star is called a red supergiant. With the shell burning creating more iron, eventually the iron core will become massive enough to overcome electron degeneracy pressure and will collapse. Neutron degeneracy pressure will halt the collapse and the core of the star will become a neutron star, essentially a giant atomic nucleus. The outer layers of the star rapidly collapse to the core and the extreme heat and pressure in the gas creates a cascade of nuclear reactions. These layers will then rapidly expand as they rebound off the neutron star, a nearly incompressible solid, and are propelled by the neutrinos created from electron capture. The neutron star can be completely torn apart in the resulting supernova, remain behind in the supernova remnant, or collapse completely into a black hole.

Many heavy elements are only created in these supernova events and therefore massive stars play a very important role in enriching the interstellar medium. As these heavier elements, from sodium to rubidium, are spread to the surrounding neighborhood, new stars will be formed with a higher abundance of metals. Any planets that form around these stars will also have this increased abundance. This will inform the resulting structure and chemical make-up of these stars and planets. Stars with higher than solar metallicities will tend to be larger, cooler, have higher mass-loss rates and rotate less rapidly (Mapelli & Bressan 2013). Higher metallicities in gas clouds help to stabilize cold, star-forming clumps and sustain star formation. Stellar winds and supernovae contribute almost equally to injection of mechanical power and turbulence in the interstellar medium (Mapelli & Bressan 2013). O stars are also the progenitors of evolved objects such as Luminous Blue Variables (LBVs) and Wolf-Rayet stars (Meynet & Maeder 2003).

O-type stars will be mostly radiative in structure with a small convective zone around the core. This lack of an outer convective zone makes it very rare for massive stars to have a strong magnetic field at the surface. Any detectable surface magnetic field would have to have been created from a past phase of magnetic activity or from deep within the star where a convective zone exists. According to Wade & MiMeS Collaboration (2015), there are only 11 established magnetic O-type stars, with 5 - 10% of all O stars being magnetic (Wade 2012). Magnetic fields will couple to stellar winds and help shed angular momentum resulting in a much slower rotational velocity for stars with strong magnetic fields.

The populations of electronic states of atoms in the outer atmospheres of massive stars

will be in non-local thermodynamic equilibrium (LTE), and this must be taken into account when attempting to understand or model their properties (Hubeny & Lanz 1995). In the presence of a strong radiation field, electron transitions to excited states occurring from processes other than collisions will become more important. The population of atomic energy levels will therefore be different than if the transitions were solely driven by thermal processes (collisions). The atomic populations of an atmosphere dominated by collisional processes would be in LTE but because other radiative processes are more important in massive stars, we must consider them to be in non-LTE.

The high luminosity of O stars causes them to be the main source of ultraviolet radiation for galaxies, and they power far infrared luminosity through the heating of dust. Their spectral energy distributions (SEDs) will peak in the ultraviolet causing the majority of their flux to be output at these very short wavelengths. A typical SED of a main sequence O star is shown in Figure 1.2. A large portion of an O star's flux will occur below 912 Å, or the Lyman limit. This limit corresponds to the energy needed to ionize an electron from the ground state of a hydrogen atom. All light waves below this wavelength limit will be absorbed by interstellar hydrogen gas preventing observation past the Lyman limit. Because of this we must rely on stellar atmosphere models to predict what the SED will look like at wavelengths short of 912 Å.

O stars are found in the spiral arms of galaxies. As the spiral arms sweep through space the increased density of gas and dust at their front will create active star forming regions (Kaplan & Pikelner 1974). Since O stars have a very short lifetime ($\tau \sim 3 - 30$ Myr), they will

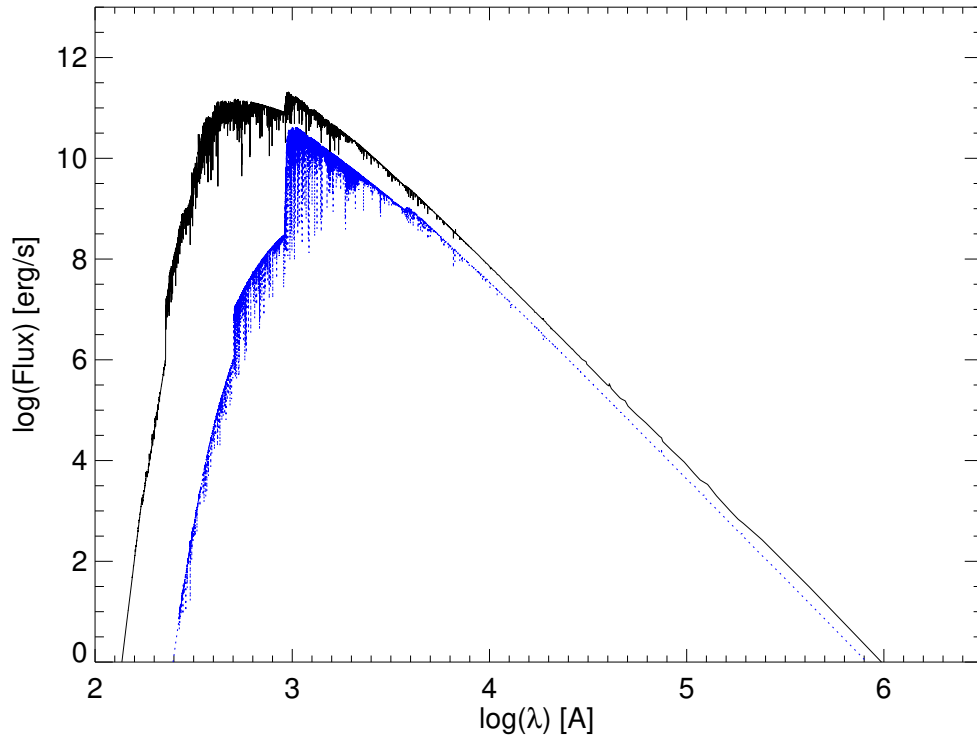


Figure 1.2 Example model SED of an O star in black with an effective temperature of 40,000 K and a log gravity of 4.5 [units of cm s^{-2}]. Example model SED of a B star in blue with an effective temperature of 25,000 K and a log gravity of 4.5 [units of cm s^{-2}]. Made using the TLUSTY O and B star models.

not get the chance to move away from the area in which they were born. This results in all O stars residing in the disk of their galaxies, making them Population I stars. Population II stars are made up of metal-poor, older, less luminous stars and can be found in the globular clusters that reside in the halo of the galaxy. It is extremely common to find O stars in double, or multiple, star systems with the rare single O star being a runaway star (Bate 2009; Mason et al. 2009). A runaway star can be caused by two binary systems having a close encounter and ejecting some stars at very high velocities or the companion to the runaway star going supernova, sending the runaway moving away at high speeds (Blaauw

1961). A runaway star will thus be moving with an unusually high velocity compared to the surrounding interstellar medium and its motion should point back toward the stellar association of origin.

1.2 The B Stars

Spectral type B stars are similar in structure and life cycle to the O stars. Main sequence B stars range in mass from 3 to 16 M_{\odot} and have an effective temperature range of 10,000 - 30,000 K (Habets & Heintze 1981). Because they are less massive and less luminous than O stars they will have a longer lifetime of 9 - 150 Myr and make up 0.1% of stars by number. Main sequence B stars will be 200 to 50,000 times more luminous than the Sun, and a supergiant B star can be up to 2.5 million times more luminous (Silaj et al. 2014). Spectral type B stars were originally defined as stars that showed He I lines, and no He II lines, in the blue-violet part of their spectra. The spectral energy distribution of a B star will have a peak at longer wavelengths than an O star, but still within the ultraviolet part of the spectrum. An example SED for a B star is shown in Figure 1.2.

After several million years on the main sequence, a B star will have a similar time line as an O star discussed above. It will become a red supergiant with a structure of many shells burning successively heavier elements until inert iron is reached at the core. Once the iron core becomes too dense to withstand the force of gravity, the star will undergo a supernova and form a neutron star remnant. Temperatures are still high enough at the core of B stars to support the CNO cycle as the dominant form of energy production for the star. Like O

stars, B stars will have a mostly radiative envelope with a small convective zone near the core. The most luminous B supergiants have a high mass loss rate and strong stellar winds with velocities up to $3,000 \text{ km s}^{-1}$ (Aschenbach et al. 1998). Many B stars are also rapid rotators with an equatorial rotation velocity of around 200 km s^{-1} (McNally 1965).

Like O stars, 5 - 10% of B stars will have a measurable magnetic field (Wade et al. 2014). These magnetic fields are often dipolar and stable and confine stellar winds. Magnetic fields in B stars are often accompanied by strong chemical peculiarities. These chemically peculiar stars will have an overabundance of some metals including strontium and chromium. Slowly rotating B stars with strong magnetic fields have also been shown to be nitrogen rich (Wade et al. 2014).

There are a few interesting subtypes of spectral type B stars. One of these is the Be star which is a rapidly rotating B star with a circumstellar disk. Emission from the disk causes hydrogen emission lines to be observed in the spectrum, as well as an infrared excess and linear polarization. The circumstellar disks can vary on timescales from days to several years, disappearing and reappearing. Recent evidence suggests that Be stars are spun up through mass transfer from a more evolved companion (Gies et al. 2007). B[e] stars are a type of Be star that shows forbidden low ionization or neutral emission lines in its spectrum. Like Be stars, B[e] stars will also show an infrared excess and linear polarization with their circumstellar disk being transient in nature. Mercury-manganese stars are chemically peculiar B stars in the B7-B9 spectral range that show a prominent spectral line at 3984 \AA due to absorption from ionized mercury. They are slow rotators and show an atmospheric excess

of some metals, including phosphorous and manganese (Makaganiuk et al. 2011).

B-type stars join the O stars as Population I stars in the spiral arms of a galaxy. B stars are still massive enough to have a fairly short lifetime making it unlikely they will move far from the association of their birth. It is common to find B stars in double or multiple systems with the rare case of single runaway stars (Bate 2009).

1.3 Importance of Directly Measured Parameters

As we have seen, massive stars are rare but have a profound impact on their surroundings and the next generation of stars and planets. To understand the structure of these stars and to place them accurately on an HR diagram for comparison with stellar evolutionary tracks, we must have accurate measurements of their fundamental properties. Very accurate measurements of mass and radius can be made with eclipsing binaries from observation of their light curves and radial velocities. However, these systems may interact and undergo mass transfer at some point in their evolution, and therefore may not be representative of the evolution of a single star.

Most of what we know for individual stars is based on their line spectrum. The temperature and gravity of the stellar atmosphere are derived from the helium line ionization balance and the pressure broadening of the hydrogen lines (Petrie 1947; Conti & Alschuler 1971). To complete this line spectrum analysis, we must rely on detailed atmospheric models that take into account non-LTE effects, line-blanketing, and spherical winds. Because of the critical part these models play in our understanding of massive stars, it is important to test them.

Here we can use directly measured parameters to compare to the values the models predict. We can use the relationship between observed bolometric flux, angular diameter, and effective temperature to determine the stellar effective temperature, T_{eff} . This relationship is given as: $f_{\text{bol}} = \frac{1}{4}\theta^2\sigma T_{\text{eff}}^4$ where θ is the angular diameter and σ is the Stefan-Boltzmann constant. This method was first used by Hanbury Brown et al. (1974) using the Narrabri Stellar Intensity Interferometer (NSII) to measure the angular diameters of 32 stars in the spectral range from O5 to F8.

There are some difficulties present when using this method. As discussed before, a majority of the flux for O and B stars is emitted at wavelengths short of the Lyman limit where we cannot observe. This means we cannot obtain observed flux for that part of the spectrum and must rely on models to contribute to our bolometric flux calculation. The part of the spectrum that we do observe for massive stars is in the Rayleigh-Jeans tail which is less sensitive to temperature. Therefore, all hot stars display SEDs with a very similar appearance. The region of the observed spectrum also has a dependence on gravity, usually expressed as $\log g$. We must have a good estimate of the star's gravity from other sources to fit reliably the spectrum to a model. Finally, we must take into account that O and B stars are very distant and their spectra are transformed by interstellar extinction. Fits of the spectrum to the model must include a fit for the correct reddening value to account for interstellar extinction (Fitzpatrick 1999; Maíz Apellániz et al. 2014).

With the observations now made possible with long baseline interferometry, we are able to combine accurately measured angular diameters with good SEDs available and well known

$\log g$ values to obtain effective temperature estimates for relatively nearby O and B stars. If the bolometric flux is known the derived effective temperature will depend on the inverse square root of the angular diameter, making the fractional uncertainty $\Delta T_{\text{eff}}/T_{\text{eff}} \approx \Delta\theta/2\theta$. However, for hot stars we are often unable to observe the bolometric flux and our observations will put us in the Rayleigh-Jean's tail of the spectrum. The relationship between the emitted F_λ and observed f_λ monochromatic flux in this part of the spectrum will result in an inverse squared relationship between effective temperature and angular size, making the fractional uncertainty $\Delta T_{\text{eff}}/T_{\text{eff}} \approx \Delta 2\theta/\theta$. Thus, it is important to obtain accurate angular diameter measurements to test effectively the predictions of the current generation of stellar atmosphere models.

1.4 Outline of Thesis Work

In this work, we present precisely measured angular diameters of 6 O stars and 25 B stars, along with effective temperature estimates based on fitting models to interferometric and spectrophotometric data. We combine our directly measured angular diameters with the total integrated flux from spectrophotometry to obtain an effective temperature estimate which can then be compared to models. An overview of the interferometric technique and its history is given in Chapter 2. Chapter 3 explains our sample selection, observational methods, and modeling methods. The results of our interferometric and spectrophotometric fitting for O stars are given in Chapter 4, and the results for the B stars are given in Chapter 5. Finally, we summarize and discuss our results in Chapter 6.

CHAPTER 2

INTERFEROMETRY

An interferometer uses the wave-like nature of light to produce constructive interference of an electromagnetic wave. Information can be extracted from this interference pattern about the source. This chapter will give a brief history of interferometry in astronomy, the theory behind it, and how it can be applied to our interest in stellar parameters.

2.1 A History of Interferometry

The underlying principle behind interferometry, that light acts as a wave, was first observed in 1803 in the famous ‘Young’s double slit’ experiment by Thomas Young. In this experiment a monochromatic light source is sent through a pair of slits and shown to propagate as waves past the slits and create an interference pattern, exactly like the ripples of a wave in water.

Hippolyte Fizeau was the first to propose that this interference of light could be used to measure stellar diameters in 1868 (Lawson 1999). In 1890, a more robust mathematical foundation of Fizeau’s proposal was developed by Albert Michelson. With these concepts in place, Michelson went on, along with Pease, to measure successfully the diameter of Betelgeuse in 1920-1921. This was achieved by attaching a 20-foot interferometer beam to the 100-inch telescope at Mt. Wilson Observatory (Michelson & Pease 1921).

Hanbury Brown (1956) developed the concepts behind intensity interferometry. This method uses the correlations of observed intensities, instead of electric fields, to measure stellar sizes. Called a ‘direct detection’ method, intensity interferometry measures temporal correlations of arrival times between photons recorded in different telescopes. Instead of

measuring the interference pattern of two or more light waves on a detector, an intensity interferometer makes use of the fact that random fluctuations in the intensity of light waves from the same source, but observed by separate telescopes, are correlated (Dravins 2016). This led to the development of the Narrabi Stellar Intensity Interferometer (NSII) which was able to measure many hot star diameters and remains the source of some of the only observed O star diameters until this work (Hanbury Brown et al. 1974).

In 1974, Labeyrie was the first to combine directly the electric field of each light wave before photon detection using a 12-m baseline (Labeyrie 1975; Monnier 2003). The Massachusetts Institute of Technology and the Naval Research Laboratory developed prototype interferometers, the Mark I, II, and III, and obtained the first successful fringe-tracking observations in 1980 (Shao et al. 1988; Monnier 2003). Fringe tracking is integral to the success of today’s modern interferometers. This requires the absolute optical path-length difference offsets to be determined for each beam being combined and applied in real-time to the interferometer’s delay lines. In addition to fringe tracking, current interferometers employ a fast ‘tip-tilt’ guiding system. This corrects for the atmospheric jitter of the stellar image which allows the observed wavefronts to be aligned for stable beam combination (Monnier 2003).

The most successful and prolific interferometers operating today are the CHARA Array, the Navy Precision Optical Interferometer (NPOI), and the Very Large Telescope Interferometer (VLTI). The CHARA Array is discussed in detail in Section 2.4. NPOI is located at Lowell Observatory in Anderson Mesa, AZ, and is a 6-element array with sub-arrays for imaging and astrometry (Armstrong et al. 1998). The astrometric sub-array contains four

fixed 50 cm siderostats, while the imaging sub-array is planned to consist of six movable 50 cm siderostats. The siderostats are currently being upgraded to 1-m telescopes. NPOI currently has a baseline range of 16 to 79 meters, with a planned maximum baseline length of 432 meters. The VLTI is located at the Paranal Observatory on Cerro Paranal, Chile, and is a 4-beam interferometer (Wallander et al. 2004). It operates four 8.2-m Unit Telescopes (UTs) and four 1.8-m Auxiliary Telescopes (ATs). The UTs are fixed while the ATs can be moved. The VLTI has a baseline range from 10 to 130 meters.

2.2 Interferometric Theory and Observables

An interferometer uses the principle that light can act as a wave and combine from multiple sources to create an interference pattern, or ‘fringe pattern.’ Monochromatic light sources will constructively interfere with each other at every point along the wave if the distance they traveled differs by $n\lambda$ where λ is the wavelength of the light and n is an integer. Polychromatic light sources will be made up of multiple wavelengths and will only constructively interfere at one point. This is caused by the fact that the light waves will only constructively interfere when their distance traveled differs by $n\lambda$ and this value will change as wavelength changes. Each beam of light is an electromagnetic wave and the intensity of the electric field reaching the detector can be given as

$$E(t) = A \cos(kx - kct + \phi) \quad (2.1)$$

where A is the amplitude of the field, k is the wave number equal to $2\pi/\lambda$, λ is the wavelength, x is the optical path length, t is the time, c is the speed of light, and ϕ is the phase of the

wavefront. The beams of light will be combined in an interferometer and the intensity of the beams sensed by a detector. It is from measuring and analyzing this intensity that we can obtain information about the source.

The contrast of the amplitude of the interference pattern, or fringe packet, is referred to as the visibility. A non-point source will have a lower contrast, or lower visibility, than a point source. This is due to the fact that waves originating from different locations on the non-point source will interfere at slightly different delay positions. This will cause the observed fringe packet to become spread out and the amplitude of the interference reduced. Additionally, the larger a non-point source is, the lower the fringe packet contrast will be. Thus, we can measure the contrast in a fringe packet and use that to obtain information about the source's size. Visibility can be defined by

$$V = \frac{I_{max} - I_{min}}{I_{max} + I_{min}} \quad (2.2)$$

where I_{max} and I_{min} are the maximum and minimum intensities of the fringe packet. A visual example of a fringe packet is given in Figure 2.1. Visibility amplitudes are normalized and the visibility of a point source will be equal to 1. The visibility function is a complex function made up of an amplitude and phase. The Van Cittert-Zernike theorem (Born & Wolf 1999) states that the complex visibility of a distant, incoherent source is equal to the Fourier Transform of the intensity over the angular spatial distribution of the source. This means that the amplitude and phase of each fringe function will be related through a Fourier Transform of the intensity pattern observed from the source.

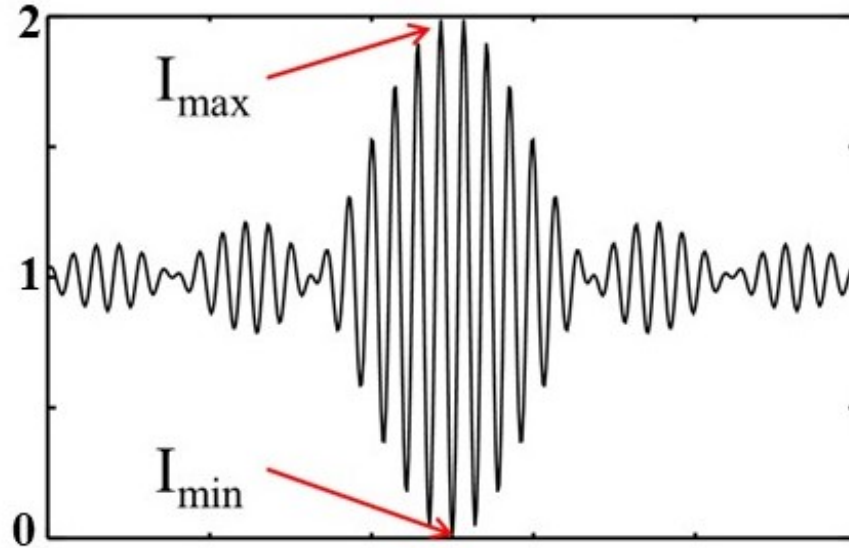


Figure 2.1 A fringe packet of net intensity as a function of delay with maximum and minimum intensity of the packet labeled as I_{max} and I_{min} , respectively.

The visibility of a simple uniform disk is given by

$$V = \frac{2J_1(x)}{x} \quad (2.3)$$

where J_1 is a Bessel function of the 1st kind of order 1 and $x = \pi\theta B/\lambda$. θ is the angular diameter of the disk, B is the projected separation between telescopes, or baseline, and λ is the wavelength. This can be used to get an estimate of a star's diameter, but does not take into account the effect of limb-darkening that will be present due to the fact that stars are composed of gas and are not uniformly bright across their disk. A more complete model for calculating the visibility of a stellar disk was developed by Hanbury Brown et al. (1974).

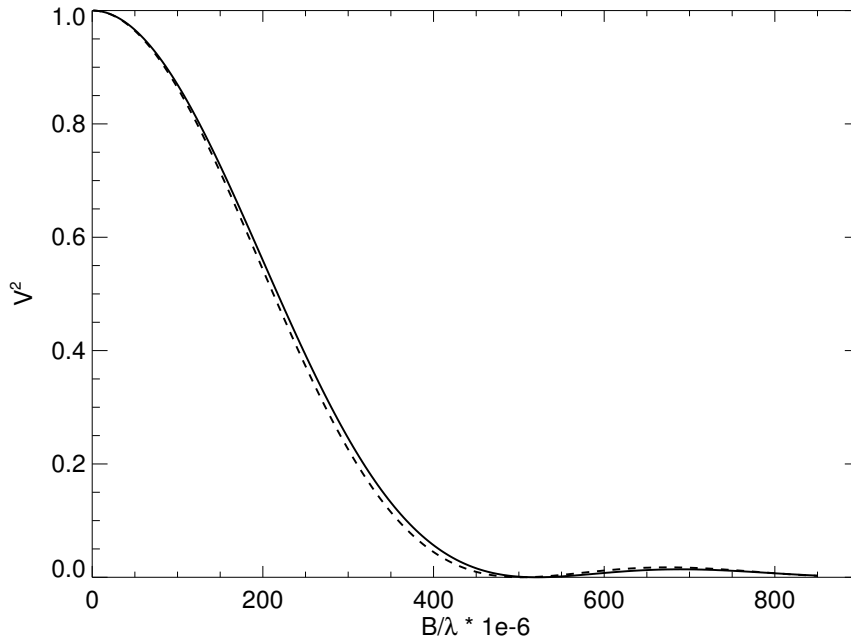


Figure 2.2 An example visibility curve for a star with a 1.0 mas diameter. The solid line shows a limb-darkened fit with a linear limb-darkening coefficient of 0.3. The dashed line shows a uniform disk fit.

This gives the function for a limb-darkened disk as

$$V = \left(\frac{1 - \mu_\lambda}{2} + \frac{\mu_\lambda}{3}\right)^{-1} \times \left[(1 - \mu_\lambda) \frac{J_1(x)}{x} + \mu_\lambda \left(\frac{\pi}{2}\right)^{1/2} \frac{J_{3/2}(x)}{x^{3/2}}\right] \quad (2.4)$$

where μ_λ is the linear limb-darkening coefficient, J_n is a Bessel function of the 1st kind of order n , and $x = \pi\theta B/\lambda$. These are the most frequently used models to determine stellar sizes with interferometric observations and are shown in Figure 2.2 to illustrate their differences.

Atmospheric turbulence will influence the phase of the waves measured by an interferometer which will affect the phase of the measured complex visibility. This results in complex visibilities having random phases that are not related to the source and from which we cannot

extract relevant information. This problem can be mitigated by using the second observable of interferometric observations, closure phase. The closure phase is the argument of the triple product of complex visibilities around a closed loop of baselines. When forming this product the terms introduced by the atmosphere cancel out and we are left with the true values of the visibility function phases on the baselines that form the closed loop. The measurements of the complex visibilities must all be made at the same time for the atmospheric errors to cancel and the closure phase will retain a large fraction of the Fourier phase information about the source. Closure phase measurements can be used to tell us about the amount of asymmetric flux present in the source. Asymmetry could be due to many things from a close companion to a disk or structure around the star. An example of closure phase for a three telescope loop is given by

$$\begin{aligned}
 \phi_{12} &= \varphi_{12} + [\phi_2 - \phi_1] \\
 \phi_{23} &= \varphi_{23} + [\phi_3 - \phi_2] \\
 \phi_{31} &= \varphi_{31} + [\phi_1 - \phi_3] \\
 \phi_c &= \phi_{12} + \phi_{23} + \phi_{31} \\
 &= \varphi_{12} + \varphi_{23} + \varphi_{31}
 \end{aligned} \tag{2.5}$$

where ϕ_{ij} is the observed phase for telescopes i and j , φ_{ij} is the inherent phase of the observation, ϕ_i is the phase introduced by the atmosphere for each telescope, and ϕ_c is the closure phase.

2.3 Measuring Stellar Sizes with Interferometry

Even nearby stars are at great distances from us ($>10^{16}$ m) and have very small angular sizes. It was not until the advent of interferometry that we were able to resolve the disk of a star other than our Sun. The closest star to us, α Centauri is 1.34 pc away and has a radius of $1.22R_{\odot}$. This would give it an angular diameter of 8.5 milli-arcseconds. The Rayleigh criterion can be used as the angular resolution for a single telescope and is given as

$$\theta = \frac{1.22\lambda}{D} \quad (2.6)$$

where λ is the wavelength of observation and D is the diameter of the telescope's primary mirror. Using this criterion, it would take a telescope with a diameter of ~ 16 meters observing in the V band ($0.55 \mu\text{m}$) to resolve α Centauri. A 10 meter telescope observing in the V band could only resolve stars with angular sizes larger than 14 mas, but the vast majority of stars are at much smaller angular sizes.

Interferometers allows us to improve the angular resolution of observations while cutting back on the costs and technical difficulties of building larger and larger single telescopes (Monnier 2003). The angular resolution of an interferometer is typically taken as

$$\theta = \frac{\lambda}{2B} \quad (2.7)$$

where λ is the wavelength of observation and B is the projected baseline separation between telescopes. An interferometer operating in the R band with a 300 meter baseline could resolve stars with an angular size as small as 0.23 mas, and could easily resolve α Centauri at 8.5 mas. This much improved resolution limit allows us to measure accurately many types

of stars.

2.4 The CHARA Array

The Center for High Angular Resolution Astronomy (CHARA) Array (ten Brummelaar et al. 2005) is located at the Mt. Wilson Observatory in California. The Array operates at optical and near-infrared wavelengths and consists of six 1-meter telescopes spread out in a Y-configuration across the mountain. A map of the Array is shown in Figure 2.3. Through combinations of different telescopes, 15 baseline configurations are available in a range from 34 to 331 meters. Each telescope is a Mersenne-type afocal beam reducer that injects a 12.5 cm output beam into the vacuum transport tubes. Light from each telescope travels through vacuum tubes, or ‘light pipes’, across the mountain to be combined at a central Beam Synthesis Facility. The path of each beam of light must be equal within sub-micron accuracy after traveling hundreds of meters from the telescope. Between arriving at the telescope and being detected at the beam combining facility, a beam of light will undergo 22 reflections. A large amount of light is lost in the many reflections causing the Array to have a fairly bright magnitude limit depending on the instrument being used. For reference, the CLASSIC beam combiner has a magnitude limit of ~ 8.5 mag.

The Array currently has six beam combiners operating at the Beam Synthesis Facility. The CLIMB and PAVO beam combiners were used for this work and will be discussed in detail in sections 2.4.1 and 2.4.2, respectively. The CLASSIC beam combiner is the original two beam combiner at CHARA, and it has the faintest magnitude limit. It is an open air,

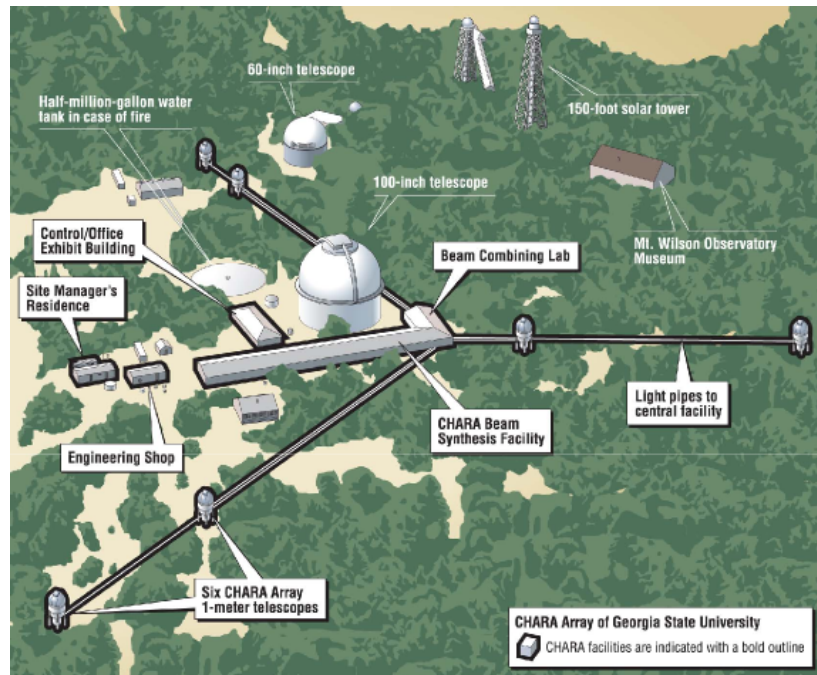


Figure 2.3 A map of the CHARA Array at the Mt. Wilson Observatory.

aperture plane, wide bandwidth single spectral channel instrument. The Michigan Infrared Beam Combiner (MIRC) beam combiner (Monnier et al. 2004) can use all six telescopes at once and operates in the H or K band. Due to its capability of making many closure phase measurements, it is exceptional for image reconstruction. The Visible spEctroGraph and polArimeter (VEGA) works in visible wavelengths and has three spectral resolution options (Mourard et al. 2009). JouFLU is a two telescope beam combiner that operates in the K band and utilizes optical fibers to obtain high precision visibility measurements (Coudé du Foresto et al. 2003; Scott et al. 2013).

2.4.1 The CLIMB Beam Combiner

The CLIMB (CLassic Interferometry with Multiple Baselines) beam combiner is a three telescope extension of the CLASSIC beam combiner. It is an open air, aperture plane beam combiner and operates using beam splitters and dispersion compensation plates (ten Brummelaar et al. 2013). Schematics of the optical layout of CLIMB are given in Figures 2.4 and 2.5. CLIMB utilizes group delay tracking, which tracks the center of the fringe envelope instead of only a small number of fringes. This allows for a fainter limiting magnitude. In the H band the resolution limit for the CLIMB combiner is ~ 0.5 milli-arcseconds. CLIMB will produce three visibilities (one for each observed baseline) and one closure phase measurement for each observation. CLIMB uses the near infra-red observer (NIRO) detector that is sensitive to light at wavelengths of 0.8 to 2.5 μm .

The H -band filter used by CLIMB is a wide band filter that assumes a central wavelength of 1.673 μm . To check that the observation of hot stars did not skew this central effective wavelength to shorter wavelengths, we used a spectral library from Lancon & Rocca-Volmerange (1992) which spans spectral types from O5V to A3V. We multiplied these spectra by the H -band filter transmission curve, the quantum efficiency curve for the NIRO detector, and the atmospheric transmission curve. We then calculated the centroid for the resulting spectra and compared the calculated central wavelength to CLIMB's assumed central wavelength. We find that the central wavelength for spectra in the H -band does not appear to depend on effective temperature, and we calculate an average central effective wavelength of 1.668 μm which is a 0.3% difference from the central wavelength used

by CLIMB. Therefore, we believe it is reasonable to assume the central effective wavelength used by CLIMB in the H -band is appropriate for all stellar temperatures and spectral types.

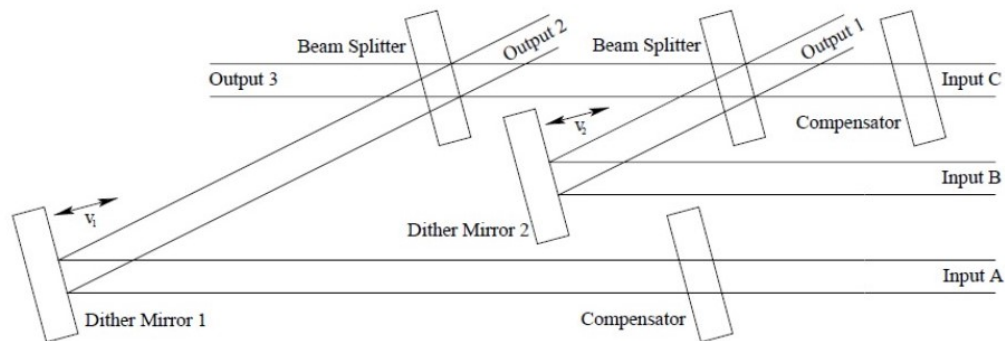


Figure 2.4 Schematic of the optical layout of the CLIMB beam combiner. From ten Brummelaar et al. (2013).

The CLIMB data reduction pipeline (ten Brummelaar et al. 2012) first displays the photometric signals for the three output pixels of the detector, and the noise subtracted power spectra for each pixel. The user can choose to use only the first or second shutter sequences if the light from a telescope was lost during a shutter event. Next the fringe scans can be edited for any loss of fringes that occurred during the scan. An example plot showing the fringes for a scan, also called a waterfall plot, is shown in Figure 2.6. Integration ranges of the power spectra from each scan can be set automatically or chosen manually by inspecting the mean power spectra plots for each baseline. Finally closure phases are calculated for each scan and the raw visibilities can be calibrated. The calibration process calibrates the brackets relative to unresolved calibrator stars and outputs the calibrated visibilities.

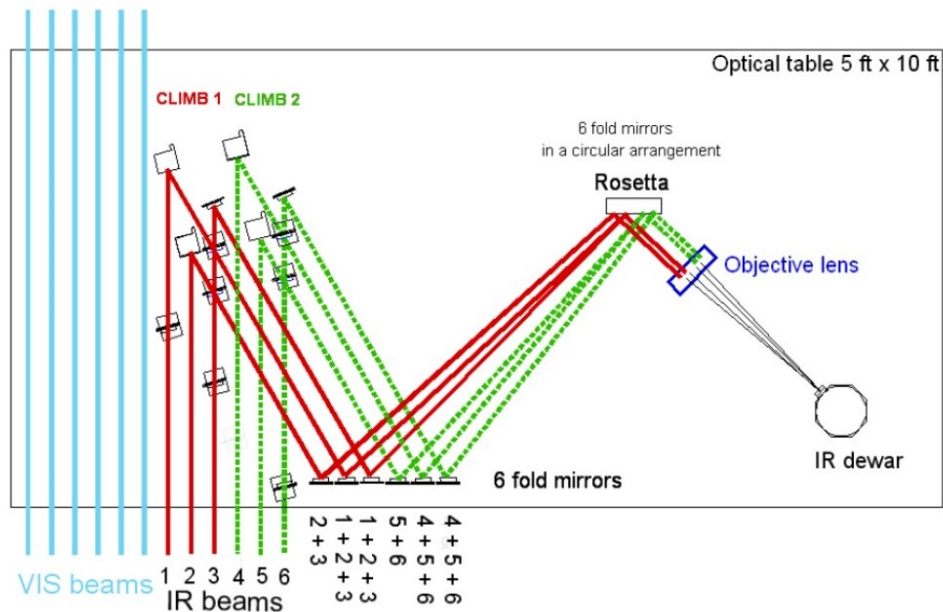


Figure 2.5 Layout of the CLASSIC/CLIMB optics with optical paths drawn. The diagram shows both beam combiners in the CLIMB configuration along with the output optics that feed the beams into the detector. From ten Brummelaar et al. (2013).

2.4.2 The PAVO Beam Combiner

The Precision Astronomical Visible Observations (PAVO) beam combiner is a spectrally-dispersed, pupil plane combiner (Ireland et al. 2008). Optics bring the beam from each telescope to a common image-plane and form spatially-modulated fringes on a cylindrical lenslet array which divides the pupil into 16 segments. The path through the optics between the lenslet array and the detector act as an integral field unit and disperses the fringes to a range of wavelengths. A schematic of the PAVO beam combiner layout is shown and explained in Figure 2.7. The detector is a back-illuminated DU-897 EMCCD camera from Andor. The PAVO beam combiner can be used as a 3-beam combiner but currently only single baseline data analysis is well modeled and understood, so it typically operates in 2-

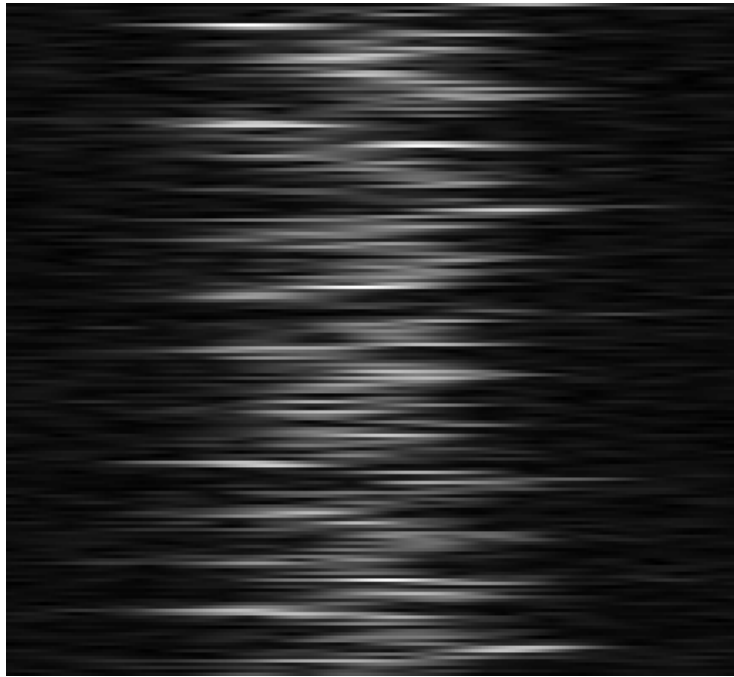


Figure 2.6 An example of the fringes on one baseline during a scan of CLIMB data, also known as a waterfall plot. Example data for HD 23850.

beam mode. PAVO operates over a 40% bandpass of the R and I bands (630-950 nm) and this shorter wavelength allows for a smaller angular resolution limit than that of the CLIMB beam combiner. Using the longest baselines available at CHARA, the angular resolution limit of PAVO is ~ 0.2 milli-arcseconds and it will produce 38 spectrally dispersed visibility measurements per baseline of observation. However, visibility measurements on each end of the wavelength spectrum are less reliable and each bracket is truncated to 23 visibility points. Throughout a night of observing the alignments of the image and pupil plane are checked for each new target, fringes are found, and adjustments made to optimize the longitudinal dispersion corrector position.

The data undergo background subtraction and photon-bias subtraction, with foreground

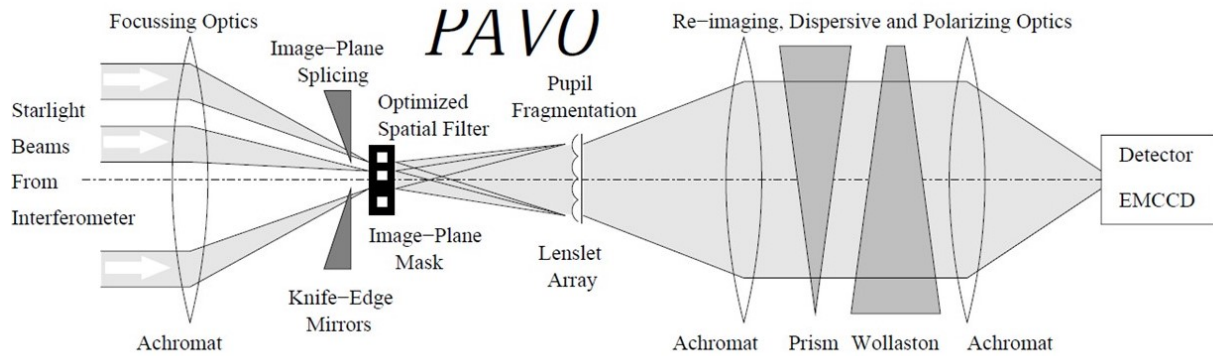


Figure 2.7 A schematic of the PAVO combiner design. The beams are focused by sets of achromat lenses in an image plane and pass through a 3-hole mask. Next, the beams interfere to produce spatially modulated pupil-plane fringes, which are then formed on a lenslet array that separates the pupil into 16 segments. The fringes in each lenslet are dispersed by a prism into independent wavelength channels and are recorded on the detector. Image from Maestro et al. (2012).

frames, ratio frames, and dark frames being taken during a shutter sequence that runs after fringe data are saved. During a foreground frame all shutters are open but fringe tracking is turned off, and during a ratio frame only one shutter is left open at a time. After this process, the visibility squared as a function of the wavelength channel is integrated over the frames with a relation that depends on the bias corrected fringe power and the total flux in the pupil pixel. The PAVO data reduction pipeline (Ireland et al. 2008; Maestro et al. 2012) first takes the raw data through a routine that allows for the rejection of bad data frames. This allows the user to make cuts based on S/N values and loss of lock on fringes. An example of raw data being taken through this routine is shown in Figure 2.8. The plots show the raw visibility for each scan (top) along with the corresponding SNR (bottom). The small dots that range in color from red to blue indicate the raw visibility measurements in each spectral channel for each scan and should show an equal distribution of colors if the

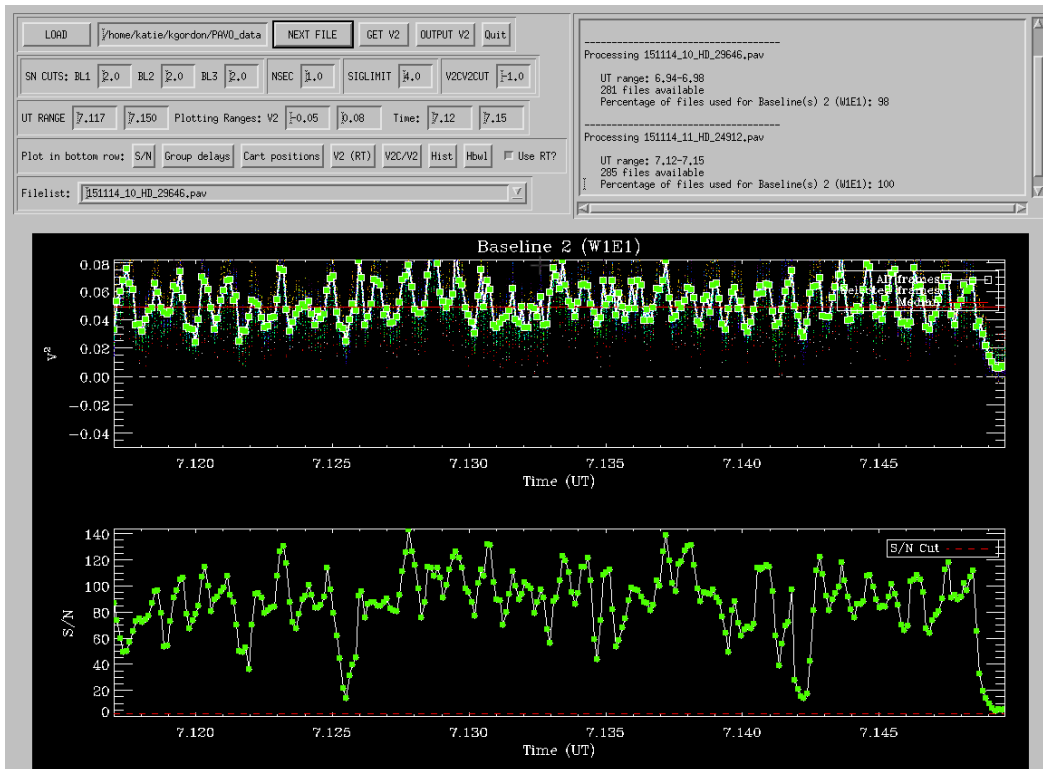


Figure 2.8 An example of a step in the PAVO data processing pipeline, *l0_l1_gui.pro*. This is showing a scan for HD 24912, or ξ Per and the plots are described in the text above.

longitudinal dispersion correctors were adjusted correctly. However, it is possible in real data that some dispersion will exist. The processed data are then sent through a second routine that calculates the projected baseline vectors for each observation, calibrates the brackets relative to unresolved calibrator stars, and outputs the calibrated visibilities.

CHAPTER 3

STELLAR SAMPLE AND METHODS

3.1 Sample Selection

It was the goal with our stellar sample to combine our directly measured angular sizes (θ_{LD}) with a known distance to calculate stellar linear radius (R_*), and to combine θ_{LD} with an observed spectral energy distribution to obtain estimates for effective temperature (T_{eff}). We then combine these radius and temperature estimates to place our stars on an HR diagram. Our sample consists of 6 O-type stars and 25 B-type stars with spectral types ranging from O7.5 to B9.5. All luminosity classes are represented with 3 supergiants, 16 giants, and 12 main sequence stars. Our stars lie in the galactic plane with a declination range of -14° to 70° and an apparent magnitude range of 1.6 to 5. Stars in our sample have an expected angular diameter of 0.2 mas to 1.0 mas. These constraints ensure that our stars have the necessary location, brightness, and angular size to be resolved with CHARA. To ensure accurate calculated parameters, only stars with a *Hipparcos* parallax error under 10% were chosen with the exception of the O stars which were all included regardless of parallax error size. Two of our O stars, λ Ori and ζ Ori are in stellar associations in Orion and three of our B stars, Electra, Maia, and Atlas, are members of the Pleiades cluster. A summary of our target stars and their parameters is given in Table 3.1.

It is very common for massive stars to be in double, or multiple, star systems, and several of our sample stars have close, bright companions that need to be considered during our interferometric fitting and/or our spectrophotometric modeling. Table 3.2 gives a summary

Table 3.1 Parameters of target stars

ID	Star Name	HD Number	Spectral Classification	V (mag)	$B - V$ (mag)	$V - K$ (mag)	T_{eff} (kK)	$\log g$ c.g.s	$v \sin i$ (km s $^{-1}$)
<i>a</i>	ξ Per	24912	O7.5 III(n)(f)	4.06	0.02	0.11	34.8 \pm 1	3.43 \pm 0.13	215
<i>b</i>	α Cam	30614	O9.5 Ia	4.29	0.05	0.05	29.5 \pm 0.8	3.04 \pm 0.13	111
<i>c</i>	λ Ori A	36861	O8 III((f))	3.47	0.01	-0.56	34.3 \pm 0.7	3.66 \pm 0.10	68
<i>d</i>	ζ Ori A	37742	O9.7 Ib	1.88	-0.11	-0.44	29.5 \pm 1	3.25 \pm 0.25	124
<i>e</i>	ζ Oph	149757	O9.2 IVnm	2.56	0.02	-0.06	32.5 \pm 0.9	3.65 \pm 0.10	348
<i>f</i>	10 Lac	214680	O9 V	4.88	-0.21	-0.62	36.4 \pm 1	3.99 \pm 0.05	124
<i>g</i>	λ Cas	2772	B8Vn	4.73	-0.10	-0.13	11.9 \pm 0.6	4.00 \pm 0.25	220
<i>h</i>	ζ Cas	3360	B2IV	3.66	-0.19	-0.59	21.5 \pm 0.5	3.91 \pm 0.03	17
<i>i</i>	γ Ari	11502	B9V	4.83	-0.03	-0.09	10.0 \pm 1	4.50 \pm 0.25	142
<i>j</i>	73 Cet	15318	B9III	4.28	-0.05	-0.09	10.6 \pm 1	4.00 \pm 0.25	57
<i>k</i>	17 Tau	23302	B6III	3.70	-0.11	-0.22	14.7 \pm 1	3.03 \pm 0.25	152
<i>l</i>	20 Tau	23408	B8III	3.87	-0.07	-0.12	13.8 \pm 1	3.50 \pm 0.25	37
<i>m</i>	27 Tau	23850	B8III	3.63	-0.09	-0.16	13.0 \pm 1	3.50 \pm 0.25	182
<i>n</i>	τ Tau	29763	B3V	4.28	-0.12	-0.36	16.6 \pm 1	4.00 \pm 0.25	147
<i>o</i>	β Tau	35497	B7III	1.65	-0.13	-0.38	13.6 \pm 0.1	3.80 \pm 0.25	67
<i>p</i>	32 Ori	36267	B5V	4.20	-0.13	-0.41	16.3 \pm 0.7	4.40 \pm 0.25	166
<i>q</i>	σ Leo	98664	B9.5V	4.05	-0.06	-0.10	10.5 \pm 0.1	3.90 \pm 0.25	60
<i>r</i>	η UMa	120315	B3V	1.86	-0.19	-0.49	17.7 \pm 0.3	4.00 \pm 0.25	158
<i>s</i>	τ Her	147394	B5IV	3.89	-0.15	-0.39	15.4 \pm 0.7	3.86 \pm 0.07	33
<i>t</i>	ζ Dra	155763	B6III	3.17	-0.11	-0.31	13.5 \pm 0.8	3.99 \pm 0.17	40
<i>u</i>	ι Her	160762	B3IV	3.80	-0.17	-0.43	18.2 \pm 1	3.82 \pm 0.13	10
<i>v</i>	γ Lyr	176437	B9III	3.24	-0.05	0.05	10.4 \pm 0.6	3.50 \pm 0.25	65
<i>w</i>	λ Aql	177756	B9Vn	3.44	-0.09	-0.22	10.7 \pm 1	4.15 \pm 0.05	125
<i>x</i>	ι Aql	184930	B5III	4.36	-0.08	-0.12	13.9 \pm 0.5	3.64 \pm 0.25	65
<i>y</i>	δ Cyg	186882	B9.5IV	2.87	-0.02	0.04	10.4 \pm 0.4	3.40 \pm 0.25	142
<i>aa</i>	α Del	196867	B9IV	3.77	-0.06	-0.08	11.0 \pm 0.1	3.96 \pm 0.25	141
<i>bb</i>	55 Cyg	198478	B3Ia	4.84	0.42	1.11	18.8 \pm 0.3	2.10 \pm 0.13	42
<i>cc</i>	β Cep	205021	B1IV	3.23	-0.22	-0.73	26.8 \pm 0.1	4.12 \pm 0.07	28
<i>ee</i>	ζ Peg	214923	B8V	3.40	-0.08	-0.15	11.4 \pm 0.6	3.89 \pm 0.09	161
<i>ff</i>	α Peg	218045	B9V	2.49	-0.04	-0.03	10.1 \pm 0.1	3.98 \pm 0.25	130
<i>gg</i>	105 Aqr	222661	B9.5V	4.49	-0.04	-0.11	10.9 \pm 0.2	4.30 \pm 0.25	136

Spectral types and magnitudes are taken from SIMBAD. Effective temperatures and gravities are average values taken from the sources listed in Table 4.4 for the O stars and listed in Section 5.2 for the B stars. $v \sin i$ values are from the Catalog of Stellar Rotational Velocities (Glebocki & Gnacinski 2005).

of these stars and their companions' properties as well as indicates whether the interferometry or spectrophotometry was corrected for the companion flux (see below). The second and third columns of 3.2 give the companion separation in arcseconds and the companion V -band magnitude difference, respectively. Columns 4 and 5 give the effective temperature and surface gravity assumed for the companion.

Table 3.2 Companions to target stars

Star	Separation (")	Δm_V	Temperature (K)	$\log g$	Spectrophotometric Correction	Interferometric Correction	Ref
HD 2772	0.42	0.15	10760	4.3	Y	Y	T00
HD 11502	7.4	-0.06	12000	4.3	Y	N	WDS
HD 23302	0.2	3.6	8400	4.3	Y	Y	WDS
HD 23850	0.013	1.62	12200	4.3	Y	Y	Z04
	0.5	3.0	9000	4.3	Y	N	Z04
HD 24912	2.4	9.8	N	N	T08
HD 29763	0.303	2.48	10500	4.3	Y	Y	B07
	...	1.5	13000	4.3	Y	N	P61
HD 36267	1.146	1.3	10500	4.3	Y	Y	F97
HD 36861	4.2	2.0	25400	4.21	Y	N	T08
HD 37742	0.037	2.2	26700	4.0	Y	Y	H13
	2.4	1.93	31000	3.8	Y	N	T08
HD 155763	0.059	1.03	13000	4.2	Y	Y	H00
HD 186882	2.51	3.38	6500	4.3	Y	N	H99
HD 196867	0.158	2.57	8300	4.6	Y	Y	H99
HD 205021	0.25	3.4	9300	4.3	Y	Y	WDS
HD 214680	3.6	10.0	N	N	T08
HD 222661	5.5	5.42	4800	4.6	Y	N	WDS

B07 = Balega et al. (2007), T00 = ten Brummelaar et al. (2000), F97 = Fu et al. (1997), H00 = Hartkopf et al. (2000), H99 = Horch et al. (1999), H13 = Hummel et al. (2013), P61 = Petrie & Ebbighausen (1961), T08 = Turner et al. (2008), WDS = Washington Double Star Catalog¹, Z04 = Zwahlen et al. (2004)

3.2 CHARA Array Observational Methods

Observations of our targets were made using the PAVO beam combiner (Ireland et al. 2008) and the CLIMB beam combiner (ten Brummelaar et al. 2013) at the CHARA Array (ten Brummelaar et al. 2005), located on Mt. Wilson Observatory in California. Combining the longest usable baseline currently available in the world offered by the CHARA Array and the operating wavelength range of the PAVO beam combiner (600 - 900 nm), we are able to achieve an extremely high angular resolution for our targets of about 0.2 milli-arcseconds. The CLIMB beam combiner was used for our larger targets and was operated in the *H*-band (1.67 μm) giving a resolution limit of about 0.5 milli-arcseconds.

Data for each target were taken using the standard ‘bracket’ method where one bracket

is three data scans in order of: calibrator - target - calibrator. Observing in brackets allows the visibilities recorded for the target to be properly calibrated and eventually fit to obtain angular diameters. Calibrators are chosen to be unresolved, single, slowly rotating stars that are close to the target in brightness and position in the sky. It is necessary to use these calibrator observations to calibrate target visibilities for instrumental losses in fringe visibility. Our calibrators are discussed further in the next section.

Observations of our targets with CHARA were accomplished from 2012 September to 2017 June with a total of 34 nights of observation. For all PAVO observations only one baseline, or two telescopes, was used at a time. For all CLIMB observations three telescopes were used at a time. Eight stars were observed with CLIMB over 13 nights and 27 stars were observed with PAVO over 21 nights. Four stars were observed with both CLIMB and PAVO to compare results from the two combiners.

The data were reduced using the standard data reduction pipelines written for use with the PAVO instrument (Ireland et al. 2008; Maestro et al. 2012) and the CLIMB instrument (ten Brummelaar et al. 2013). Details of the optical layout and data reduction process for each combiner are also discussed in sections 2.4.1 and 2.4.2. The PAVO data undergo background subtraction and photon-bias subtraction, with foreground frames, ratio frames and dark frames being taken during a shutter sequence that runs after fringe data are saved. The PAVO pipeline first takes the raw data through a routine that allows for the rejection of bad data frames. This allows the user to make cuts based on S/N values and loss of lock on fringes. The processed data are then sent through a second routine that calculates

the projected baseline vectors for each observation, calibrates the brackets and outputs the calibrated visibilities.

The CLIMB pipeline also takes the data through several steps during the reduction. The data file is separated into shutter and data sequences and fringes are identified in the data scans. At this point, the user may edit the data scans if fringes were lost for a portion of the scan. Finally, the background noise power spectra, mean power spectra of the fringes, and fringe visibility magnitude in frequency space are calculated. In CLIMB data, the fringes from each baseline must be separated by applying bandpass filters at the appropriate frequencies. The visibility estimator in the frequency domain is calculated by integrating the fringe peak in the power spectrum. This estimator is the most commonly used method and can be used in low SNR data (ten Brummelaar et al. 2012). Finally, the data are calibrated against the calibrator scans and a V^2 estimate based on the V_LOGNORM estimator is calculated. The derivation of this estimator can be found in ten Brummelaar et al. (2005). Closure phase was measured for CLIMB 3-telescope data. However, these measurements were not used because they were generally not different from zero within errors.

The visibility data were fit with a limb-darkened, single star, disk model with each point weighted by the error in V^2 . Linear limb-darkening coefficients were interpolated from the tables available in Claret & Bloemen (2011), using the photospheric parameters given in Table 3.1. These limb darkening coefficients μ were calculated for model atmospheres that adopt a solar metallicity and a microturbulent velocity of 2 km s^{-1} . It is important to note that a linear limb-darkening law is a rough approximation and may not reflect the actual limb-

darkening function. Additionally, the limb-darkening coefficient for a given star will have a different value in the R - and H -band. Limb-darkening effects will not be as pronounced for hot stars as for cooler star with more extended atmospheres. For this reason we have chosen to fix the limb-darkening coefficient instead of fitting for it as a free parameter with angular size. For stars close to the resolution limit of the combiner, or sometimes for poorly calibrated visibility points, a few calibrated visibilities ($\sim 7\%$) would have an unphysical value ($V^2 > 1$). This occurred for only a few stars in our sample ($\sim 5\%$) and these points were rejected from the fitting process.

Observing data, including dates, baselines and calibrated visibilities, are given in a table in a separate machine readable text file. Table 3.3 shows example data and defines each column. Column 4 gives the spatial frequency, or baseline λ^{-1} , and Column 5 and 6 give the u and v coordinates in cycles arcsec^{-1} . Column 10 gives the adjusted values for visibility squared for the cases where the visibilities were corrected for the flux of a close companion (see Section 3.2.1 and Table 3.2).

Table 3.3 Calibrated Visibilities

HD Number	MJD	Telescope Pair	$10^{-6}B/\lambda$ (rad^{-1})	u ($''^{-1}$)	v ($''^{-1}$)	Baseline (m)	V^2	ΔV^2	V_c^2	ΔV_c^2
(1)	(2)	(3)	(4)	(5)	(6)	(7)	(8)	(9)	(10)	(11)
24912	57340	W1E1	391.03	-1857.16	-380.64	310.28	0.668	0.025
24912	57340	W1E1	394.91	-1875.60	-384.42	310.28	0.674	0.052
24912	57340	W1E1	398.87	-1894.40	-388.28	310.28	0.675	0.035
24912	57340	W1E1	402.65	-1912.35	-391.96	310.28	0.666	0.031
37742	57340	W1E1	348.55	-1631.83	-438.96	276.58	0.151	0.031	0.193	0.031
37742	57340	W1E1	352.01	-1648.03	-443.32	276.58	0.243	0.089	0.311	0.089
37742	57340	W1E1	358.91	-1680.32	-452.01	276.58	0.175	0.048	0.224	0.048
37742	57340	W1E1	362.34	-1696.39	-456.33	276.58	0.115	0.020	0.148	0.020
37742	57340	W1E1	365.65	-1711.87	-460.49	276.58	0.172	0.053	0.221	0.053

3.2.1 Interferometric Correction for Companion Flux

For stars with close, bright companions (indicated in Table 3.2) a correction was made to the calibrated visibilities to account for the presence of incoherent flux introduced by the companion. The projected angular separation, difference in magnitude, and the seeing estimate during the observation are used to calculate the intensity for each component assuming a Gaussian profile for the seeing distribution. The squared visibility is then corrected with a scale factor of $(1 + I_{\text{secondary}}/I_{\text{primary}})^2$ (Boyajian et al. 2008). The integration range for the intensities depends on the field of view for each combiner’s detector. For CLIMB, the pixel scale of 0.808 arcsec per pixel for the NIRO camera was used, and for PAVO a field of view of 1 arcsec was used.

3.2.2 Calibrators

Our stars have very small angular diameters so it was difficult to find good calibrators. A good calibrator will be a similar magnitude to the target and close to it in the sky. It will also have as small an angular size as possible given these constraints. The underlying concept here is to have the calibrator small enough to be unresolved by the combiner. This will allow any uncertainty in the calibrator’s size or error to be negligible as an unresolved target will have a visibility equal to 1 regardless of its angular size. It was the goal to have two calibrators used for each target but in some cases this was not possible and only one was used.

However, for some O-type stars it was not possible to use a calibrator with a smaller

angular size than the target and careful consideration of the error analysis was required. For all O stars the angular size of the calibrator was varied by plus and minus one sigma and the visibilities were re-calibrated using these sizes. The range in the spread of the fits for each O star was then included in our final error estimation. Calibrators used for each target and their angular sizes are given in Table 3.4 with the calibrators used for the O stars at the top of the table. JMMC angular diameters were used for all calibrator sizes in analysis, with the exception of the calibrator for ζ Oph, HD 154445. JMMC diameters are predicted by making a polynomial fit of the differential surface brightness of a star as a function of spectral type. The fit is computed by using measured stellar diameters and photometry and can then be applied to stars without these direct measurements. The differential surface brightness is independent of distance and only depends on the stellar diameter and observed magnitudes (Chelli et al. 2016). In a recent study, Swihart et al. (2017) found an angular size for HD 154445 of 0.18 mas. CADARS reports an angular size of 0.16 mas and a spectroscopic study by Lyubimkov et al. (2002) results in a diameter of 0.21 mas. These diameters are all significantly different than the JMMC value of 0.28 mas so we have adopted the angular diameter found by Swihart et al. (2017) of 0.18 mas for this calibrator. The JMMC diameters are in good agreement with independent measurements for all other calibrators.

Table 3.4: Calibrators used for this study. Target ID is the star ID given in Table 3.1.

Star	JMMC		Target	CADARS Swihart et al. (2017)	
	θ_{LD} (mas)	SpTy		θ_{LD} (mas)	θ_{LD} (mas)
HD 27777	0.172±0.012	B8V	<i>a</i>	0.20	0.175±0.037
HD 29646	0.199±0.014	A2V	<i>a, d, n</i>	...	0.249±0.019

HD 34233	0.132±0.009	B5V	<i>b</i>	0.13	...
HD 34989	0.132±0.009	B1V	<i>c</i>	0.10	0.118±0.026
HD 37320	0.158±0.011	B8III	<i>c</i>	...	0.163±0.035
HD 38831	0.149±0.010	A0Vs	<i>b</i>	0.17	...
HD 154445	0.280±0.019	B1V	<i>e</i>	0.16	0.180±0.041
HD 204403	0.171±0.006	B3V	<i>f</i>	0.16	0.154±0.048
HD 212978	0.106±0.004	B2V	<i>f</i>	0.10	...
HD 213272	0.175±0.005	A2V	<i>f</i>	0.16	...
HD 1279	0.189±0.005	B8III	<i>h</i>	...	0.166±0.040
HD 4142	0.164±0.005	B5V	<i>g</i>	0.16	0.160±0.034
HD 10982	0.208±0.006	B9.5V	<i>i</i>	0.19	0.203±0.034
HD 14263	0.269±0.007	A1V	<i>j</i>	0.29	...
HD 15633	0.265±0.007	A3V	<i>j</i>
HD 17036	0.218±0.006	B9Vn	<i>j</i>	0.22	...
HD 18216	0.145±0.004	B9V	<i>j</i>
HD 19600	0.176±0.005	A0V	<i>k</i>	0.17	...
HD 23338	0.324±0.030	B6IV	<i>m</i>	0.33	0.363±0.018
HD 23753	0.229±0.006	B8V	<i>m</i>	0.22	...
HD 23923	0.171±0.005	B8V	<i>k, l</i>	0.18	...
HD 27309	0.237±0.006	A0sp	<i>n</i>
HD 35600	0.329±0.010	B9Ib	<i>o</i>	0.28	0.277±0.020
HD 36371	0.401±0.039	B4Ib	<i>o</i>	0.38	...
HD 36653	0.149±0.005	B3V	<i>p</i>	...	0.137±0.042
HD 97585	0.270±0.009	A0V	<i>q</i>	0.25	0.273±0.017
HD 119024	0.315±0.009	A2Vnp	<i>r</i>	...	0.275±0.028
HD 119124	0.417±0.010	F7.7V	<i>r</i>
HD 149081	0.174±0.005	A1V	<i>s</i>
HD 149212	0.329±0.009	A0III	<i>t</i>	0.35	...
HD 149650	0.236±0.006	A2V	<i>s</i>	...	0.262±0.012
HD 156295	0.366±0.011	A7V	<i>t</i>	0.39	0.319±0.008
HD 161693	0.260±0.008	A2V	<i>u</i>	...	0.267±0.021
HD 167965	0.190±0.005	B7IV	<i>u</i>	0.18	0.167±0.036
HD 170920	0.303±0.008	A5IV/V	<i>w</i>
HD 171301	0.222±0.006	B8IV	<i>v</i>	...	0.189±0.040
HD 178187	0.281±0.008	A4III	<i>v</i>	...	0.266±0.012
HD 180782	0.199±0.005	A0V	<i>x</i>
HD 181440	0.249±0.007	B9III	<i>x</i>
HD 192514	0.497±0.036	A5IIIIn	<i>y</i>	0.40	0.411±0.060
HD 194012	0.433±0.011	F7V	<i>aa</i>	0.47	...
HD 195556	0.214±0.008	B2.5IV	<i>bb</i>	0.21	0.217±0.050
HD 196724	0.318±0.027	A0V	<i>aa</i>	0.33	0.331±0.020

HD 196740	0.215±0.007	B5IV	<i>aa</i>	0.22	0.245±0.012
HD 197076	0.459±0.012	G5V	<i>aa</i>
HD 197392	0.200±0.005	B8II-III	<i>bb</i>	...	0.174±0.042
HD 203245	0.166±0.005	B6V	<i>bb</i>	0.15	...
HD 204770	0.218±0.007	B7V	<i>cc</i>	0.20	0.192±0.041
HD 207636	0.166±0.005	A0V	<i>cc</i>
HD 216735	0.322±0.030	A1V	<i>ee, ff</i>	0.33	0.368±0.029
HD 217891	0.296±0.009	B6Ve	<i>ee</i>	0.28	0.278±0.059
HD 218700	0.247±0.007	B9III	<i>ee, ff</i>	...	0.227±0.041
HD 218918	0.390±0.033	A5Vn	<i>ff</i>	0.37	0.325±0.028
HD 222847	0.254±0.007	B9V	<i>gg</i>	0.23	...

3.3 Spectral Energy Distribution Modeling Methods

The goal of our spectrophotometric analysis was to compare our results from directly measured angular sizes and observed spectra to predictions of parameters from a stellar atmosphere model. Given a wavelength range and flux from a spectrum, a model can predict what the best fit effective temperature and angular size should be. We can then compare the model predictions against our interferometrically determined angular sizes and effective temperature estimates determined from spectral line studies in the literature.

We used spectrometry from multiple sources and compared these spectra to TLUSTY O or B star models (Lanz & Hubeny 2003, 2007), or the ATLAS9 models (Kurucz 1992; Castelli & Kurucz 2004) depending on what was appropriate to the temperature of the star. Our fitting routine used a grid search method to estimate the goodness of fit for models based on three parameters: angular size (θ_{LD}), effective temperature (T_{eff}), and extinction ($E(B - V)$). The temperature range and step size was chosen to match the models in the TLUSTY or ATLAS9 grid. We rebinned the UV and optical spectra to a low resolving

power of $R = \lambda/\Delta\lambda = 60$ on a $\log \lambda$ grid in order to better balance the sampling across the whole spectrum. For each pair of θ_{LD} and T_{eff} , a reduced χ^2 fit was used to find the best fit $E(B - V)$ value for a fixed value of $R = 3.1$. This created a matrix of minimum χ^2 values for each θ_{LD} and T_{eff} . The routine searches a grid of 1,000 $E(B - V)$ values ranging from 0 to 1 with a step size of 0.001. The $E(B - V)$ value was not allowed to be negative or greater than 1 during the fitting process and was reset to 0 or 1 respectively when this happened. The grid for angular size has 200 values ranging from 0.01 mas to 2 mas with a step size of 0.01 mas. The temperature grid and step size matches the grid of the atmospheric model being used for the fit. The model spectrum was rebinned to $R = 60$ in the same way as the observed SED, and then the fluxes were attenuated for interstellar extinction using the IDL Code *fmrcurve.pro* for a ratio of total-to-selective extinction of 3.1 (Fitzpatrick 1999). Finally the model spectra were rescaled according to the assumed angular diameter and interpolated to the observed wavelength points for direct comparison with the observed SED.

Contour maps were created by plotting the χ^2 matrix resulting from the best fit reddening as a function of effective temperature and angular size for each star. The shape of the contours show that effective temperature has an approximately inverse square dependence on angular size. This can be expected by looking at the relationship between the emitted F_λ and observed f_λ monochromatic flux:

$$F_\lambda(T_{\text{eff}}, \log g, Z) = f_\lambda 10^{0.4A_\lambda} / (\theta/2)^2 \quad (3.1)$$

where A_λ is the extinction (in magnitudes) and θ is the angular diameter (in radians). The monochromatic flux in the Rayleigh-Jeans tail varies with temperature as $F_\lambda \propto T_{\text{eff}}$, so for

a given observed monochromatic flux and extinction, the derived temperature will vary as $T_{\text{eff}} \propto \theta^{-2}$ and the fractional uncertainty will be $\Delta T_{\text{eff}}/T_{\text{eff}} \approx 2\Delta\theta/\theta$. The contours for the $E(B - V)$ values are parallel sequences that follow the curve of the minimum in chi-squared space. Therefore, any temperature and angular size combination chosen along the minimum will have a very similar $E(B - V)$ value.

For our extinction curves we have used a fixed value of $R = 3.1$. However, allowing R to vary will shift the SED contours to larger angular sizes and lower temperatures for larger R , and smaller angular sizes and higher temperatures for smaller values of R . For example, fitting the SED of ξ Per with $R = 3.45$ yields a model diameter of ~ 0.27 mas, compared to the model diameter of 0.243 mas at $R = 3.1$. In the region of observation for our spectra, the assumed value of surface gravity will have a minimal contribution. To test this, we compared models at $\log g = 3.5$ and $\log g = 4.5$ for a single star. Even with a large difference in $\log g$ of 1 dex, the flux for each model only differed on the 1% level.

3.3.1 Spectrophotometric Correction for Companion Flux

In cases where there was a close, bright companion (Table 3.2), the extra flux from the companion was accounted for in our fitting. The effective temperature and surface gravity of the companion were used to calculate a model companion spectrum in the same way as above using the TLUSTY O star models (Lanz & Hubeny 2003), B star models (Lanz & Hubeny 2007), or ATLAS9 models (Kurucz 1992; Castelli & Kurucz 2004), depending on the temperature of the companion. The companion flux was then rescaled according to the V -band magnitude difference Δm_V (Table 3.2), with the relation $\frac{f_2}{f_1} = 10^{-0.4\Delta m_V}$, and added

to the model flux calculated for the primary. This combined flux spectrum was used for spectrophotometric fitting of the observed SED.

3.3.2 TLUSTY Models

The TLUSTY models have a grid of atmospheric models for O stars and B stars. They are metal line-blanketed, non-LTE, plane-parallel, hydrostatic model atmospheres. The models make use of efficient numerical methods, including Accelerated Lambda Iteration and Complete Linearization, to compute the equations of radiative transfer, hydrostatic equilibrium, statistical equilibrium, and charge and particle conservation (Hubeny & Lanz 1995). Model grids can be found at <http://nova.astro.umd.edu/index.html>.

The O star models (Lanz & Hubeny 2003) have a temperature range of 27,500 to 55,000 K with a step size of 2,500 K. The surface gravities range from $\log g = 3.0$ to 4.75 (c.g.s. units) with a step size of 0.25 dex. The models have 10 different chemical compositions available from metal rich compared to solar, to metal free. We have used the models with solar abundances because massive stars will be relatively young and should have close to solar metallicities. The O star models assume a solar helium abundance and a microturbulent velocity of $v_t = 10 \text{ km s}^{-1}$.

The B star model grid (Lanz & Hubeny 2007) has a temperature range of 15,000 to 30,000 K with a step size of 1,000 K. The surface gravities range from $\log g = 1.75$ to 4.75 (c.g.s. units) with a step size of 0.25 dex. There are 6 different chemical compositions available, ranging from metal rich to metal poor, and we have again chosen models with solar abundances. The B star models assume a solar helium abundance and a microturbulent

velocity of $v_t = 2 \text{ km s}^{-1}$.

3.3.3 ATLAS9 Models

The ATLAS9 models are LTE, plane-parallel stellar atmospheric models that use the opacity distribution function method to handle line opacities (Kurucz 1992; Castelli & Kurucz 2004). These models do not take into account non-LTE effects. The effective temperatures of the models range from 3,500 to 50,000 K. However, we have only used the ATLAS9 models up to the limit of the TLUSTY B models, with some overlap, at 20,000 K. The TLUSTY models incorporate the effects of line-blanketing and non-LTE, so they will be more accurate for our higher temperature B stars. With that restriction, our range of temperatures for the ATLAS9 models goes from 5,000 to 20,000 K with a step size of 1,000 K. Surface gravities range from $\log g = 0.0$ to 5.0 (c.g.s. units) with steps of 0.5 dex. The models are scaled for 19 different abundances and 5 different microturbulent velocities. For our fits we assumed solar abundance and a microturbulent velocity of $v_t = 2 \text{ km s}^{-1}$. Model grids can be found at <http://kurucz.harvard.edu/grids.html>.

CHAPTER 4

EFFECTIVE TEMPERATURES AND ANGULAR SIZES OF O STARS

4.1 CHARA Array Interferometry

The visibility measurements for our O stars were obtained from interferometric observations with the PAVO beam combiner and were fit to a limb-darkened, single star, disk model with each point weighted by the error in V^2 . Linear limb-darkening coefficients in the R -band were interpolated from the tables available in Claret & Bloemen (2011), using the photospheric parameters given in Table 3.1. These limb darkening coefficients μ were calculated for model atmospheres that adopt a solar metallicity and a microturbulent velocity of 2 km s^{-1} . Figures 4.1 through 4.6 show the visibility measurements for each star (or visibility corrected for the

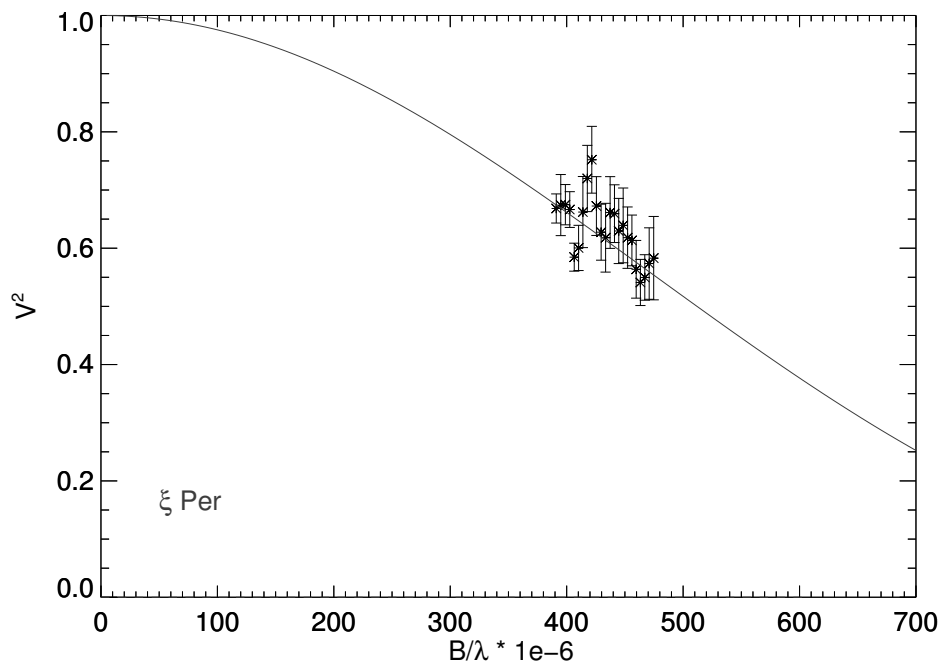


Figure 4.1 Squared visibility versus spatial frequency for ξ Per (HD 24912). The solid line indicates the best fit for a single star limb-darkened disk model.

companion flux in the case of ζ Ori A) plus an error-weighted fit of all the data with a limb-darkened disk model. Table 4.1 lists the derived uniform disk (UD) and limb-darkened (LD) disk angular diameters θ , the latter calculated for a linear limb-darkening coefficient μ .

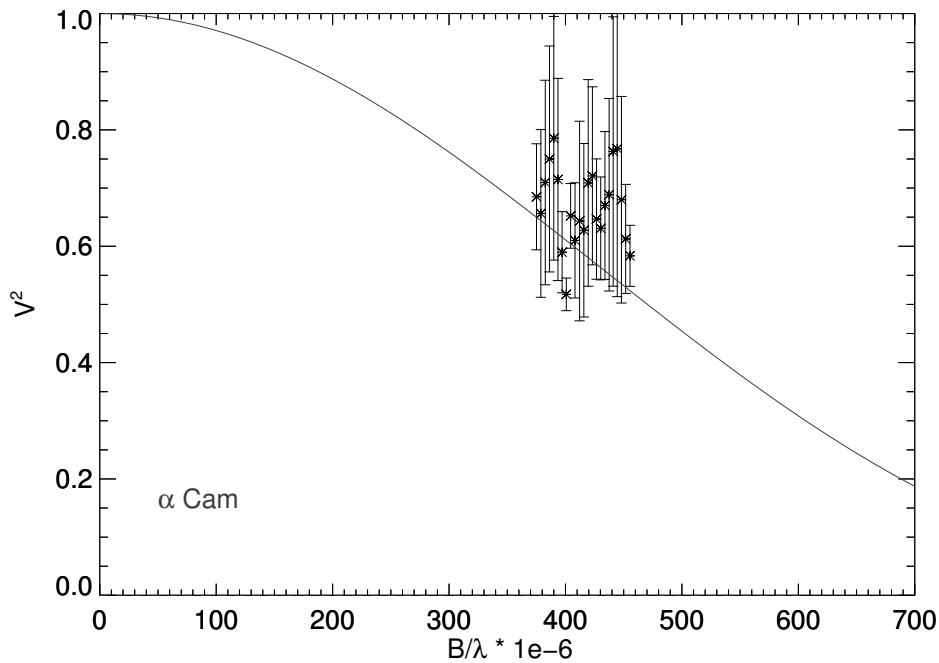


Figure 4.2 Squared visibility versus spatial frequency for α Cam (HD 30614). The solid line indicates the best fit for a single star limb-darkened disk model.

The fitting scheme assigned an uncertainty to the angular diameter based upon the size of the residuals to the fit. However, multiple-night observations of stellar diameters with PAVO show an external night-to-night scatter that is larger than indicated by the uncertainty from measurements within a night by about 5% (Maestro et al. 2013). We applied this 5% uncertainty to our error budget. Two of the calibrators used for 10 Lac are larger than the star itself (0.12 mas). These calibrators can still be used in the analysis but the error in their sizes will play a much bigger role than usual in the final fitted size of the target. To

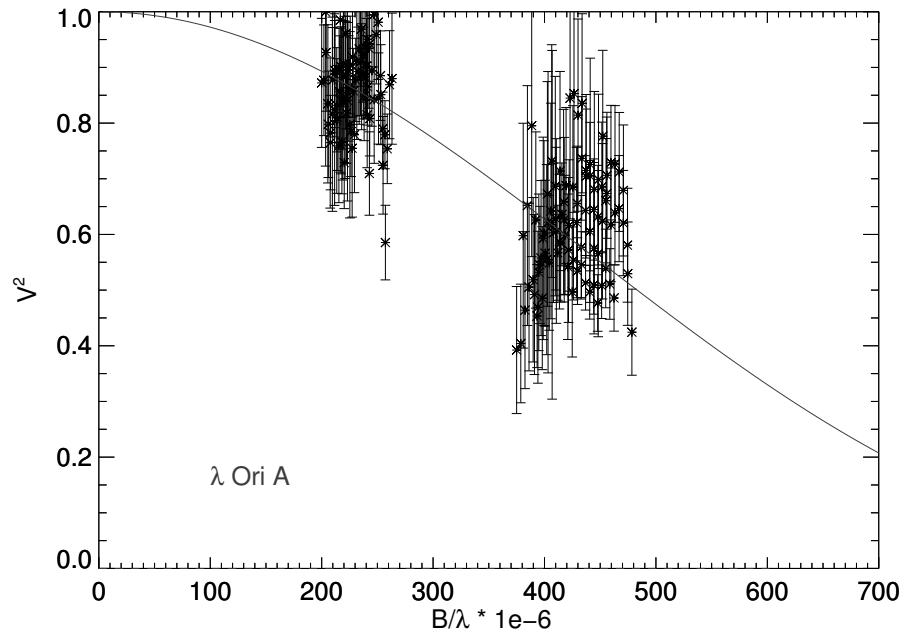


Figure 4.3 Squared visibility versus spatial frequency for λ Ori A (HD 36861). The solid line indicates the best fit for a single star limb-darkened disk model.

account for this effect, we fit the data for 10 Lac after adjusting the calibrator sizes by plus and minus one sigma. We then averaged the resulting sizes for our final angular size and took the range between the sizes. We subsequently applied this method to all O stars in the sample. Thus, the final uncertainties given in Table 4.1 are the quadratic sum of 1) the uncertainty from the residuals of the error weighted fit, 2) the uncertainties from the night-to-night external error, 3) the half-range from varying the calibrator size, and 4) the errors introduced by removing the calibration bias in V^2 (only for ξ Per, α Cam, and ζ Ori A; see Section 4.1.1 below). A comparison of our measured angular diameters to previously estimated values is given in Table 4.2.

The observations on different nights were not averaged for ζ Oph as there is a true physical difference in size at different baselines due to its rotational distortion (Section 4.4.3). ζ Oph's

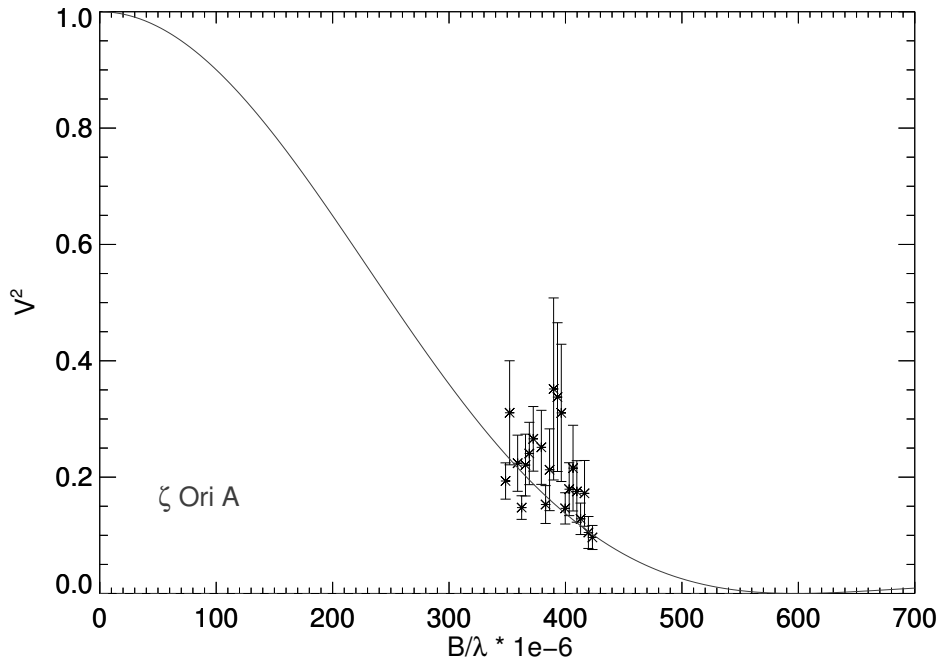


Figure 4.4 Squared visibility versus spatial frequency for ζ Ori A (HD 37742). The solid line indicates the best fit for a single star limb-darkened disk model.

Table 4.1 Observations and measured angular diameters of O stars

Star	HD	Baselines	N_{V^2}	θ_{UD} (mas)	μ	θ_{LD} (mas)
ξ Per	24912	W1E1	23	0.210 ± 0.016	0.174	0.220 ± 0.015^1
α Cam	30614	S1E1	23	0.226 ± 0.014	0.250	0.250 ± 0.023^1
λ Ori A	36861	S1E1;W1E1	168	0.217 ± 0.012	0.253	0.224 ± 0.012
ζ Ori A	37742	W1E1	21	0.424 ± 0.023	0.203	0.460 ± 0.040^1
ζ Oph	149757	S2W1	69	0.454 ± 0.025	0.204	0.462 ± 0.025
		S2E2	161	0.532 ± 0.029		0.540 ± 0.029
10 Lac	214680	S1E1	119	0.12 ± 0.02	0.183	0.12 ± 0.02

¹ θ_{LD} corrected for calibration bias effects (discussed in Section 4.1.1) and represents a lower limit on the angular size.

rapid rotation caused our angular size measurements on different baselines to differ by $\sim 15\%$.

An ellipsoidal fit of the angular diameter as a function of position angle is shown in Figure

4.7 and these measurements are discussed further in Section 4.4.3.

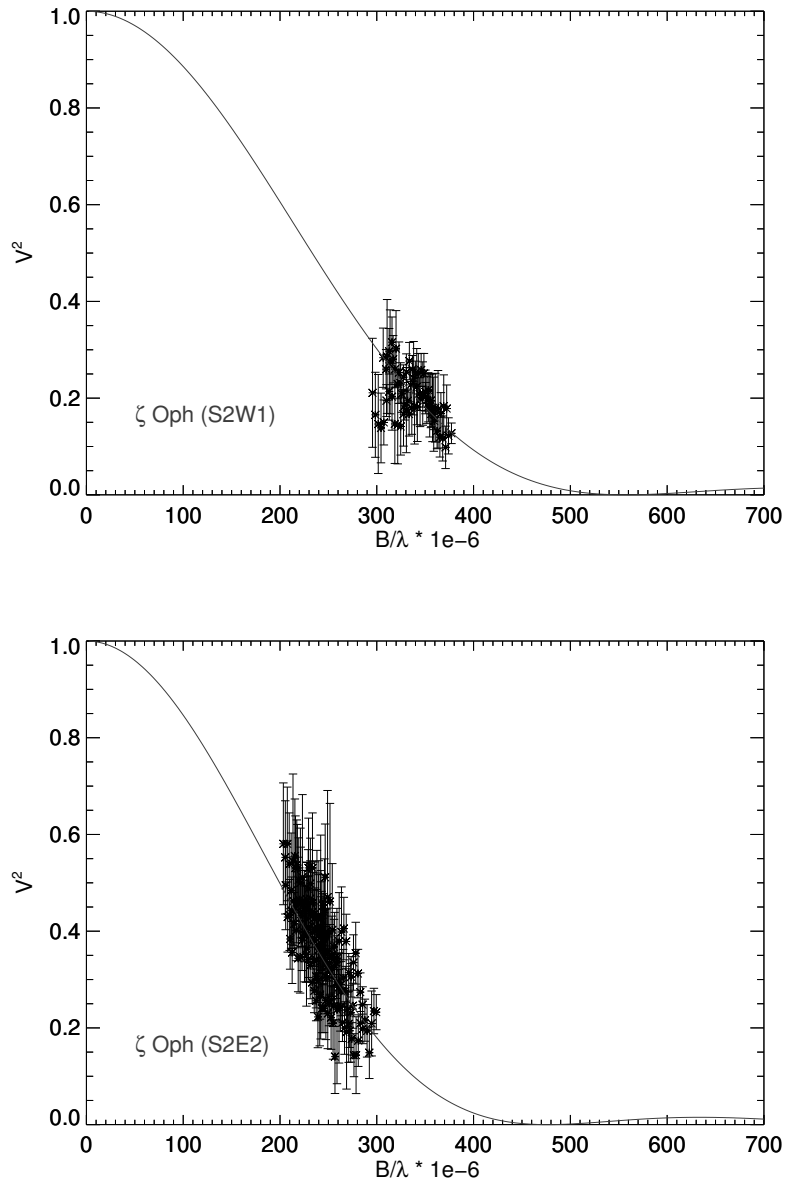


Figure 4.5 Squared visibility versus spatial frequency for ζ Oph (HD 149757). The solid line indicates the best fit for a single star limb-darkened disk model.

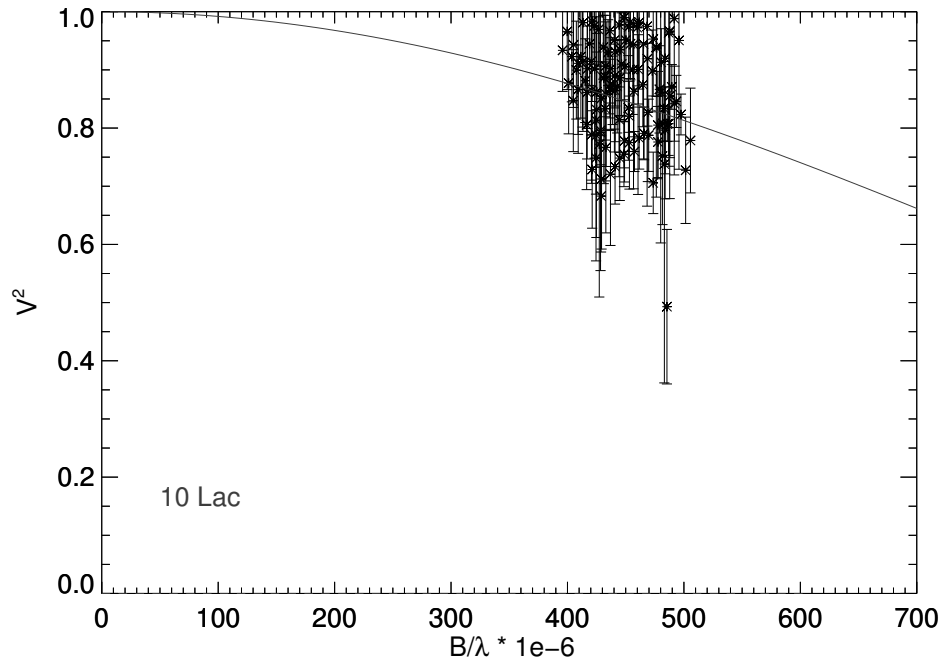


Figure 4.6 Squared visibility versus spatial frequency for 10 Lac (HD 214680). The solid line indicates the best fit for a single star limb-darkened disk model.

Table 4.2 Comparison of measured O star angular diameters to literature values

Star	θ_{LD} (mas)	Underhill 1979 θ_{LD} (mas)	Hanbury Brown 1974 θ_{LD} (mas)	CADARS θ_{LD} (mas)	T_{eff} θ_{LD} (mas)
ξ Per	0.220 ± 0.015^1	0.26	0.243 ± 0.010
α Cam	0.250 ± 0.023^1	0.292 ± 0.003	...	0.29	0.245 ± 0.010
λ Ori A	0.224 ± 0.012	0.235 ± 0.003	...	0.24	0.228 ± 0.009
ζ Ori A	0.460 ± 0.040^1	0.527 ± 0.010	0.48 ± 0.04	0.47	0.485 ± 0.019
ζ Oph	0.462 ± 0.025 0.540 ± 0.029	0.494 ± 0.003	0.51 ± 0.05	0.54	0.536 ± 0.021
10 Lac	0.11 ± 0.02	0.123 ± 0.002	...	0.13	0.120 ± 0.005

¹ θ_{LD} corrected for calibration bias effects (discussed in Section 4.1.1) and represents a lower limit on the angular size. CADARS = Pasinetti Fracassini et al. (2001), T_{eff} = diameter derived from the literature temperature and SED.

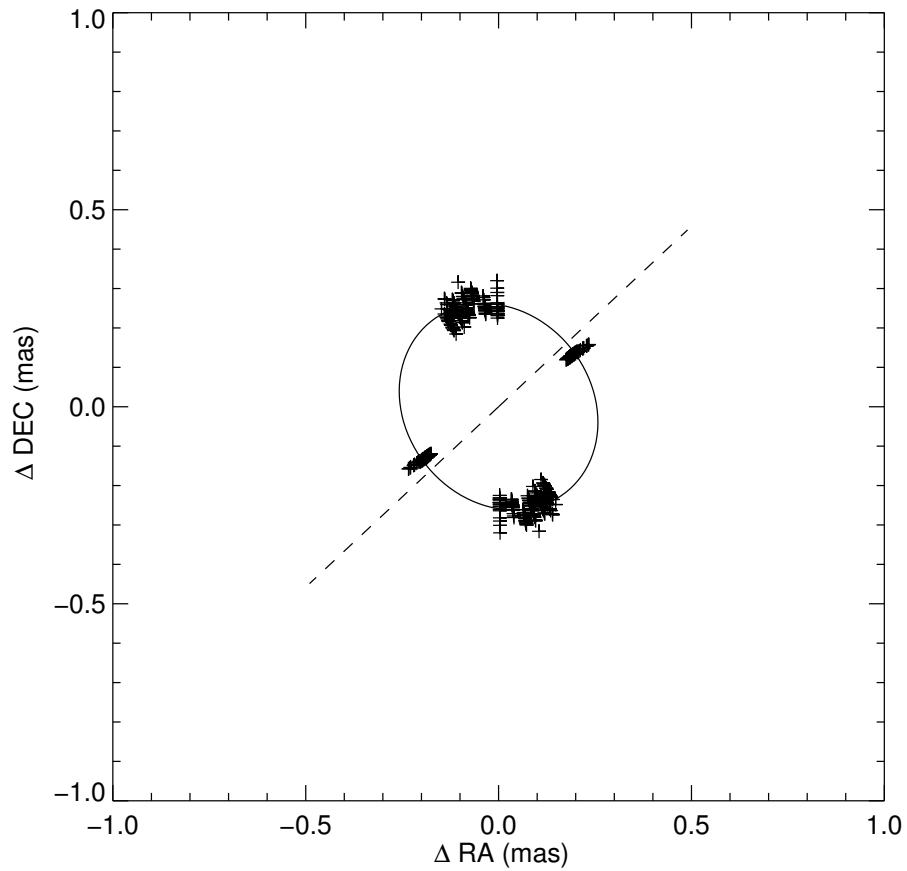


Figure 4.7 A simple ellipse fitted to our interferometric data for ζ Oph. Each symbol shows the derived angular size of a limb-darkened star whose visibility equals the observed value, and each is plotted at a position angle derived from the (u, v) spatial frequencies of the observation. The fit was made of the major and minor axes with the position angle of the minor axis set by published polarimetry. The dashed line shows the adopted rotational axis of the star at a position angle of 132.5° .

4.1.1 Angular Size Calibration Bias Correction

Upon inspection of the visibility curves for our O stars (shown in Figures 4.1 through 4.6) it appeared that there may exist a systematic bias in the data for some stars. This trend results in systematically larger errors for higher visibilities (smaller angular diameters) and is revealed in the fact that the V^2 measurements with the lowest uncertainties appear to fall below the fit while those with larger uncertainties lie above the fit. This trend is seen in the data for ξ Per, α Cam, and ζ Ori A. These are also the three stars with only one bracket of data on one night of observation with less than optimal observing conditions. We suspect that the bias arises because the fainter calibrator stars had more gaps in coverage and a lower SNR during periods of poor seeing, and consequently the raw visibilities of the calibrators vary widely over one observation instead of giving a consistent measurement as expected. The pattern in the visibility errors matches the instability of the calibrator visibilities with the points with the smallest errors corresponding to the points where the raw visibilities of the calibrators changed the least from one scan to the next.

To investigate and correct for this bias we considered the derived limb-darkened diameter for each visibility measurement as a function of the fractional uncertainty in the visibility, $\Delta V^2/V^2$. An error weighted fit of this trend was made and is shown for each star in Figures 4.8, 4.9, and 4.10. The presence of this bias means that the derived angular size from a simple error weighted fit $\theta_{LD}(wt)$ will underestimate the actual angular diameter. We decided to replace these estimates with the results from the linear bias fits evaluated at the lowest observed fractional uncertainty $\Delta V^2/V^2$ (best measurements). These biased corrected

estimates $\theta_{LD}(\text{corr})$ are listed in Tables 4.1 and 4.2. It is important to note that these may be lower limits of the angular size as the linear trend may continue to smaller values of $\Delta V^2/V^2$ where we do not have data coverage. However, it is likely that as $\Delta V^2/V^2$ approaches 0 the bias corrected angular diameters will reach a constant value and the V^2 distributions of the target and calibrators will become similar as expected in normal quality data.

The uncertainties in the corrected estimates $\sigma(\theta_{LD}(\text{corr}))$ were taken as the quadratic sum of the size of the correction term ($\theta_{LD}(\text{corr}) - \theta_{LD}(\text{wt})$) plus the errors associated with the bias trend fit and with the original weighted fit. Note that the fits shown in the visibility plots in Figures 4.1, 4.2, 4.4, 4.8, 4.9, and 4.10 all correspond to the initial weighted fits ($\theta_{LD}(\text{wt}) = 0.21, 0.23,$ and 0.43 mas for ξ Per, α Cam, and ζ Ori A, respectively) rather than the bias corrected angular diameters. Given the presence of a calibrator bias in the visibility measurements of these three stars, we regard their derived angular diameters as preliminary results that will need verification.

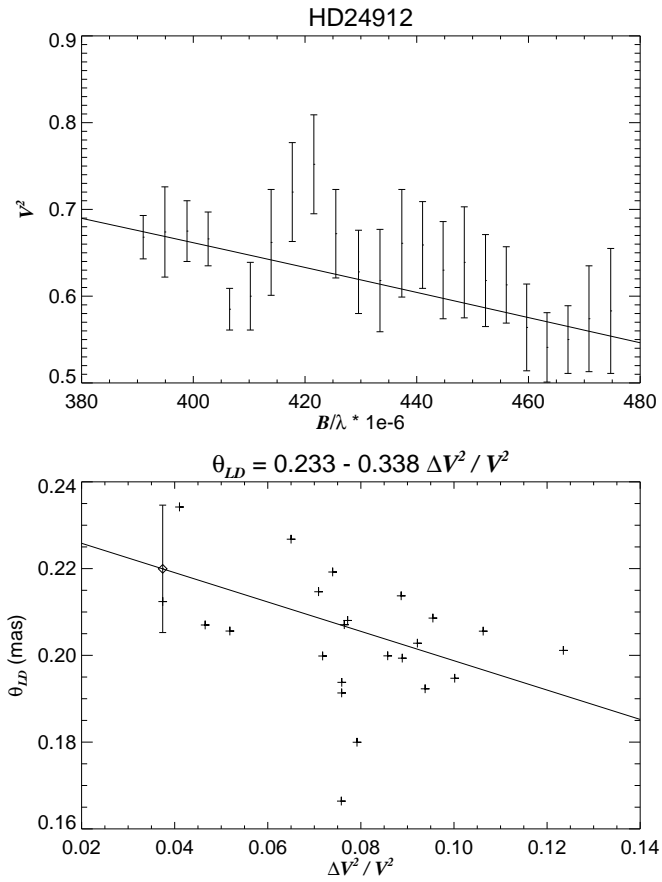


Figure 4.8 Top panel: An enlarged portion of the visibility curve for ξ Per together with fit from simple uncertainty weighting. Lower panel: The derived limb darkened angular diameter for each measurement plotted as a function of the fractional error in visibility. The linear fit of the trend is shown as a solid line and written as a formula above the plot. The diamond symbol on the left side of the fit shows the bias corrected angular diameter that we adopt.

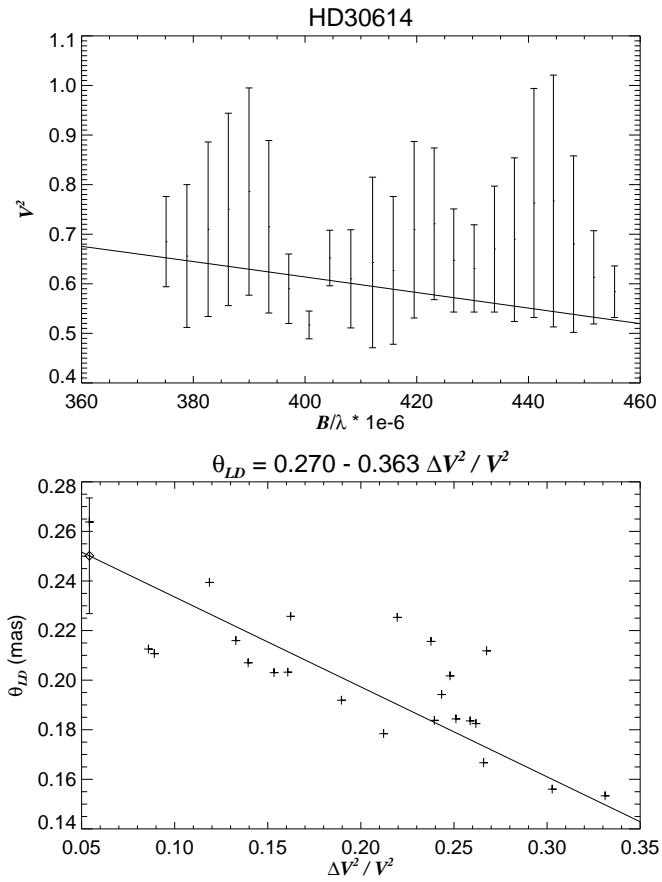


Figure 4.9 Top panel: An enlarged portion of the visibility curve for α Cam together with fit from simple uncertainty weighting. Lower panel: The derived limb darkened angular diameter for each measurement plotted as a function of the fractional error in visibility. The linear fit of the trend is shown as a solid line and written as a formula above the plot. The diamond symbol on the left side of the fit shows the bias corrected angular diameter that we adopt.

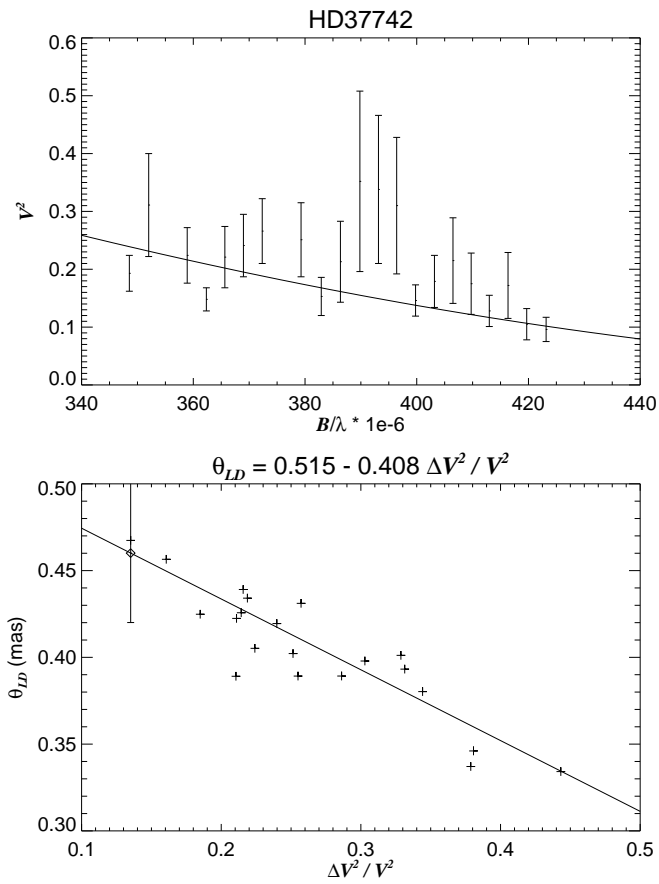


Figure 4.10 Top panel: An enlarged portion of the visibility curve for ζ Ori A together with fit from simple uncertainty weighting. Lower panel: The derived limb darkened angular diameter for each measurement plotted as a function of the fractional error in visibility. The linear fit of the trend is shown as a solid line and written as a formula above the plot. The diamond symbol on the left side of the fit shows the bias corrected angular diameter that we adopt.

4.2 Spectrophotometry

We used spectrometry from multiple sources for our targets to span the wavelength range from ultraviolet to infrared. Sources used for each part of the spectrum are given in Table 4.3. Infrared WISE points were not used for our supergiant and giant O stars because they often have winds that give off excess flux in the far infrared. This would skew our fitting as we are interested in the size of the star itself and not any winds associated with it. Spectra obtained from IUE were recalibrated with a routine by Massa & Fitzpatrick (2000) to correct the flux values. All flux values in the spectra were assigned a uniform 3% error to ensure our fitting program fit all points equally and did not give more weight to one part of the spectrum. The exception to this was 10 Lac which had very good data available in the ultraviolet and optical from HST/STIS. The errors on these flux values were much lower than 3%, and the original error values were used for the fitting.

The spectra were compared to the TLUSTY O star stellar atmosphere models that assumed solar metallicity and a microturbulent velocity of 10 km s^{-1} (Hubeny & Lanz 1995). Our fitting routine used a grid search method to fit for three parameters and is described in detail in Section 3.3. In cases where there was a close, bright companion, as with ζ Ori A, the extra flux from the companion was accounted for in our fitting. The effective temperature and surface gravity of the companion were used to calculate the flux using either the TLUSTY O star or B star models, depending on the temperature of the companion. This flux was then added to the model flux calculated for the primary and this combined flux was used for our spectrophotometric fitting and spectral energy distributions.

Table 4.3 O Star Spectrophotometry Sources

Star	Far UV	Near UV	Optical	IR
ξ Per	SWP45474	LWP23809	SP1	2MASS
α Cam	HUT	LWP17592	SP2	2MASS
λ Ori A	OAD	OAD	SP1	2MASS
ζ Ori A	SWP33049	LWP11671	SP3	2MASS
ζ Oph	SWP33050 SWP06776 SWP18252	LWP12826 LWP12637 LWP14381	SP1	2MASS, WISE, AKARI, Spitzer, IRAS
10 Lac	SWP*+STIS	HST/STIS	HST/STIS	2MASS, WISE, AKARI, IRAS

The UV spectra are primarily from the archive of the *International Ultraviolet Explorer* (low dispersion, large aperture) where the file number is related to the camera: SWP = Short Wavelength Prime and LWP = Long Wavelength Prime. SWP* refers to the average of 52 SWP spectra covering the 1160 – 1646 Å range. All the fluxes were corrected using the algorithm from Massa & Fitzpatrick (2000). Other UV fluxes are from HUT = Hopkins Ultraviolet Telescope (Buss et al. 1995), OAO = Orbiting Astronomical Observatory 2 (Code & Meade 1979), and HST/STIS from the CALSPEC database (Bohlin et al. 2017). Optical spectrophotometry sources are coded as SP1 = Burnashev (1985), SP2 = Kharitonov et al. (1988), and SP3 = Krisciunas et al. (2017). IR fluxes are from 2MASS (Cutri et al. 2003), WISE (Cutri & et al. 2012), AKARI (Ishihara et al. 2010), Spitzer (Ardila et al. 2010), and IRAS (Helou & Walker 1988).

Table 4.4 O Star Literature Temperatures (kK)

Source	ξ Per	α Cam	λ Ori A	ζ Ori A	ζ Oph	10 Lac
Bouret et al. (2008)	29.5
Herrero et al. (1992)	36.0	32.5	37.5
Herrero et al. (2002)	35.5
Marcolino et al. (2009)	32.0	...
Markova et al. (2004)	34.0	31.0	33.6
Martins et al. (2012)	29.5
Martins et al. (2015)	35.0
Martins et al. (2017)	33.5	...	35.0
Mokiem et al. (2005)	32.1	36.0
Najarro et al. (2011)	...	28.9	34.5
Puls et al. (1996)	36.0	30.0	32.5	...
Puls et al. (2006)	...	29.0	33.6
Repolust et al. (2004)	34.0	29.0	32.0	...
Repolust et al. (2005)	...	29.0	33.5	...
Simón-Díaz et al. (2006)	36.0
Villamariz et al. (2002)	37.5
Villamariz & Herrero (2005)	34.0	37.5

Contour maps were created by plotting the χ^2 matrix resulting from the best fit reddening as a function of effective temperature and angular size for each star, and these are shown in Figures 4.11 through 4.16. Overplotted are vertical lines showing the angular size obtained from our interferometry with a 1σ margin, and horizontal lines showing the average literature temperature (from values in Table 4.4) with a 1σ margin. A diamond symbol indicates the best fit temperature based on our interferometric size. For our temperature estimate we took a vertical line along the value of our observed angular size and found where that line was the closest to the minimum of the contour. Uncertainty in the temperature was estimated by

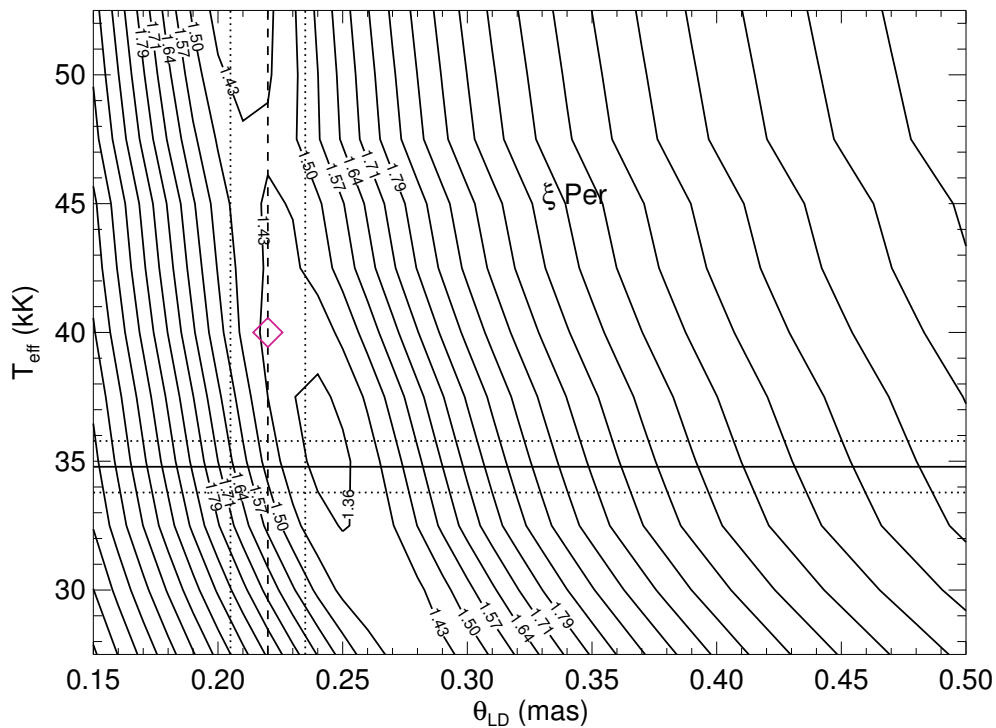


Figure 4.11 Contour map of fitted TLUSTY O star model to observed spectra for ξ Per (HD 24912). Overplotted are vertical lines showing angular size obtained from our interferometry and horizontal lines showing the average literature temperature. Dotted lines show an error margin of 1σ for the angular size and temperature. The diamond indicates the best fit model temperature for our directly determined angular size.

Table 4.5 Comparison of best fit and literature values for O stars

Star	Best Fit Temperature (kK)	Literature Temperature (kK)	Best Fit $E(B - V)$ (mag)	S77 $E(B - V)$ (mag)	M17 $E(B - V)$ (mag)
ξ Per	$<40.0 \pm 0.9$	34.8 ± 1.0	0.291	0.25	0.278 ± 0.007
α Cam	$<29.0 \pm 1.5$	29.5 ± 0.8	0.298	0.26	0.262 ± 0.006
λ Ori A	35.5 ± 0.9	34.3 ± 0.7	0.107	0.12	0.177 ± 0.011
ζ Ori A	$<32.0 \pm 0.5$	29.5 ± 1.0	0.067	0.08	0.044 ± 0.007
ζ Oph	33.5 ± 1.3	32.5 ± 0.9	0.350	0.29	0.297 ± 0.006
10 Lac	36.0 ± 1.3	36.4 ± 1.0	0.096	0.08	0.077 ± 0.006

S77 - Savage et al. (1977), M17 - Maíz Apellániz & Barbá (2017)

applying the same method to the vertical lines indicating plus and minus 1σ of the angular size. For our reddening estimates we looked at a contour plot of the $E(B - V)$ values and took the value where our observed angular size and best fit temperature met. The best estimates for effective temperature and reddening based on our interferometric sizes from the contour plots are given in Table 4.5, along with comparisons to previously estimated values.

Similarly, we took a horizontal line along the value of the average literature temperature for each star and found where that line was closest to the minimum of the contour to measure the best fit angular size as predicted by the model. The comparison of our interferometric angular size and the model's predicted size is shown in Figure 4.23 and discussed in Section 4.3.

The shapes of the contours show that effective temperature has an inverse square dependence on angular size which was expected from our discussion in Section 3. The contours for the $E(B - V)$ values (not shown) are parallel lines that follow the curve of the minimum in chi-squared space. Therefore, any temperature and angular size combination chosen along

the minimum will have a very similar $E(B - V)$ value.

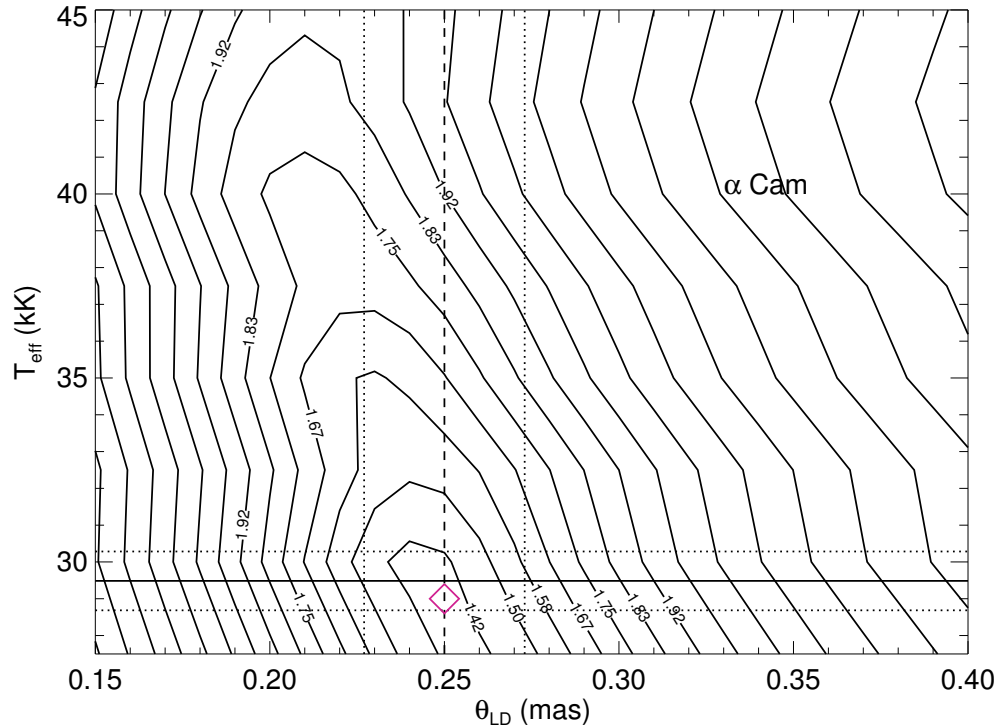


Figure 4.12 Contour map of fitted TLUSTY O star model to observed spectra for α Cam (HD 30614). Overplotted are vertical lines showing angular size obtained from our interferometry and horizontal lines showing the average literature temperature. Dotted lines show an error margin of 1σ for the angular size and temperature. The diamond indicates the best fit model temperature for our directly determined angular size.

Spectral energy distributions (SEDs) using these best fit values for each star are shown in Figures 4.17 through 4.22. The symbols represent the observed spectral data used in our fitting while the solid green line shows the SED for our interferometric size and best fit temperature and reddening. For comparison, the dashed line shows the SED derived from the literature temperature and the angular size predicted by the model.

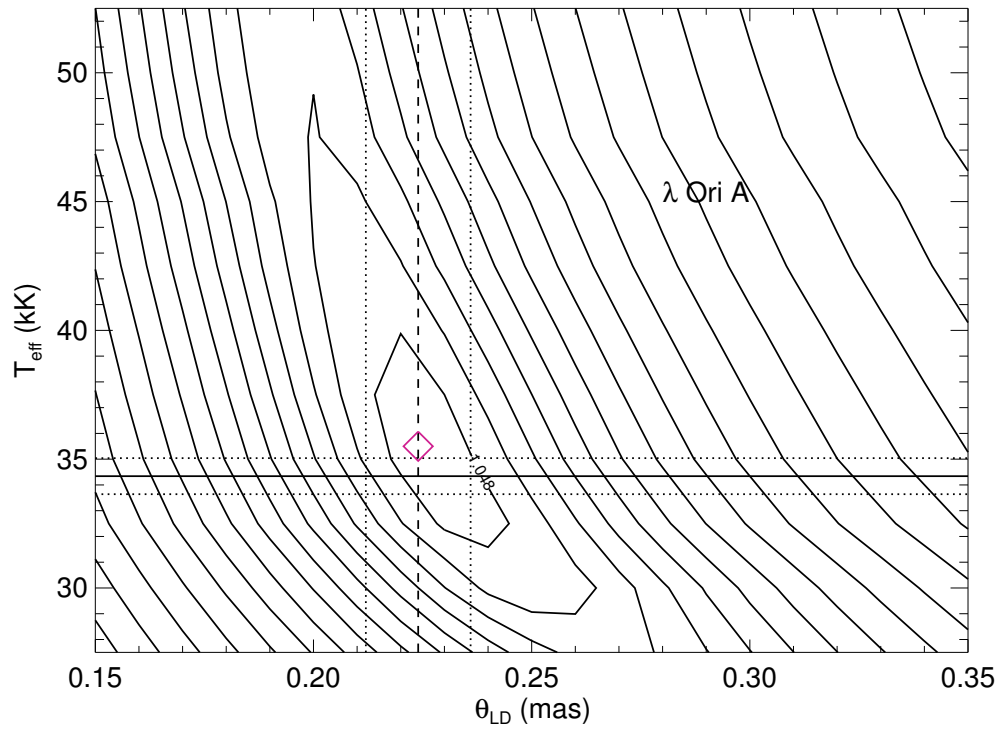


Figure 4.13 Contour map of fitted TLUSTY O star model to observed spectra for λ Ori A (HD 36861). Overplotted are vertical lines showing angular size obtained from our interferometry and horizontal lines showing the average literature temperature. Dotted lines show an error margin of 1σ for the angular size and temperature. The diamond indicates the best fit model temperature for our directly determined angular size.

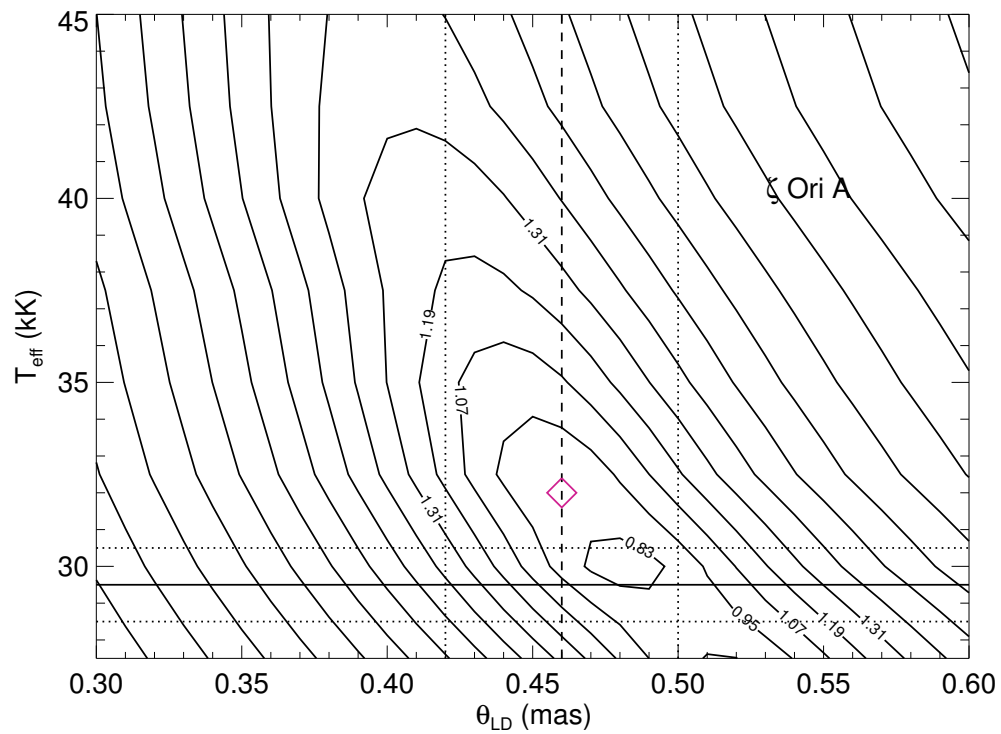


Figure 4.14 Contour map of fitted TLUSTY O star model to observed spectra for ζ Ori A (HD 37742). Overplotted are vertical lines showing angular size obtained from our interferometry and horizontal lines showing the average literature temperature. Dotted lines show an error margin of 1σ for the angular size and temperature. The diamond indicates the best fit model temperature for our directly determined angular size.

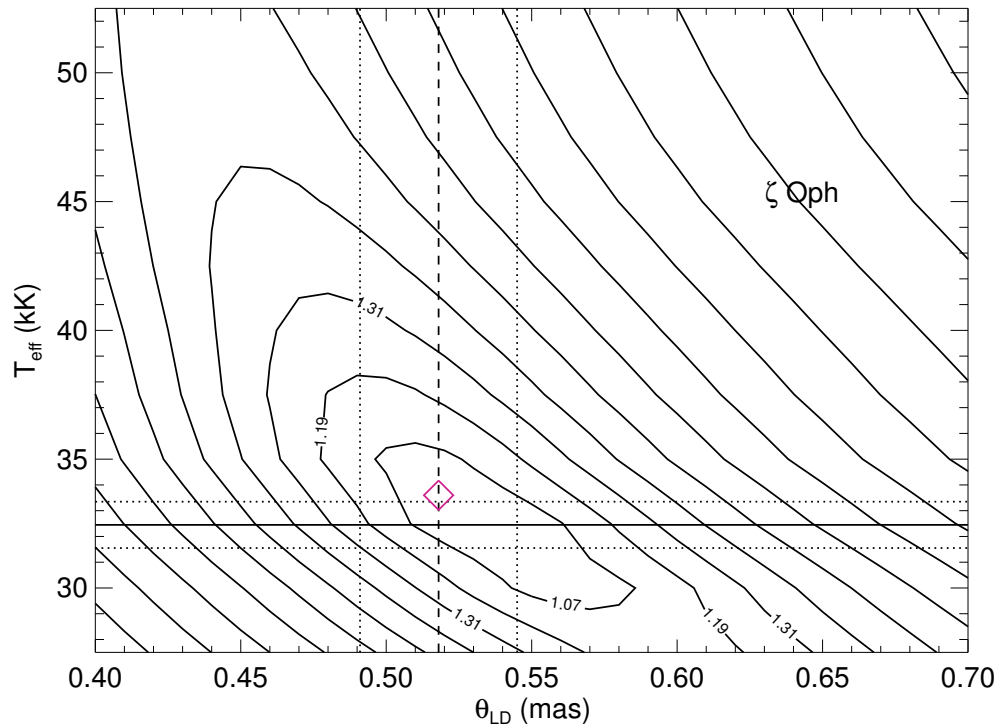


Figure 4.15 Contour map of fitted TLUSTY O star model to observed spectra for ζ Oph (HD 149757). Overplotted are vertical lines showing angular size obtained from our interferometry and horizontal lines showing the average literature temperature. Dotted lines show an error margin of 1σ for the angular size and temperature. The diamond indicates the best fit model temperature for our directly determined angular size.

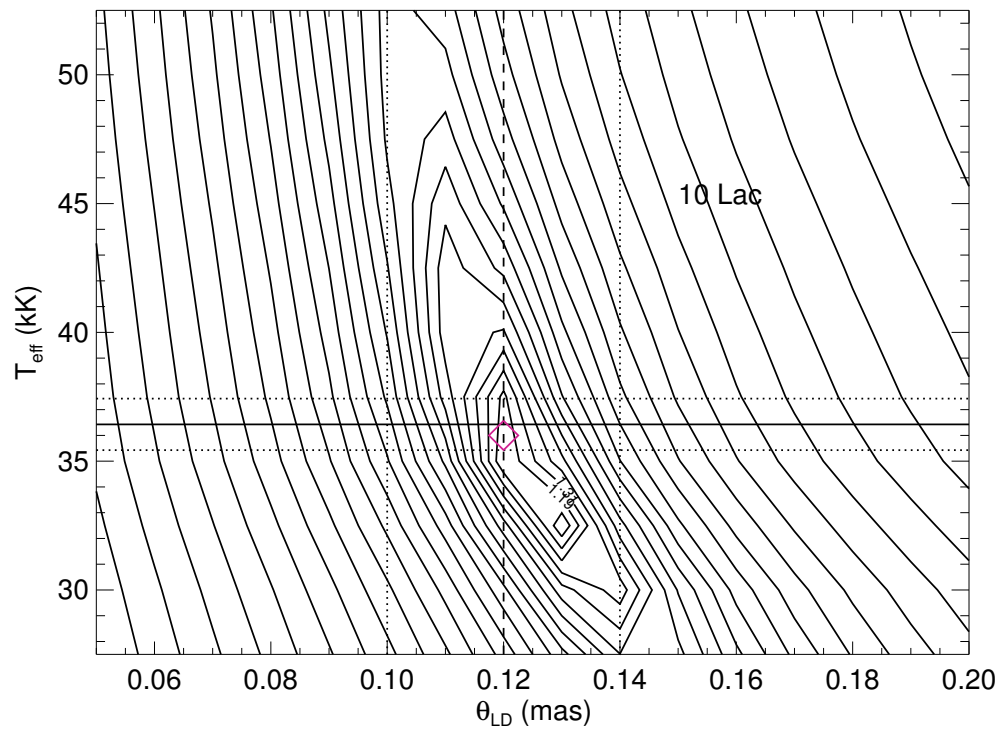


Figure 4.16 Contour map of fitted TLUSTY O star model to observed spectra for 10 Lac (HD 214680). Overplotted are vertical lines showing angular size obtained from our interferometry and horizontal lines showing the average literature temperature. Dotted lines show an error margin of 1σ for the angular size and temperature. The diamond indicates the best fit model temperature for our directly determined angular size.

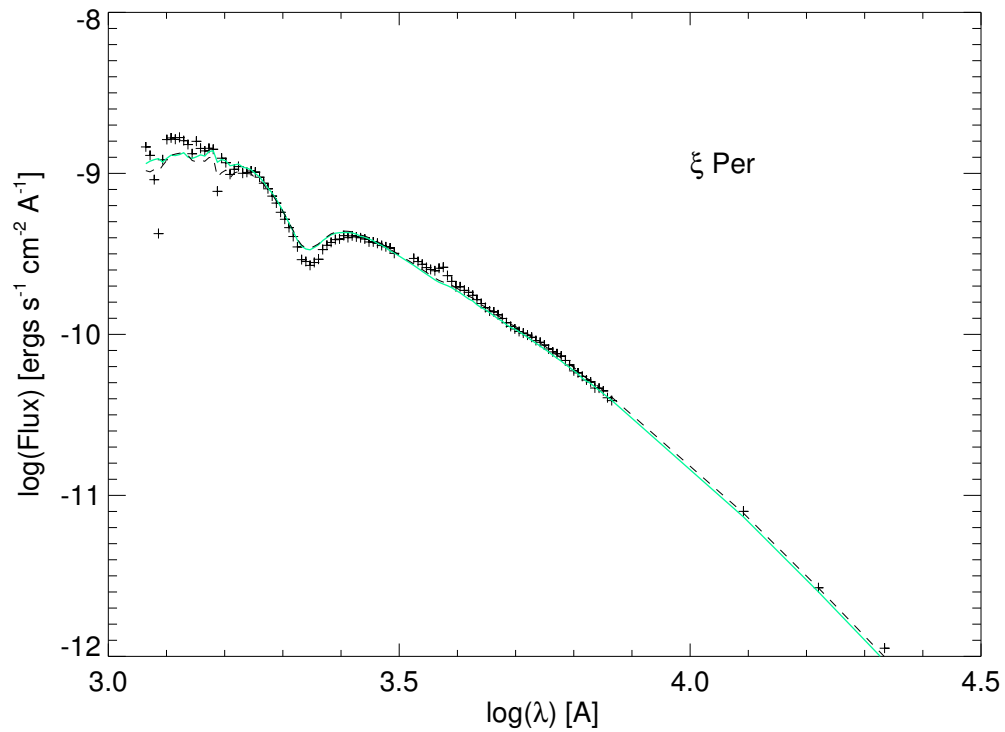


Figure 4.17 Spectral energy distributions for ξ Per (HD 24912) with the best fit model shown in the solid green line. The best fit model was chosen using our observed angular diameter from interferometry combined with the best fit temperature and reddening value found from our contour map. The dashed line indicates the SED derived using the average published T_{eff} and the corresponding best fit angular size.

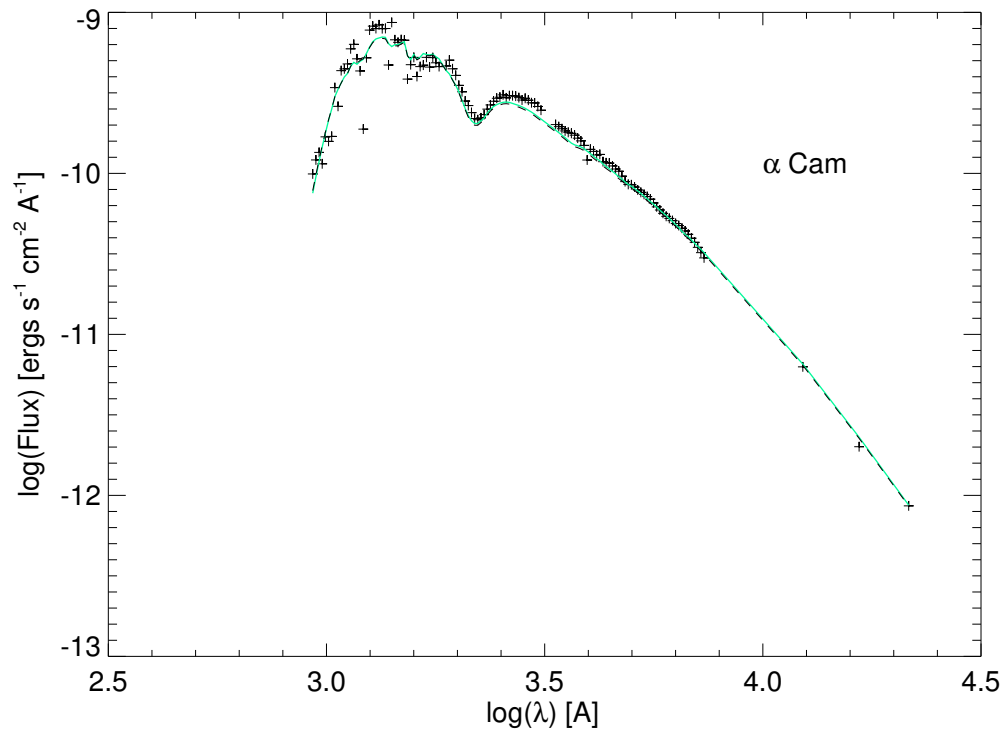


Figure 4.18 Spectral energy distributions for α Cam (HD 30614) with the best fit model shown in the solid green line. The best fit model was chosen using our observed angular diameter from interferometry combined with the best fit temperature and reddening value found from our contour map. The dashed line indicates the SED derived using the average published T_{eff} and the corresponding best fit angular size.

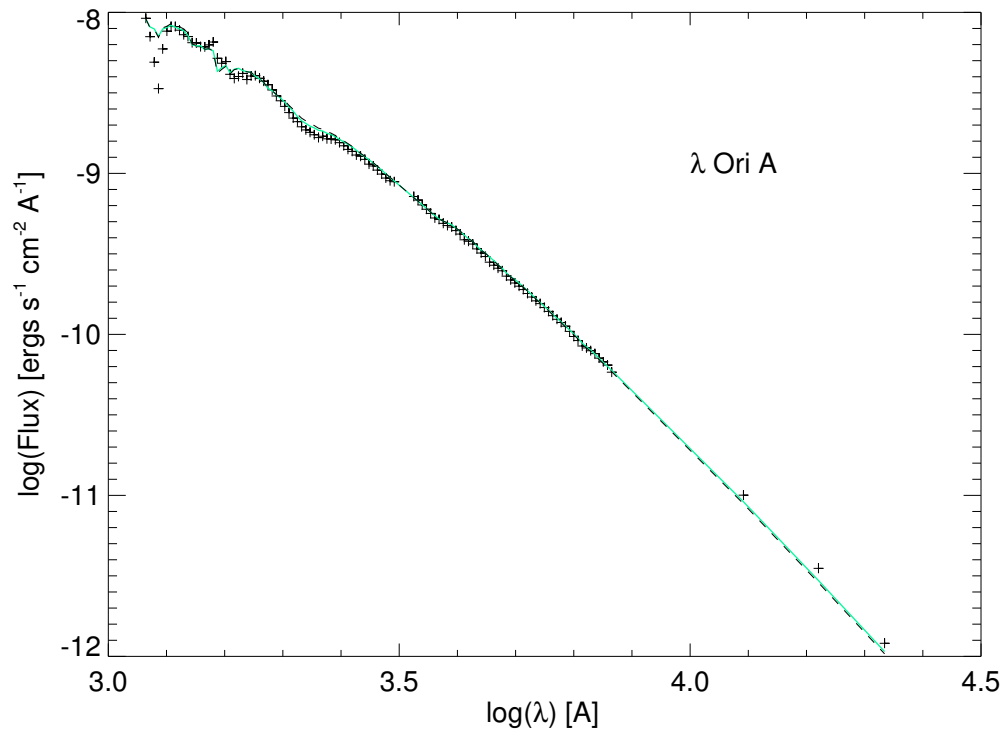


Figure 4.19 Spectral energy distributions for λ Ori A (HD 36861) with the best fit model shown in the solid green line. The best fit model was chosen using our observed angular diameter from interferometry combined with the best fit temperature and reddening value found from our contour map. The dashed line indicates the SED derived using the average published T_{eff} and the corresponding best fit angular size.

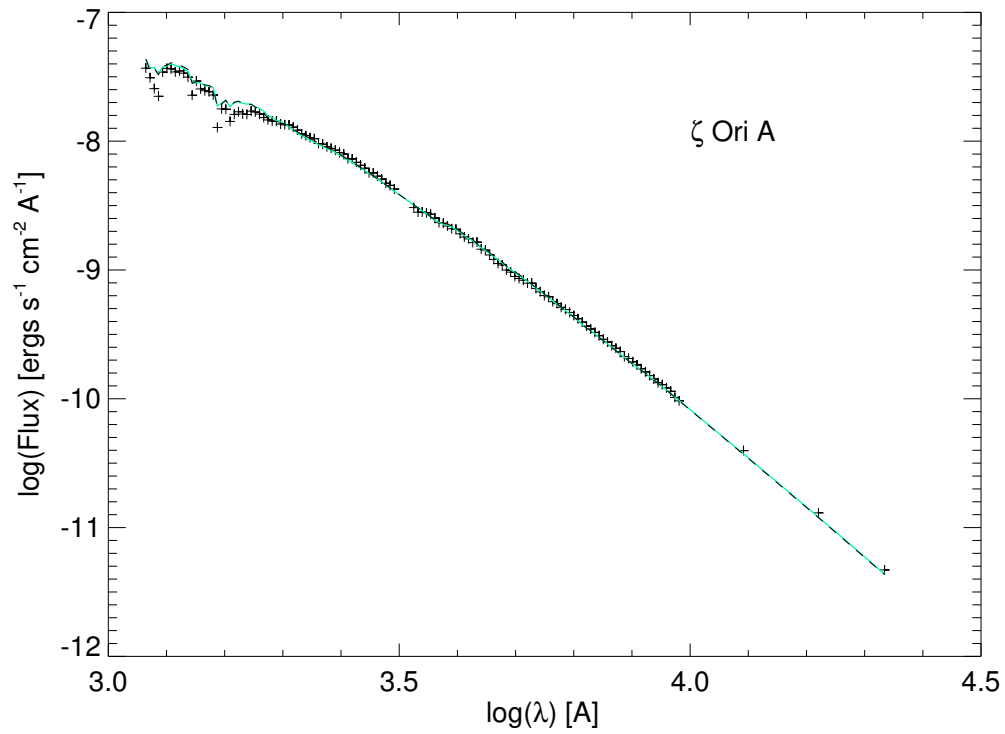


Figure 4.20 Spectral energy distributions for ζ Ori A (HD 37742) with the best fit model shown in the solid green line. The best fit model was chosen using our observed angular diameter from interferometry combined with the best fit temperature and reddening value found from our contour map. The dashed line indicates the SED derived using the average published T_{eff} and the corresponding best fit angular size.

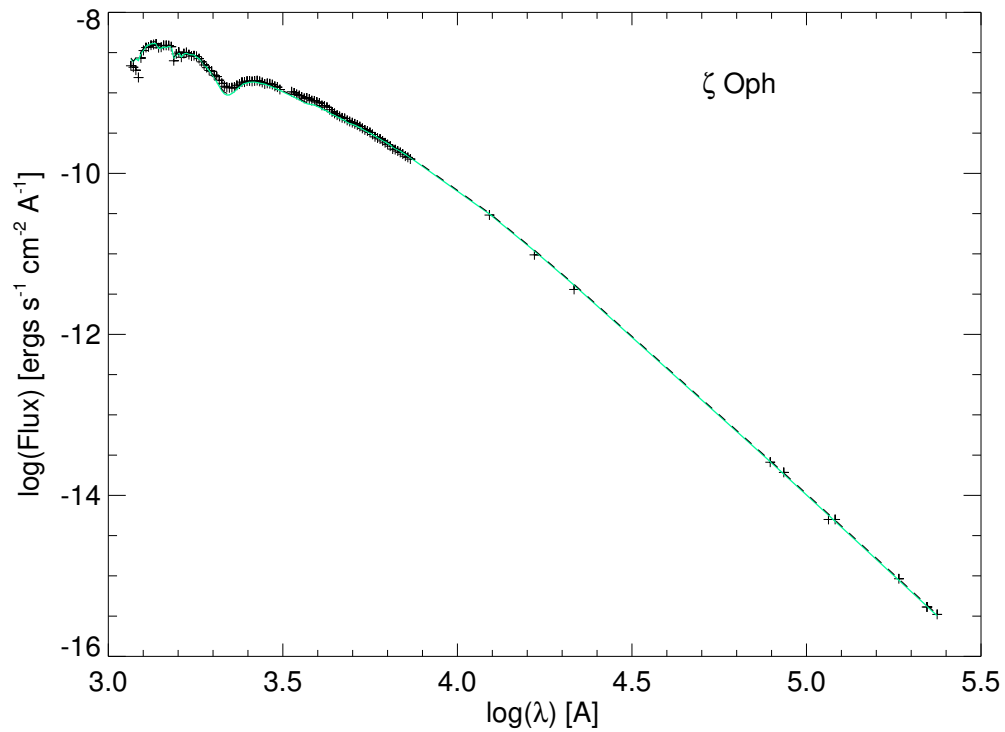


Figure 4.21 Spectral energy distributions for ζ Oph (HD 149757) with the best fit model shown in the solid green line. The best fit model was chosen using our observed angular diameter from interferometry combined with the best fit temperature and reddening value found from our contour map. The dashed line indicates the SED derived using the average published T_{eff} and the corresponding best fit angular size.

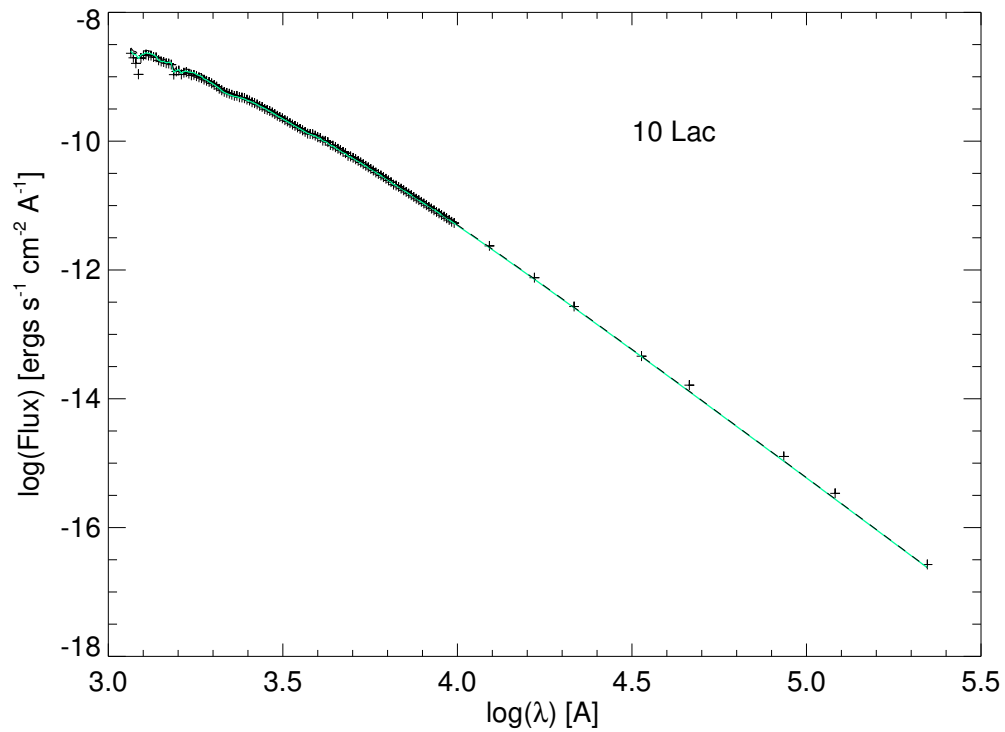


Figure 4.22 Spectral energy distributions for 10 Lac (HD 214680) with the best fit model shown in the solid green line. The best fit model was chosen using our observed angular diameter from interferometry combined with the best fit temperature and reddening value found from our contour map. The dashed line indicates the SED derived using the average published T_{eff} and the corresponding best fit angular size.

4.3 Results and Comparison to Models

When comparing our observed diameters to model predictions, we find that the angular diameters estimated from the published effective temperatures and fits of the SEDs ($\theta_{LD}(T_{\text{eff}})$ given in the final column of Table 4.2) are in good agreement with the interferometric angular diameters. A comparison of observed θ_{LD} and the predicted angular size $\theta_{LD}(T_{\text{eff}})$ is shown in Figure 4.23. This figure shows that the average ratio of $\theta_{LD}(T_{\text{eff}})$ to θ_{LD} is approximately 1.04 ± 0.03 . Note that the three stars with the greatest discrepancy in angular size are ξ Per, ζ Ori A, and ζ Oph. However, due to a calibration bias found in the data (discussed in Section 4.1.1) we consider our results for ξ Per and ζ Ori A to be preliminary and a lower limit on the angular size. A larger angular size for these stars would result in a better agreement. ζ Oph is rotationally distorted, so gravity darkening will complicate the meaning of θ_{LD} and the comparison to a model predicted size may not be valid. Aside from ζ Oph, λ Ori A and 10 Lac have the most measurements and show no discrepancy with model estimations.

Four out of our six O stars have derived effective temperatures from our interferometric observations that exceed the average literature values. However, if we consider the angular sizes for ξ Per, α Cam and ζ Ori A to be lower limits then we must take the derived effective temperatures as upper limit estimates. The two stars without biased measurements that have higher than expected effective temperatures, λ Ori A and ζ Oph, exceed literature temperature estimates by an average of 1.4 kK or 4%.

We can use the angular size and distance to obtain the stellar radius. This is done by

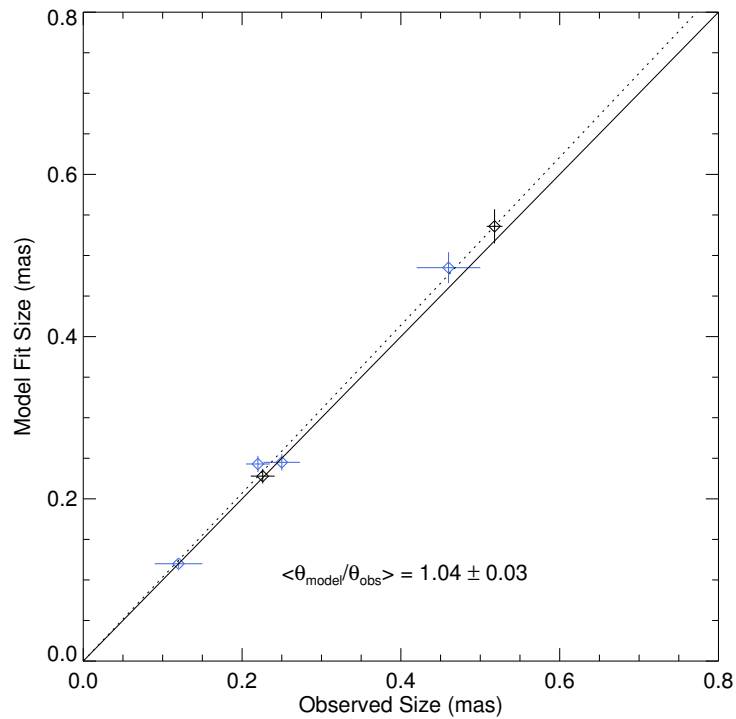


Figure 4.23 Observed angular size θ_{LD} compared to the angular size $\theta_{LD}(T_{\text{eff}})$ derived from the published T_{eff} and fit to the SED. The mean of the small and large diameters is plotted for the oblate star ζ Oph. The solid line shows a line with a slope of unity for reference, and the dashed line shows the trend for the mean ratio of these diameters. Blue points indicate stars likely dominated by systematic errors due to only a single bracket of data, or an extremely small angular size in the case of 10 Lac.

considering the right triangle formed by the distance to a star and the star's radius. A

derivation of the relation is shown below, where R is the radius of the star, d is the distance

to the star and θ_{LD} is the limb-darkened angular size of the star.

$$\begin{aligned}
 \frac{R}{d} &= \frac{\theta_{LD} \text{ (rad)}}{2} \\
 \frac{R}{R_{\odot}} &= \frac{d}{R_{\odot}} \frac{1}{2} \theta_{LD} \text{ (rad)} = \frac{d}{pc} \frac{pc}{R_{\odot}} \frac{1}{2} \theta_{LD} \text{ (mas)} \frac{1}{\text{mas/radians}} \\
 &= \frac{d}{pc} \frac{3.085678 \times 10^{16} m}{6.9566 \times 10^8 m} \frac{1}{2} \frac{1}{\frac{180}{\pi} 3600000} \theta_{LD} \\
 &= \frac{\theta_{LD}}{9.30 \text{ mas}} \left(\frac{d}{pc} \right)
 \end{aligned} \tag{4.1}$$

In Table 4.6 we list distance estimates from six sources. The columns labeled by d_1 and d_2 give distances based upon a calibration of absolute magnitude and spectral classification from Shull & van Steenberg (1985) and Underhill et al. (1979), respectively. The next estimate d_3 is based upon the interstellar Ca II line strengths (Megier et al. 2009). The fourth estimate d_4 is derived from the *Hipparcos* parallax (van Leeuwen 2007) with a correction term for the Lutz-Kelker bias (Maíz Apellániz et al. 2008). The next estimate d_5 is the distance to the host cluster (Kharchenko et al. 2005) or association (de Zeeuw et al. 1999) if the target is a known member. The final value d_6 is derived from the parallaxes from Gaia DR2 (Gaia Collaboration et al. 2018). The DR2 parallaxes for λ Ori A, B have large errors, so we adopted the mean of the parallaxes for components C and D. There is no parallax given for ζ Ori A, so we used the listing for the C component. We applied the parallax of component B for 10 Lac, because of the much larger error associated with component A. The last two columns list the mean and standard deviation of the distant estimates and the corresponding stellar radius from our angular size measurements (Table 4.1). The range listed for ζ Oph (HD 149757) relates to the smaller and larger angular sizes found at different position angles.

Table 4.6 O Star Distance and Radius Estimates

Star	d_1 (pc)	d_2 (pc)	d_3 (pc)	d_4 (pc)	d_5 (pc)	d_6 (pc)	$\langle d \rangle$ (pc)	R (R_\odot)
24912	398	...	486	416	433 ± 46	10.2 ± 1.3
30614	1010	1175	1607	...	821	731	1068 ± 346	28.6 ± 9.7
36861	501	398	...	361	438	417	423 ± 51	$10.2 \pm 1.4^*$
37742	501	350	297	239	391	381	359 ± 89	$17.7 \pm 4.7^*$
149757	154	188	222	112	145	172	165 ± 37	$8.2 - 9.6$
214680	603	631	579	542	...	478	566 ± 59	7.3 ± 1.4

Distance references: 1. Shull & van Steenberg (1985), 2. Underhill et al. (1979), 3. Megier et al. (2009), 4. van Leeuwen (2007) and Maíz Apellániz et al. (2008), 5. de Zeeuw et al. (1999) and Kharchenko et al. (2005), 6. Gaia Collaboration et al. (2018). * indicates stars with close companions (Table 3.2).

The derived radii generally agree within the uncertainties with those associated with their spectral classifications as given by Martins et al. (2005).

4.4 Notes on Individual Stars

4.4.1 λ Ori A

λ Ori A shows excellent agreement between θ_{LD} and $\theta_{LD}(T_{\text{eff}})$ (Table 4.2). During the data analysis one of the stars used as a calibrator, HD 35149, was found to be a binary. This was evidenced by a modulation in the visibility curve for λ Ori A that disappeared when the data were not calibrated with HD 35149. This calibrator was rejected from the calibration process and the final data for λ Ori A are calibrated with only one calibrator for several brackets. This causes the visibilities to be slightly more noisy than otherwise expected.

4.4.2 ζ Ori A

ζ Ori A is the brightest component of a triple system and has a close companion at a separation of 37 mas at the time of our observations and a V -band delta magnitude of 2.2

(Hummel et al. 2013). The light from this companion will affect the spectrum and the visibility curve of ζ Ori A, which will then make the fitted angular size incorrect if not accounted for. For the spectrophotometry, models were computed for both the companions and target then added together to compare with the observed spectrum (Section 3.3.1). Using our knowledge of the angular separation and seeing, we calculated how much of the companion point spread function enters the interferometric field of view (essentially 100% in this case), and then we use this with the magnitude difference to determine the fraction of incoherent flux from the companion in the visibility measurement. This allowed a single limb-darkened disk model to be fit to the corrected visibilities (discussed in more detail in Section 3.2.1). We also calculated a binary model for the visibilities using the predicted position angle and separation from the orbit of Hummel et al. (2013) and using our derived angular size $\theta_{LD} = 0.46$ mas for Aa and $\theta_{LD} = 0.17$ mas for Ab (from the radius ratio given by Hummel et al. 2013). The model indicated the presence of fast and low amplitude oscillations of the visibility curve that are consistent with the observations. Consequently, the small derived angular size of ζ Ori A is not due to the flux of Ab. ζ Ori A was recently observed with the FRIEND beam combiner at the CHARA Array (M.-A. Martinod, private communication). An angular diameter of 0.54 ± 0.01 mas was found from these observations, which is 17% larger than our (lower limit) measurement of 0.460 ± 0.040 mas. Additional interferometric observations are needed to resolve the discrepancy between the initial results.

4.4.3 ζ Oph

ζ Oph is a special case as it is a very rapidly rotating star with a projected rotational velocity of $v \sin i = 348 \text{ km s}^{-1}$ (Glebocki & Gnacinski 2005), and it will have a rotationally distorted shape. We observed ζ Oph on two nearly orthogonal baselines to have a range in u, v coverage and be able to observe sizes at different position angles across the star. The star is both large enough and close enough at 165 pc (Table 4.6) for this distortion to be observed with CHARA. ζ Oph is a runaway star that resulted from a supernova in a binary system, which broke apart the binary components. Its path and that of a pulsar have been traced back to a common origin before the supernova (Hoogerwerf et al. 2000). This puts it in a rare position as a single O star, the product of a dissolved binary. ζ Oph sometimes appears as a Be star, and in the past it has had a disk surrounding it. Currently, it does not show H α emission in its spectra, so it is reasonable to assume that any disk has dissipated and we are measuring the angular size of the star itself. However, during a past epoch when a disk was present, Poeckert et al. (1979) used spectropolarimetry to determine the position angle of the disk minor axis as 132.5 ± 6.0 deg east from north. We assume that the circumstellar disk axis is parallel to the stellar rotation axis, so that this is also the position angle of the projected minor axis of the star's shape.

By observing ζ Oph on different baselines with different position angles (S2W1 at -42.8° and S2E2 at 17.9°) we were able to observe directly this distortion from a perfect sphere. We measured an angular size of 0.462 ± 0.025 mas along the short axis of the star and 0.540 ± 0.029 mas along the long axis. This is in good agreement with a fit of a simple ellipse to the data,

using the previously determined position angle of 132.5° (Poeckert et al. 1979), which gives a major axis of 0.56 mas and a minor axis of 0.48 mas. The fitted ellipse is shown in Figure 4.7. The ratio of minor to major axis of 0.86 is similar to the polar to equatorial radius ratio of $7.5R_\odot/9.1R_\odot = 0.82$ found by Howarth & Smith (2001), although the absolute radii we find are slightly larger because we adopt a larger distance. This star is a good target for future interferometric imaging to determine better the rotational distortion and the associated gravity and limb darkening (Che et al. 2011).

4.4.4 10 Lac

At 0.12 mas, 10 Lac is the smallest star in angular size that has been resolved with CHARA to date. Due to its extremely small size we did have a few ($\sim 5\%$) visibility points with values greater than 1. These points were excluded from the fitting process and a check was done to ascertain that they did not have a significant effect on the final fit. Because we were working below the accepted resolution limit of PAVO at 0.2 mas we wanted to check very carefully the associated uncertainty in our measurement. Three calibrators were used for the observations of 10 Lac and all calibrator sizes and errors were obtained from JMMC. The fitted angular size is very sensitive to the error in the calibrator size when the target star is smaller in angular size than the calibrator as in this case. To account for this, we varied each calibrator in size by plus and minus one sigma, then refit the data with the new calibrator size. We then took the weighted average of these sizes for our final size and used the standard deviation between all fits as part of our error budget. This method was subsequently applied to all the O stars in the sample. The result is a fairly large error for the small size of 0.12

mas, but our result agrees with the SED fitting outcome (Table 4.2). Both spectroscopic observations and our interferometric results arrive at relatively high effective temperatures, 36.0 kK and 36.4 kK, respectively, that are well above the 31.9 kK temperature associated with its classification of O9 V (Martins et al. 2005).

CHAPTER 5

EFFECTIVE TEMPERATURES AND ANGULAR SIZES OF B STARS

5.1 CHARA Array Interferometry

The visibility measurements we obtained for each B star from our interferometric observations were fitted with an error weighted fit to a limb-darkened, single star, disk model. Linear limb-darkening coefficients in the R -band for PAVO observations, and the H - and K -band for CLIMB observations, were interpolated from the tables available in Claret & Bloemen (2011), using the photospheric parameters given in Table 3.1. These limb darkening coefficients were calculated for model atmospheres that adopt a solar metallicity and a microturbulent velocity of 2 km s^{-1} . None of our B stars are extreme rapid rotators, so we assumed spherical symmetry for all fitting purposes. Example visibility points for PAVO and CLIMB data are shown in Figure 5.1, for stars HD 98664 and HD 120315, plus an error-

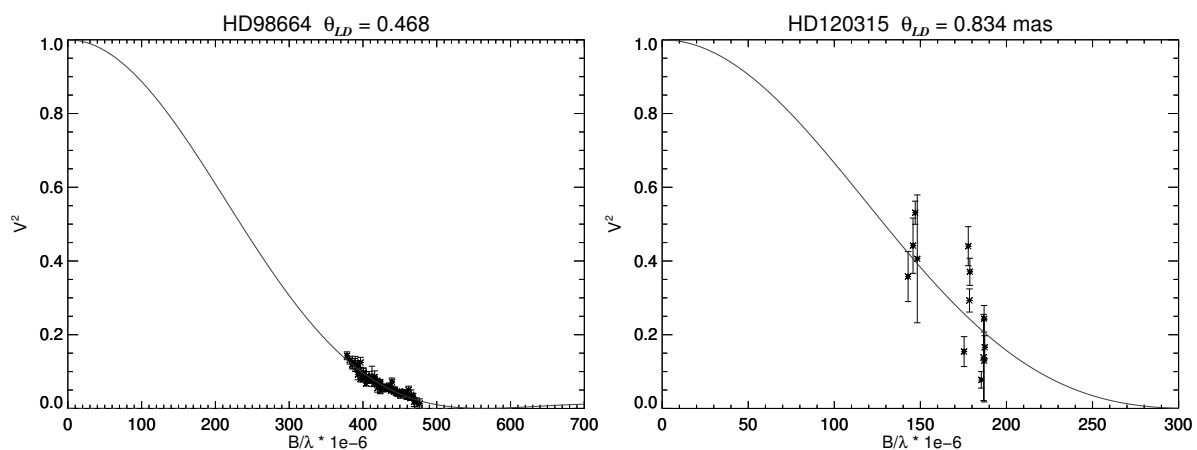


Figure 5.1 Visibility data for HD 98664 and HD 120315. PAVO data is shown to the left and H -band CLIMB data to the right. Solid line is the best fit linear limb-darkened single star disk model.

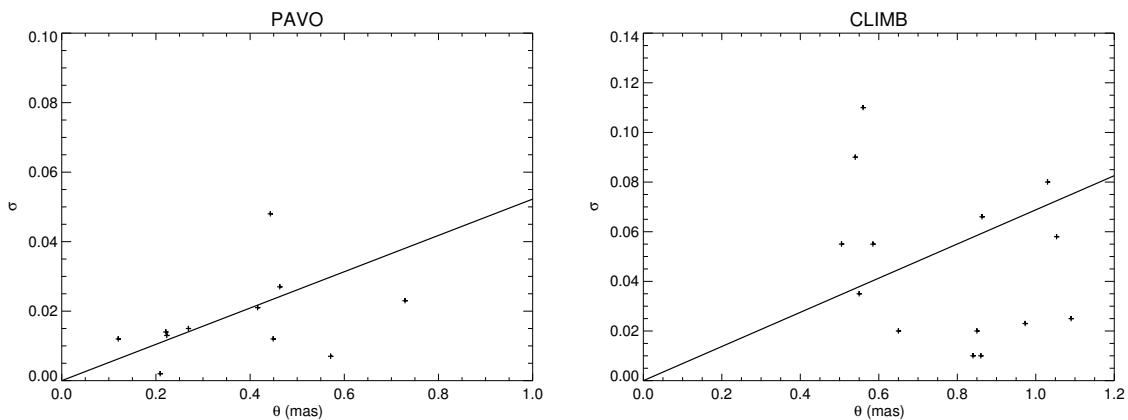


Figure 5.2 Nightly variation in size (σ) plotted vs. measured angular diameter each night (θ) for each beam combiner.

weighted fit of all the data with a limb-darkened disk model. The visibility measurements and fits for all B stars are given in Appendix A. All visibility plots show visibilities corrected for the presence of a companion where appropriate. Table 5.1 lists the derived uniform disk (UD) and limb-darkened (LD) disk angular diameters θ , the latter calculated for a linear limb-darkening coefficient μ .

Errors for our angular diameters were calculated using two components. The first component was an uncertainty assigned to the angular diameter based upon the size of the residuals to the fit. For the second component we took all stars that were observed on more than one night and calculated how the standard deviation from nightly variations changed with the stellar angular diameter. This was done separately for PAVO and CLIMB data. We found an inter-night scatter of $\sigma=0.052\theta$ for PAVO data and $\sigma=0.069\theta$ for CLIMB data, where σ is the night-to-night standard deviation and θ is the angular diameter in mas. Plots showing these relations are given in Figure 5.2. The uncertainty from the residuals and this inter-

night standard deviation from the fit were added in quadrature for our final error estimate. For B stars whose angular size, uncorrected for companion flux, was close to that of the calibrator (HD 3360, HD 29763, and HD 36267), we added the uncertainty due to the error in the calibrator size to the error budget. To account for this effect, we fit the data for these stars after adjusting the calibrator sizes by plus and minus one sigma. We then averaged the resulting sizes for our final angular size and took the standard deviation between the sizes. These error estimates are given with the limb-darkened and uniform disk diameters in Table 5.1. Table 5.2 gives a comparison of our measured angular diameters for our B stars to previously estimated values based upon the colors or SED.

Our angular diameter measurements are in good agreement with previously estimated values with the exception of HD 23850, known as Atlas and a member of the Pleiades star cluster. CADARS reports an angular diameter for this star of 0.8 mas while we measure 0.388 mas. Atlas is a triple system with a spectroscopic binary inner pair Aa1, Aa2 with an angular separation of 0.013" and a V -band magnitude difference of 1.62 mags (Table 3.2). The outer companion, Aa, Ab, has an angular separation of 0.5" and a V -band magnitude difference of 3 mags. It is likely the flux from one, or both, of these companions was not taken into account for the CADARS diameter estimate and this is the cause of the discrepancy between sizes.

Table 3.2 shows which stars have companions close enough and bright enough to require a correction to the visibilities. This was done with the same method used for the O stars by using the companion's separation and V -band delta magnitude, together with the seeing

estimate for the night of the observation, to calculate how much incoherent flux the companion would contribute to the visibility curve. The visibilities are then scaled up based on the calculation and fit with single star model.

Table 5.1 Observations and measured angular diameters of sample B stars

Star	B.C.	Baselines	N_{V^2}	θ_{UD} (mas)	R -band μ	H -band μ	K -band μ	θ_{LD} (mas)
HD 2772	P	W1S2	115	0.224 ± 0.017	0.36	0.230 ± 0.017
HD 3360	P	E1W1	46	0.264 ± 0.018	0.22	0.270 ± 0.018
	P	E1S1						
HD 11502	P	E1S1	69	0.336 ± 0.019	0.34	0.346 ± 0.019
HD 15318	P	W1S2	91	0.388 ± 0.023	0.33	0.400 ± 0.023
	P	E1S1						
HD 23302	P	E1S1	46	0.472 ± 0.025	0.27	0.478 ± 0.025
HD 23408	P	E1S1	46	0.422 ± 0.023	0.32	0.436 ± 0.023
HD 23850	C	E1W1S1	24	0.384 ± 0.028	...	0.16	...	0.388 ± 0.028
HD 29763	P	E1S1	46	0.220 ± 0.016	0.34	0.226 ± 0.016
HD 35497	C	E1W1S1	6	1.074 ± 0.076	...	0.16	...	1.090 ± 0.076
HD 36267	P	E1S1	69	0.196 ± 0.015	0.25	0.200 ± 0.015
HD 98664	P	E1S1	69	0.452 ± 0.025	0.40	0.468 ± 0.025
HD 120315	C	E1W1S1	28	0.818 ± 0.060	...	0.18	0.12	0.834 ± 0.060
HD 147394	P	E1W1	115	0.354 ± 0.020	0.32	0.364 ± 0.020
HD 155763*	P	W1S2	87	0.474 ± 0.026	0.33	0.15	...	0.488 ± 0.026
	C	E1W1S1						
HD 160762	P	E1W1	46	0.326 ± 0.018	0.29	0.334 ± 0.018
HD 176437	P	W2S2	92	0.712 ± 0.038	0.33	0.734 ± 0.038
HD 177756	P	W2S2	106	0.556 ± 0.030	0.32	0.570 ± 0.030
HD 184930	P	E1W1	115	0.328 ± 0.020	0.33	0.338 ± 0.020
HD 186882	C	E1W1S1	9	0.884 ± 0.062	...	0.16	...	0.896 ± 0.062
HD 196867*	P	E2S2	138	0.407 ± 0.022	0.31	0.15	...	0.420 ± 0.022
	C	E1W1S1						
HD 198478	P	W1S2	161	0.434 ± 0.023	0.36	0.448 ± 0.023
	P	W2S2						
HD 205021	P	W1S2	115	0.274 ± 0.016	0.28	0.280 ± 0.016
HD 214923*	P	E2S2	139	0.551 ± 0.030	0.34	0.14	...	0.562 ± 0.030
	C	E1W1S1						
HD 218045*	P	E2W2	312	1.056 ± 0.066	0.34	0.16	...	1.069 ± 0.066
	P	E2S2						
	C	E1W1S1						
HD 222661	P	E1S1	21	0.338 ± 0.018	0.39	0.348 ± 0.018

B.C. = beam combiner used for observations; P=PAVO, C=CLIMB. * denotes stars with both PAVO and CLIMB data. The weighted average is used for HD 218045. Only PAVO data are used for HD 155763, HD 196867 and HD 214923. Discussed in Section 5.1.1.

Table 5.2 Comparison of measured B star angular diameters to literature values

Star	This Work θ_{LD} (mas)	Underhill (1979) θ_{LD} (mas)	CADARS θ_{LD} (mas)	Swihart (2017) θ_{LD} (mas)	T_{eff} θ_{LD} (mas)
HD 2772	0.230 ± 0.017	...	0.29	...	0.218 ± 0.080
HD 3360	0.270 ± 0.018	0.303 ± 0.002	0.27	0.319 ± 0.013	0.304 ± 0.010
HD 11502	0.346 ± 0.019	...	0.40	...	0.398 ± 0.019
HD 15318	0.400 ± 0.023	...	0.42	0.387 ± 0.058	0.421 ± 0.010
HD 23302	0.478 ± 0.025	...	0.40	...	0.445 ± 0.007
HD 23408	0.436 ± 0.023	...	0.43	0.410 ± 0.099	0.460 ± 0.040
HD 23850	0.388 ± 0.028	...	0.80	...	0.469 ± 0.030
HD 29763	0.226 ± 0.016	...	0.27	...	0.245 ± 0.005
HD 35497	1.090 ± 0.076	1.065 ± 0.010	1.10	...	1.130 ± 0.005
HD 36267	0.200 ± 0.015	...	0.40	...	0.270 ± 0.010
HD 98664	0.468 ± 0.025	...	0.45	0.418 ± 0.075	0.466 ± 0.018
HD 120315	0.834 ± 0.060	0.826 ± 0.006	0.84	0.670 ± 0.141	0.835 ± 0.020
HD 147394	0.364 ± 0.020	0.358 ± 0.001	0.37	...	0.370 ± 0.015
HD 155763	0.488 ± 0.026	0.586 ± 0.003	0.59	...	0.461 ± 0.010
HD 160762	0.334 ± 0.018	0.332 ± 0.003	0.34	...	0.332 ± 0.010
HD 176437	0.734 ± 0.038	...	0.75	0.647 ± 0.117	0.720 ± 0.070
HD 177756	0.570 ± 0.030	0.563 ± 0.002	0.56	0.565 ± 0.085	0.567 ± 0.030
HD 184930	0.338 ± 0.020	0.322 ± 0.003	0.35	...	0.340 ± 0.005
HD 186882	0.896 ± 0.062	...	0.86	0.831 ± 0.050	0.866 ± 0.110
HD 196867	0.420 ± 0.022	0.531 ± 0.006	0.51	...	0.464 ± 0.030
HD 198478	0.448 ± 0.023	0.531 ± 0.003	0.44	...	0.530 ± 0.013
HD 205021	0.280 ± 0.016	0.309 ± 0.004	0.30	...	0.340 ± 0.010
HD 214923	0.562 ± 0.030	...	0.55	0.545 ± 0.093	0.578 ± 0.040
HD 218045	1.069 ± 0.066	...	0.94	0.975 ± 0.059	1.000 ± 0.100
HD 222661	0.348 ± 0.018	...	0.36	0.349 ± 0.052	0.370 ± 0.040

CADARS = Pasinetti Fracassini et al. (2001), T_{eff} = diameter derived from temperature and SED.

5.1.1 Comparing CLIMB and PAVO

Four of our B stars were observed with both the PAVO and CLIMB beam combiners, with PAVO operating in the R -band and CLIMB in the H -band. However, we were unsuccessful at correcting for the incoherent flux of one star, HD 155763, and it is excluded from Table 5.3. This issue is discussed in more detail in Section 5.4.9. We also have one star, HD 120315, that was observed in both H - and K -band with CLIMB. We note that for HD 120315 the angular diameter measurements for CLIMB H - and K -band agree within errors. For consistency we have adopted the H -band angular size measurement for HD 120315 in

Tables 5.1 and 5.2. Here we give a comparison of the angular diameters measurements from the two combiners, shown in Table 5.3.

To investigate the discrepancy between PAVO and CLIMB diameters, CLIMB data were run through three different data reduction pipelines. The first, denoted as CLIMB *H*-band in Table 5.3, is the original, default CLIMB data reduction pipeline described in Section 2.4.1. The second, WM CLIMB, is the data run through the original pipeline but using a weighted mean of the visibility estimates derived from the power spectra measured from each scan. The third, JDM, is a CLIMB reduction pipeline written by John Monnier that uses bootstrapping to estimate visibility uncertainties. A graphical representation of the comparison is shown in Figure 5.3. Although there is some fluctuation in the results from each of these pipelines, there is no apparent systematic trend and they are consistent with each other within errors. The errors on individual visibility points are larger, and more realistic, when the data are reduced with John Monnier’s pipeline, while the errors are much too small to account for the scatter in visibility when the data are reduced with the weighted mean CLIMB pipeline.

Table 5.3 Comparison of measured angular diameters from PAVO and CLIMB

Star	PAVO θ_{LD} (mas)	CLIMB <i>H</i> -band θ_{LD} (mas)	CLIMB <i>K</i> -band θ_{LD} (mas)	WM CLIMB θ_{LD} (mas)	JDM θ_{LD} (mas)
HD 120315	...	0.834±0.060	0.870±0.060		
HD 196867	0.420±0.022	0.614±0.044	...	0.618±0.043	0.640±0.045
HD 214923	0.562±0.030	0.644±0.045	...	0.672±0.051	0.616±0.043
HD 218045	1.052±0.055	1.108±0.077	...	1.106±0.076	1.102±0.076

WM CLIMB = CLIMB data reduced using a weighted mean to combine power spectra, *H*-band data only; JDM = John Monnier’s CLIMB pipeline, *H*-band data only

Out of the three stars compared, one star (HD 196867) had no calibrators in common

between the PAVO and CLIMB observations. For HD 196867, the calibrators used for PAVO observations were HD 196724 and HD 196740, and the calibrators used for CLIMB observations were HD 194012 and HD 197076. For HD 214923, the calibrators used for PAVO observations were HD 216735 and HD 218700, and the calibrators used for CLIMB observations were HD 216735 and HD 217891. For HD 218045, the calibrators used for PAVO observations were HD 216735 and HD 218700, and the calibrators used for CLIMB observations were HD 216735 and HD 218918.

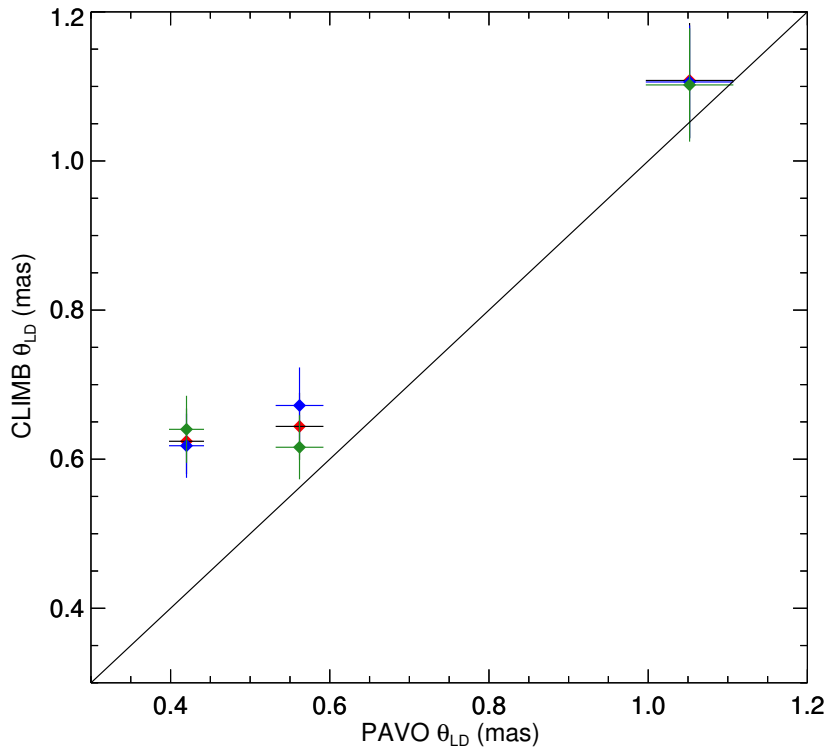


Figure 5.3 A comparison of PAVO and CLIMB measurements from Table 5.3. Red points represent CLIMB data reduced with the original CLIMB pipeline, blue points with the weighted mean CLIMB pipeline, and green points with John Monnier’s CLIMB pipeline. Solid line shown with a slope of one for reference.

There is a trend of PAVO diameter measurements yielding smaller angular sizes than CLIMB diameters with an average difference of 9% between them if HD 196867 is excluded or an 17% difference with the addition of HD 196867. HD 196867 is the most discrepant with a 33%, or 5σ , difference between the PAVO and CLIMB measurements. A similar discrepancy has been previously noted and discussed in White et al. (2018), who compared diameter measurements from PAVO, Classic, VEGA and NPOI. Observations in the R -band with PAVO tend to sample farther down on the visibility curve for a given star than is the case for the H - or K -band with CLIMB (recall from Section 2.3 that a shorter wavelength will yield higher angular resolution). This will result in a more stringent measurement of the stellar diameter. Higher visibility measurements closer to 1 may be more vulnerable to calibration uncertainties and will not provide as accurate a measurement of the angular diameter. In addition, the K -band results in particular are more sensitive to details of the thermal background subtraction. The discrepancy between PAVO and CLIMB diameters becomes more pronounced as we move to smaller diameters. With these findings we suggest that PAVO observations will give more accurate results than observations with CLIMB for stars smaller than ~ 0.8 mas. In accordance with this, we have decided to adopt the angular diameters for HD 155763, HD 196867 and HD 214923 from our PAVO observations only.

Ongoing work is being done to compare the results from different beam combiners at the CHARA Array and includes a program being carried out by Fabien Baron and Daniel Huber to compare measurements from several combiners at the Array and a comparison of PAVO and VEGA with one observation in Karovicova et al. (2018).

5.2 Spectrophotometry

The spectrophotometric fitting was conducted using the same method for the B stars as for the O stars. Spectrometry from multiple sources was used to span the wavelength range from ultraviolet to infrared (1200 \AA to $2\mu\text{m}$), except for HD 11502 (discussed in Section 5.4.2). The sources used include IUE (International Ultraviolet Explorer) data and the Ultraviolet Bright-Star Spectrophotometric Catalog (Jamar et al. 1976) for the near and far UV, Burnashev (1985) and Alekseeva et al. (1996) for the optical, and 2MASS (Two Micron All Sky Survey, Cutri et al. 2003) and WISE (Wide-field Infrared Survey Explorer, Cutri & et al. 2012) in the IR. Spectra obtained from IUE were recalibrated with a routine by Massa & Fitzpatrick (2000) to correct the flux values. All flux values in the spectra were assigned a uniform 3% error to ensure our fitting program fit all points equally and did not give more weight to one part of the spectrum.

The spectra were compared to TLUSTY B star or ATLAS9 stellar atmosphere models.

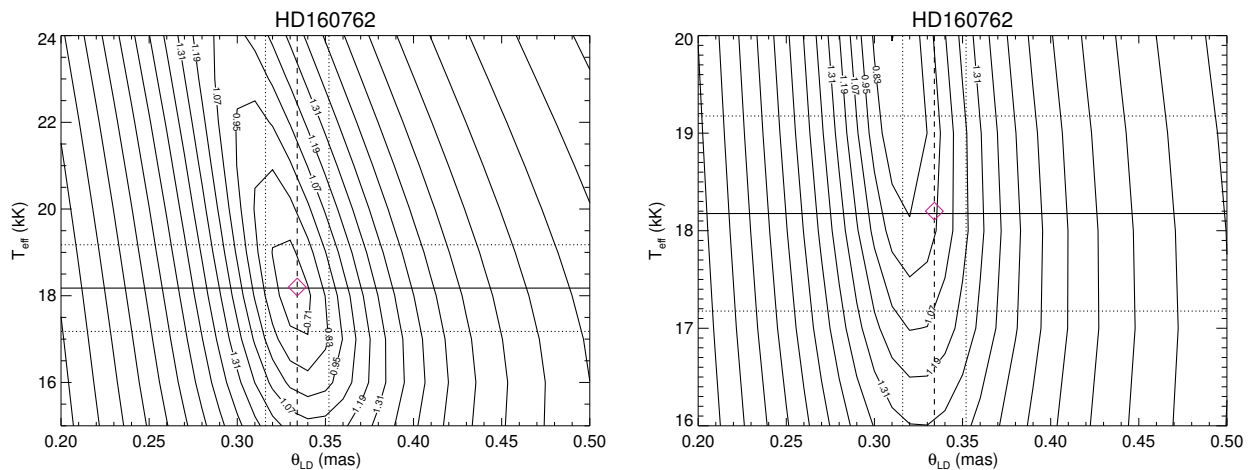


Figure 5.4 A comparison of a star near the cut-off temperature of 17kK fit with both the TLUSTY B star model (left) and the ATLAS9 model (right). For hotter stars the TLUSTY B star models appear to better fit observations.

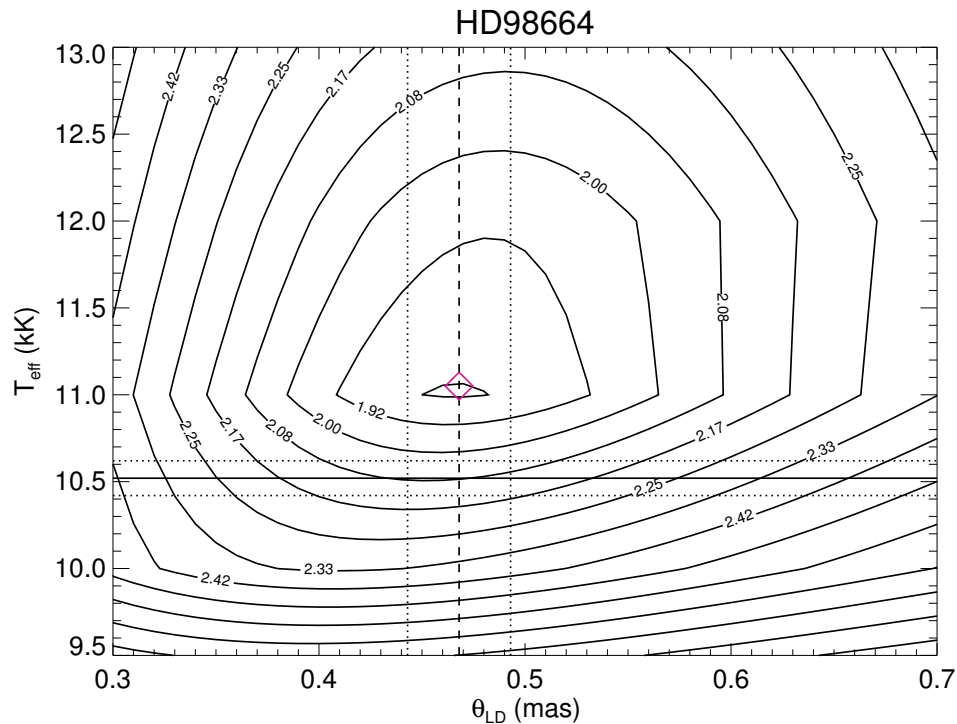


Figure 5.5 Contour map of a fitted ATLAS9 stellar atmosphere model to observed spectra for HD 98664. Overplotted are vertical lines showing angular size obtained from our interferometry and horizontal lines showing the average literature temperature. Dotted lines show an error margin of 1σ for the angular size and average literature temperature. The diamond symbol indicates the best fit model temperature for our directly determined angular size.

The TLUSTY models assume solar abundances and a microturbulent velocity of $v_t=2 \text{ km s}^{-1}$.

The ATLAS9 models assume solar metallicity and a microturbulent velocity of $v_t=2 \text{ km s}^{-1}$.

Details of the models are discussed in Section 3.3. Stars with effective temperatures above 17,000 K were fit with the TLUSTY B star models, while stars under 17,000 K were fit with the ATLAS9 models. Stars around the cut-off temperature range between models were fit with both models to ensure good agreement. An example comparison between the models is shown in Figure 5.4. While the models are in general agreement, the TLUSTY B star models seem to better fit observations for hot stars. Literature values for effective

temperature and surface gravity were taken as the average from several sources: the PASTEL catalog (Soubiran et al. 2016), the ELODIE archive (Prugniel & Soubiran 2001), the Indo-US Library (Valdes et al. 2004), the STELIB library (Le Borgne et al. 2003), the MILES library (Cenarro et al. 2007), Cenarro et al. (2001), Gullikson et al. (2016), Kraus et al. (2015), Lyubimkov et al. (2004), Morales et al. (2001), and Zorec et al. (2009).

Contour maps were created by plotting the χ^2 matrix resulting from the best fit reddening as a function of effective temperature and angular size for each star, and a χ^2 contour plot for HD 98664 is shown in Figure 5.5. χ^2 contour plots for all B stars are given in Appendix B. Overplotted are vertical lines showing the angular size obtained from our interferometry with a 1σ margin, and horizontal lines showing the average literature temperature with a 1σ margin. A diamond symbol indicates the best fit temperature based on our interferometric size. For our temperature estimate we took a vertical line along the value of our observed angular size and found where that line was the closest to the minimum of the contour. For our reddening estimates we looked at a contour plot of the $E(B - V)$ values and took the value where our observed angular size and best fit temperature met.

The best estimates for effective temperature and reddening based on our interferometric sizes from the contour plots are given in Table 5.4, along with comparisons to previously determined values. Uncertainties for our effective temperatures were found by normalizing the minimum χ^2 and fitting the χ^2 points with a parabolic curve. The temperature uncertainty was then taken as the value on the curve with a reduced χ^2 equal to $(1 + \frac{1}{(N_{points} - DoF)})$.

We took a horizontal line along the value of the temperature matching the global χ^2

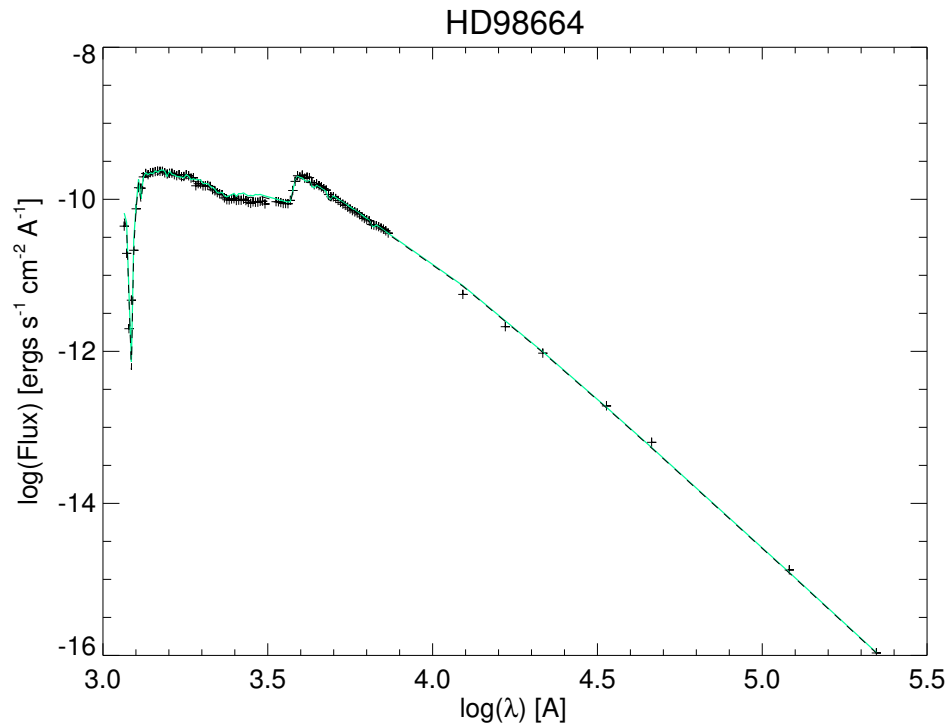


Figure 5.6 Spectral energy distribution for HD 98664. The solid green line shows the SED derived from our interferometric size and best fit temperature and reddening. The dashed line indicates the SED derived from the temperature and angular size predicted by the model.

minimum for each star and measured the corresponding best fit angular size as predicted by the model. The comparison of our interferometric angular size and the model's predicted size is shown in Figure 5.7 and discussed in Section 5.3.

Spectral energy distributions (SEDs) using these best fit values for each B star are shown in Appendix B. An example SED for HD 98664 is given in Figure 5.6. The symbols represent the spectral data used in our fitting while the solid green line shows the SED for our interferometric size and best fit temperature and reddening. For comparison, the dashed line shows the SED derived from the predicted model temperature and the angular size.

Table 5.4 Comparison of best fit and literature values for B stars

Star	Derived Temperature (kK)	Model Temperature (kK)	Literature Temperature (kK)	Best Fit $E(B - V)$ (mag)	Literature $E(B - V)$ (mag)
HD 2772	12.0 ± 0.5	12.8 ± 0.5	11.9 ± 0.6	0.024	0.02
HD 3360	25.5 ± 0.8	21.5 ± 0.8	21.5 ± 0.5	0.061	0.05
HD 11502	11.0 ± 1.1	9.5 ± 1.0	10.0 ± 1.0	0.048	0.04
HD 15318	11.1 ± 1.4	11.0 ± 1.0	10.6 ± 1.0	0.036	0.03
HD 23302	14.7 ± 0.8	14.7 ± 0.8	14.7 ± 1.0	0.124	0.05
HD 23408	14.7 ± 0.9	14.7 ± 0.9	13.8 ± 1.0	0.152	0.04
HD 23850	13.5 ± 0.3	13.5 ± 0.3	13.0 ± 1.0	0.057	0.04
HD 29763	18.5 ± 0.8	17.0 ± 0.8	16.6 ± 1.0	0.048	0.08
HD 35497	14.0 ± 1.1	14.0 ± 1.0	13.6 ± 0.1	0.043	0.01
HD 36267	...	15.7 ± 0.5	16.3 ± 0.7	...	0.03
HD 98664	11.1 ± 1.4	11.0 ± 1.0	10.5 ± 0.1	0.067	0.03
HD 120315	17.0 ± 0.9	17.0 ± 0.9	17.7 ± 0.3	0.007	0.03
HD 147394	16.9 ± 0.7	16.9 ± 0.7	15.4 ± 0.7	0.050	0.02
HD 155763	15.0 ± 0.8	15.0 ± 0.8	13.5 ± 0.8	0.064	0.03
HD 160762	18.2 ± 0.7	18.2 ± 0.7	18.2 ± 1.0	0.036	0.03
HD 176437	11.0 ± 1.4	11.0 ± 1.0	10.4 ± 0.6	0.133	0.04
HD 177756	12.0 ± 1.3	12.0 ± 1.0	10.7 ± 1.0	0.048	0.02
HD 184930	14.5 ± 0.6	14.5 ± 0.6	13.9 ± 0.5	0.095	0.10
HD 186882	12.0 ± 1.4	12.0 ± 1.0	10.4 ± 0.4	0.190	0.01
HD 196867	13.3 ± 1.3	13.3 ± 1.3	11.1 ± 0.1	0.107	0.02
HD 198478	18.8 ± 1.4	16.5 ± 1.0	18.8 ± 0.3	0.679	0.53
HD 205021	29.5 ± 2.5	23.6 ± 1.0	26.8 ± 0.1	0.067	0.05
HD 214923	12.3 ± 1.4	12.3 ± 1.0	11.4 ± 0.6	0.057	0.04
HD 218045	10.0 ± 1.0	10.0 ± 1.0	10.1 ± 0.1	0.057	0.04
HD 222661	11.0 ± 1.3	11.0 ± 1.3	10.9 ± 0.2	0.024	0.01

Literature $E(B-V)$ values averaged from Neckel et al. (1980) and Savage et al. (1985).

5.3 Results and Comparison to Models

The predicted angular diameters for our B stars are in fairly good agreement with our directly measured angular diameters. Looking at the comparison of predicted model sizes to our measured angular diameters in Figure 5.7, no obvious trend away from a linear correlation is apparent. However, the weighted average ratio of $\theta_{model}/\theta_{observed}$ differs from 1 by about 4% suggesting the models may be slightly over-estimating the diameters of some stars. The most discrepant star is 55 Cyg, a supergiant discussed in Section 5.4.11. Overall, it appears that the literature temperatures and associated TLUSTY B and ATLAS9 models lead to

overestimates of the angular diameters of some B stars. However, measuring early-type stars with interferometry is still a fairly new and difficult undertaking and we must take this into consideration before suggesting that the spectral line-based temperatures and/or atmospheric models need revision. In some cases, the larger angular size from the literature and models may result from the extra flux of unknown binary companions. Upon inspection of the angular diameter comparison plot in Figure 5.7, it appears there are slightly different trends between the stars observed with CLIMB and those observed with PAVO. Conducting a linear fit of each data set separately, and allowing the y-intercept to be a variable, yields a fit of $y = 0.893x + 0.058$ for the PAVO data and $y = 0.885x + 0.098$ for the CLIMB data.

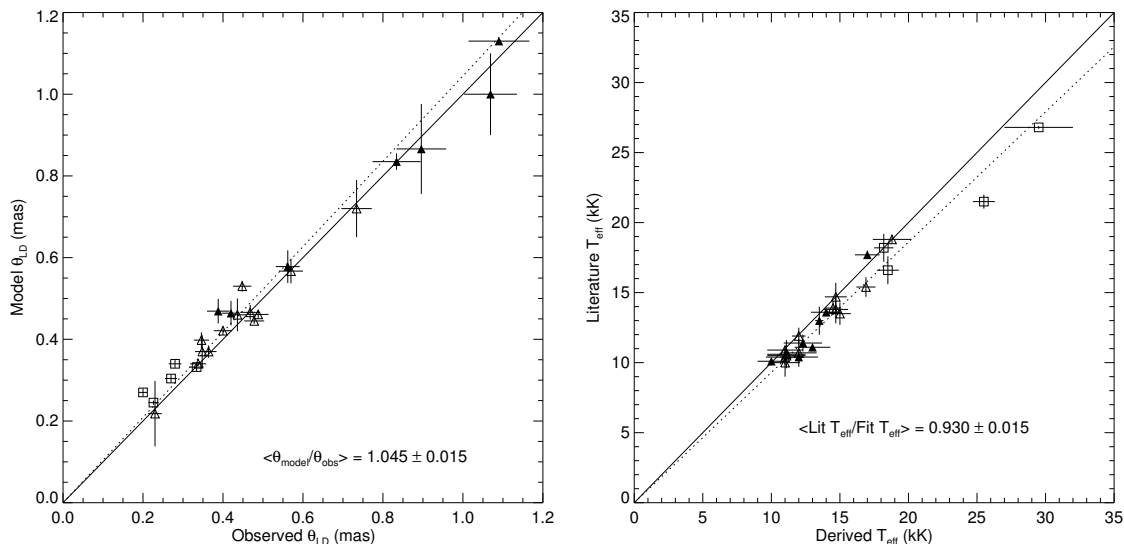


Figure 5.7 The left panel shows a comparison of our observed angular diameters to the predicted model size. The right panel shows a comparison of our derived temperatures to the average literature temperature. In both plots the solid line is a unit line for reference and the dotted line indicates the weighted mean of $\theta_{model}/\theta_{obs}$ and Literature $T_{eff}/Fit T_{eff}$, respectively. Square symbols indicate stars fit the TLUSTY B models, triangles indicate stars fit with ATLAS9 models, and filled triangles indicate stars with CLIMB data or CLIMB+PAVO data.

These fits suggest that the angular diameters obtained from PAVO slightly better agree with model predictions than those measured with CLIMB.

Table 5.5 B Star Distance and Radius Estimates

Star	d_1 (pc)	d_2 (pc)	d_3 (pc)	R/R_\odot (R_\odot)
HD 2772	...	115.7±5.8	93.6±4.0	2.3 ± 0.2*
HD 3360	179	181.8±5.3	108.8±4.0	3.2 ± 0.2
HD 11502	...	50.3±2.4	53.0±1.2	2.0 ± 0.1*
HD 15318	...	59.2±4.2	60.4±1.7	2.6 ± 0.2
HD 23302	...	124.1±3.8	114.9±6.9	5.9 ± 0.5*
HD 23408	...	117.5±3.9	105.5±7.6	4.9 ± 0.4
HD 23850	...	117.2±5.4	118.6±7.8	4.9 ± 0.5*
HD 29763	...	122.1±13.1	93.4±5.2	2.3 ± 0.2*
HD 35497	37	41.1±0.6	...	4.8 ± 0.3
HD 36267	...	92.9±5.5	108.4±8.2	2.3 ± 0.2*
HD 98664	...	67.5±1.1	61.0±3.2	3.1 ± 0.2
HD 120315	39	31.9±0.2	...	2.9 ± 0.2
HD 147394	102	94.3±1.0	97.1±3.3	3.8 ± 0.2
HD 155763	98	100.7±3.5	118.0±6.8	6.2 ± 0.5*
HD 160762	145	139.5±2.5	132.0±6.3	4.7 ± 0.3
HD 176437	...	190.1±9.8	168.2±11.7	13.3 ± 1.2
HD 177756	42	37.9±0.9	37.0±0.7	2.3 ± 0.1
HD 184930	123	119.9±11.4	100.6±1.7	3.7 ± 0.2
HD 186882	...	50.6±1.2	...	4.9 ± 0.4*
HD 196867	62	77.8±2.7	66.8±2.4	3.0 ± 0.2*
HD 198478	1072	714.3±86.7	1177.0±186.8	56.7 ± 9.5
HD 205021	231	210.1±13.2	239.8±1.7	7.2 ± 0.4*
HD 214923	...	62.7±0.7	70.0±1.8	4.2 ± 0.3
HD 218045	...	40.8±0.3	...	4.7 ± 0.3
HD 222661	...	45.5±0.5	48.6±0.8	1.8 ± 0.1*

Distance references: 1. Underhill et al. (1979), 2. van Leeuwen (2007) and Maíz Apellániz et al. (2008), 3. Gaia Collaboration et al. (2018). Stellar radii are calculated from the derived Gaia DR2 distances where available. Derived *Hipparcos* distances were used when no Gaia DR2 parallax was measured. * indicates stars with close companions (Table 3.2).

Our effective temperature estimates agree fairly well with published literature values. However, there is a trend, apparent in Figure 5.7, of our temperature estimates exceeding the literature values by an average of 800 K. Angular size and temperature have an approximately inverse square relationship, so this is to be expected from the model overestimation of our angular diameters discussed above. Casagrande et al. (2014) compared photometrically and

interferometrically determined effective temperatures and found that there is a systematic trend of higher effective temperatures determined from interferometry for stars smaller than ~ 0.8 mas. There is also a larger scatter in values at smaller diameters. They find that the estimate of T_{eff} from interferometry can be hotter by up to 400 K than that derived from their method which relies on the ratio between the bolometric flux and the monochromatic infrared flux of a star measured on the Earth. They determine that more interferometric measurements and comparisons are needed. However, this is not a direct comparison as the sample of stars studied in Casagrande et al. (2014) are cooler than our target stars. The literature effective temperature estimates are derived from spectroscopic line studies, while our approach relies on the continuum flux combined with our observed angular diameters to obtain temperature estimates.

As with the O stars, we can combine our observed angular diameters with known distances to calculate stellar radius. Table 5.5 lists distance estimates from four sources and our stellar radius estimates. The estimate d_1 is based on spectral classification by Underhill et al. (1979). The second estimate d_2 is derived from the *Hipparcos* parallax (van Leeuwen 2007). The third estimate d_3 is derived from Gaia DR2 parallaxes (Gaia Collaboration et al. 2018). The last column gives the calculated stellar radius based on the Gaia DR2 distance estimate where available and our measured angular diameter. If no Gaia DR2 parallax was listed, then the *Hipparcos* value was used. The DR2 parallaxes for HD 186882 and HD 205021 have large errors so we have used the listing for the B component for these stars.

5.4 Notes on Individual Stars

5.4.1 HD 3360

ζ Cas (HD 3360) was previously observed with the PAVO beam combiner by Maestro et al. (2013). They obtained two brackets of data, or 46 visibility points, on a single baseline (S1E1). They measured a limb-darkened diameter for ζ Cas of 0.311 ± 0.010 mas. This is 15% larger than our measured diameter at 0.270 ± 0.015 mas. We also obtained two brackets of data on this star but on two different baselines (S1E1 and E1W1). ζ Cas is not a rapid rotator, with a $v \sin i$ of only 17 km s^{-1} (Table 3.1), so we should not be observing any rotational distortion on different baselines. Maestro et al. (2013) also used the same calibrator for their observations as ours, HD 1279, but assumed a larger angular size of 0.202 mas. This could explain the larger angular size they measure for ζ Cas.

Maestro et al. (2013) also conducted spectral fitting for their stars using optical and near-infrared photometry and low-resolution IUE spectra with ATLAS9 models. They find a best fit temperature of 18562 ± 151 K which is 13% lower than their adopted literature temperature of 21061 ± 706 K. We used observed spectra in the ultraviolet and optical, and near-infrared photometry for our spectrophotometric fitting. Due to its higher effective temperature, we used the TLUSY B star models to fit the SED of ζ Cas. We find a best fit temperature of 24.5 ± 0.8 kK, which is 14% higher than our adopted literature temperature of 21.5 kK and 32% higher than the effective temperature determined by Maestro et al. (2013). ζ Cas is a B2IV star and has an expected temperature of ~ 21 kK based on spectral type (Gray 2005).

5.4.2 *HD 11502*

HD 11502, or γ^1 Ari, is a binary star system with a very similar companion. Its companion, γ^2 Ari, is an A2IVp star 7.4 arcsec away and with a Δm_V of -0.06 mags. Due to the two star's similarity, there has been confusion over which star is labeled HD 11502. Our observations agree with SIMBAD's designation making γ^1 Ari the more northerly and slightly fainter star of the pair. All optical spectral sources we were able to find for this star included the spectra of both stars in the pair. However, all UV spectral sources available contained the spectra of γ^1 Ari alone. Thus, it would only be correct to apply a companion correction to the optical spectral data, and not the spectrum as a whole. For this reason, we have used only the optical spectral data for HD 11502 for our spectrophotometric fitting, and the subsequent χ^2 contour plot and SED show only the fitted optical spectrum.

5.4.3 *HD 23302*

Electra (HD 23302) is a member of the Pleiades and sometimes has a circumstellar disk as a Be star. The BeSS database (<http://basebe.obspm.fr/basebe/>) maintains a catalog of spectra of Be stars. At the time of our observations, 2013 December, Electra showed evidence for the presence of a small disk in the weak emission filling of the $H\alpha$ core. The presence of a disk implies that our angular diameter may be slightly overestimated. However, Electra was observed with PAVO, operating in the R -band, where any flux contributed from a disk will be minimal.

5.4.4 *HD 23408*

There is a companion listed for HD 23408, or Maia, in the *Washington Double Star Catalog* from a lunar occultation observation with a separation of less than 1" and a Δm_V of 1. However, in a recent study by White et al. (2017), no companion was considered for their interferometric and photometric fitting. They found an angular diameter of 0.451 ± 0.006 mas ($\sim 3\%$ larger than our size), and an effective temperature of $12,550 \pm 150$ K ($\sim 17\%$ cooler than our estimate). Our spectrophotometric fitting also works well without the presence of a companion. White et al. (2017) found that Maia has a large chemical spot on its surface, and it is possible that the rotational modulation of the light curve due to the spot is what was believed to be a signature of a companion during the occultation observation. Due to this evidence we have not included a companion into the analysis for HD 23408.

5.4.5 *HD 23850*

Atlas (HD 23850) is a triple system in the Pleiades. There is a close, spectroscopic binary companion with a period of 290.81 days (Pan et al. 2004; Zwahlen et al. 2004). There is another farther companion at 0.5" with a Δm_V of 3. Due to the close inner companion a binary solution may be necessary to measure θ_{LD} for the primary so our angular diameter may be overestimated. The spectrophotometry, including the contour plot and SED, has been corrected for both known companions.

The data for Atlas on two nights of observation (2014 September 24 and 2015 September 13) were fit with a grid search binary model fitting routine (Schaefer et al. 2016). The

predicted binary separation for each night of data was compared to the companion’s predicted position based on the orbit derived by Zwahlen et al. (2004). The fitted separation, flux ratio and primary diameter for each night are given in Table 5.6. These are preliminary binary fits but show fair agreement with the companion’s predicted position based on the known orbit. The average of the two fitted primary diameters is in good agreement with our incoherent flux corrected, single star fit of 0.388 ± 0.028 mas.

Table 5.6 Fitted binary parameters for Atlas

Date	Separation (mas)	Flux Ratio	Primary Diameter (mas)
2014/09/24	8.22 ± 0.03	0.142 ± 0.002	0.34 ± 0.05
2015/09/13	11.8 ± 0.2	0.126 ± 0.002	0.41 ± 0.03

5.4.6 HD 29763

HD 29763, or τ Tau, is a spectroscopic binary with a more distant visual companion. The spectroscopic binary has a 2.9 day orbit and contributes 25% of the flux to the system (Petrie & Ebbighausen 1961). However, the orbital inclination, i , and the longitude of the ascending node, Ω , are not known for this orbit. This companion is close enough to show up as a modulation in the visibility curve but in order to model τ Tau as a binary we would have to fit for i , Ω and θ simultaneously. Therefore, our interferometry has not been corrected for the close companion of τ Tau. The spectrophotometry, including the contour plot and SED, has been corrected for both known companions.

5.4.7 HD 35497

β Tau (HD 35497) is a HgMn star and has a companion listed in the *Washington Double Star Catalog* with a separation of $0.1''$ and a Δm_V of 0. However, we have been unable to find any corroborating sources in the literature. With a companion this close to our target, and this bright, our spectrophotometric fitting should be very far off without accounting for the companion, but this is not the case. Due to the lack of evidence to support the existence of this companion we have not included it in our analysis for β Tau.

However, Adelman et al. (2006) find β Tau to be a spectroscopic binary based on radial velocity observations. They find it to be a single lined spectroscopic binary, so if a companion exists it will be significantly fainter than the primary.

5.4.8 HD 36267

Contour mapping was not successful for HD 36267 so no fitted values for temperature or reddening are given in Table 5.4 for this star. HD 36267 is a probable triple system with an inner spectroscopic binary with a period of 3.964 days (Morrell & Levato 1991). It has a farther companion that is listed in Table 3.2 and was taken into account for the interferometric and spectrophotometric fitting. However, no correction was made for the possible inner pair and this may be affecting the SED. HD 36267 is also one of the smallest B stars in our sample and has a fair amount of noise in its visibility data. It is possible that the data are not good enough quality in this case to produce a reliable angular diameter measurement so close to the resolution limit of PAVO.

5.4.9 HD 155763

HD 155763 was observed with both the PAVO and CLIMB beam combiners. However, it has a close, bright companion with a separation of $0.059''$ and a magnitude difference of 1.03. The correction for the incoherent flux contributed by this companion was computed for the PAVO data, but was not able to be calculated for the CLIMB data due to many non-physical values (greater than 1) for the visibilities after the incoherent flux correction was applied. Working in the H -band, CLIMB has a lower angular resolution than PAVO and this resulted in the non-physical corrected visibilities. For this reason we have exclusively used the PAVO data for HD 155763 for the final angular diameter measurements given in Table 5.1 and Table 5.2.

A binary fit was made to the CLIMB data on the night of observation with several brackets (2015 August 14) using a grid search binary model fitting routine (Schaefer et al. 2016). The fit resulted in a primary diameter of 0.494 mas which is consistent with our single star fit (corrected for incoherent flux) of the PAVO data of 0.488 ± 0.026 mas.

The literature T_{eff} will be underestimated if the companion has not been accounted for. Fainter companions are generally cooler, and they may contribute to making the spectrum appear as if it were due to a star that is slightly cooler than the actual temperature.

5.4.10 HD 176437

γ Lyr (HD 176437) was previously observed with the PAVO beam combiner by Maestro et al. (2013). They obtained 7 brackets, or 161 visibility points, on three different baselines

(W1W2, W2E2, S1W2). They measure a limb-darkened angular diameter of 0.753 ± 0.009 mas. This is 3% larger than our measured angular diameter of 0.734 ± 0.038 mas. However, the two measurements agree within errors. We obtained 4 brackets of data, or 92 visibility points, on a single baseline (W2S2).

Maestro et al. (2013) also conducted spectral fitting for their stars using optical and near-infrared photometry and low-resolution IUE spectra with ATLAS9 models. They find a best fit temperature of 9640 ± 60 K which is 14% lower than their adopted literature temperature of 10959 ± 973 K. We used observed spectra in the ultraviolet and optical, and near-infrared photometry for our spectrophotometric fitting. We also use the ATLAS9 models to fit the SED of γ Cas and find a best fit temperature of 11.0 ± 1.4 kK, which is 9% higher than our adopted literature temperature of 10.1 kK and 14% higher than the temperature determined by Maestro et al. (2013).

5.4.11 HD 198478

HD 198478, or 55 Cyg, is the only spectral type B supergiant in our sample. It is very heavily reddened with a best fit $E(B - V)$ of 0.679. It was observed over two nights with CHARA on different, but similar, baselines. Our observed angular size, at 0.448 ± 0.023 mas, is 25% smaller than the model prediction. This, in turn, causes our best fit temperature, at 18.8 ± 1.4 kK, to be 15% higher than the model fit value. However, both the models we use in this work, TLUSTY and ATLAS9, do not account for wind effects which become very important in supergiant stars. Additionally, the ATLAS9 models do not include non-LTE effects. 55 Cyg was fit with both models and they showed good agreement with each other.

In a recent study by Kraus et al. (2015), spectra of 55 Cyg were examined with the FASTWIND code (Santolaya-Rey et al. 1997; Puls et al. 2005) to search for photospheric variability and mass loss variability in the stellar wind. FASTWIND is a non-LTE, spherically symmetric stellar atmosphere code. It includes line-blanketing effects and calculates the structure of the photosphere and the stellar wind. Using this modeling method and their observed spectra, Kraus et al. (2015) found an effective temperature for 55 Cyg of 18.8 kK and a stellar radius of $57R_{\odot}$. This translates to an angular diameter of 0.74 mas using their assumed distance of 714 pc. However, the recent Gaia DR2 parallax (Gaia Collaboration et al. 2018) puts it at a distance of 1177 ± 187 pc. This distance results in an angular size of 0.45 ± 0.07 mas which is in good agreement with our measured diameter. They found that all $H\alpha$ profiles in their spectra could not be modeled with a fixed size. They suggest that the star therefore has a variable wind opacity or real radial changes, due to processes such as radial pulsations. The fits for stellar radius result in a range from $52R_{\odot}$ to $65R_{\odot}$. Using the distance derived from the Gaia DR2 parallax, this translates to an angular diameter range of 0.41 mas to 0.51 mas. Thus, the temperature and stellar radius derived by Kraus et al. (2015) are in excellent agreement with our best fit temperature and interferometric observations.

This higher temperature and smaller angular size do not fit the SED well using the TLUSTY or ATLAS9 models. A lower temperature around 16 kK and a larger angular size of 0.53 mas would result in better agreement with the SED. The FASTWIND atmosphere code considers specific spectral lines while we are fitting the continuum flux with our models.

It may be that the models that do not take into account wind effects do not predict stellar parameters well for B supergiants. However, to make a direct comparison we would need to model the continuum flux with the presence of a stellar wind.

5.4.12 HD 205021

β Cep (HD 205021) is the prototype variable star for a class of rapid pulsators. It has a companion at $0.25''$ that is a Be star (discussed in Wheelwright et al. 2009). The flux from the disk may cause the companion to be redder than expected and this may cause the SED fit to be incorrect for the companion correction. In a spectropolarimetry study by Henrichs et al. (2013), they suggest a stellar radius of $6.5R_{\odot}$ which gives an angular diameter of 0.25 mas at our adopted distance of 240 pc. This is in good agreement with our measured angular size of 0.280 ± 0.016 .

5.4.13 HD 218045

α Peg (Markab, HD 218045) was observed with both the PAVO and CLIMB beam combiners. It was observed with PAVO over two nights on baselines E2S2 and E2W2. Due to the large angular size (1.069 mas) of α Peg, we were able to obtain data in the second lobe of the visibility curve on one night of observation with PAVO. This area of the visibility curve is most sensitive to changes in the limb-darkening coefficient. An enlarged look at the second lobe data is shown in Figure 5.8 while Figure 5.9 shows the data by individual bracket. The angular size for the disk fit model was based on the error weighted fit from the first lobe data. This fit is then shown in the following figures using our adopted limb-darkening coefficient

and with no limb-darkening for comparison. It seems from the sequence of brackets in Figure 5.9 that the data agree well with the adopted limb-darkening coefficient at the beginning of the observations followed by degrading observing conditions apparent in the larger visibility uncertainties.

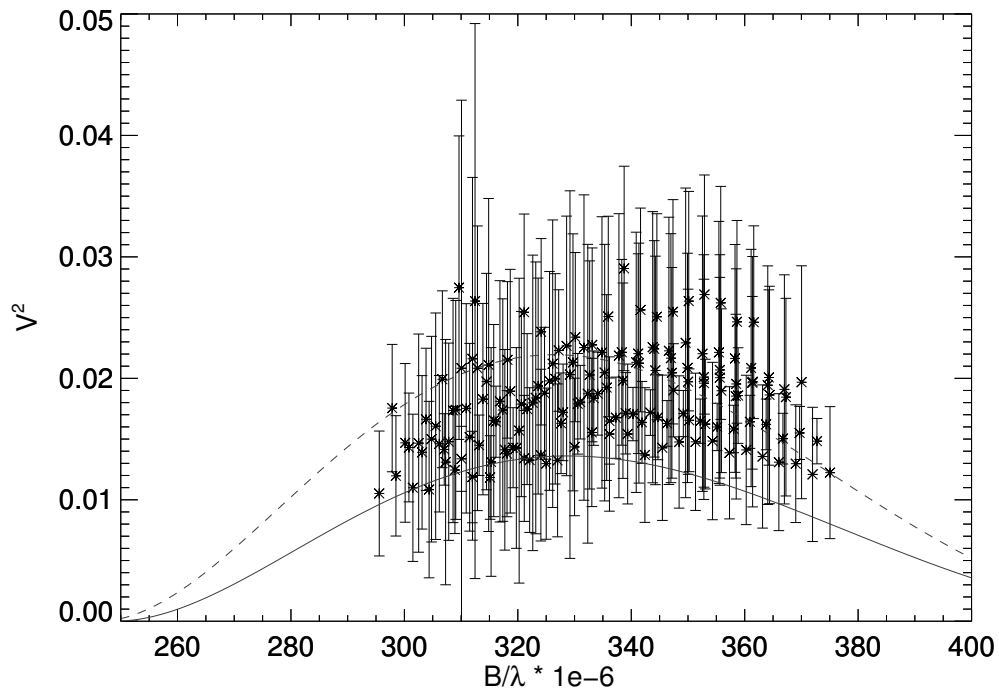


Figure 5.8 Squared visibility versus spatial frequency of second lobe data for HD 218045. The dashed line indicates a fit with no limb-darkening and the solid line indicates a fit with a limb-darkening coefficient of $\mu = 0.34$.

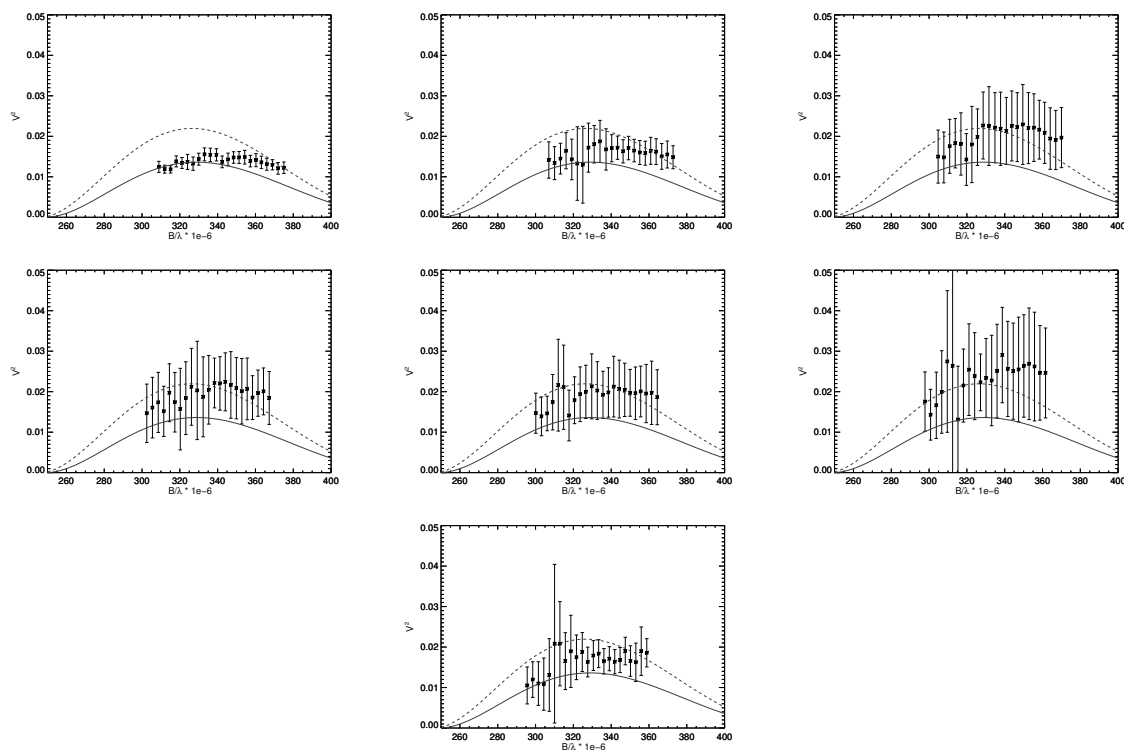


Figure 5.9 Squared visibility versus spatial frequency for individual brackets of second lobe data for HD 218045. The dashed line indicates a fit with no limb-darkening and the solid line indicates a fit with a limb-darkening coefficient of $\mu = 0.34$. Moving from left to right, the plots represent a chronological sequence during a single night of observation.

CHAPTER 6

SUMMARY

Together O- and B-type stars only make up 0.1% of all stars but are among the most luminous objects in the sky. They can be observed at great distances and heavily influence the composition of the interstellar medium, and future stars, with their mass loss from strong winds and supernovae. Historically early-type stars have been difficult to study and to obtain fundamental parameters because they are far away and tend to have complex environments from winds to circumstellar disks to multiple companions. Because these stars play such a large role in determining their environment and informing the chemistry of future stellar generations, it is important to gain a firm understanding of their stellar structure and properties. Due to the observational difficulties related to measurements of O and B stars, we rely heavily on stellar atmospheric models to estimate their fundamental parameters, such as stellar radius and effective temperature.

With the advent of long-baseline optical interferometry, we are now able to make direct measurements of early-type stars and test the predictions of stellar models. An interferometer uses several smaller telescopes spread far apart that work together to obtain an angular resolution like that of a large effective aperture telescope. The light from each telescope interferes and creates interference fringes. We can measure the contrast in the observed fringes, or visibility, and calculate the angular diameter of the source. We achieved a resolution limit of 0.2 milli-arcseconds and obtained direct angular diameter measurements for six O stars and 25 B stars with observations using the PAVO (operating in the *R*-band) and

CLIMB (operating in the H -band) beam combiners at the CHARA Array on Mt. Wilson, California.

We used an error weighted fitting method to fit our calibrated visibilities to a linear limb-darkened, single star, disk model to obtain angular diameter measurements. Where targets had close, bright companions (Table 3.2), we accounted for the incoherent flux the companion was contributing to the visibility curve and rescaled the visibilities accordingly. Eight stars were observed with the CLIMB beam combiner and 27 stars were observed with the PAVO beam combiner. Four stars were observed with both CLIMB and PAVO to compare results from the two combiners. For the O stars, our angular diameter errors were the result of the quadratic sum of nightly variations and fluctuations in the fits from adjusting calibrator sizes to plus and minus one sigma. The errors on the angular diameter of the B stars were obtained by adding the uncertainties from the residuals in the fit and the average nightly variation in quadrature.

Spectra were gathered for each star from multiple sources to span the wavelength range from ultraviolet to infrared (1200 Å to $2\mu\text{m}$ or longer). We then fit these spectra with TLUSTY O star, TLUSTY B star, or ATLAS9 models depending on what was appropriate for the effective temperature of the star. Where a companion was present, the companion's flux was added to the model flux calculated for the primary. This combined flux spectrum was used for spectrophotometric fitting of the observed SED. We used a grid search method to fit for effective temperature (T_{eff}), angular diameter (θ_{LD}), and reddening ($E(B - V)$). A χ^2 matrix was calculated based on the best fit $E(B - V)$ value for each pair of (θ_{LD} ,

T_{eff}), and contour plots of the χ^2 space over angular diameter vs. effective temperature were created. This allowed us to compare our interferometrically determined angular diameters to sizes predicted by the models based on the observed spectrum. We were also able to combine our directly determined angular sizes with the model fits to obtain an estimate for effective temperature. We then compared these estimates to average literature values for effective temperatures.

For our sample of 6 O-type stars we find that the angular diameters estimated from the published effective temperatures and fits of the SEDs ($\theta_{LD}(T_{\text{eff}})$ given in the final column of Table 4.1) are in good agreement with the interferometric angular diameters. The set of stars with the greatest discrepancy, ξ Per, ζ Ori A, and ζ Oph, consists of two stars (ξ Per and ζ Ori A) where a systematic bias was detected in the data and we consider the results as preliminary. ξ Per, α Cam, and ζ Ori A were observed in only a single bracket, and in each case we needed to correct the fitted size for a systematic variation of V^2 with fractional error $\Delta V^2/V^2$ (see Section 4.1.1). The presence of the trend indicates that our derived θ_{LD} values may be underestimated for these three stars. We were also able to confirm the rotational distortion expected of the O star ζ Oph which is rotating at 90% of its critical equatorial, angular rotational velocity (Howarth & Smith 2001). We found a ratio of minor to major axis of 0.86, which is similar to the polar to equatorial radius ratio of 0.82 found by Howarth & Smith (2001). The O star 10 Lac was resolved with an angular diameter of 0.12 mas, working below the nominal resolution limit of PAVO at 0.2 mas, making it the smallest star resolved with the CHARA Array to date. However, effective temperatures derived from our

interferometric results and from spectroscopic studies in the literature, result in a higher temperature ($\sim 36\text{kK}$) than expected for its O9 V spectral classification.

From our observational sample of 25 B-type stars, we find that the interferometric angular diameters and predicted model diameters are in good agreement. However, we find that the average literature temperature underestimates the effective temperatures compared to the estimates we derive from fits of the SED and our interferometric sizes. Casagrande et al. (2014) finds a trend of interferometrically determined effective temperatures yielding higher results than photometrically determined temperatures. However, our literature temperature were determined from spectral line studies. We suggest that the T_{eff} scale for O and B stars may need revision, but caution that interferometric observations of early-type stars are still relatively new and difficult and this must be taken into consideration.

Four B stars were observed with both the PAVO and CLIMB beam combiners to check for consistency between instruments, and three were used for the comparison (see Section 5.1.1). We find that diameter measurements from the PAVO beam combiner are smaller than those from CLIMB. This discrepancy has been previously observed and discussed in White et al. (2018) for different targets. The original CLIMB data reduction does not use an error weighted mean to combine power spectra from scans. Equal addition of the lower quality data can cause smaller visibility estimates, resulting in a larger angular size. This could explain some of the size discrepancy we measure from CLIMB observations. However, the CLIMB data for the three stars were subsequently run through the updated CLIMB pipeline using a weighted mean to combine power spectra and through an independent pipeline created

by John Monnier that uses bootstrapping to estimate visibility errors. All three reduction pipelines resulted in angular sizes that agreed within errors and gave consistently larger angular sizes by $\sim 9\%$ (33% for the very discrepant HD 196867) for CLIMB data compared to PAVO data. Since it is operating at a longer effective wavelength, CLIMB observations will result in visibilities closer to 1 than observations with PAVO for a given star. Higher visibility measurements may be more vulnerable to calibration uncertainties and will not provide as accurate a measurement of the angular diameter. We suggest that PAVO observations will give more accurate results than observations with CLIMB for stars smaller than ~ 0.8 mas. A larger sample size is necessary to investigate this issue fully.

The angular size and effective temperature of the one supergiant in our B star sample, 55 Cyg, was not fit well by either the TLUSTY or ATLAS9 models. However, fits of the spectra with the FASTWIND model by Kraus et al. (2015) result in excellent agreement with our directly measured angular diameter and interferometrically determined temperature. Our best fit temperature and angular size of 18.8 kK and 0.45 mas do not fit the SED well using TLUSTY or ATLAS9 models. A lower temperature and larger angular size would result in better agreement with the SED. We suggest that models which do not account for wind effects may be inadequate for supergiant type B stars.

A comparison of our measured angular diameters to previous interferometric measurements is shown in Figure 6.1. These include measurements from Challouf et al. (2014), Maestro et al. (2013), White et al. (2017), and Hanbury Brown et al. (1974) and show that our interferometric measurements are in good agreement with previous measurements.

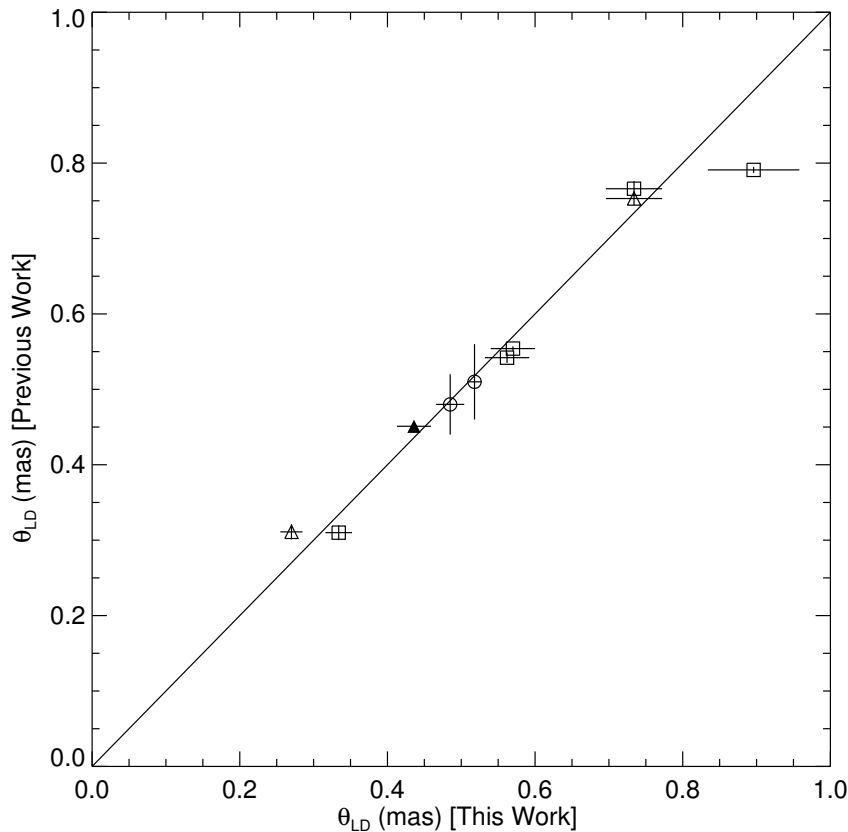


Figure 6.1 Comparison of our measured θ_{LD} to previous work. Square = VEGA observations by Challouf et al. (2014), open triangle = PAVO observations by Maestro et al. (2013), filled triangle = PAVO observation by White et al. (2017), circle = NSII observations by Hanbury Brown et al. (1974).

We used our derived estimates for stellar radius and effective temperature to place our stars on an observational HR diagram. This is shown in Figure 6.2 and includes both our O star and B star samples. Blue circles indicate the O stars, while the dark blue triangles are the three O stars for which we only have upper estimates on the effective temperature. Overplotted are evolutionary tracks and isochrones for the MESA grid (Dotter 2016; Choi et al. 2016; Paxton et al. 2013). The models chosen are for non-rotating stars and solar metallicity. These show evolutionary tracks for stellar masses of $2.5M_{\odot}$, $5M_{\odot}$, $10M_{\odot}$, $20M_{\odot}$,

and $40M_{\odot}$ and isochrones for ages of 1 Myr, 3.2 Myr, 10 Myr and 32 Myr. Pre-main sequence and the evolutionary endpoint sections of the tracks have been omitted for clarity. With stellar radius and effective temperature derived from direct measurements we can begin to use evolutionary models like these to obtain estimates for mass and age. Jones et al. (2015) did this for a sample of A-type stars which tend to be rapid rotators and this rotation can effect their evolution and determined age. It will be important to extend our derived

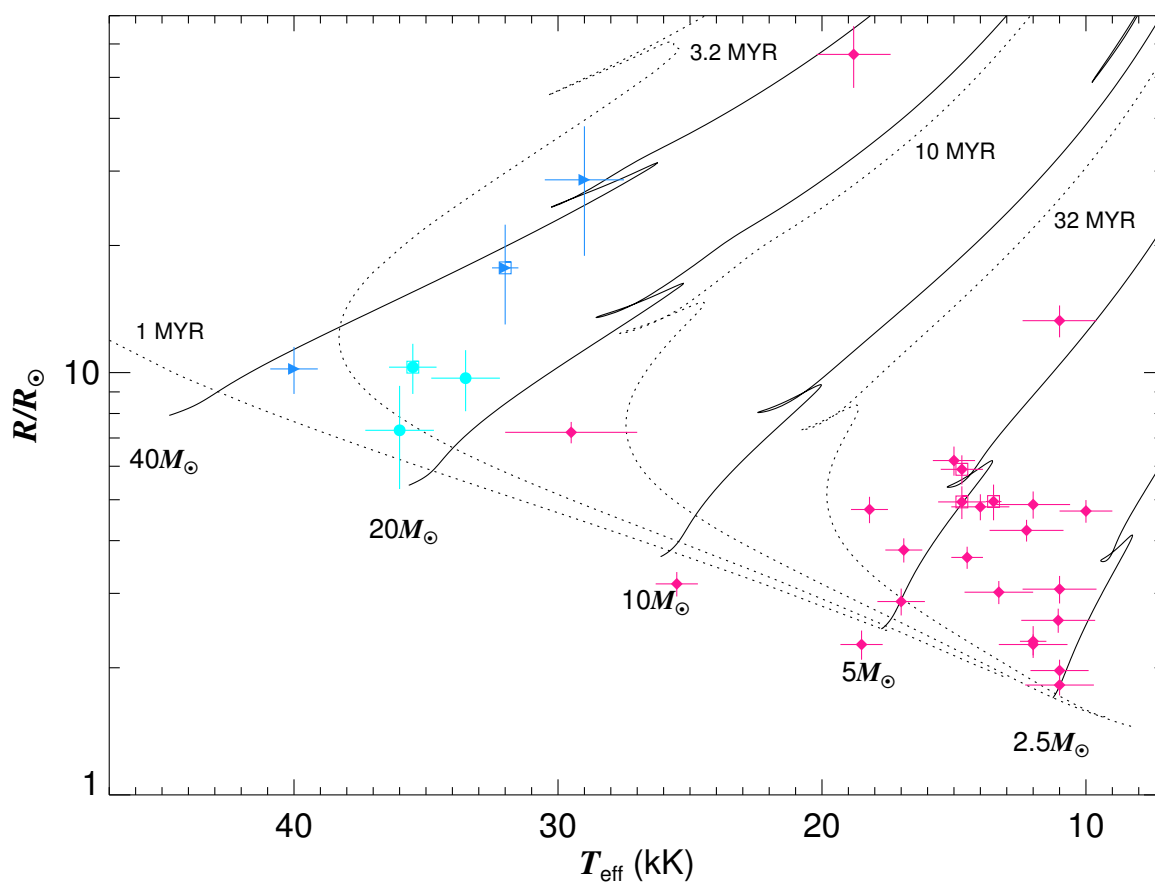


Figure 6.2 Observational HR diagram for our targets. The pink diamonds indicate B stars, blue circles O stars, and dark blue triangles are O stars with only upper effective temperature estimates. Symbols enclosed by squares indicate stars that are cluster members. Evolutionary tracks and isochrones from the MESA grid.

parameters to similarly obtain accurate determinations of stellar mass and age for O and B stars in the future. Masses and ages of massive stars are still not well constrained and estimates based on direct measurements will help solidify our understanding of early-type stars.

Two of our observed O stars are in stellar clusters or associations and this can provide an independent check of stellar age. λ Ori (HD 36861) is a member of the Collinder 69 cluster in the Lambda Orionis association which has an estimated age of 5 Myr (Wu et al. 2009). ζ Ori (HD 37742) is a member of the Orion OB1b association which has an estimated age of 8 Myr (Warren & Hesser 1977). Both of these stars appear to fall in a reasonable location on our observational HR-diagram in Figure 6.2 to agree with these age estimates. We have three B sample stars that are members of the Pleiades star cluster: Electra (HD 23302), Maia (HD 23408), and Atlas (HD 23850). Recent calculations by Meynet et al. (1993) give the Pleiades an estimated age of 100 Myr. Again, our observations for these three stars result in an age estimate based on our observational HR-diagram that is in good agreement with independent measurements.

The frequency of multiplicity in O and B stars presents another prospect for future work. The range of baselines and effective wavelengths available at the CHARA Array means that for many systems it is possible to resolve the angular size of each star in a binary system, as well as the separation of the binary itself. This can be combined with masses, distances, and radii found by previous methods, such as astrometric studies or radial velocity measurements, to constrain very accurately the parameters of the system. Often an observer

is interested only in the angular size of the star or the separation of the binary, but the range of angular sizes and separations of many O and B star multiple systems affords us the valuable opportunity to measure both.

This work has provided new interferometric observations of an important subset of stars. With these observations we were able to test the accuracy of stellar atmosphere models and gain insight into the fundamental properties of O and B stars. It will be important to expand the size of this observational sample in the future to gain a firmer statistical understanding of the trends we have seen here.

Appendices

A Observing logs and visibility curves

A.1 HD 2772

Table A.1 HD 2772 Observing Log

Baseline	Combiner	Brackets	N_{V^2}	Date
WIS2	PAVO	5	115	2014-09-12

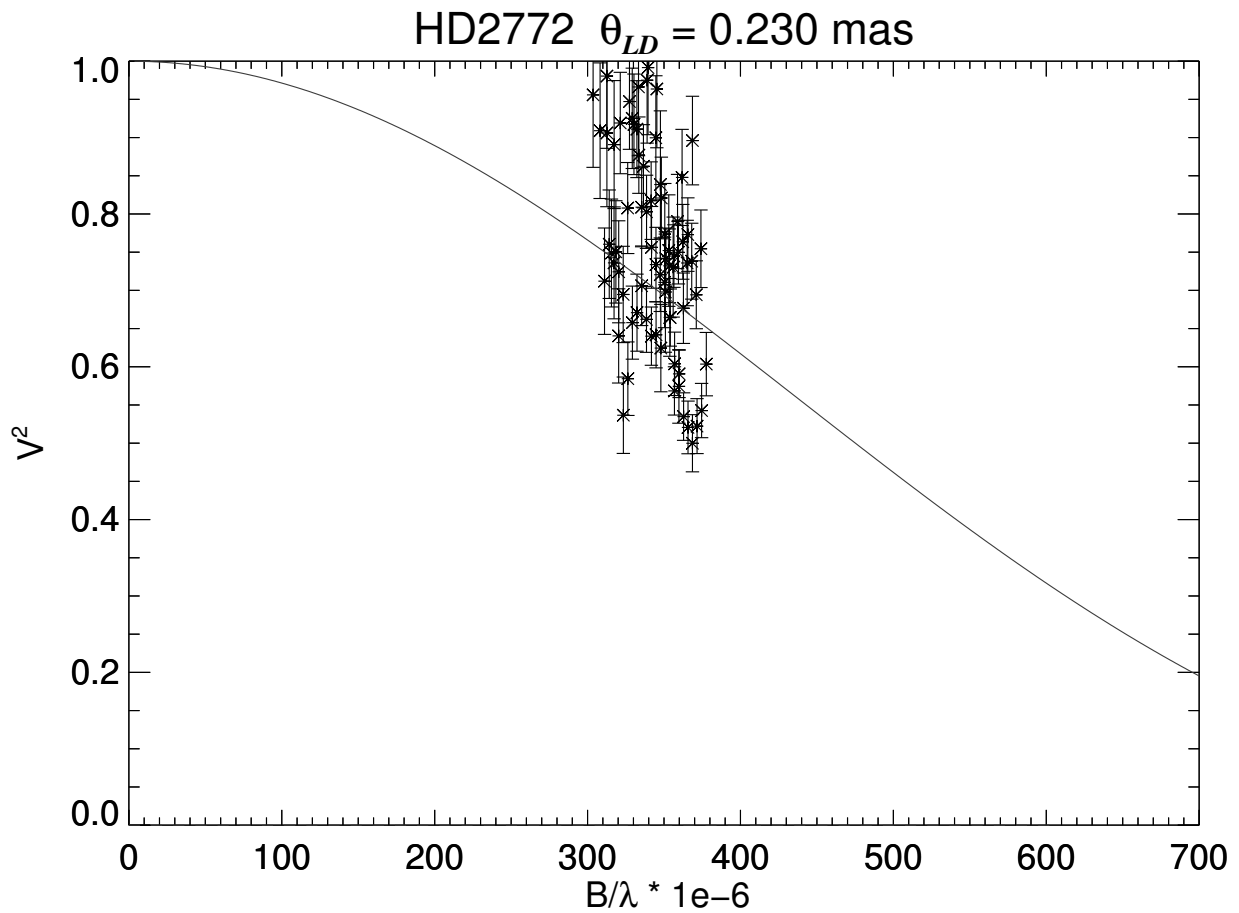


Figure A.1 Squared visibility versus spatial frequency for HD 2772. The solid line indicates the best fit for a single star limb-darkened disk model.

A.2 HD 3360

Table A.2 HD 3360 Observing Log

Baseline	Combiner	Brackets	N_{V^2}	Date
E1S1	PAVO	1	23	2012-11-15
E1W1	PAVO	1	23	2015-11-14

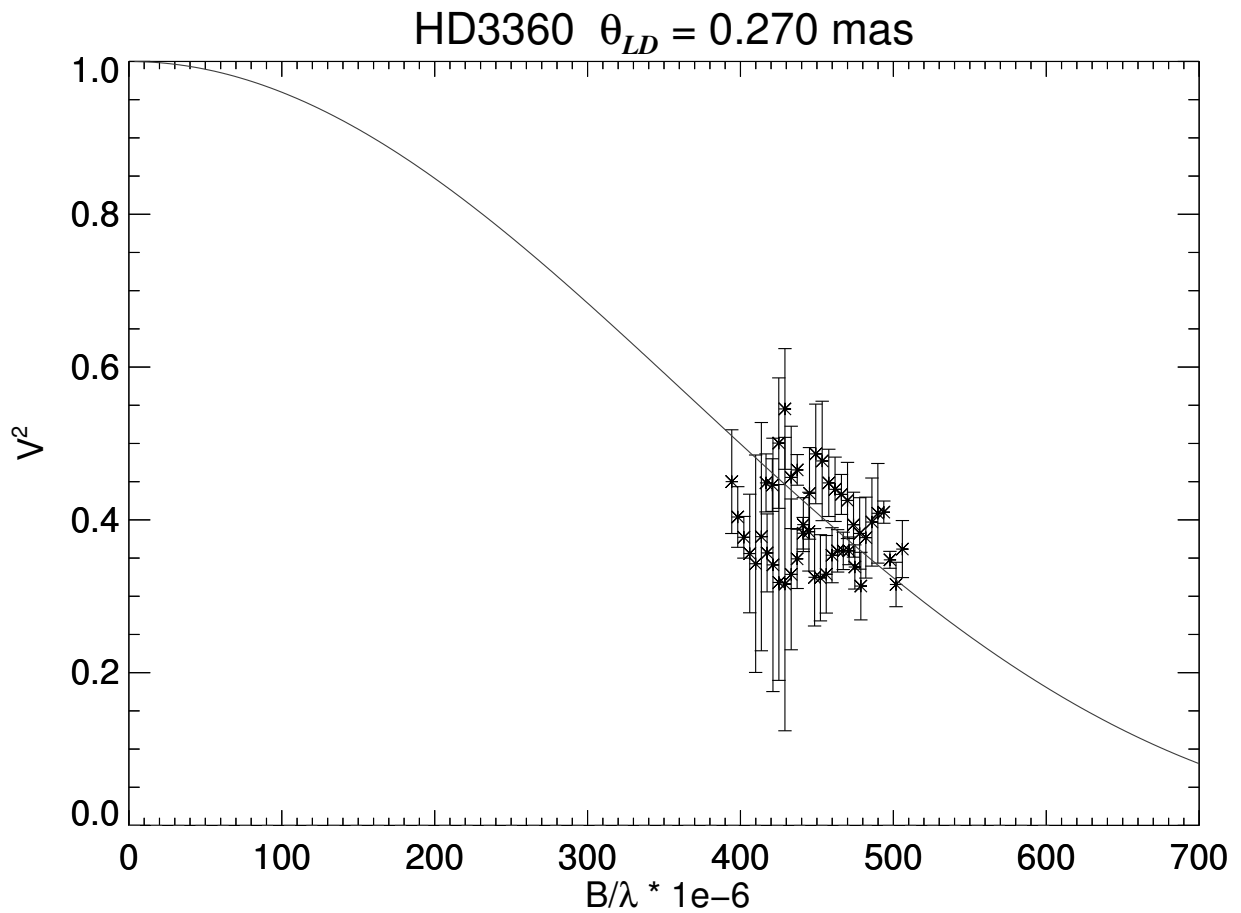


Figure A.2 Squared visibility versus spatial frequency for HD 3360. The solid line indicates the best fit for a single star limb-darkened disk model.

A.3 HD 11502

Table A.3 HD 11502 Observing Log

Baseline	Combiner	Brackets	N_{V^2}	Date
E1S1	PAVO	3	69	2012-10-14

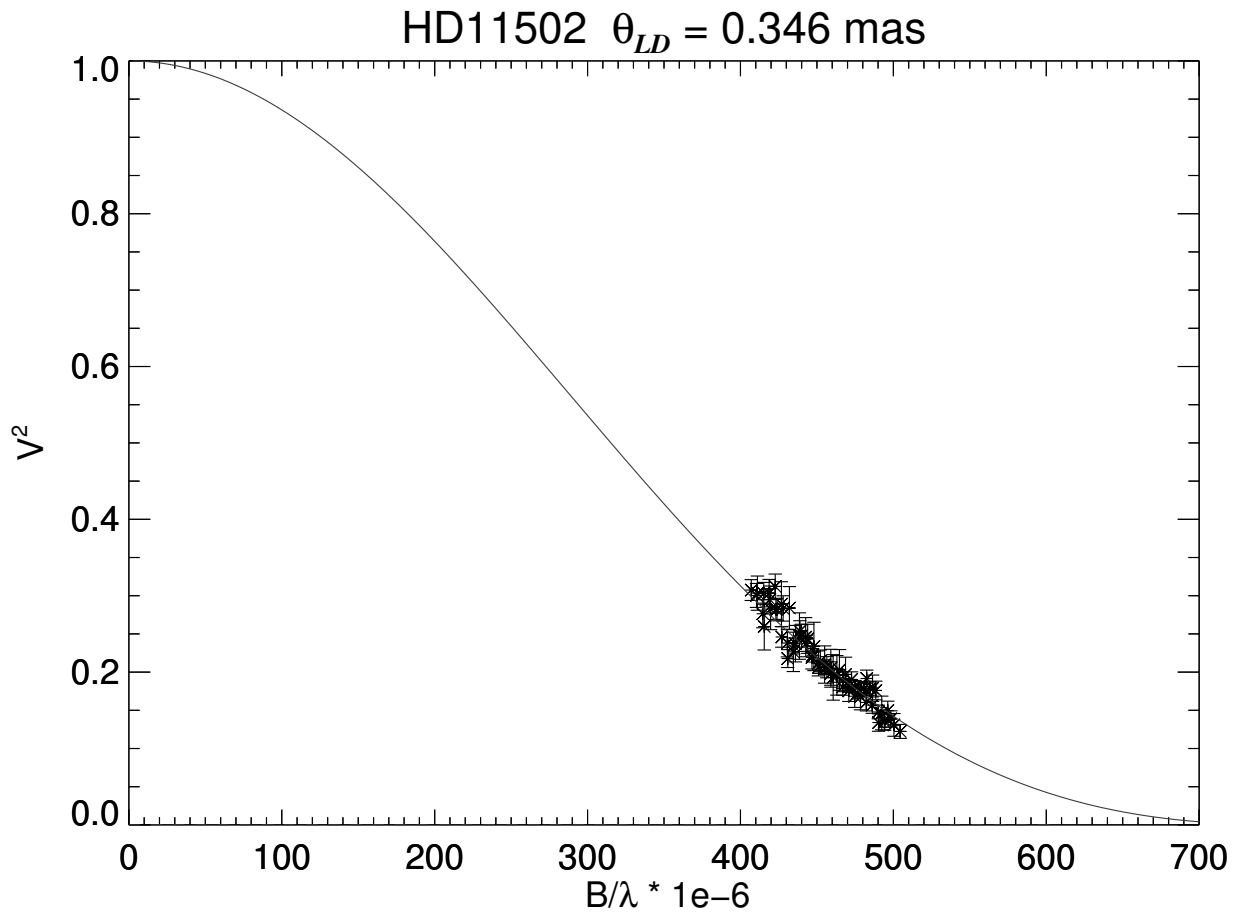


Figure A.3 Squared visibility versus spatial frequency for HD 11502. The solid line indicates the best fit for a single star limb-darkened disk model.

A.4 HD 15318

Table A.4 HD 15318 Observing Log

Baseline	Combiner	Brackets	N_{V^2}	Date
E1S1	PAVO	2	44	2013-09-11
W1S2	PAVO	2	47	2014-09-12

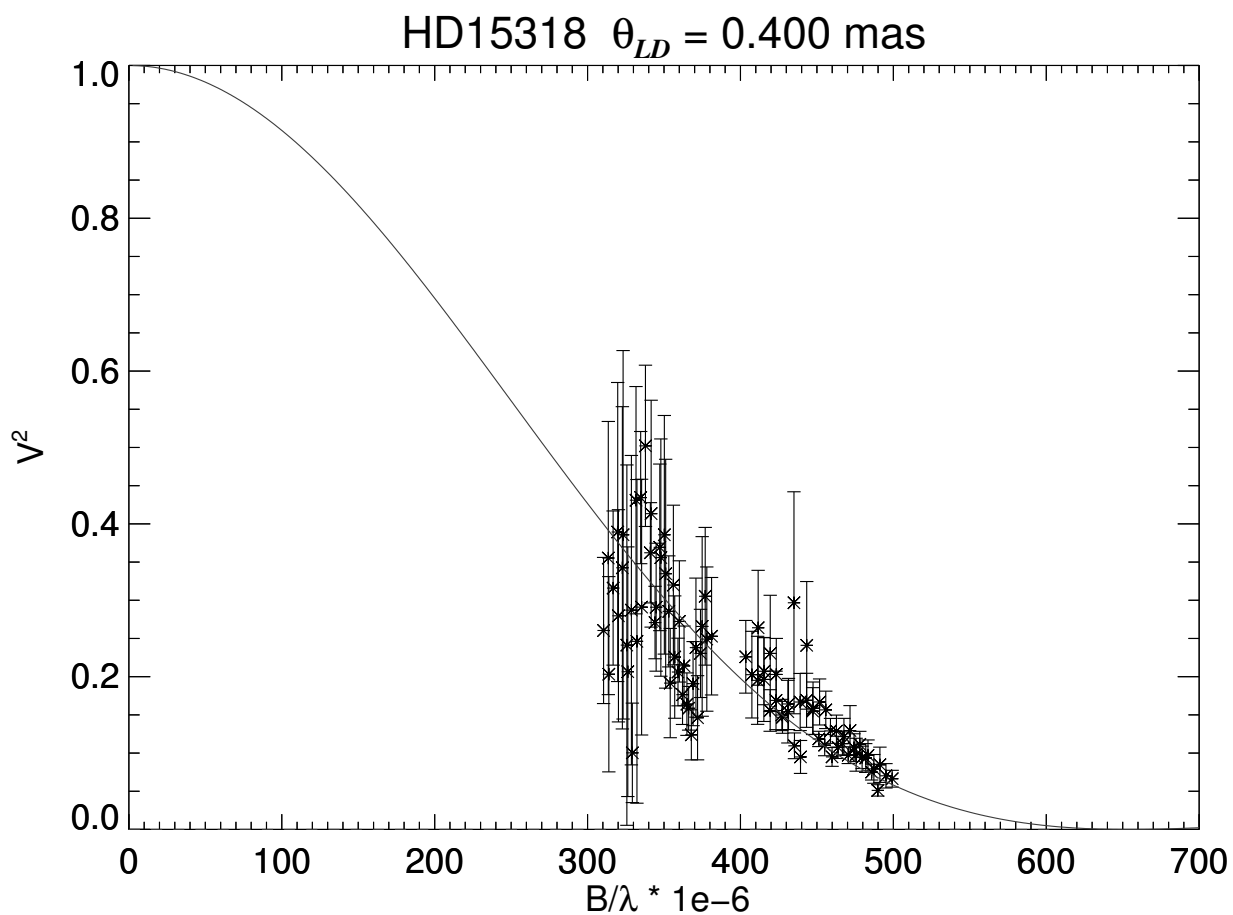


Figure A.4 Squared visibility versus spatial frequency for HD 15318. The solid line indicates the best fit for a single star limb-darkened disk model.

A.5 HD 23302

Table A.5 HD 23302 Observing Log

Baseline	Combiner	Brackets	N_{V^2}	Date
E1S1	PAVO	2	46	2013-12-11

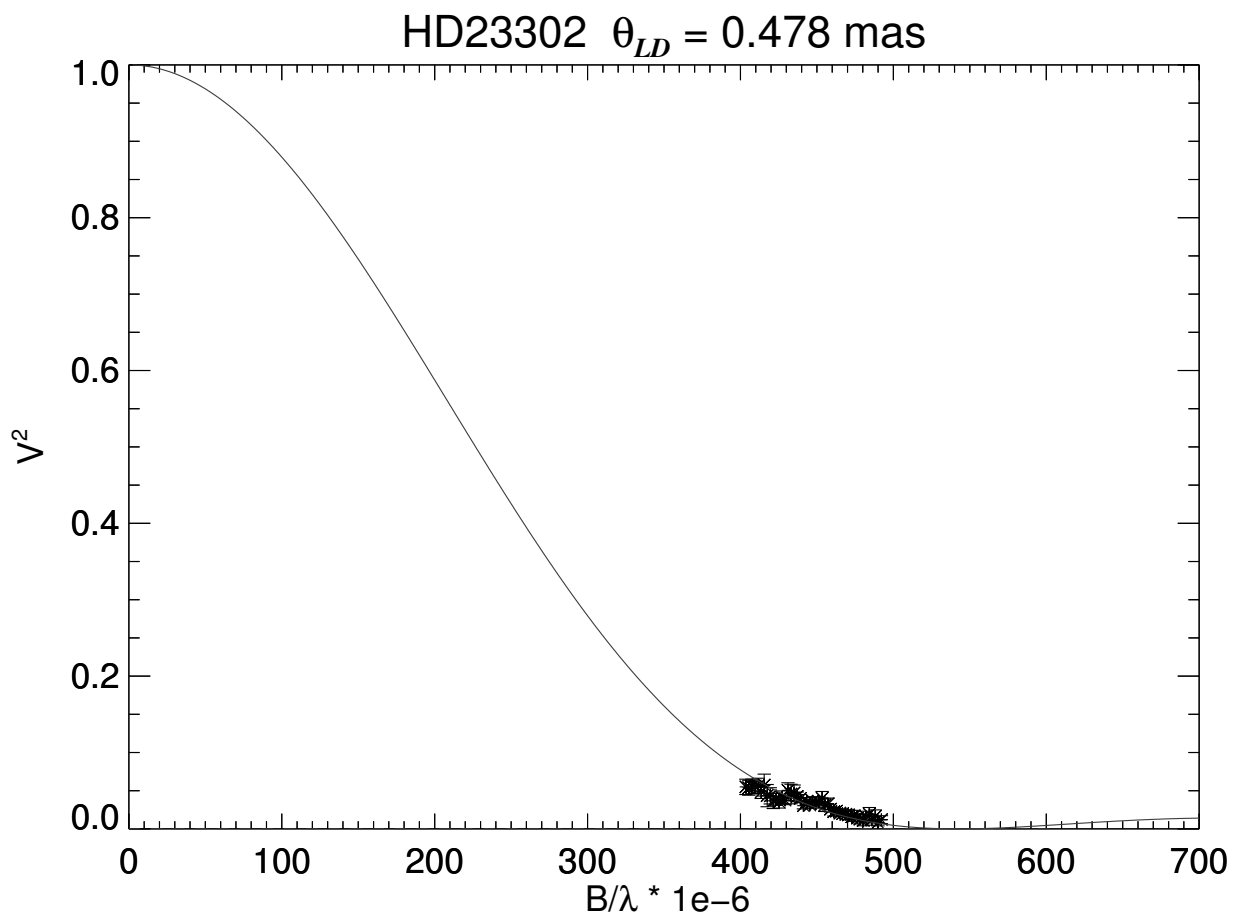


Figure A.5 Squared visibility versus spatial frequency for HD 23302. The solid line indicates the best fit for a single star limb-darkened disk model.

A.6 HD 23408

Table A.6 HD 23408 Observing Log

Baseline	Combiner	Brackets	N_{V^2}	Date
E1S1	PAVO	2	46	2013-09-13

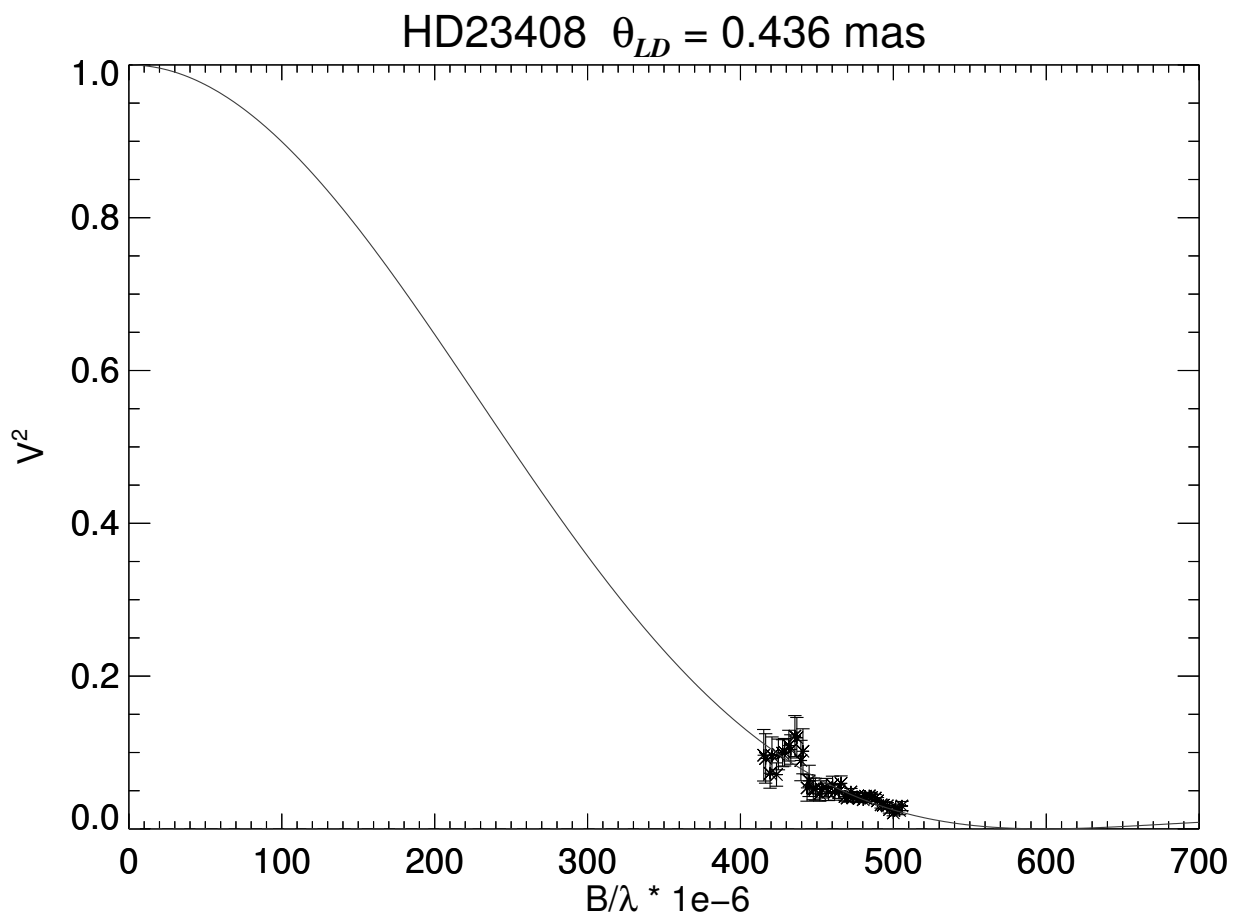


Figure A.6 Squared visibility versus spatial frequency for HD 23408. The solid line indicates the best fit for a single star limb-darkened disk model.

A.7 HD 23850

Table A.7 HD 23850 Observing Log

Baseline	Combiner	Brackets	N_{V^2}	Date
W1E1S1	CLIMB	2	6	2014-09-23
W1E1S1	CLIMB	3	9	2014-09-24
W1E1S1	CLIMB	3	9	2015-09-13

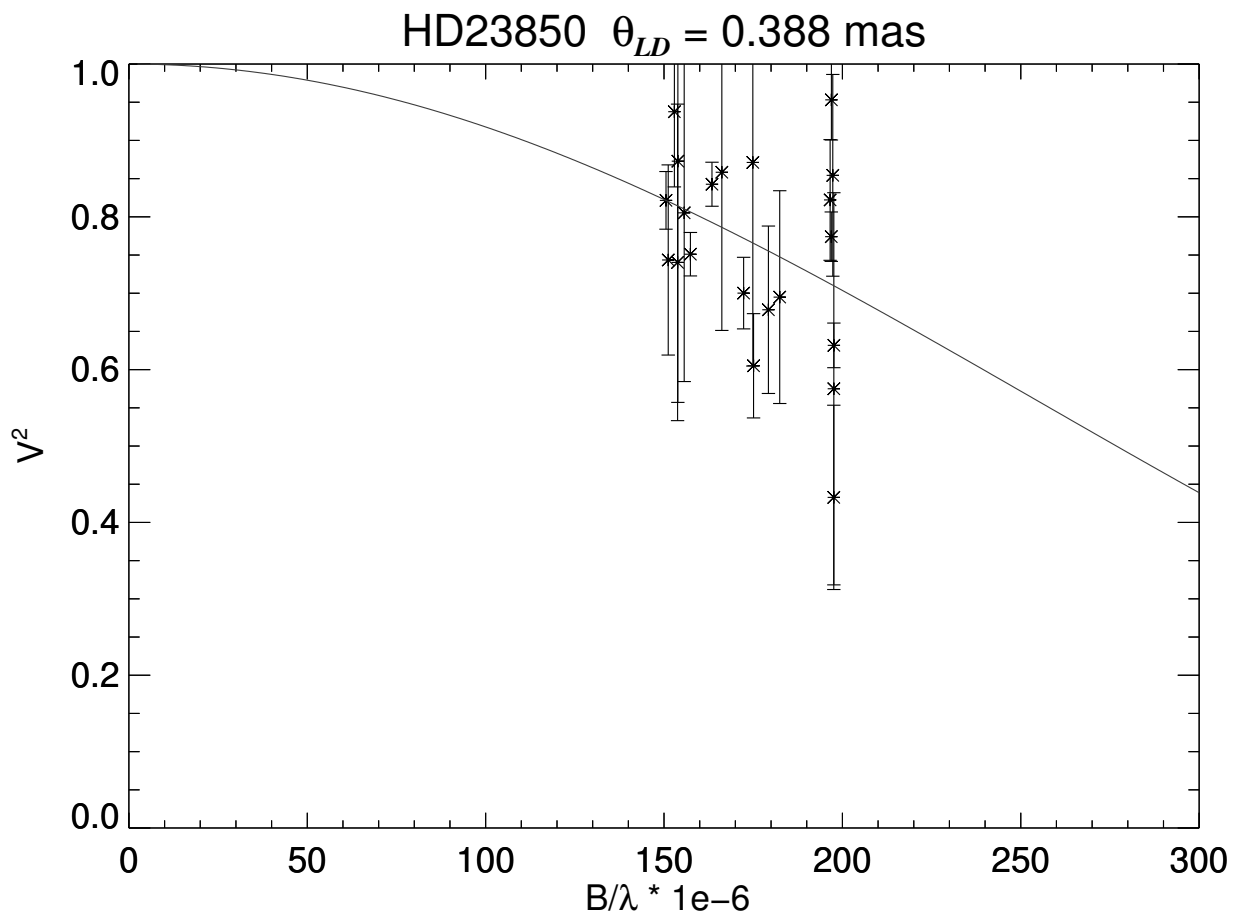


Figure A.7 Squared visibility versus spatial frequency for HD 23850. The solid line indicates the best fit for a single star limb-darkened disk model.

A.8 HD 24912

Table A.8 HD 24912 Observing Log

Baseline	Combiner	Brackets	N_{V^2}	Date
W1E1	PAVO	1	23	2015-11-14

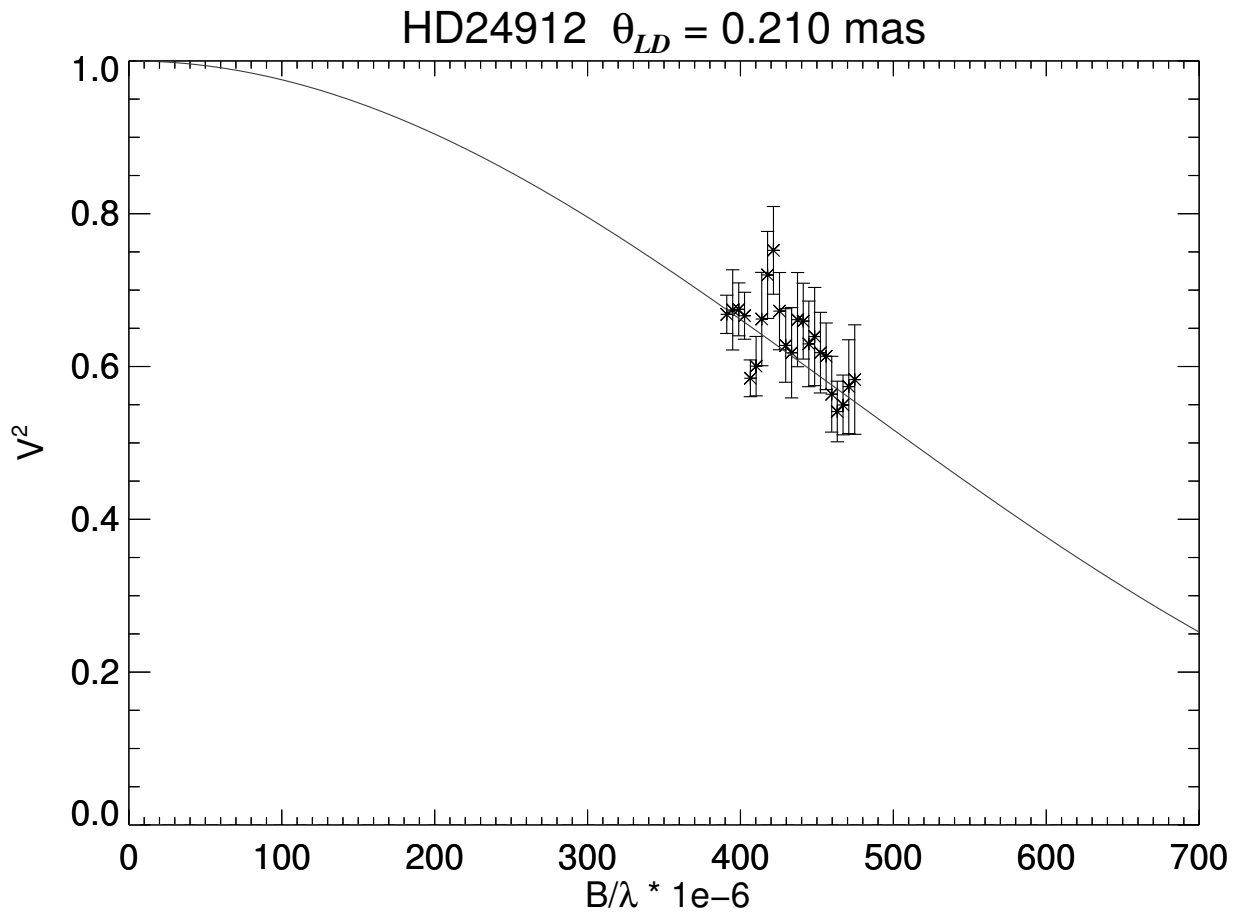


Figure A.8 Squared visibility versus spatial frequency for HD 24912. The solid line indicates the best fit for a single star limb-darkened disk model.

A.9 HD 29763

Table A.9 HD 29763 Observing Log

Baseline	Combiner	Brackets	N_{V^2}	Date
E1S1	PAVO	2	46	2012-10-14

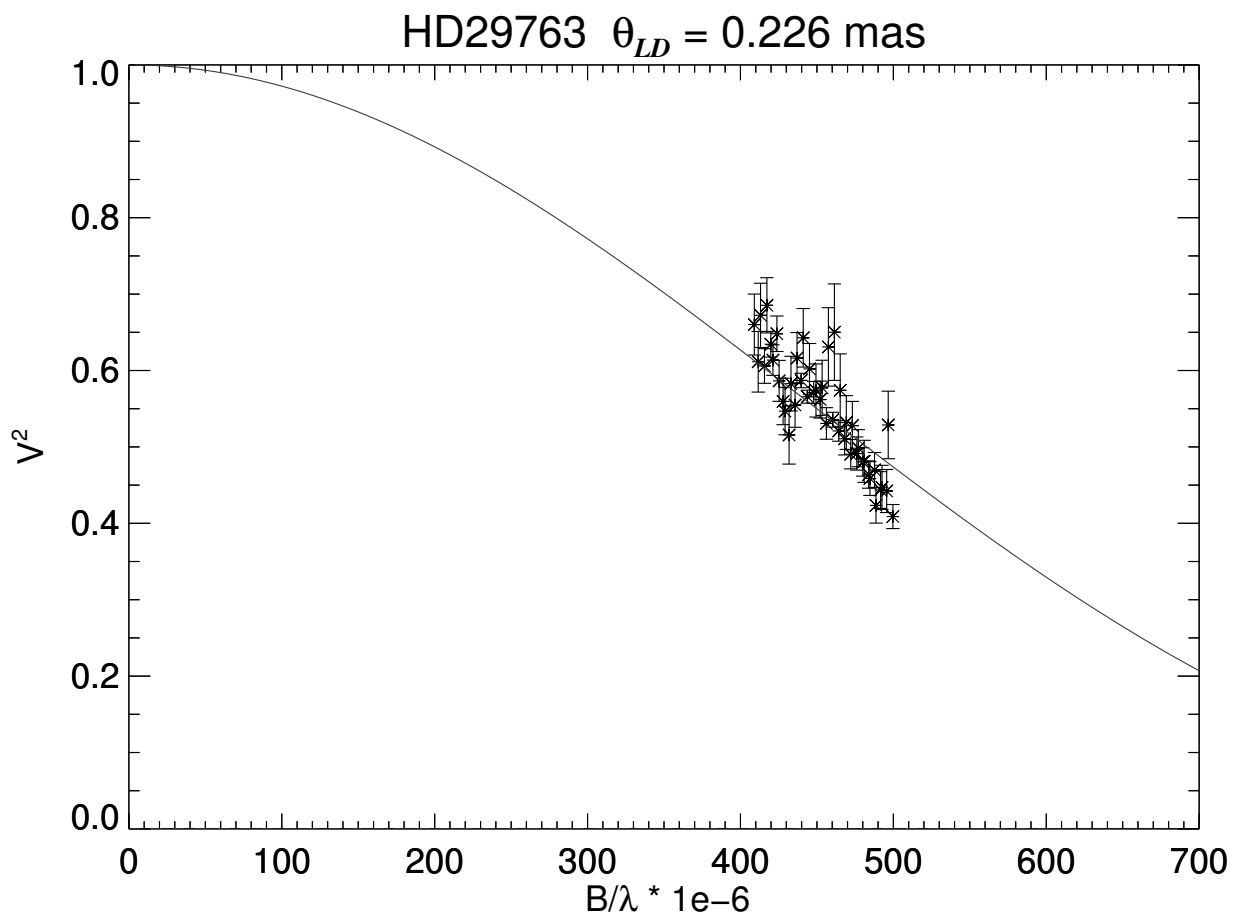


Figure A.9 Squared visibility versus spatial frequency for HD 29763. The solid line indicates the best fit for a single star limb-darkened disk model.

A.10 HD 30614

Table A.10 HD 30614 Observing Log

Baseline	Combiner	Brackets	N_{V^2}	Date
E1S1	PAVO	1	23	2013-11-09

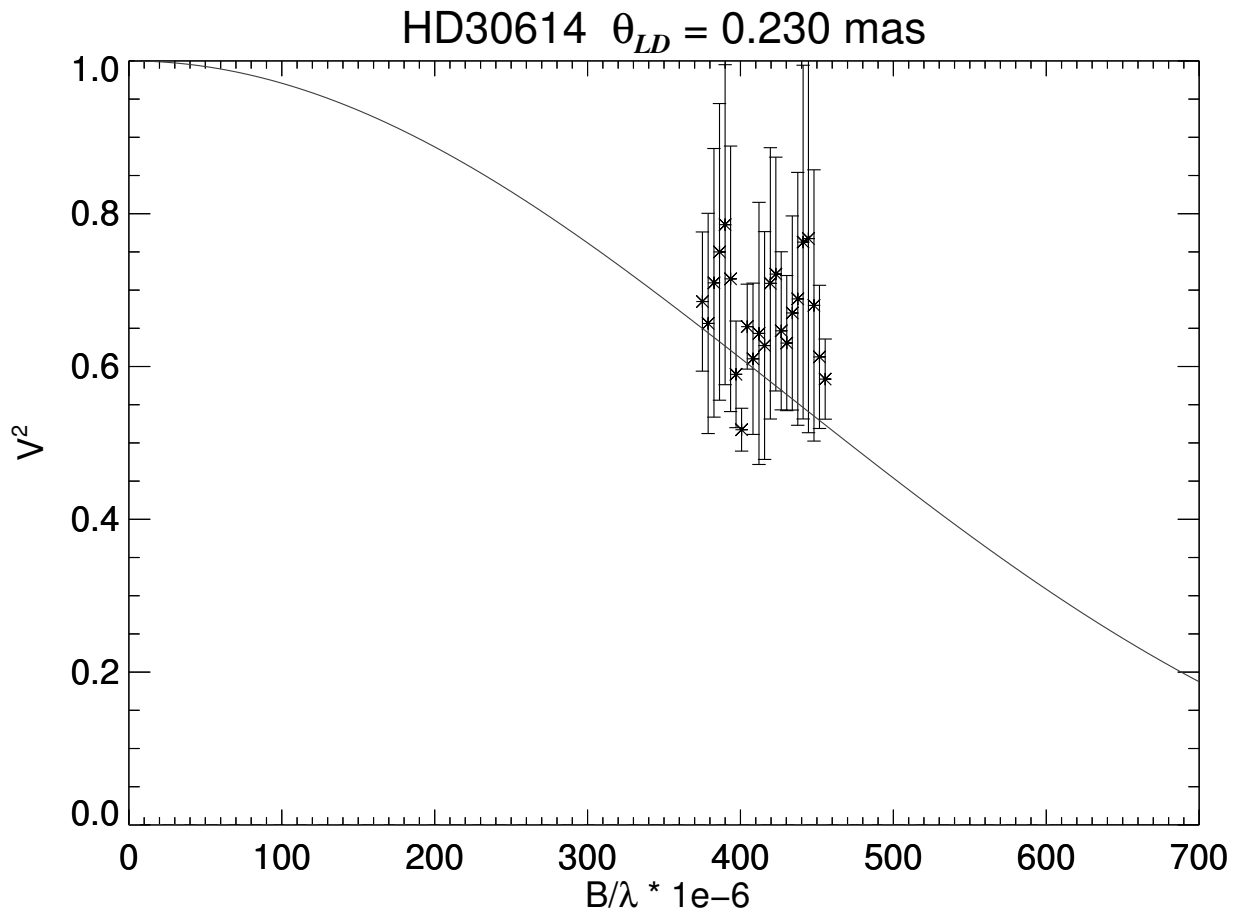


Figure A.10 Squared visibility versus spatial frequency for HD 30614. The solid line indicates the best fit for a single star limb-darkened disk model.

A.11 HD 35497

Table A.11 HD 35497 Observing Log

Baseline	Combiner	Brackets	N_{V^2}	Date
W1E1S1	CLIMB	2	6	2014-09-24

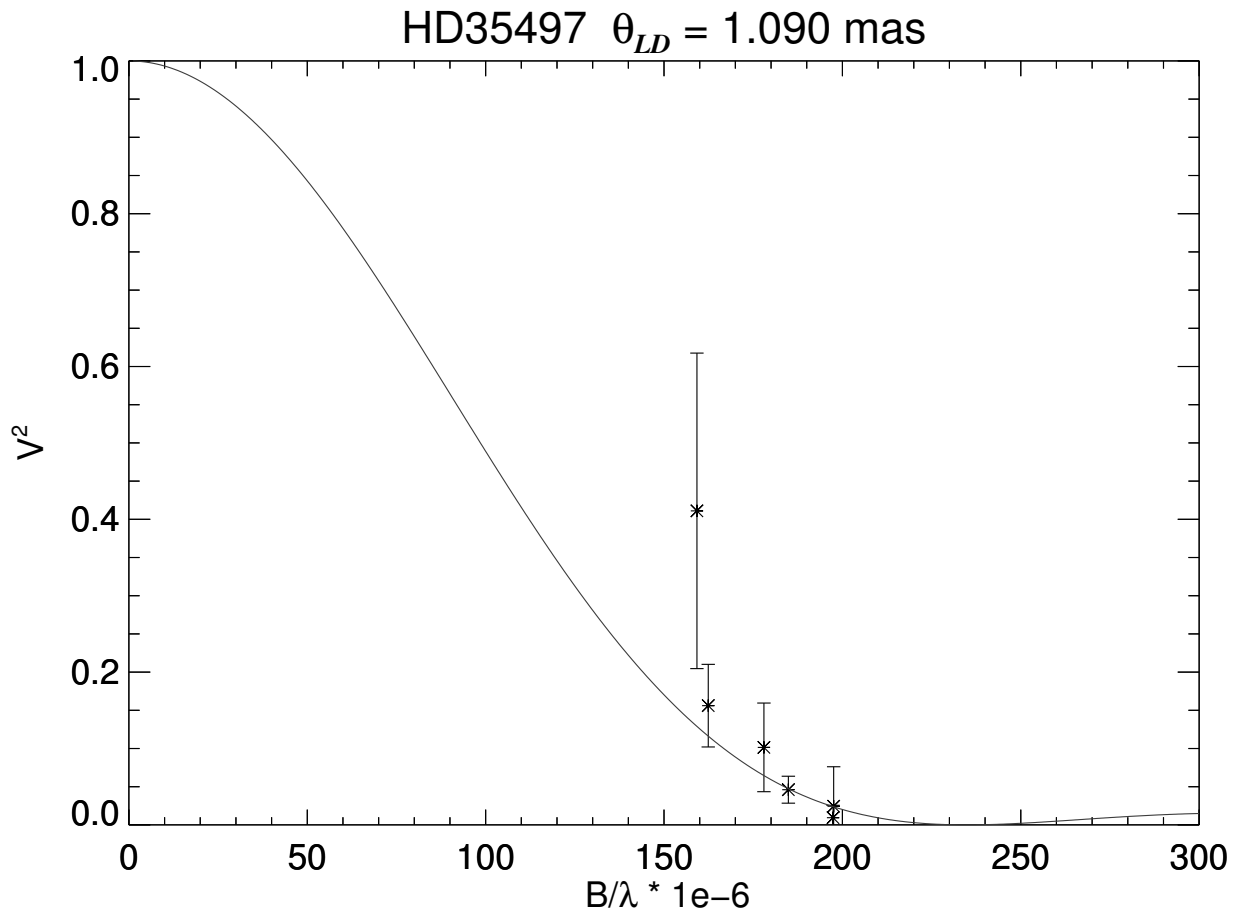


Figure A.11 Squared visibility versus spatial frequency for HD 35497. The solid line indicates the best fit for a single star limb-darkened disk model.

A.12 HD 36267

Table A.12 HD 36267 Observing Log

Baseline	Combiner	Brackets	N_{V^2}	Date
E1S1	PAVO	3	69	2013-11-09

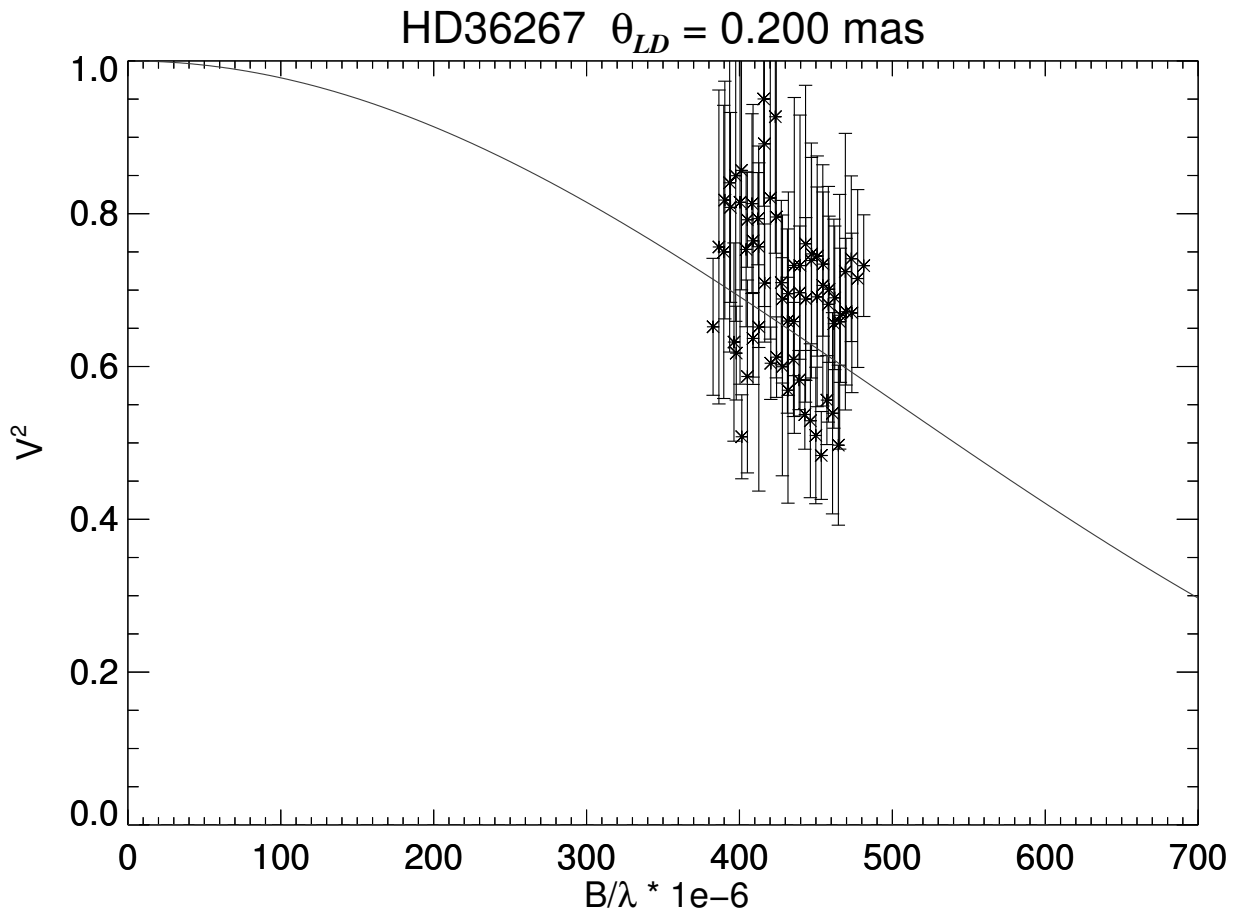


Figure A.12 Squared visibility versus spatial frequency for HD 36267. The solid line indicates the best fit for a single star limb-darkened disk model.

A.13 HD 36861

Table A.13 HD 36861 Observing Log

Baseline	Combiner	Brackets	N_{V^2}	Date
E1S1	PAVO	2	46	2013-11-06
W1E1	PAVO	3	69	2013-11-07
W1E2	PAVO	2	46	2014-04-09

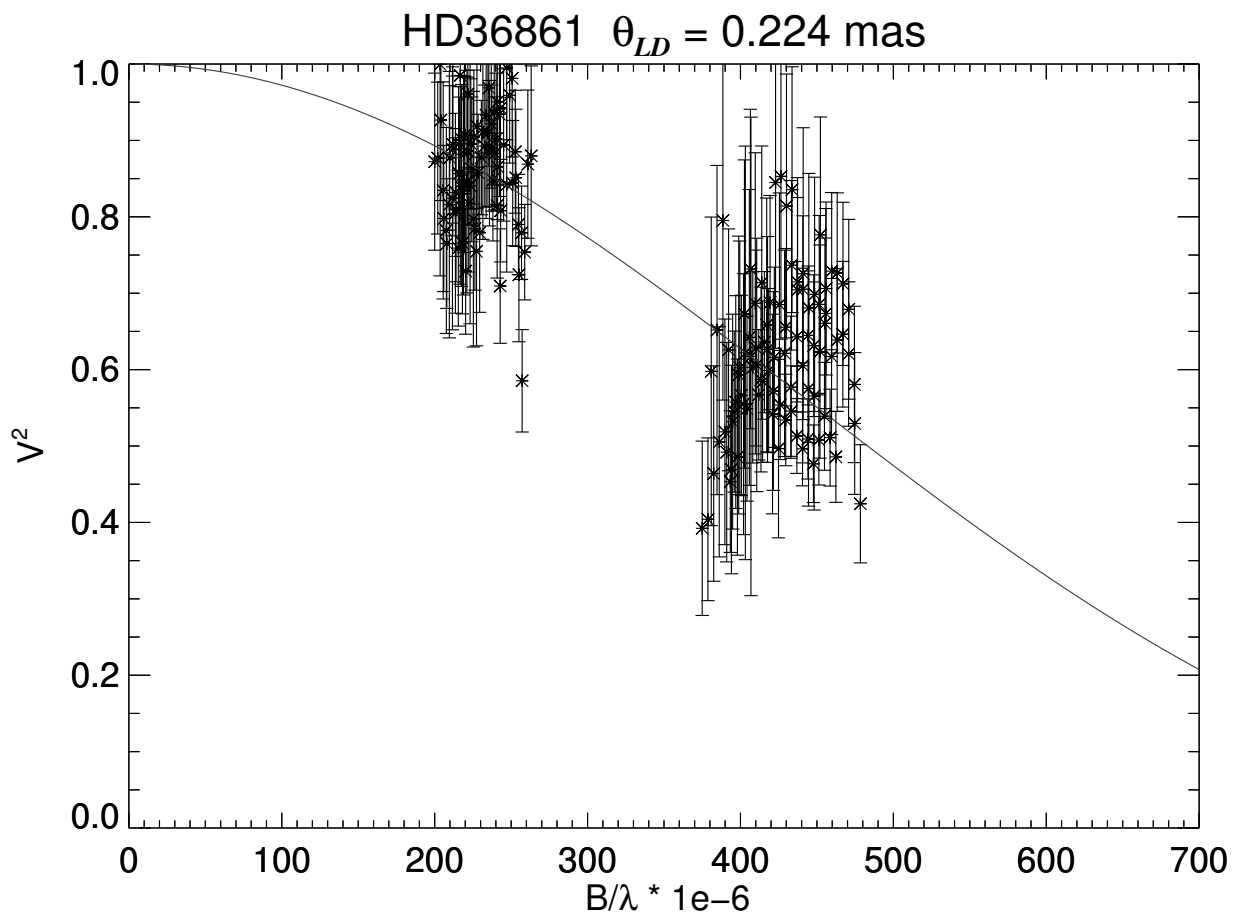


Figure A.13 Squared visibility versus spatial frequency for HD 36861. The solid line indicates the best fit for a single star limb-darkened disk model.

A.14 HD 37742

Table A.14 HD 37742 Observing Log

Baseline	Combiner	Brackets	N_{V^2}	Date
W1E1	PAVO	1	23	2015-11-14

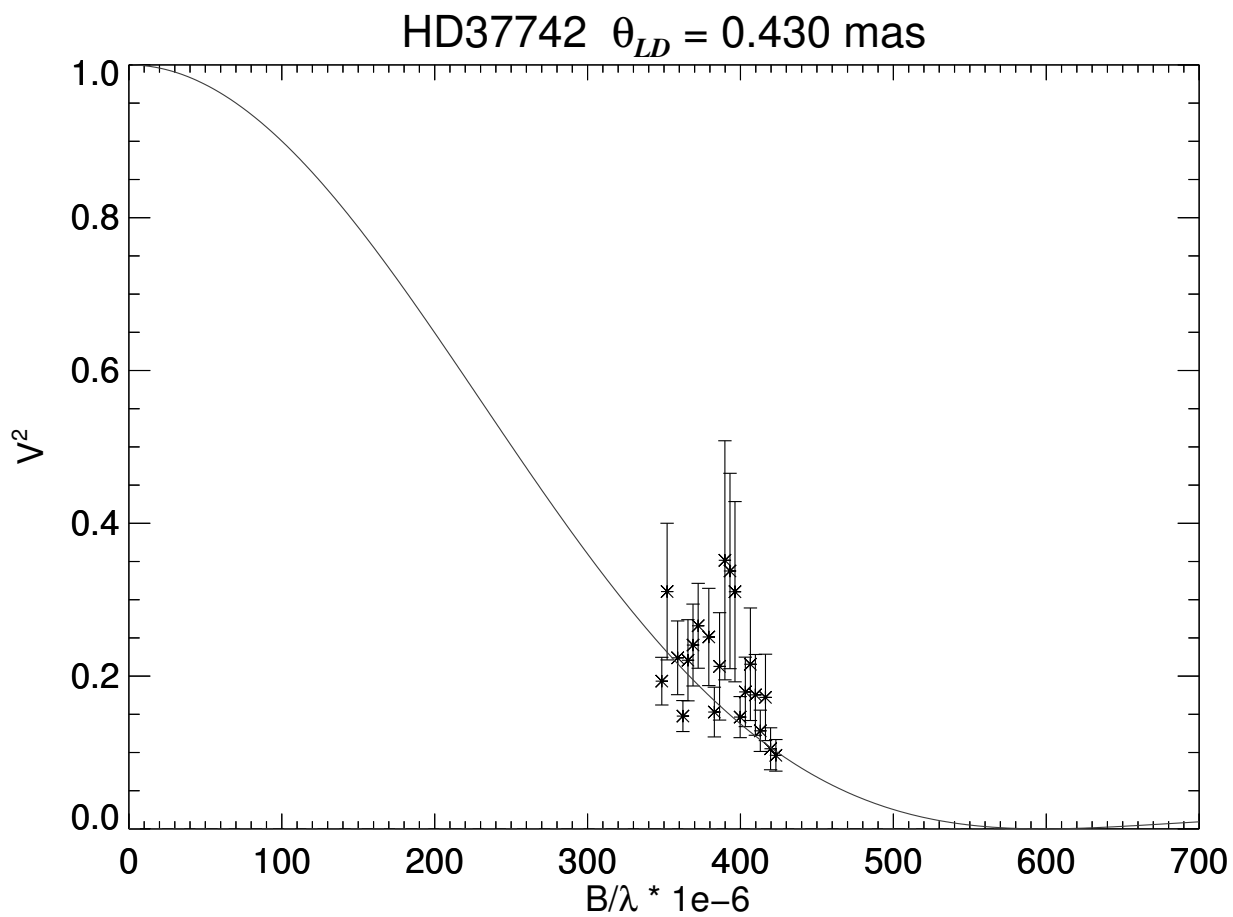


Figure A.14 Squared visibility versus spatial frequency for HD 37742. The solid line indicates the best fit for a single star limb-darkened disk model.

A.15 HD 98664

Table A.15 HD 98664 Observing Log

Baseline	Combiner	Brackets	N_{V^2}	Date
E1S1	PAVO	3	69	2013-12-11

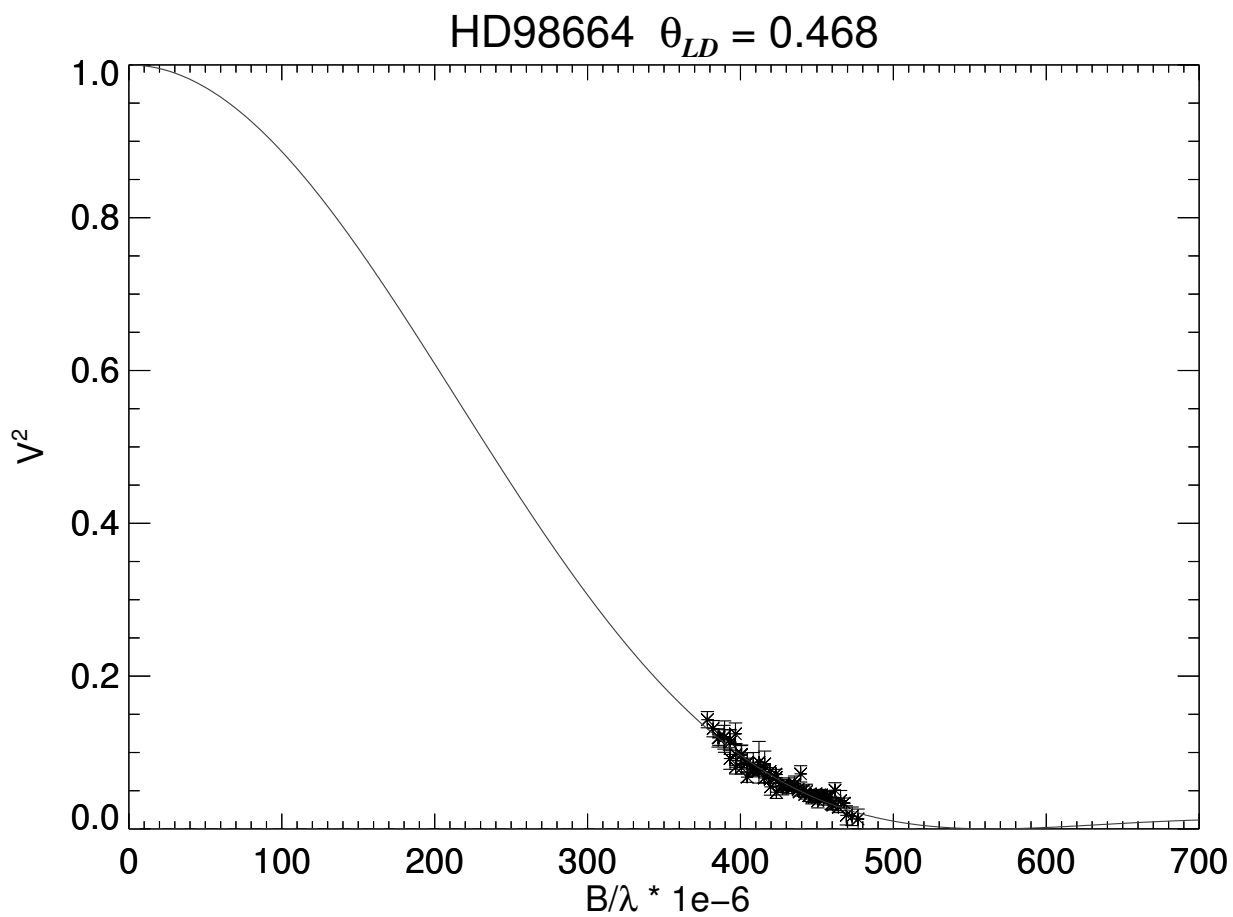


Figure A.15 Squared visibility versus spatial frequency for HD 98664. The solid line indicates the best fit for a single star limb-darkened disk model.

A.16 HD 120315

Table A.16 HD 120315 Observing Log

Baseline	Combiner	Brackets	N_{V^2}	Date
W1E1S1	CLIMB	5	15	2014-04-17
W1E1S1	CLIMB	5	15	2014-06-02

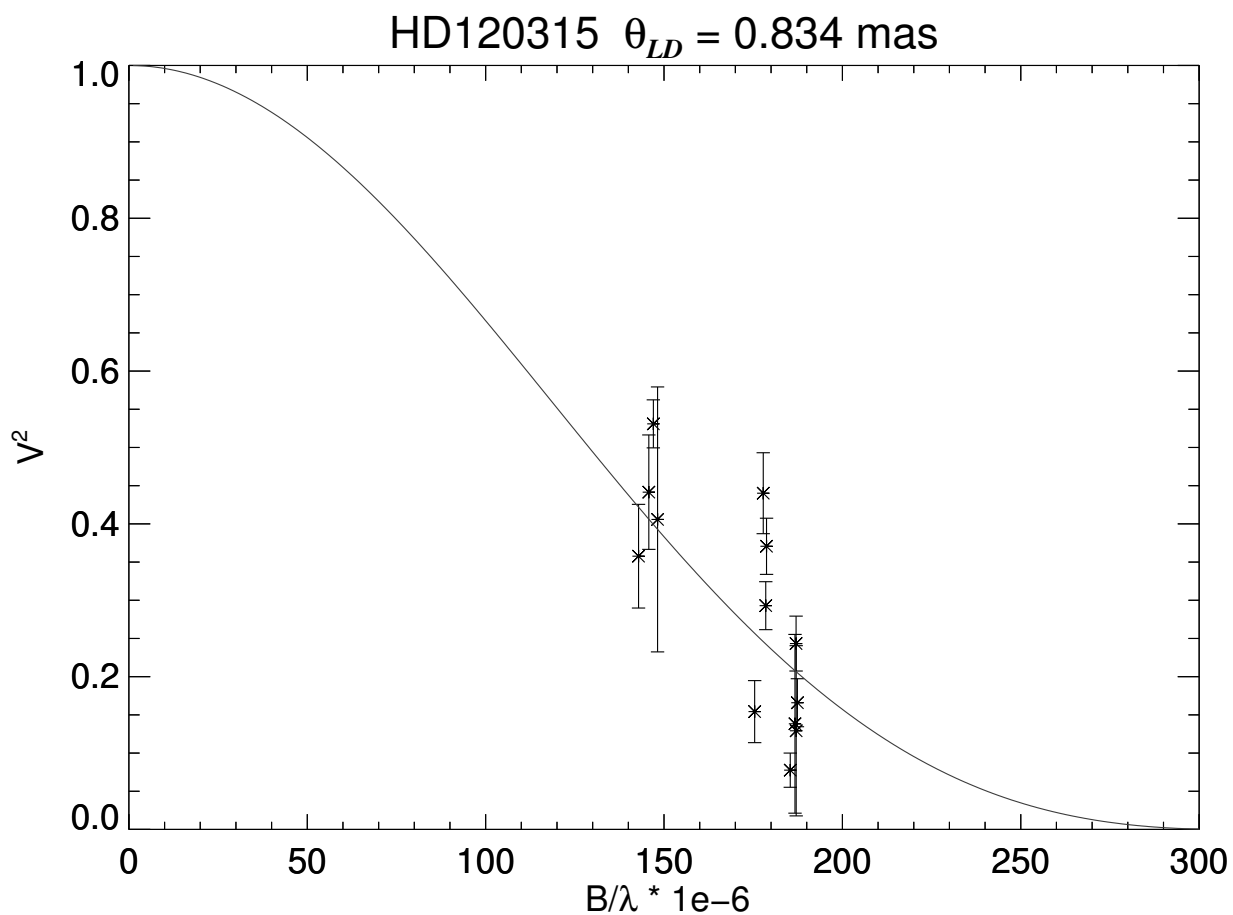


Figure A.16 Squared visibility versus spatial frequency for HD 120315, H -band data only. The solid line indicates the best fit for a single star limb-darkened disk model.

A.17 HD 147394

Table A.17 HD 147394 Observing Log

Baseline	Combiner	Brackets	N_{V^2}	Date
W1E1	PAVO	5	115	2016-07-02

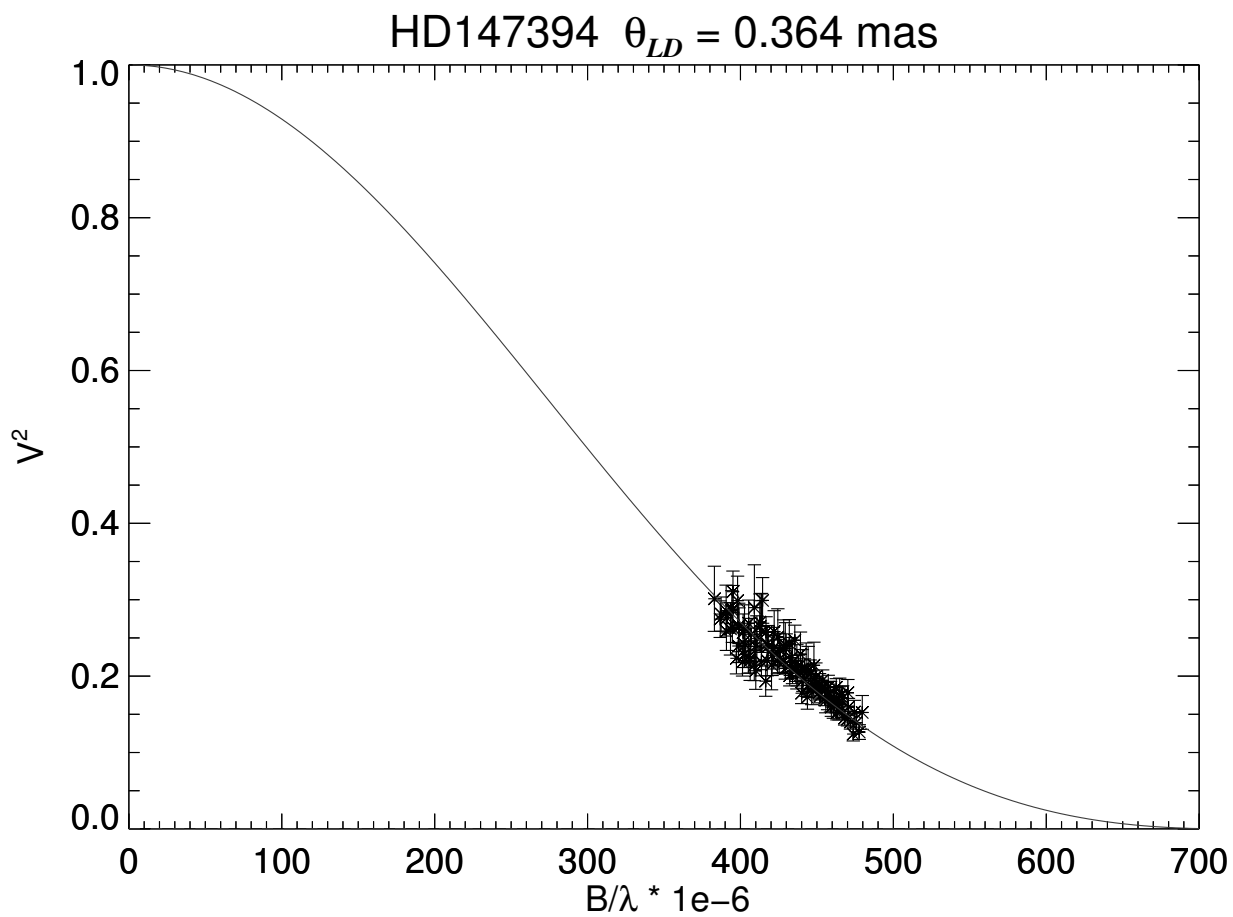


Figure A.17 Squared visibility versus spatial frequency for HD 147394. The solid line indicates the best fit for a single star limb-darkened disk model.

A.18 HD 149757

Table A.18 HD 149757 Observing Log

Baseline	Combiner	Brackets	N_{V^2}	Date
W1S2	PAVO	3	69	2016-07-04
E2S2	PAVO	7	161	2017-06-29

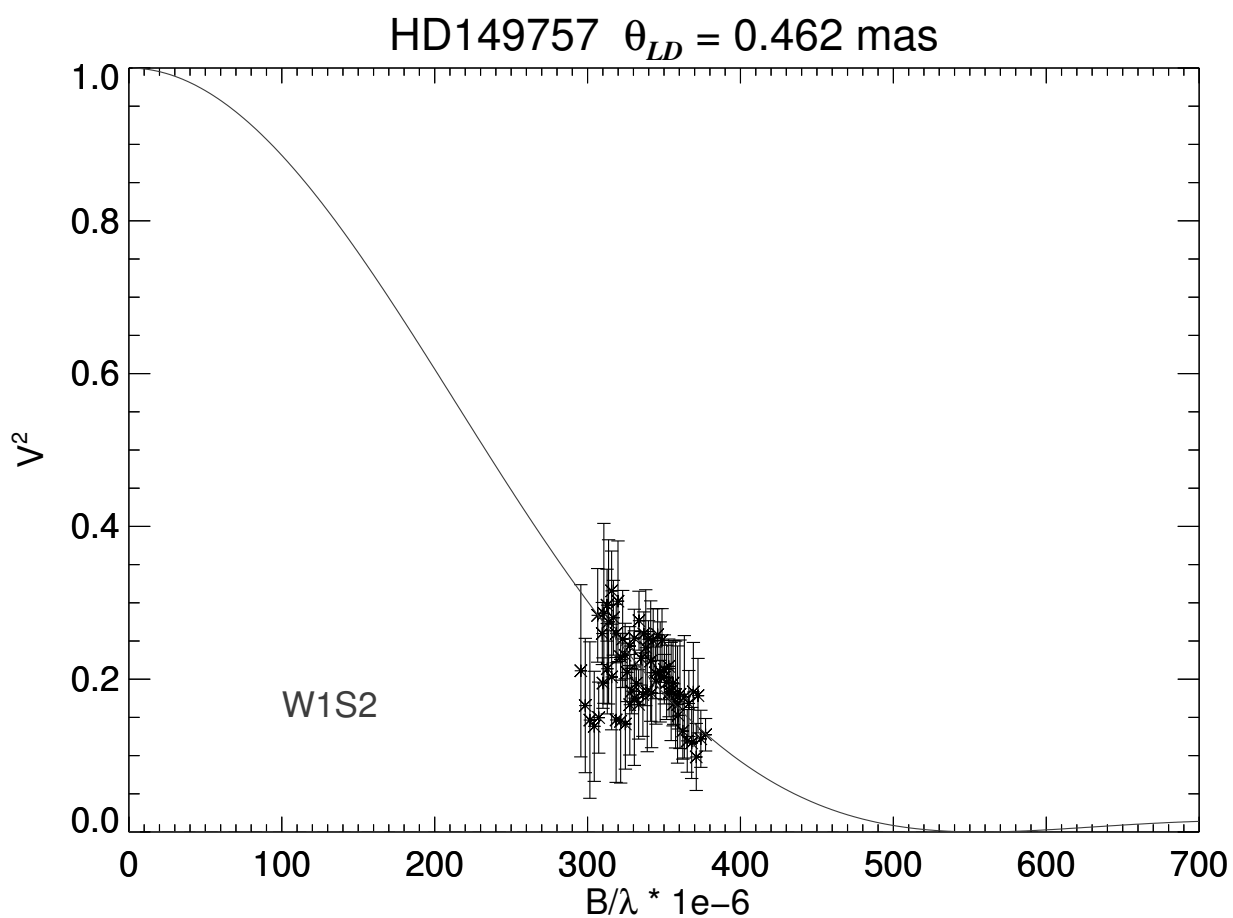


Figure A.18 Squared visibility versus spatial frequency for HD 149757 (w1S2). The solid line indicates the best fit for a single star limb-darkened disk model.

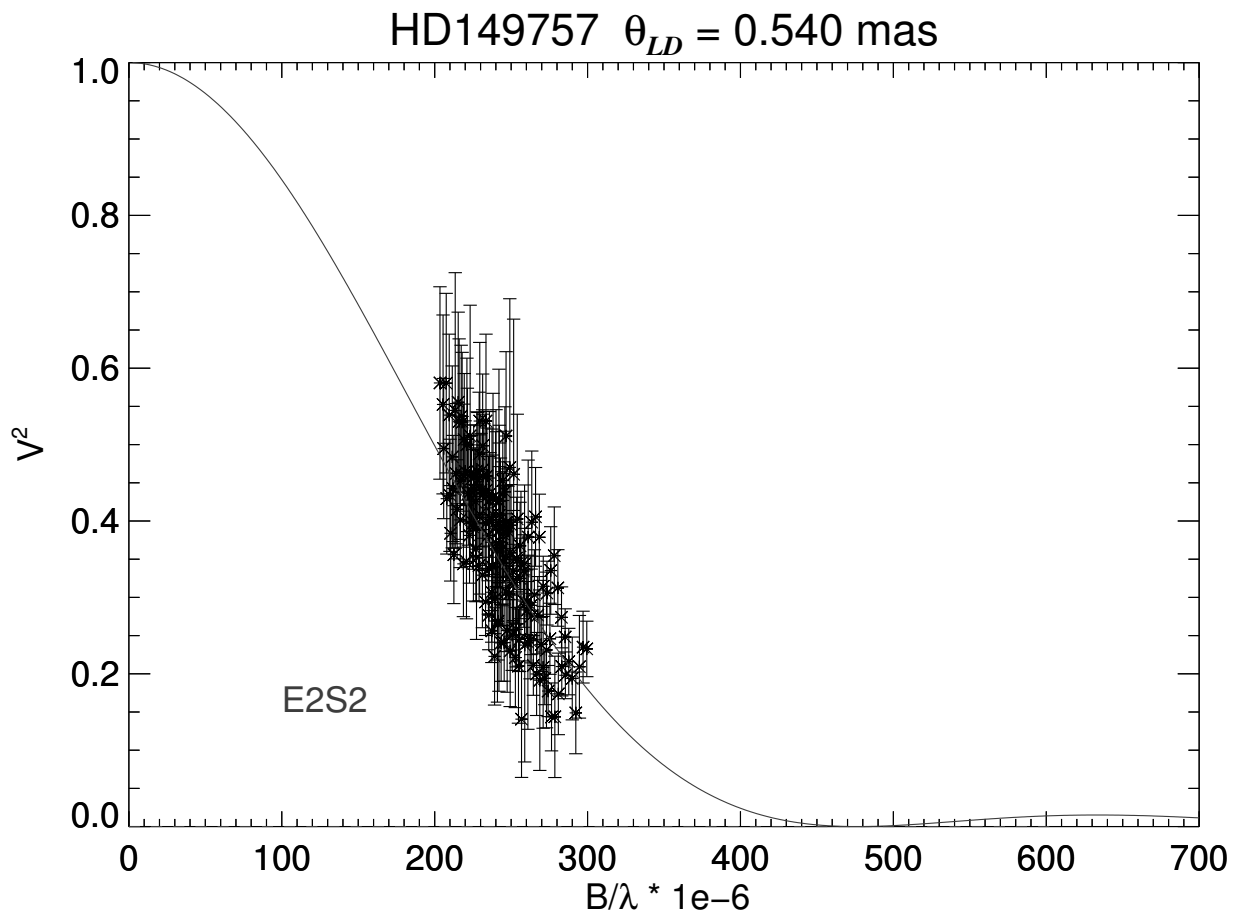


Figure A.19 Squared visibility versus spatial frequency for HD 149757 (E2S2). The solid line indicates the best fit for a single star limb-darkened disk model.

A.19 HD 155763

Table A.19 HD 155763 Observing Log

Baseline	Combiner	Brackets	N_{V^2}	Date
WIS2	PAVO	3	69	2016-07-04

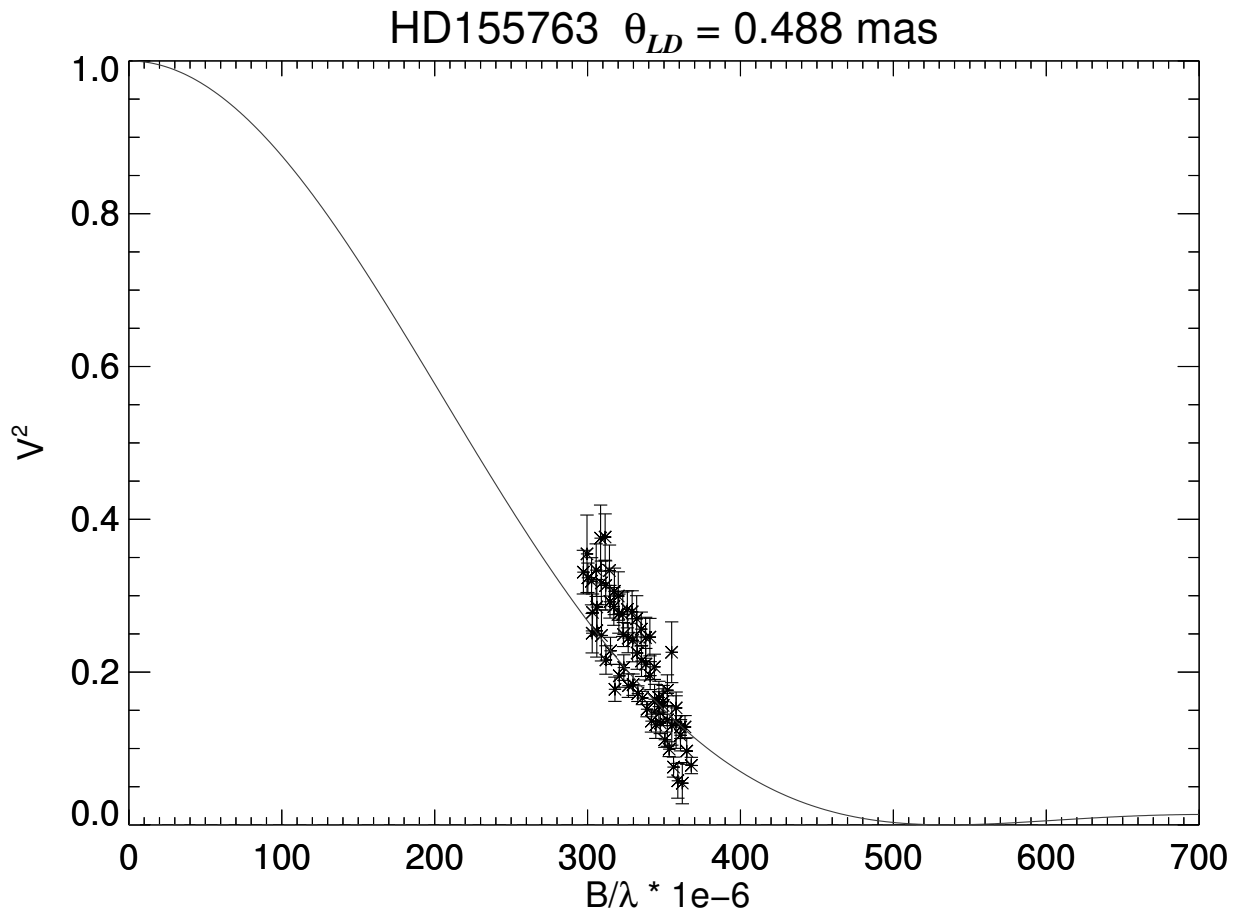


Figure A.20 Squared visibility versus spatial frequency for HD 155763. The solid line indicates the best fit for a single star limb-darkened disk model.

A.20 HD 160762

Table A.20 HD 160762 Observing Log

Baseline	Combiner	Brackets	N_{V^2}	Date
W1E1	PAVO	2	46	2016-07-02

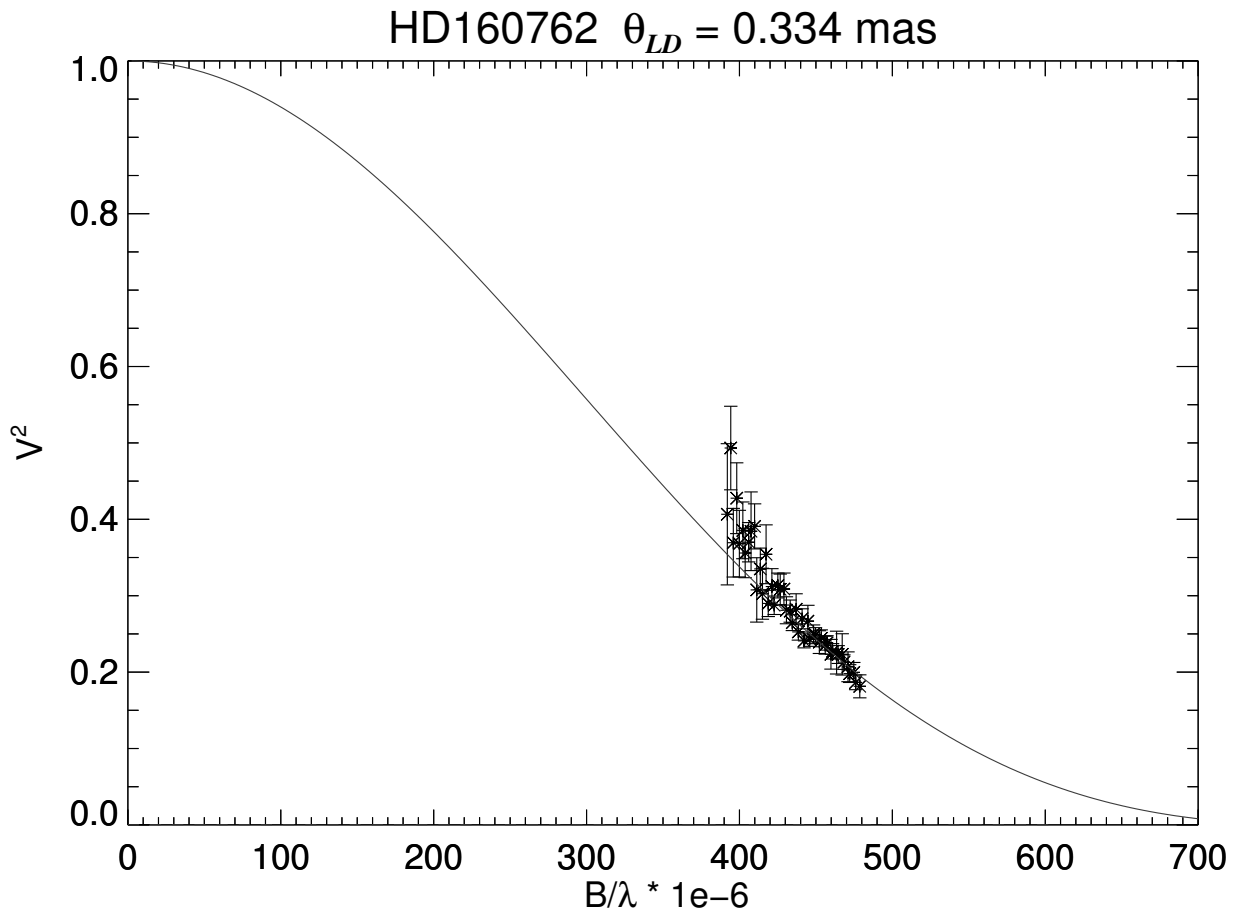


Figure A.21 Squared visibility versus spatial frequency for HD 160762. The solid line indicates the best fit for a single star limb-darkened disk model.

A.21 HD 176437

Table A.21 HD 176437 Observing Log

Baseline	Combiner	Brackets	N_{V^2}	Date
W2S2	PAVO	1	23	2016-06-26
W2S2	PAVO	3	69	2016-06-27

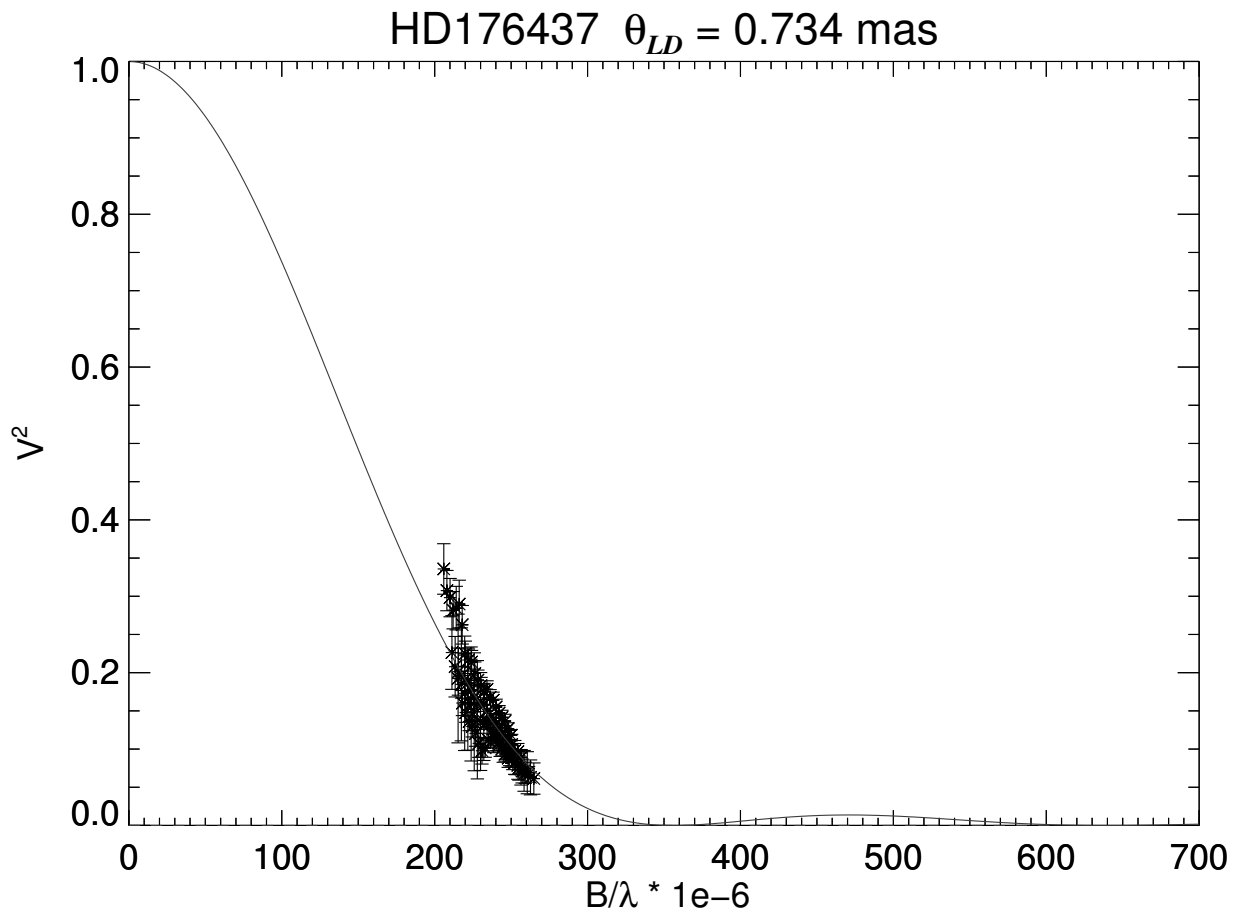


Figure A.22 Squared visibility versus spatial frequency for HD 176437. The solid line indicates the best fit for a single star limb-darkened disk model.

A.22 HD 177756

Table A.22 HD 177756 Observing Log

Baseline	Combiner	Brackets	N_{V^2}	Date
W2S2	PAVO	3	69	2016-06-26
W2S2	PAVO	2	46	2016-06-27

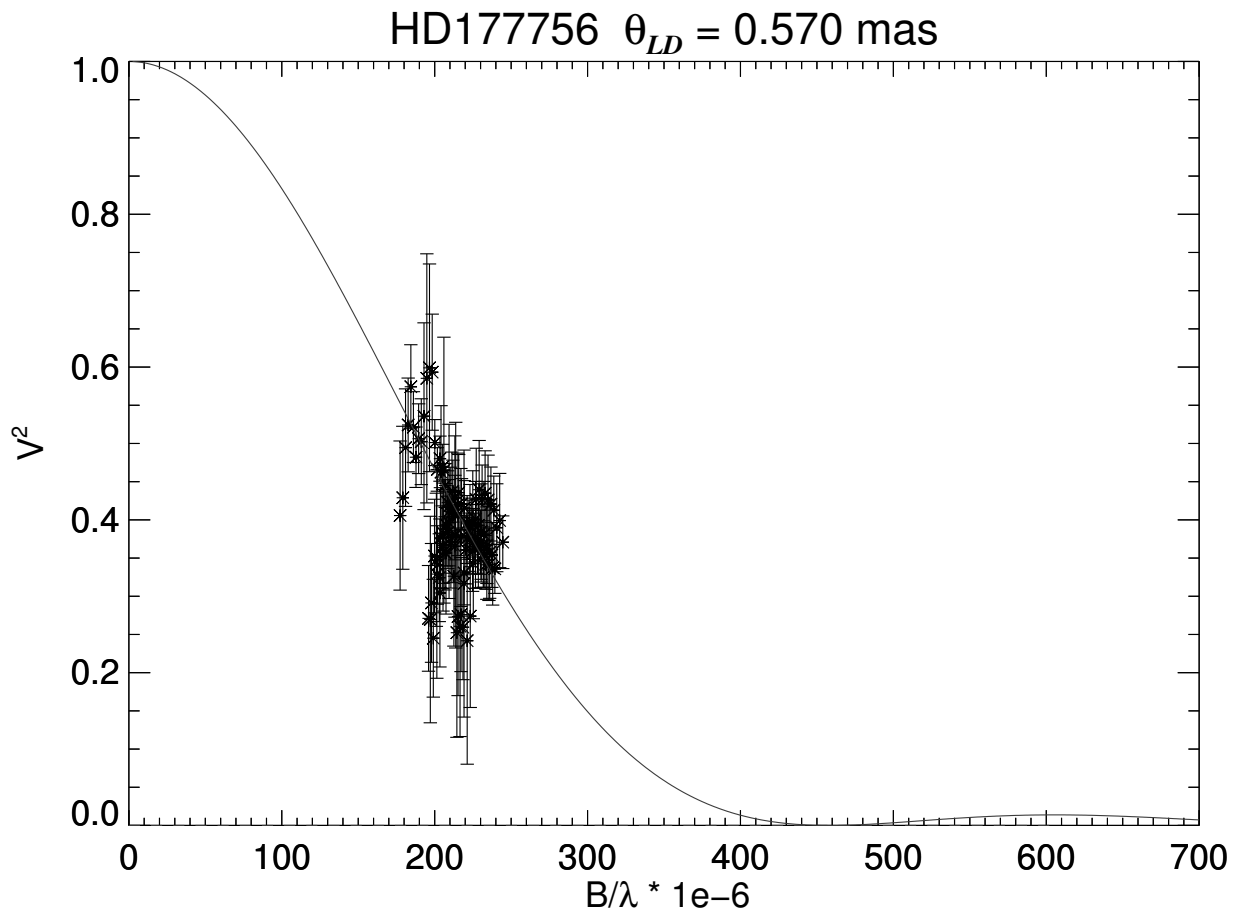


Figure A.23 Squared visibility versus spatial frequency for HD 177756. The solid line indicates the best fit for a single star limb-darkened disk model.

A.23 HD 184930

Table A.23 HD 184930 Observing Log

Baseline	Combiner	Brackets	N_{V^2}	Date
W1E1	PAVO	5	115	2016-07-02

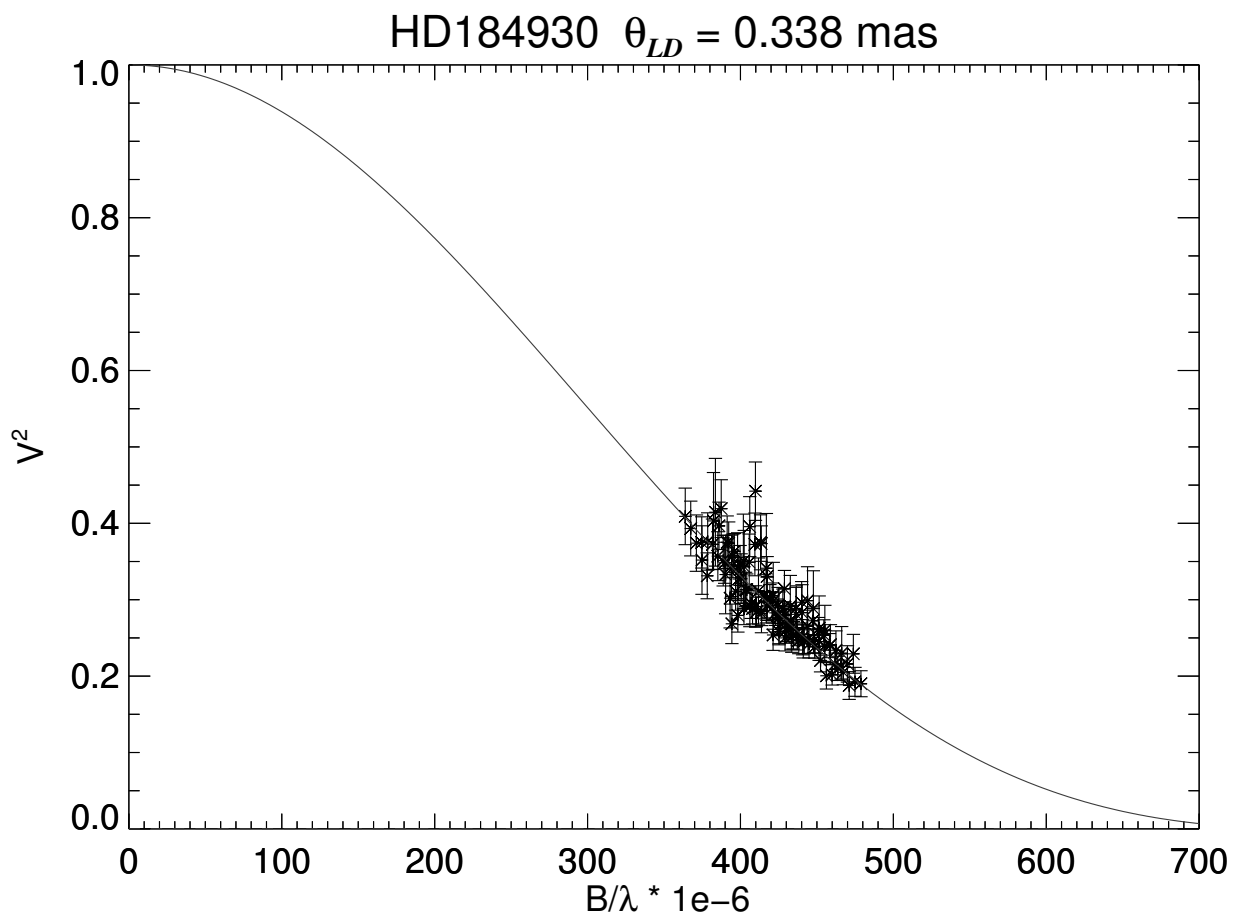


Figure A.24 Squared visibility versus spatial frequency for HD 184930. The solid line indicates the best fit for a single star limb-darkened disk model.

A.24 HD 186882

Table A.24 HD 186882 Observing Log

Baseline	Combiner	Brackets	N_{V^2}	Date
W1E1S1	CLIMB	3	9	2014-09-24

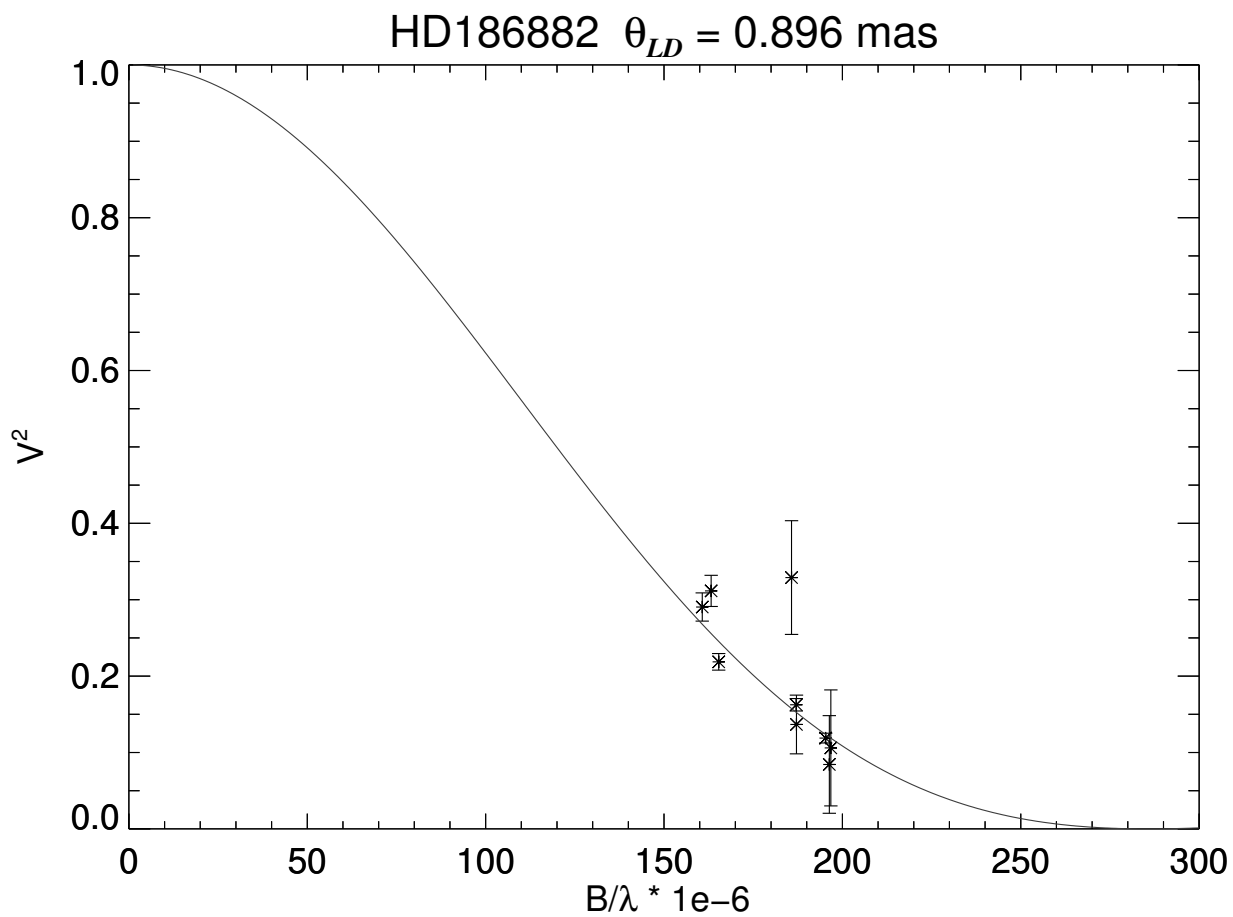


Figure A.25 Squared visibility versus spatial frequency for HD 186882. The solid line indicates the best fit for a single star limb-darkened disk model.

A.25 HD 196867

Table A.25 HD 196867 Observing Log

Baseline	Combiner	Brackets	N_{V^2}	Date
E2S2	PAVO	4	92	2015-08-09
W1E1S1	CLIMB	5	15	2012-09-02
W1E1S1	CLIMB	5	15	2014-09-22

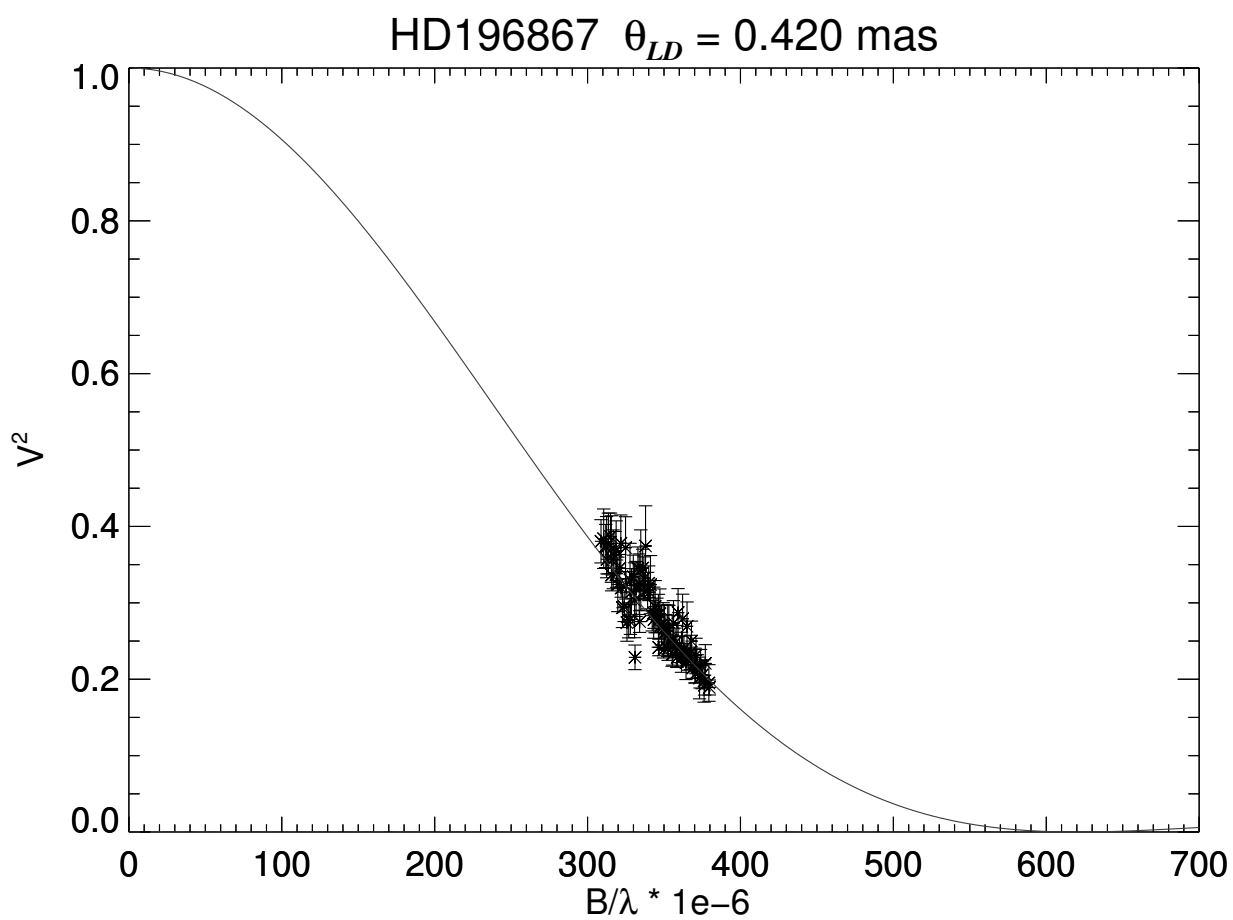


Figure A.26 Squared visibility versus spatial frequency for HD 196867 (PAVO). The solid line indicates the best fit for a single star limb-darkened disk model.

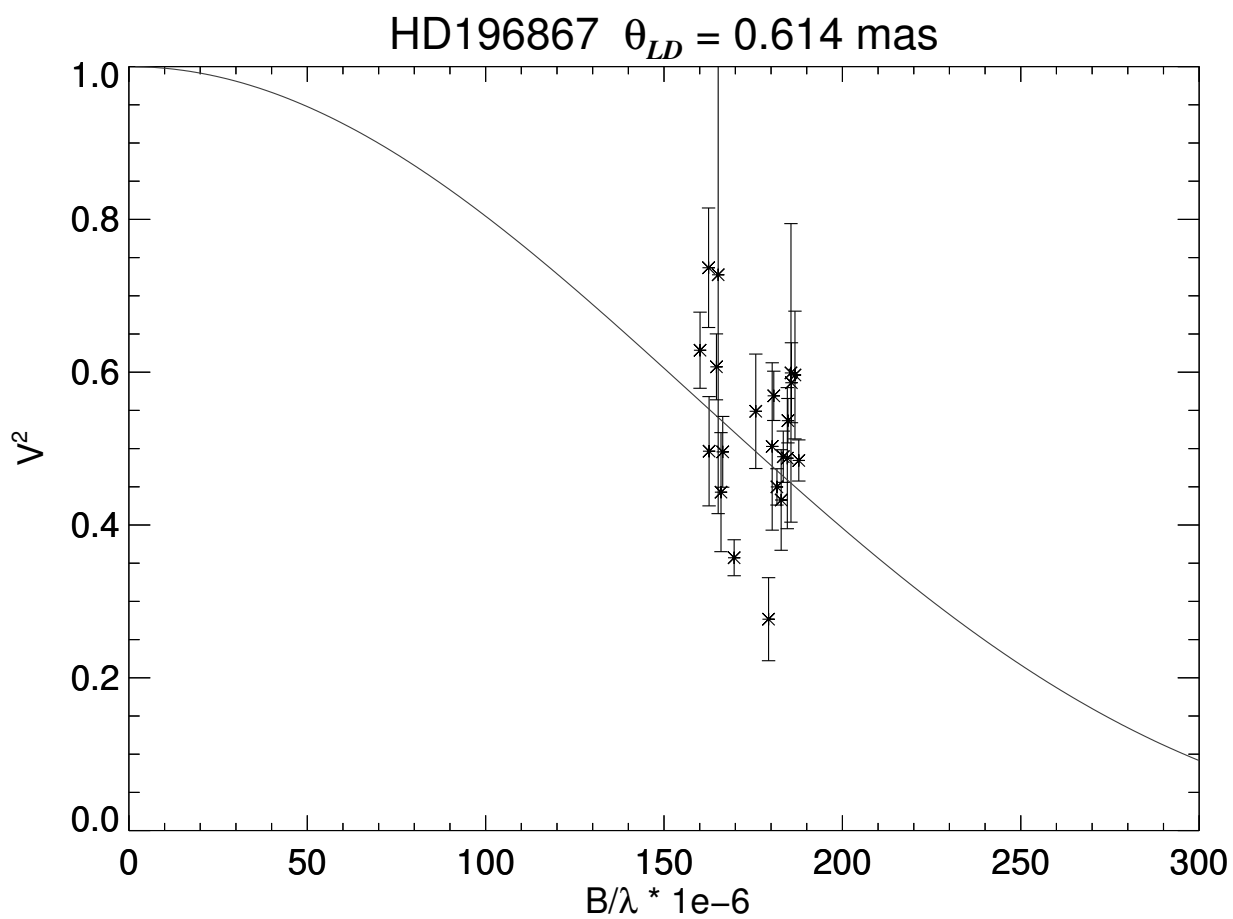


Figure A.27 Squared visibility versus spatial frequency for HD 196867 (CLIMB). The solid line indicates the best fit for a single star limb-darkened disk model.

A.26 HD 198478

Table A.26 HD 198478 Observing Log

Baseline	Combiner	Brackets	N_{V^2}	Date
W2S2	PAVO	3	69	2016-07-03
W1S2	PAVO	4	92	2016-07-04

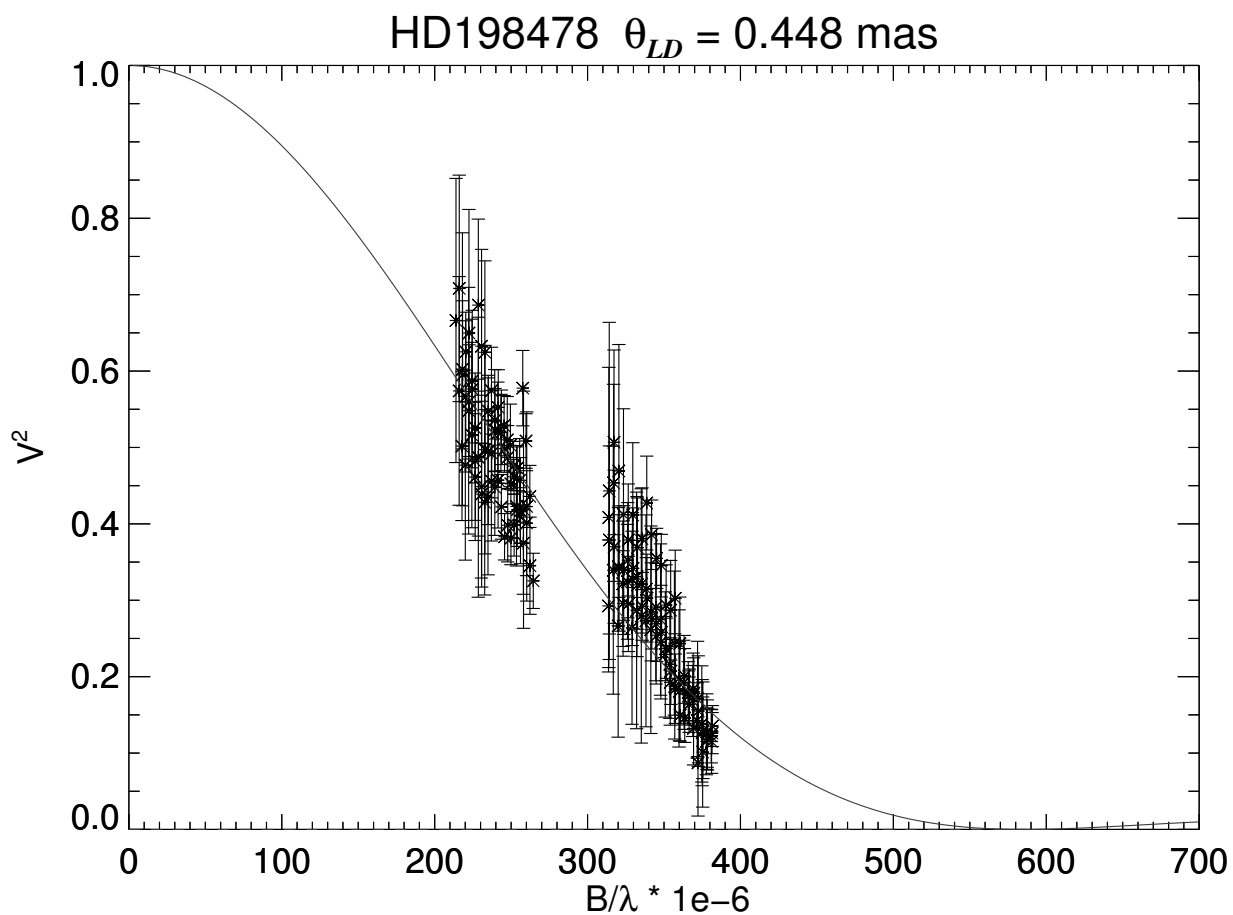


Figure A.28 Squared visibility versus spatial frequency for HD 198478. The solid line indicates the best fit for a single star limb-darkened disk model.

A.27 HD 205021

Table A.27 HD 205021 Observing Log

Baseline	Combiner	Brackets	N_{V^2}	Date
WIS2	PAVO	6	138	2014-09-12

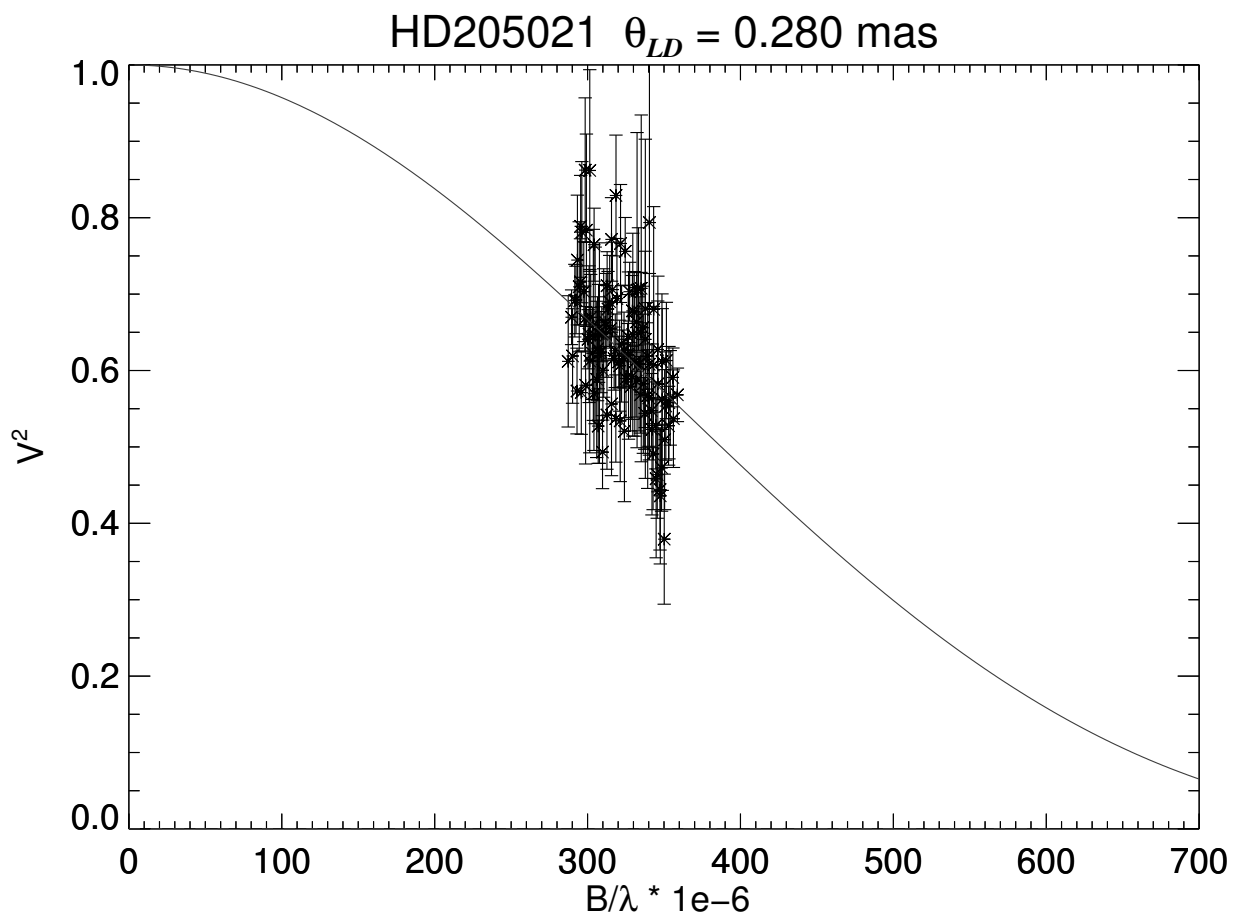


Figure A.29 Squared visibility versus spatial frequency for HD 205021. The solid line indicates the best fit for a single star limb-darkened disk model.

A.28 HD 214680

Table A.28 HD 214680 Observing Log

Baseline	Combiner	Brackets	N_{V^2}	Date
E1S1	PAVO	1	23	2013-12-11
E1S1	PAVO	6	138	2017-06-30

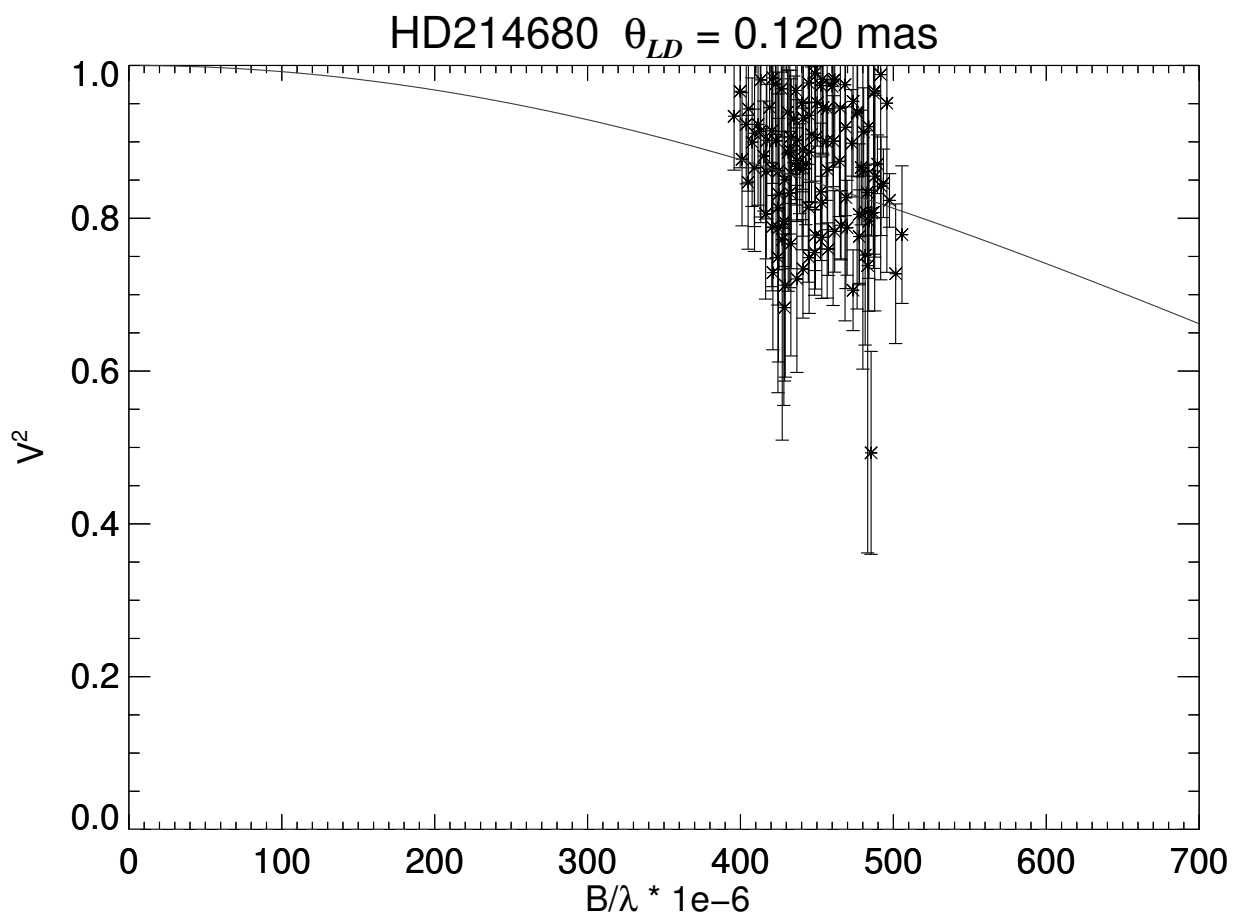


Figure A.30 Squared visibility versus spatial frequency for HD 214680. The solid line indicates the best fit for a single star limb-darkened disk model.

A.29 HD 214923

Table A.29 HD 214923 Observing Log

Baseline	Combiner	Brackets	N_{V^2}	Date
E2S2	PAVO	5	115	2015-08-09
W1E1S1	CLIMB	3	9	2014-09-22
W1E1S1	CLIMB	3	9	2014-09-23
W1E1S1	CLIMB	2	6	2014-09-24

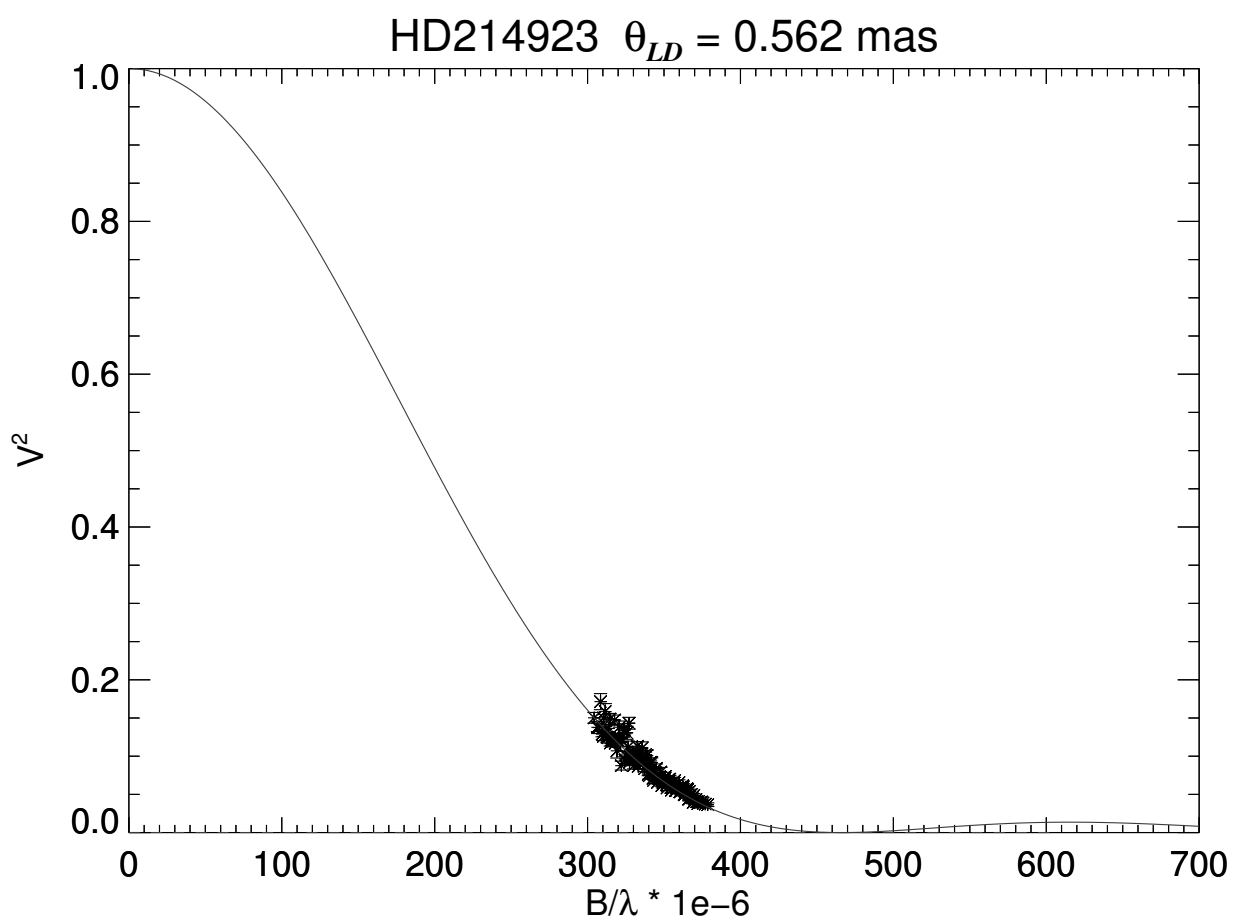


Figure A.31 Squared visibility versus spatial frequency for HD 214923 (PAVO). The solid line indicates the best fit for a single star limb-darkened disk model.

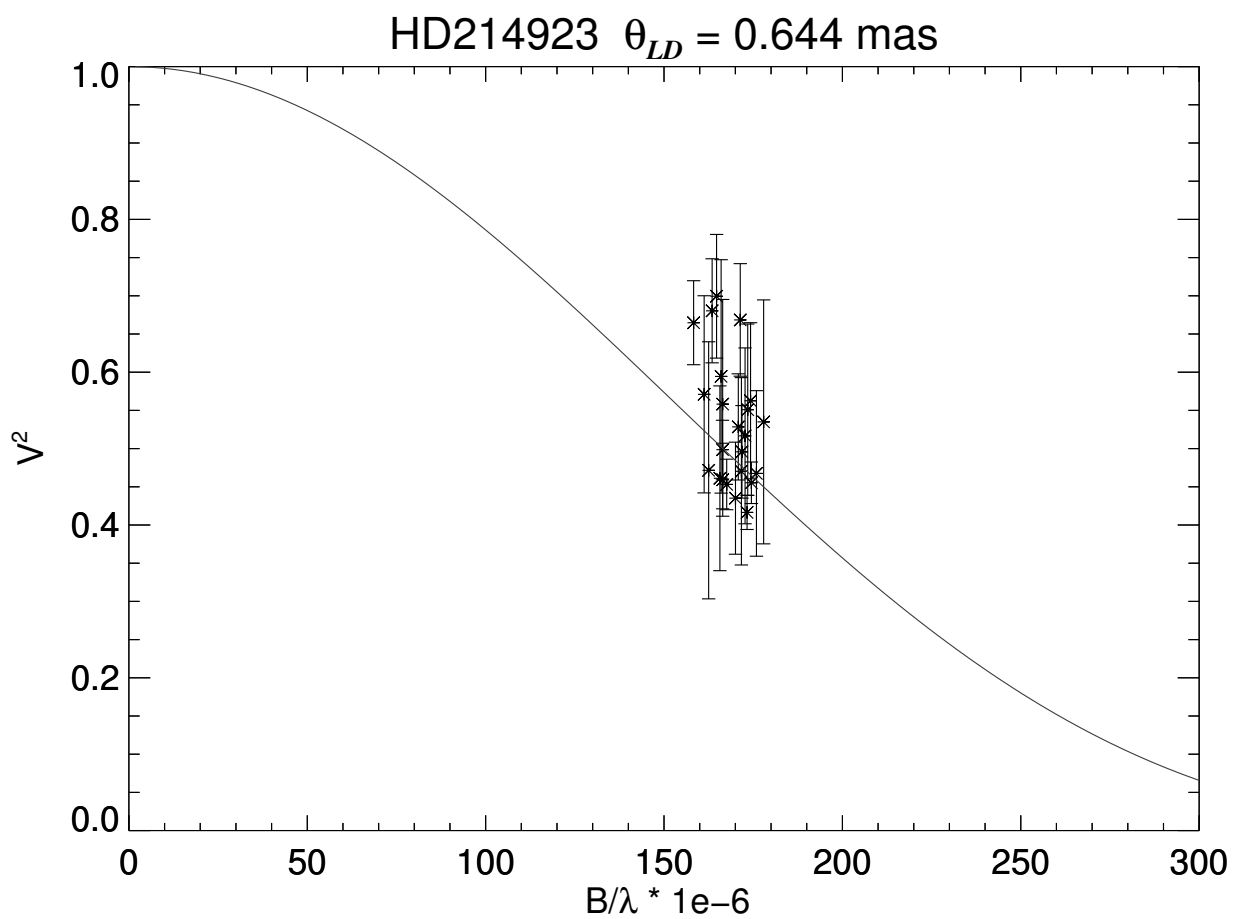


Figure A.32 Squared visibility versus spatial frequency for HD 214923 (CLIMB). The solid line indicates the best fit for a single star limb-darkened disk model.

A.30 HD 218045

Table A.30 HD 218045 Observing Log

Baseline	Combiner	Brackets	N_{V^2}	Date
E2S2	PAVO	7	161	2015-08-09
W2E2	PAVO	5	115	2015-08-10
W1E1S1	CLIMB	4	12	2012-10-06
W1E1S1	CLIMB	5	15	2013-08-14
W1E1S1	CLIMB	3	9	2013-08-15

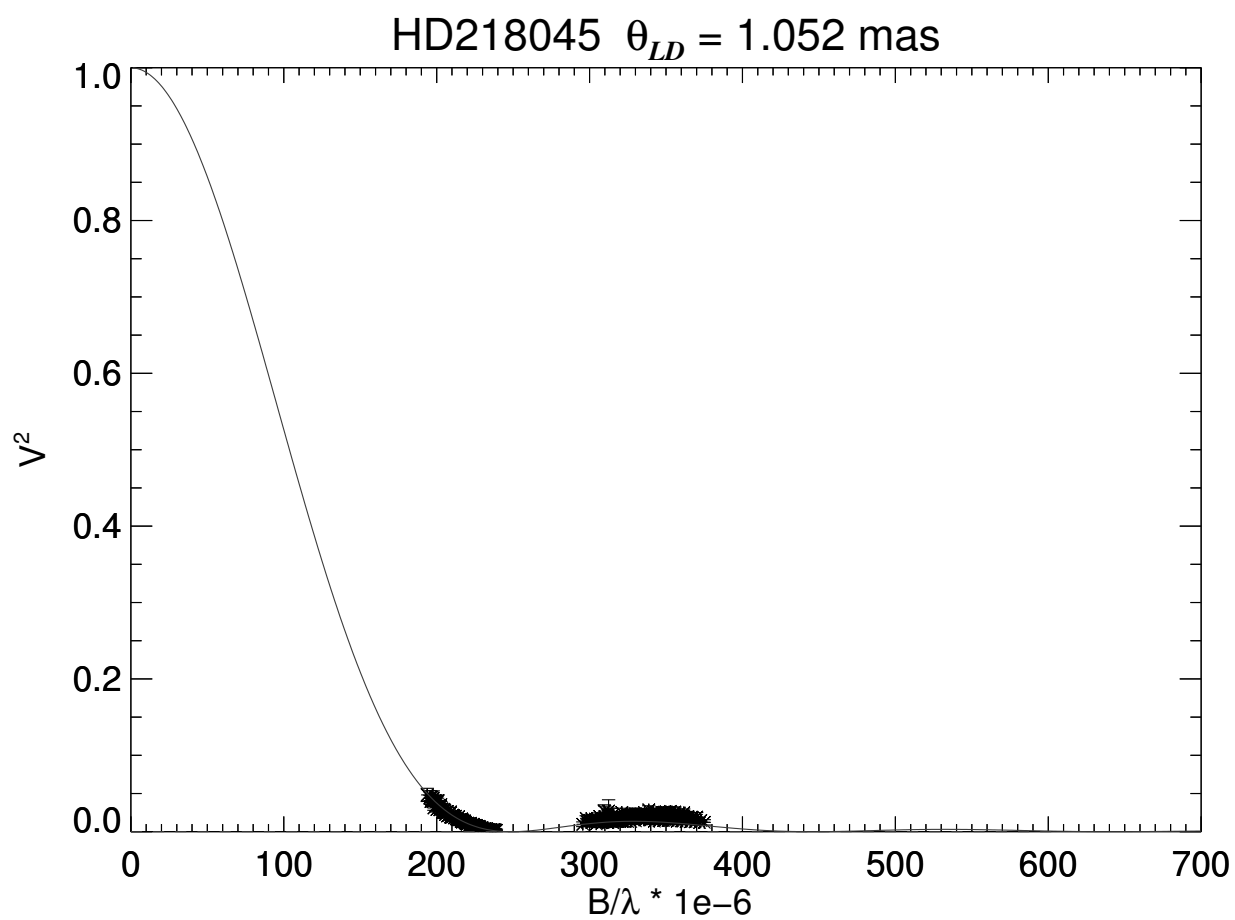


Figure A.33 Squared visibility versus spatial frequency for HD 218045 (PAVO). The solid line indicates the best fit for a single star limb-darkened disk model.

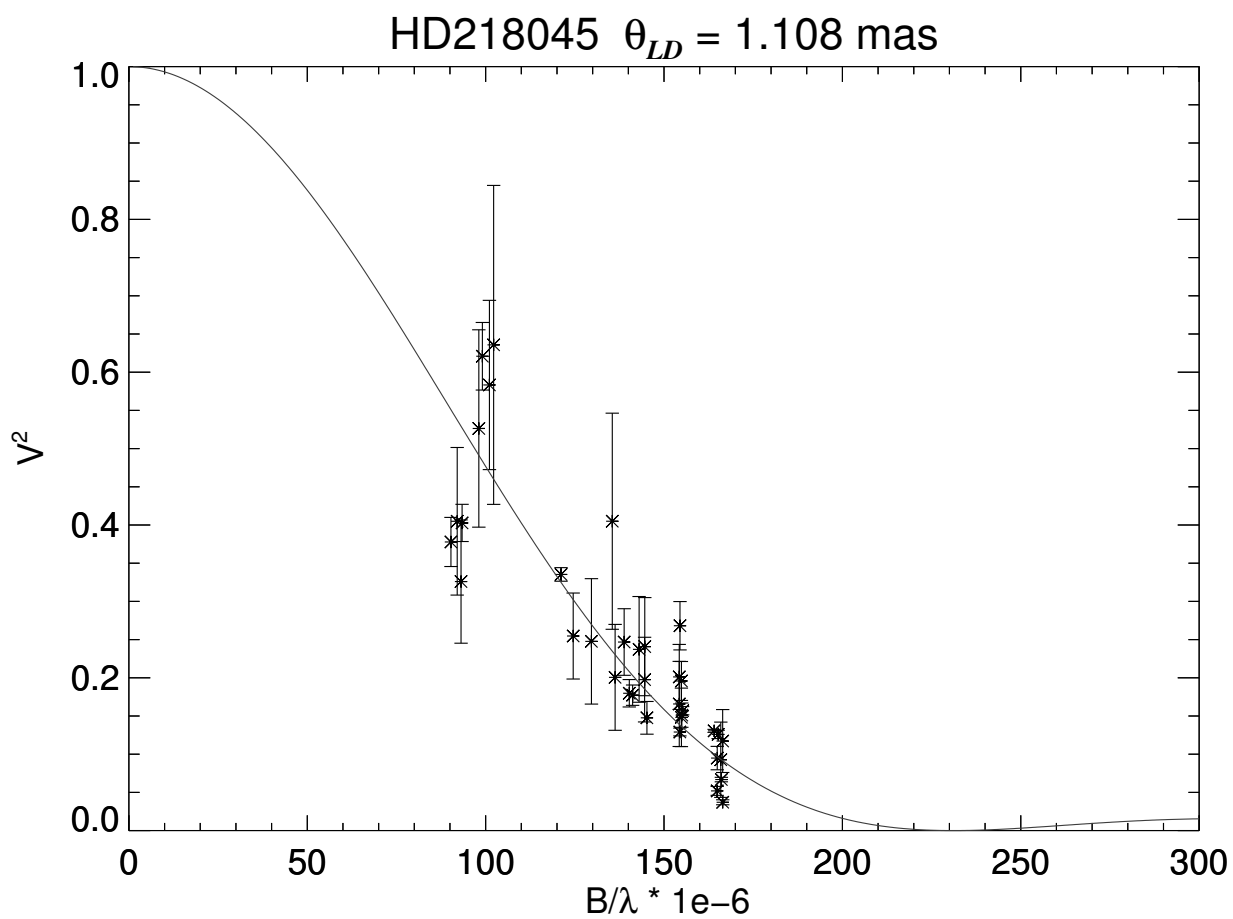


Figure A.34 Squared visibility versus spatial frequency for HD 218045 (CLIMB). The solid line indicates the best fit for a single star limb-darkened disk model.

A.31 HD 222661

Table A.31 HD 222661 Observing Log

Baseline	Combiner	Brackets	N_{V^2}	Date
E1S1	PAVO	1	23	2014-09-10

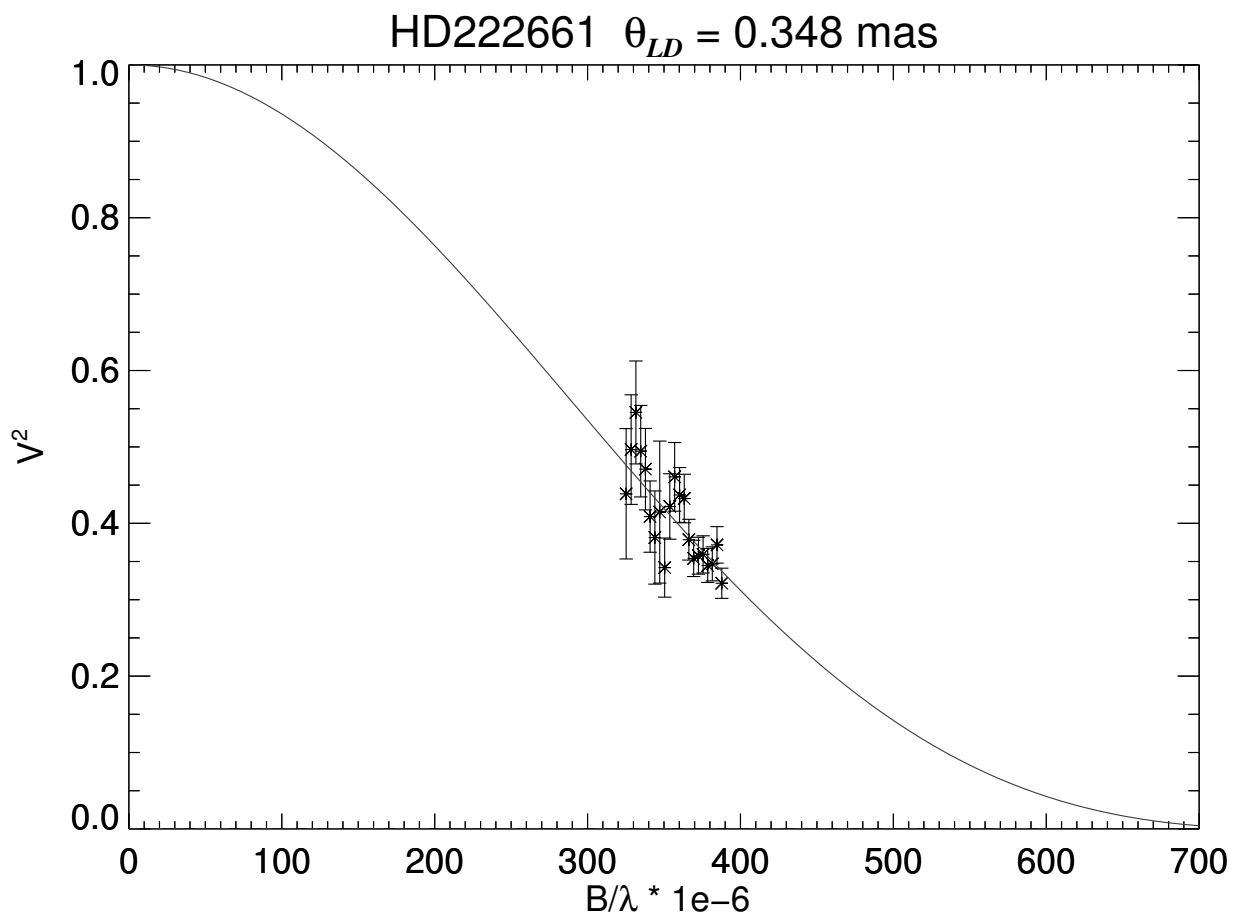


Figure A.35 Squared visibility versus spatial frequency for HD 222661. The solid line indicates the best fit for a single star limb-darkened disk model.

B B Star Contours and SEDs

Contour plots: χ^2 contour maps of fitted TLUSTY or ATLAS9 stellar atmosphere models to observed spectra for each star. Overplotted are vertical lines showing angular size obtained from our interferometry and horizontal lines showing the average literature temperature. Dotted lines show an error margin of 1σ for the angular size and the temperature. The diamonds indicate the best fit model temperature for our directly determined angular size.

SED plots: Spectral energy distributions for targets stars with the best fit model shown in the solid green line. Best fit models were chosen using our observed angular diameter from interferometry combined with the best fit temperatures and reddening values found from our contour maps. The dashed line indicates the SED derived using the predicted model T_{eff} and angular size.

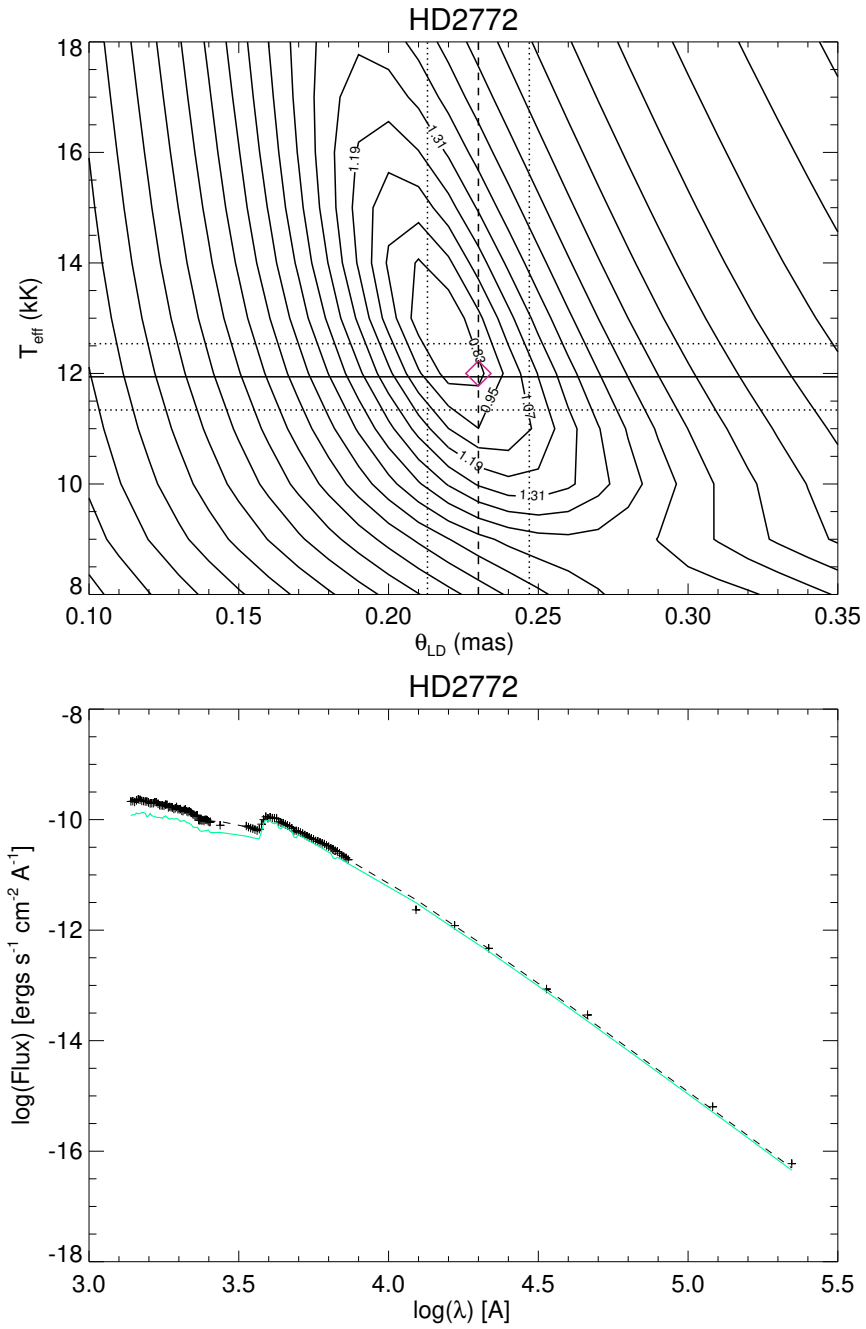
B.1 HD 2772

Figure B.1 Contour (top) and SED (bottom) plots for HD 2772. Fit with the ATLAS9 model.

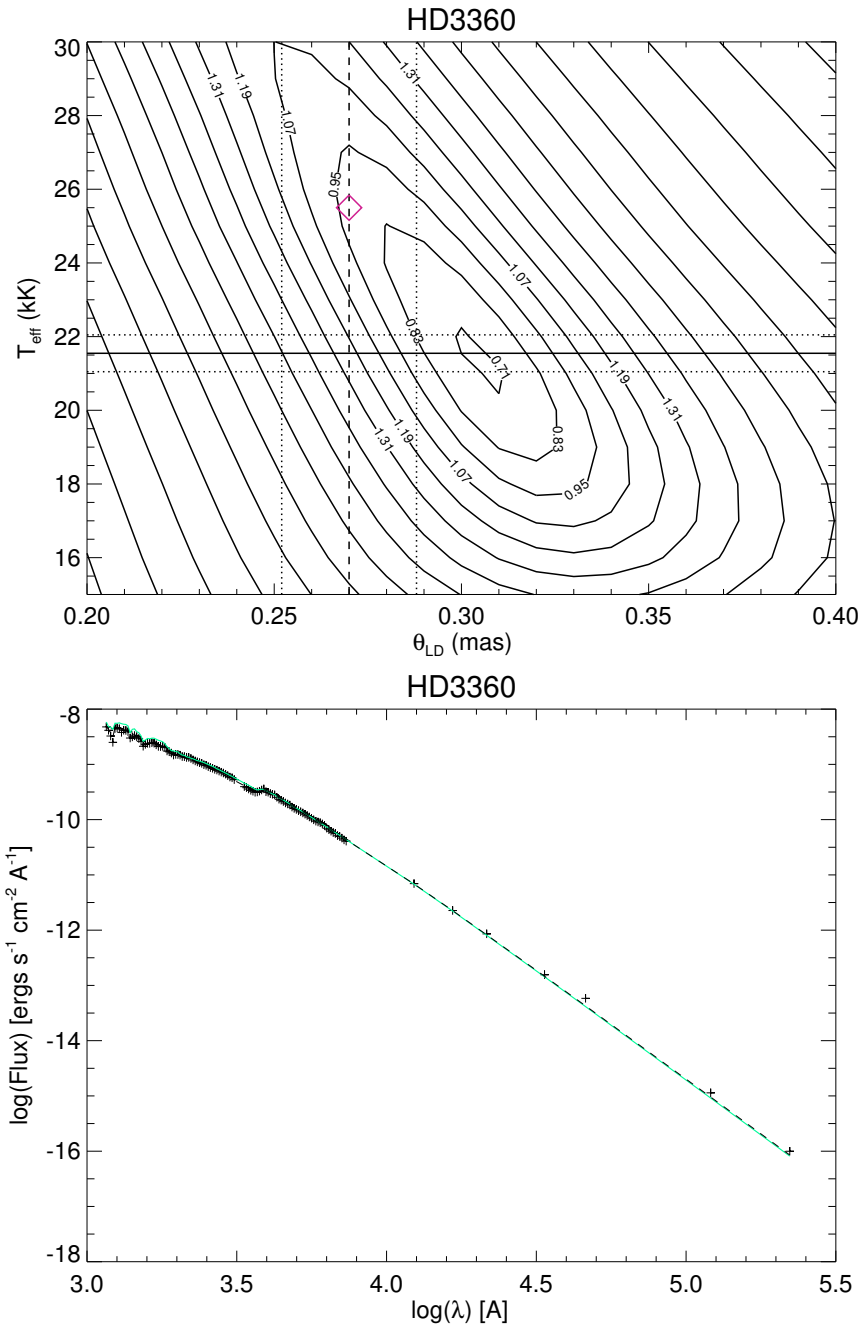
B.2 HD 3360

Figure B.2 Contour (top) and SED (bottom) plots for HD 3360. Fit with the TLUSTY B star model.

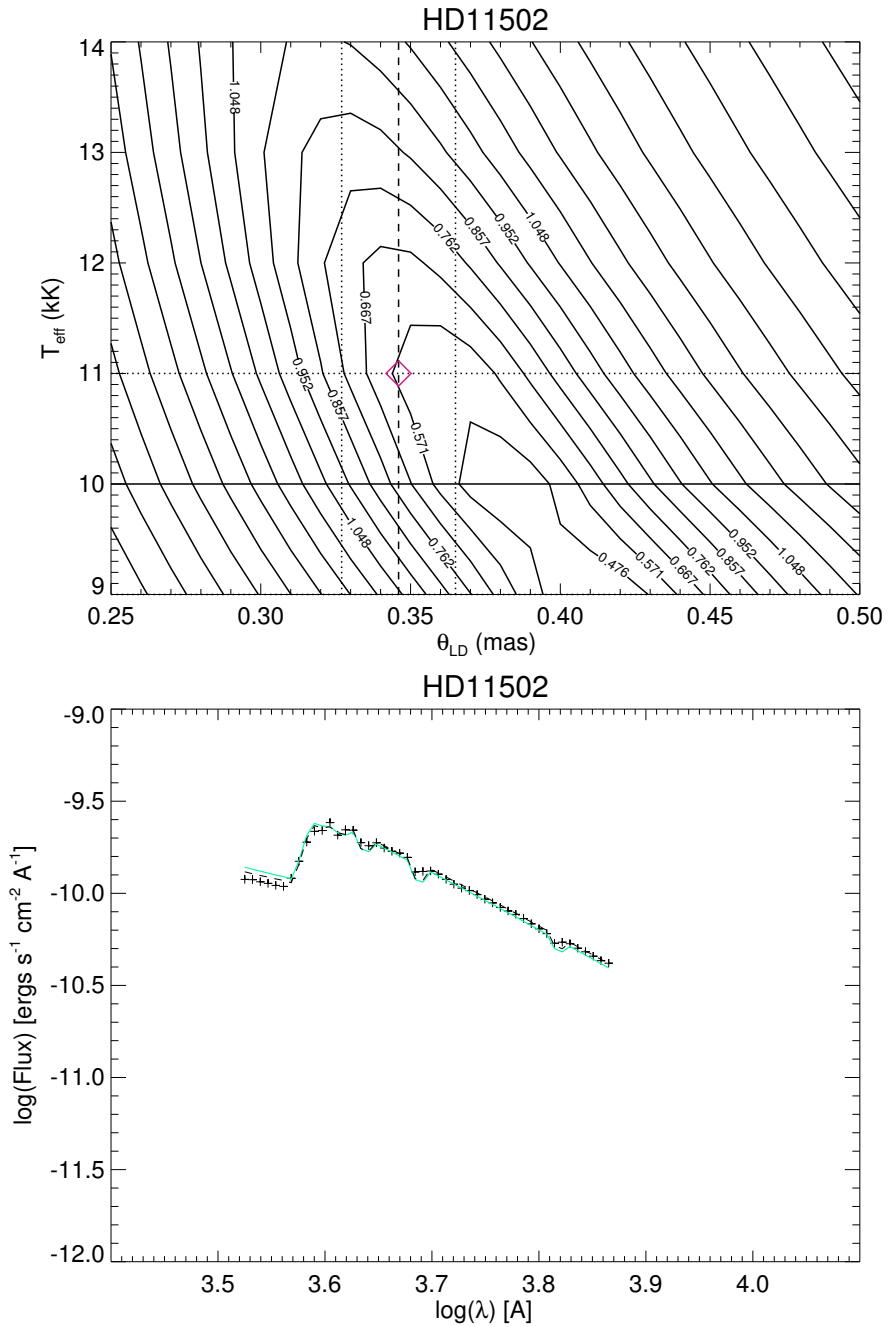
B.3 HD 11502

Figure B.3 Contour (top) and SED (bottom) plots for HD 11502. Fit with the ATLAS9 model.

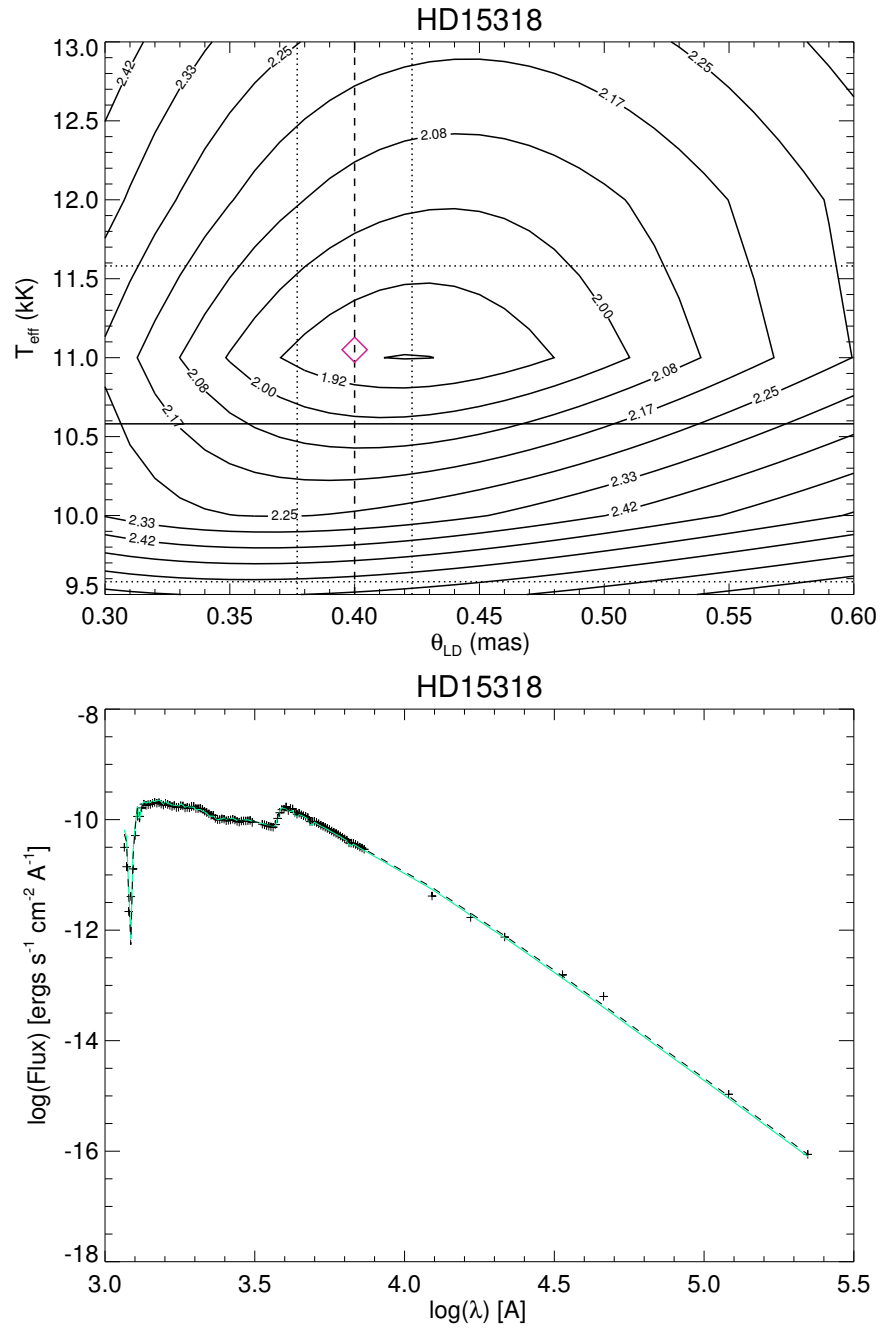
B.4 HD 15318

Figure B.4 Contour (top) and SED (bottom) plots for HD 15318. Fit with the ATLAS9 model.

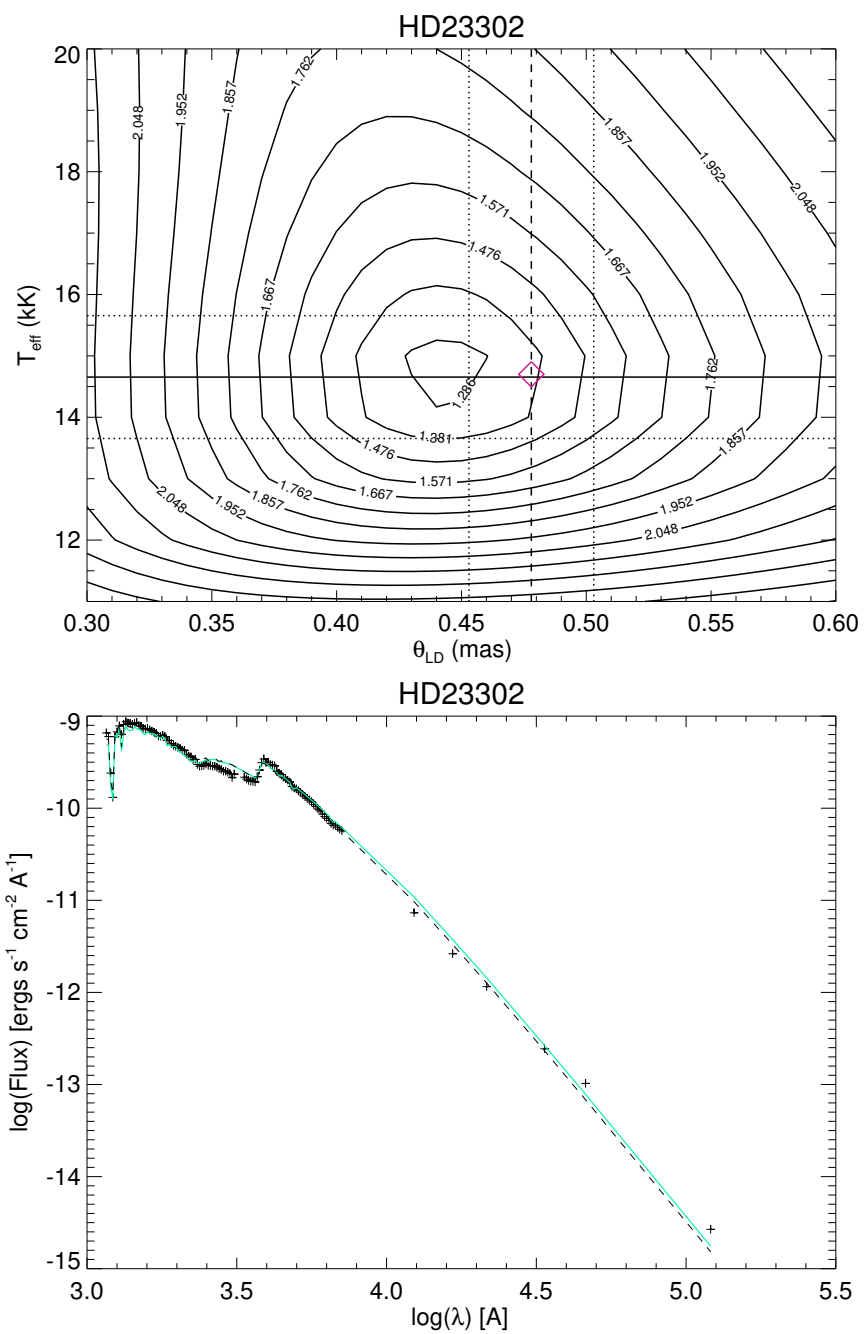
B.5 HD 23302

Figure B.5 Contour (top) and SED (bottom) plots for HD 23302. Fit with the ATLAS9 model.

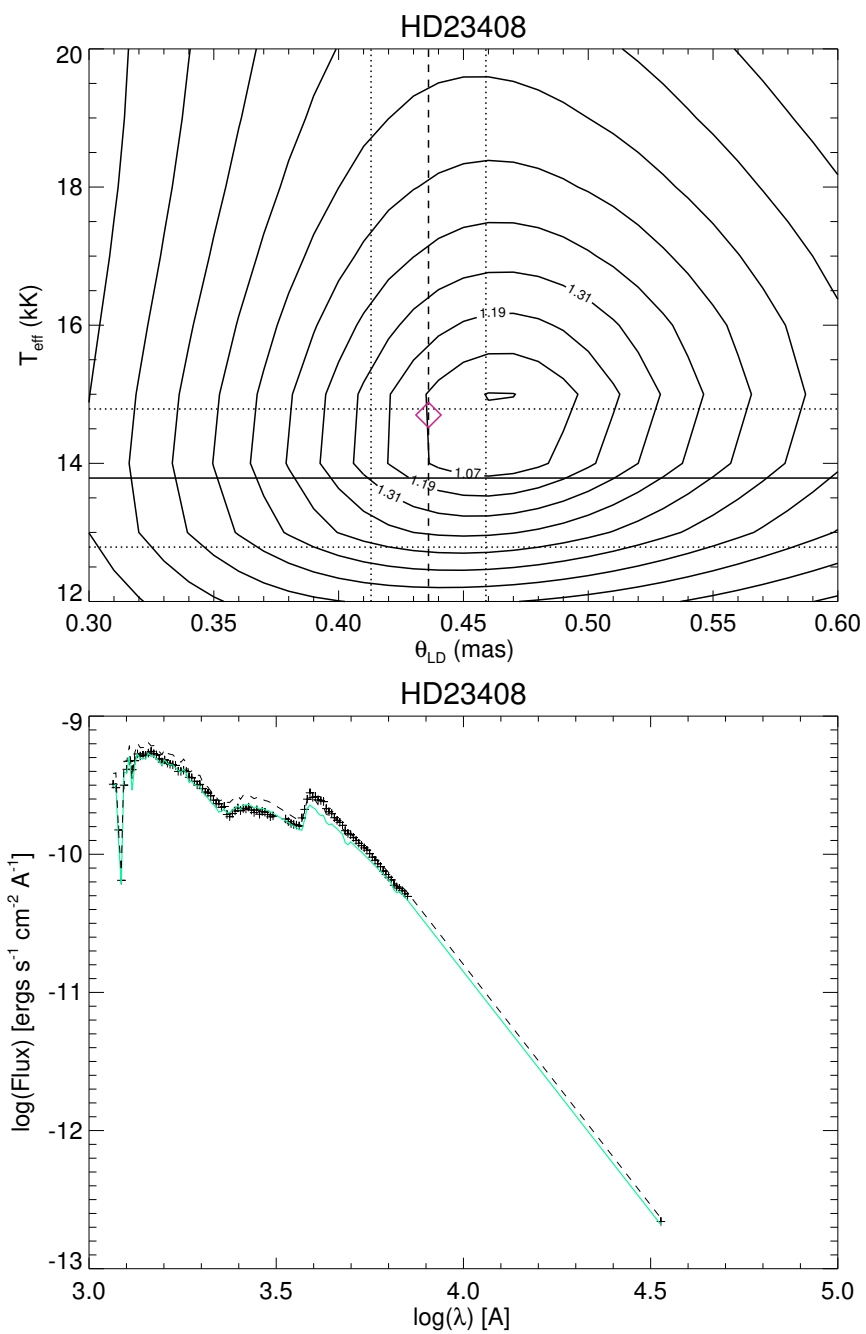
B.6 HD 23408

Figure B.6 Contour (top) and SED (bottom) plots for HD 23408. Fit with the ATLAS9 model.

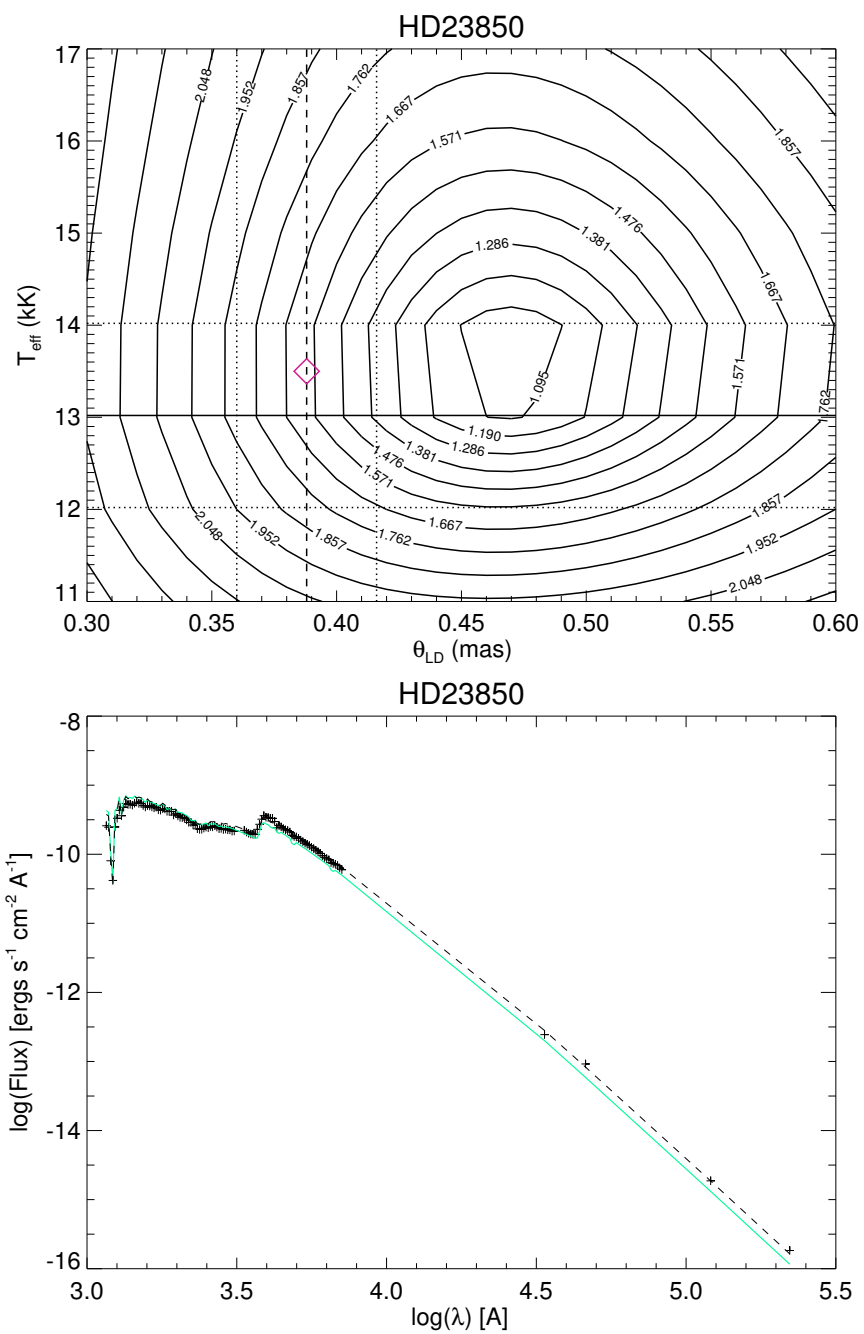
B.7 HD 23850

Figure B.7 Contour (top) and SED (bottom) plots for HD 23850. Fit with the ATLAS9 model.

B.8 HD 29763

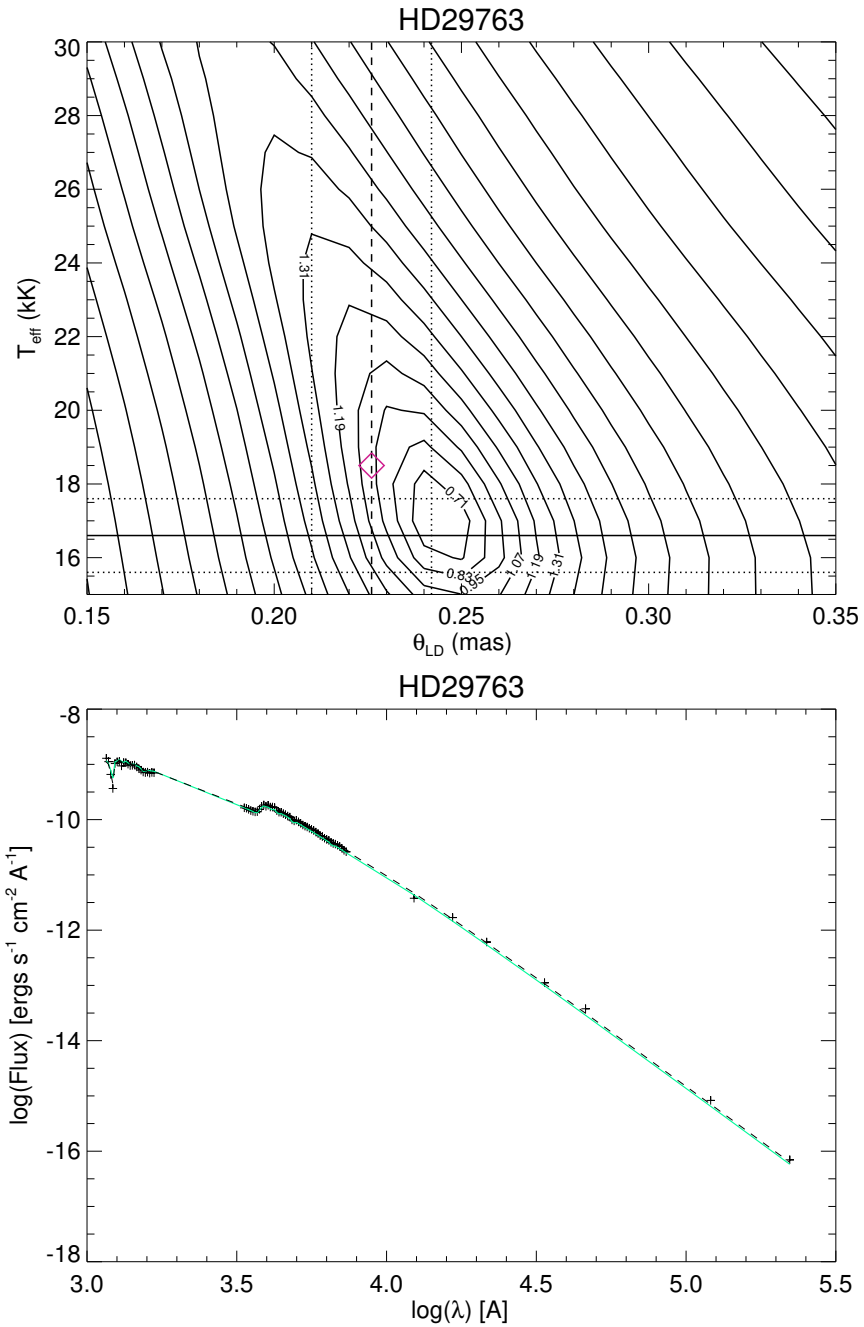


Figure B.8 Contour (top) and SED (bottom) plots for HD 29763. Fit with the TLUSTY B star model.

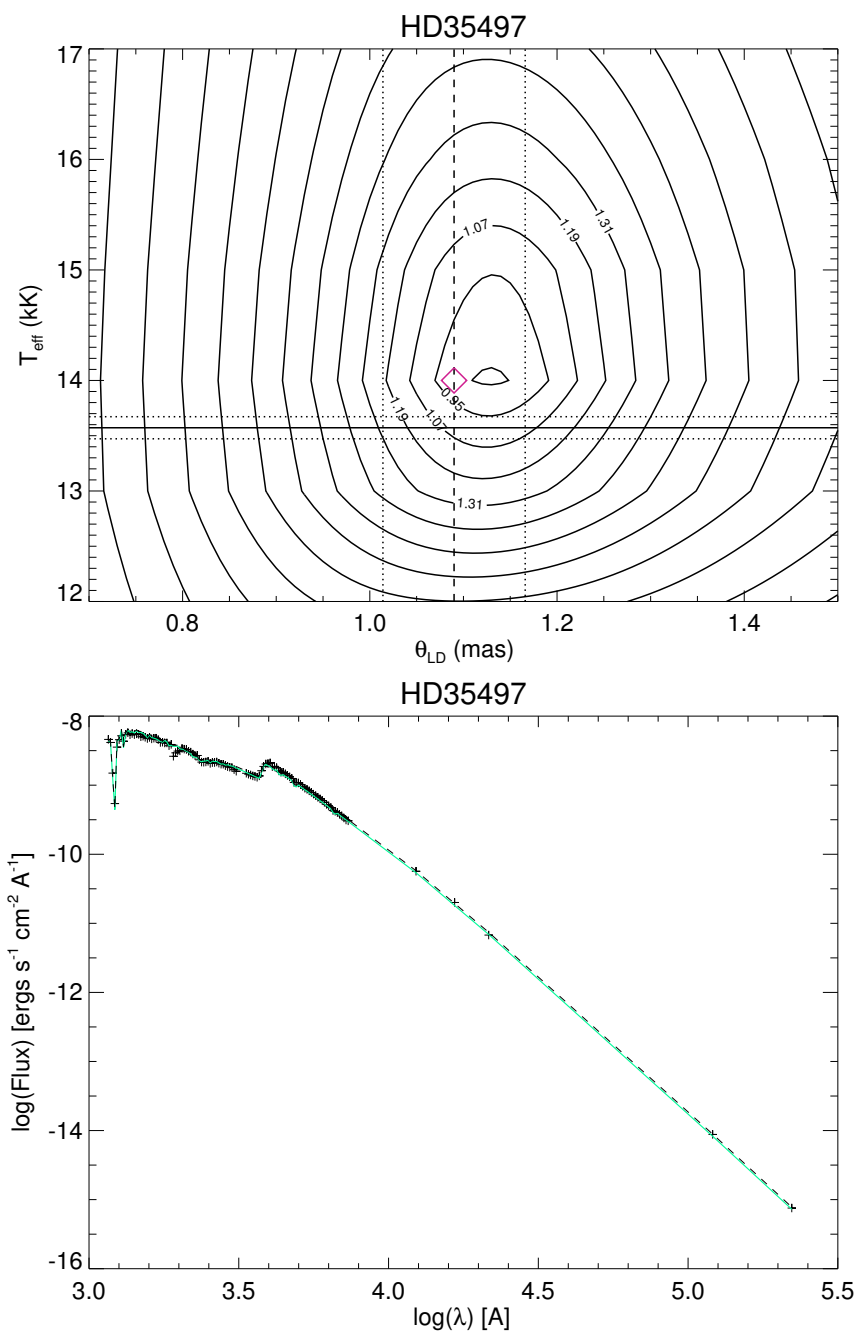
B.9 HD 35497

Figure B.9 Contour (top) and SED (bottom) plots for HD 35497. Fit with the ATLAS9 model.

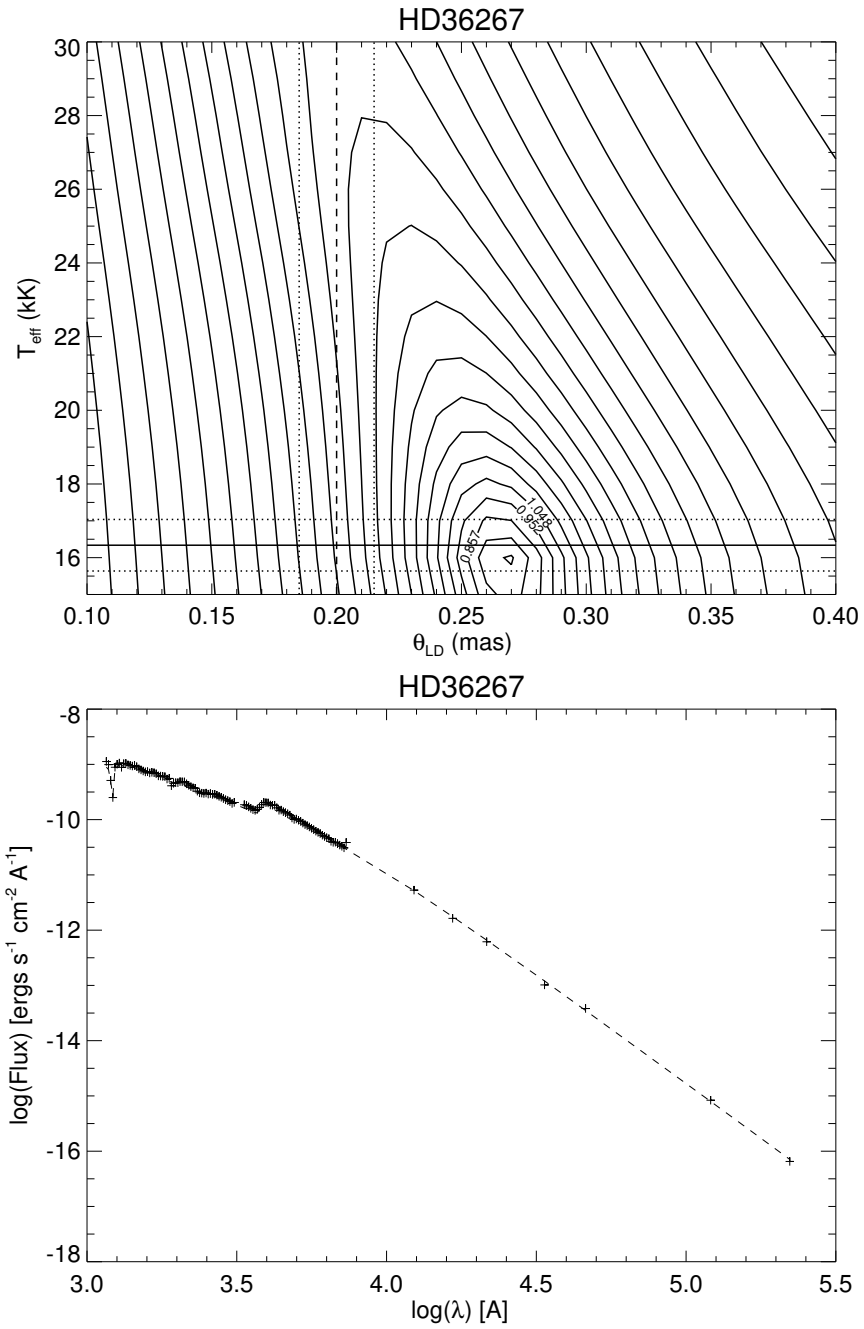
B.10 HD 36267

Figure B.10 Contour (top) and SED (bottom) plots for HD 36267. Fit with the TLUSTY B star model.

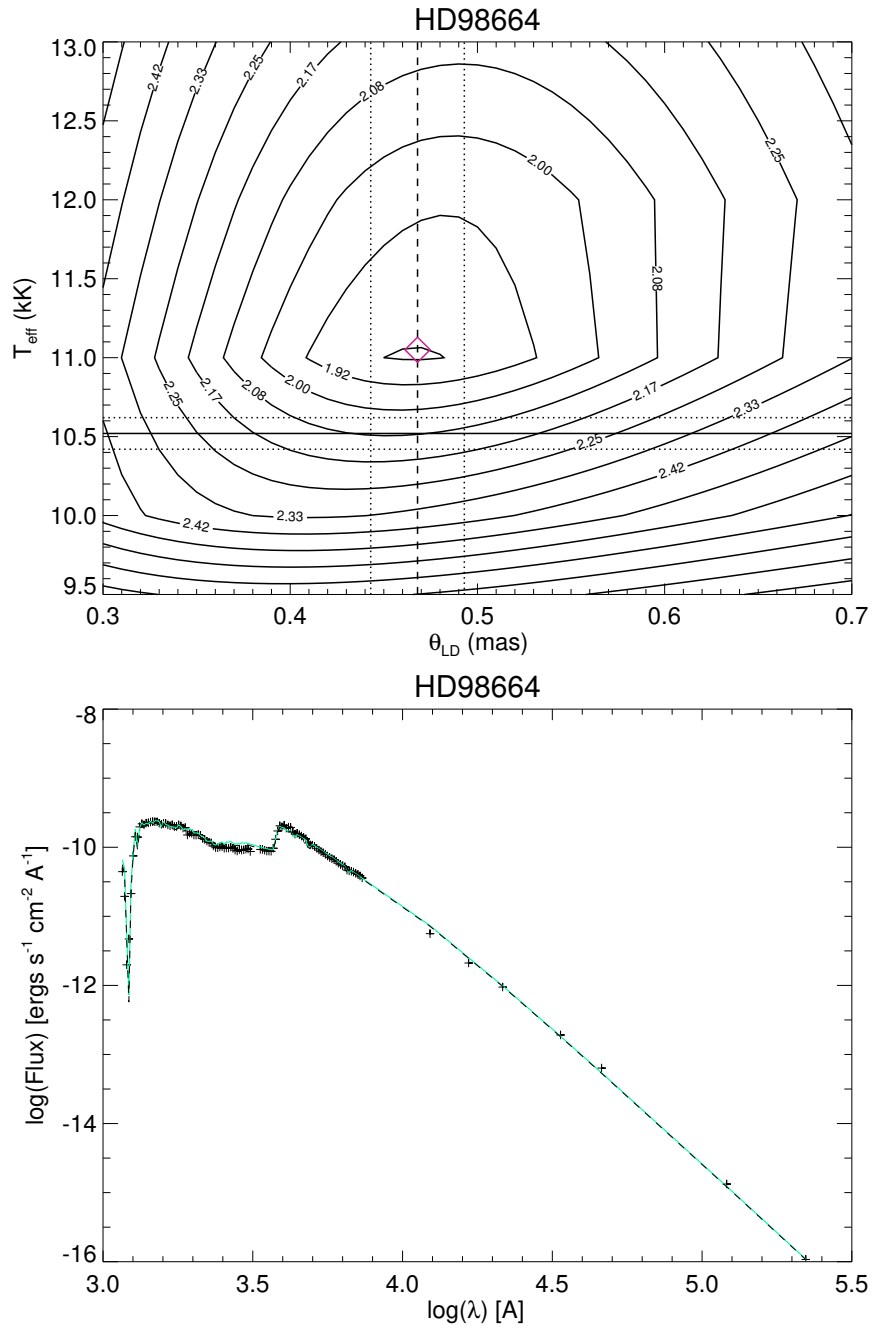
B.11 HD 98664

Figure B.11 Contour (top) and SED (bottom) plots for HD 98664. Fit with the ATLAS9 model.

B.12 HD 120315

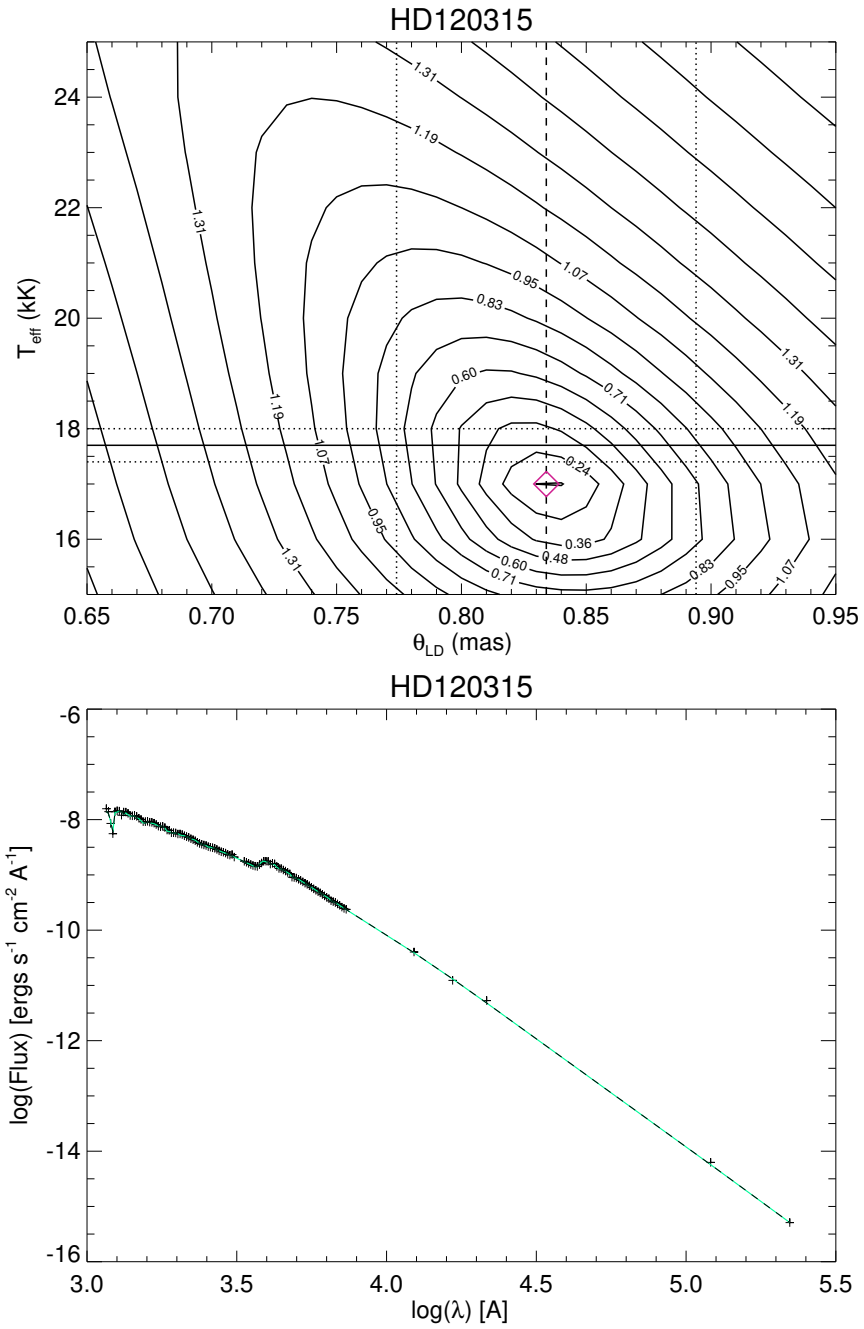


Figure B.12 Contour (top) and SED (bottom) plots for HD 120315. Fit with the TLUSTY B star model.

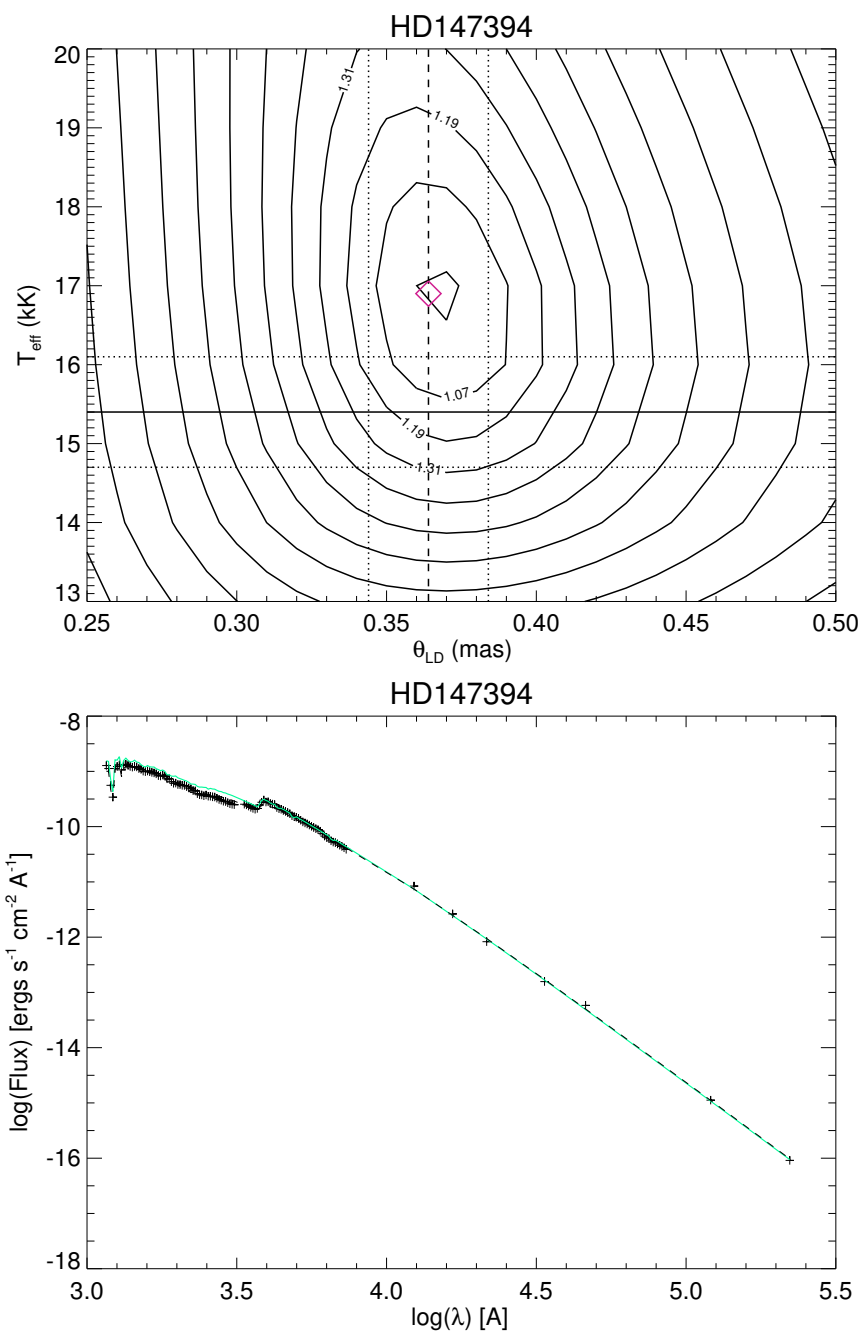
B.13 HD 147394

Figure B.13 Contour (top) and SED (bottom) plots for HD 147394. Fit with the ATLAS9 model.

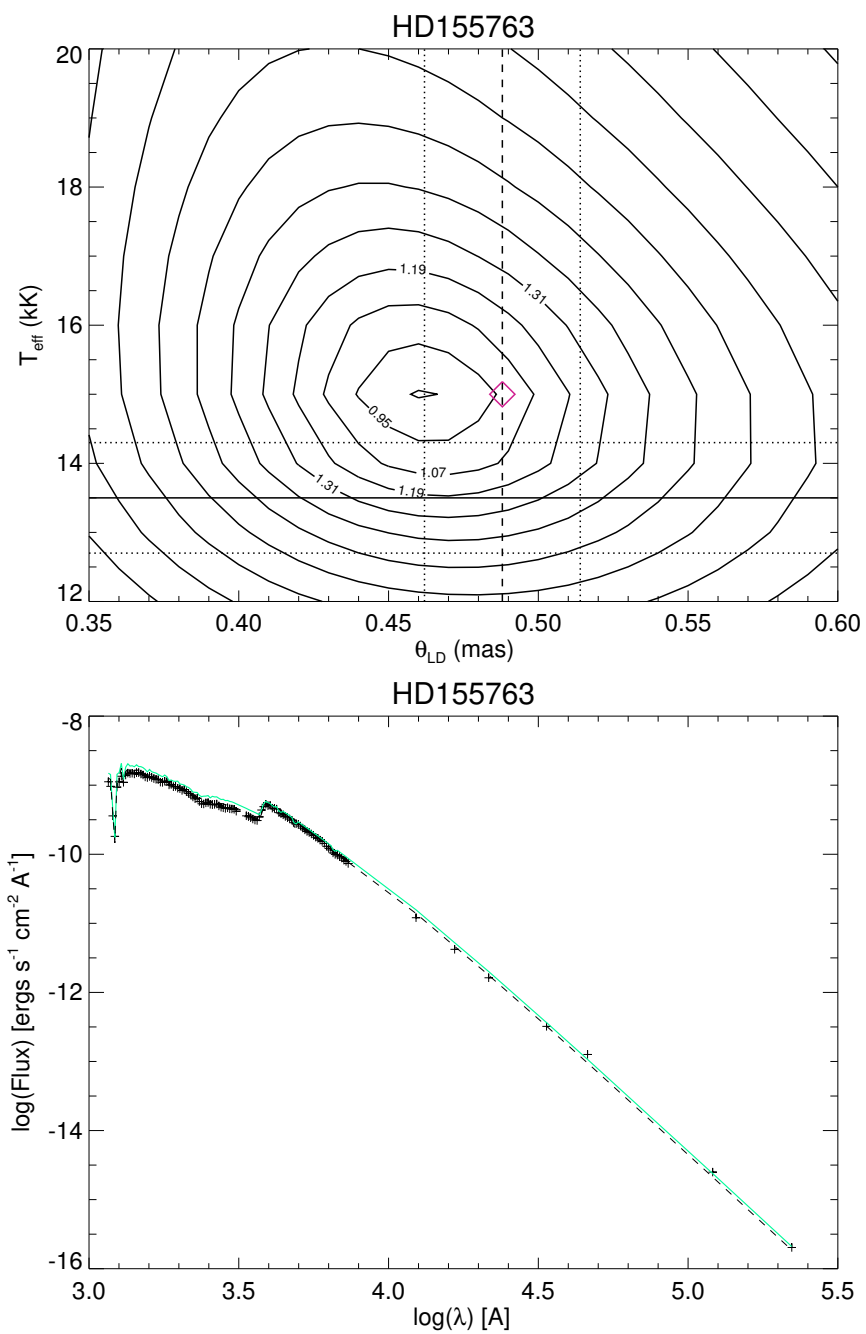
B.14 HD 155763

Figure B.14 Contour (top) and SED (bottom) plots for HD 155763. Fit with the ATLAS9 model.

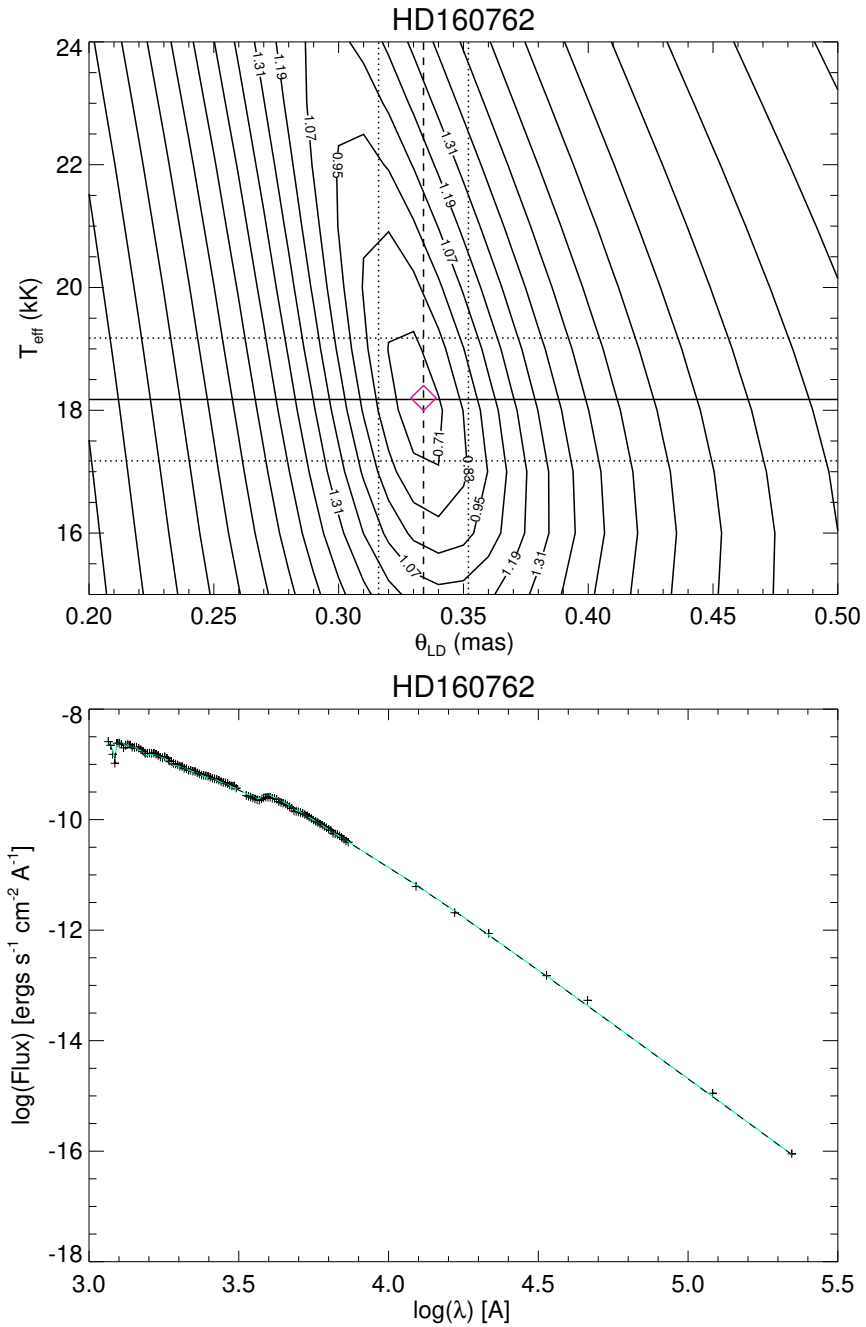
B.15 HD 160762

Figure B.15 Contour (top) and SED (bottom) plots for HD 160762. Fit with the TLUSTY B star model.

B.16 HD 176437

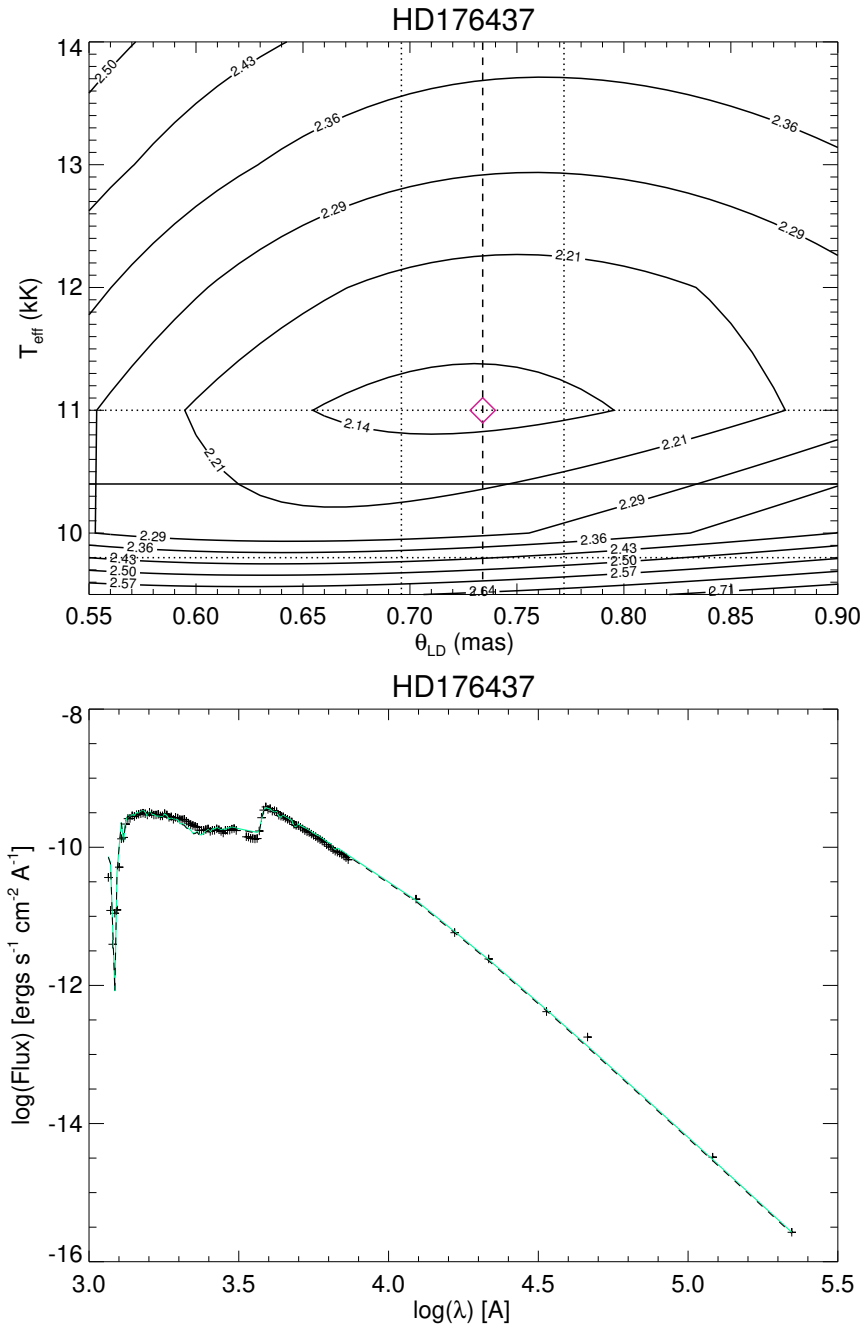


Figure B.16 Contour (top) and SED (bottom) plots for HD 176437. Fit with the ATLAS9 model.

B.17 HD 177756

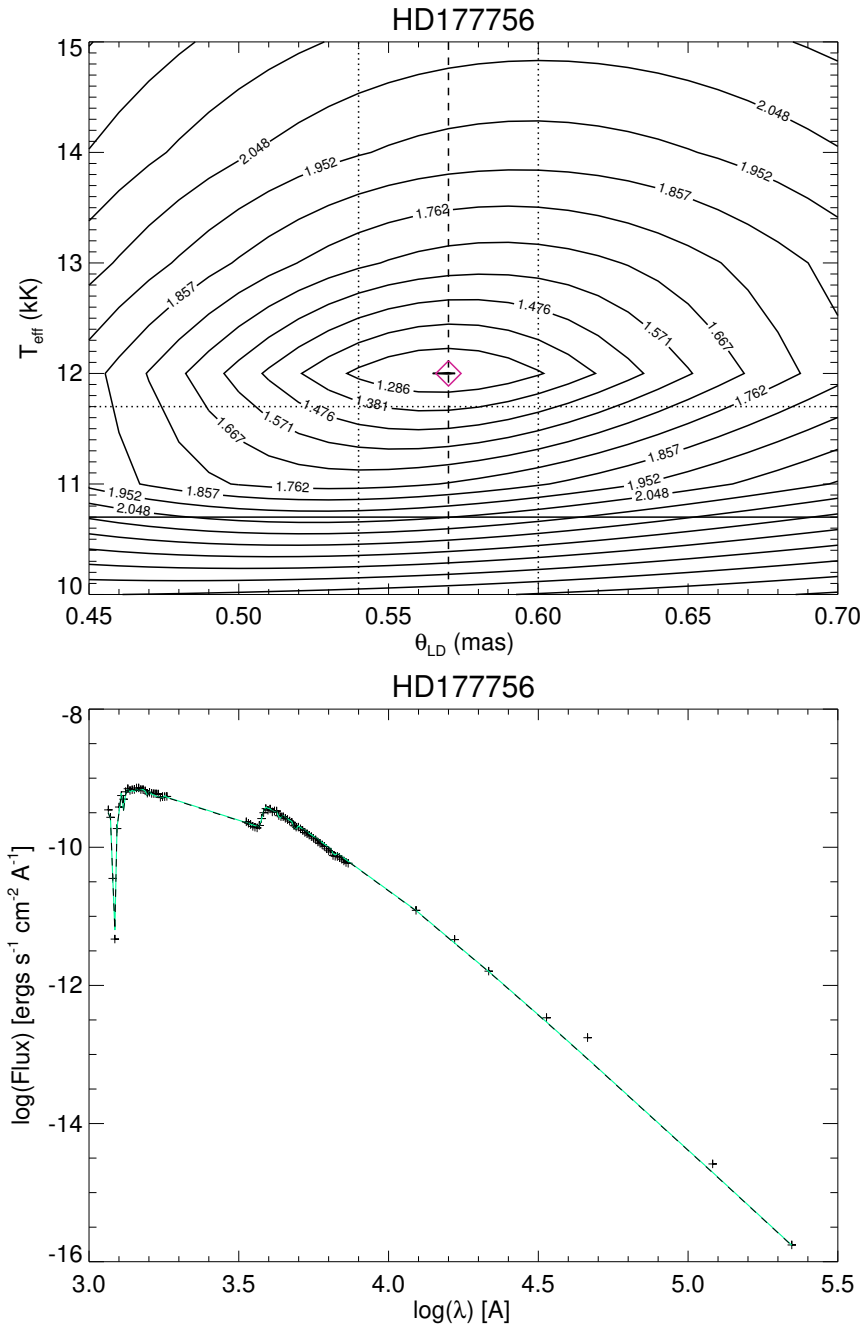


Figure B.17 Contour (top) and SED (bottom) plots for HD 177756. Fit with the ATLAS9 model.

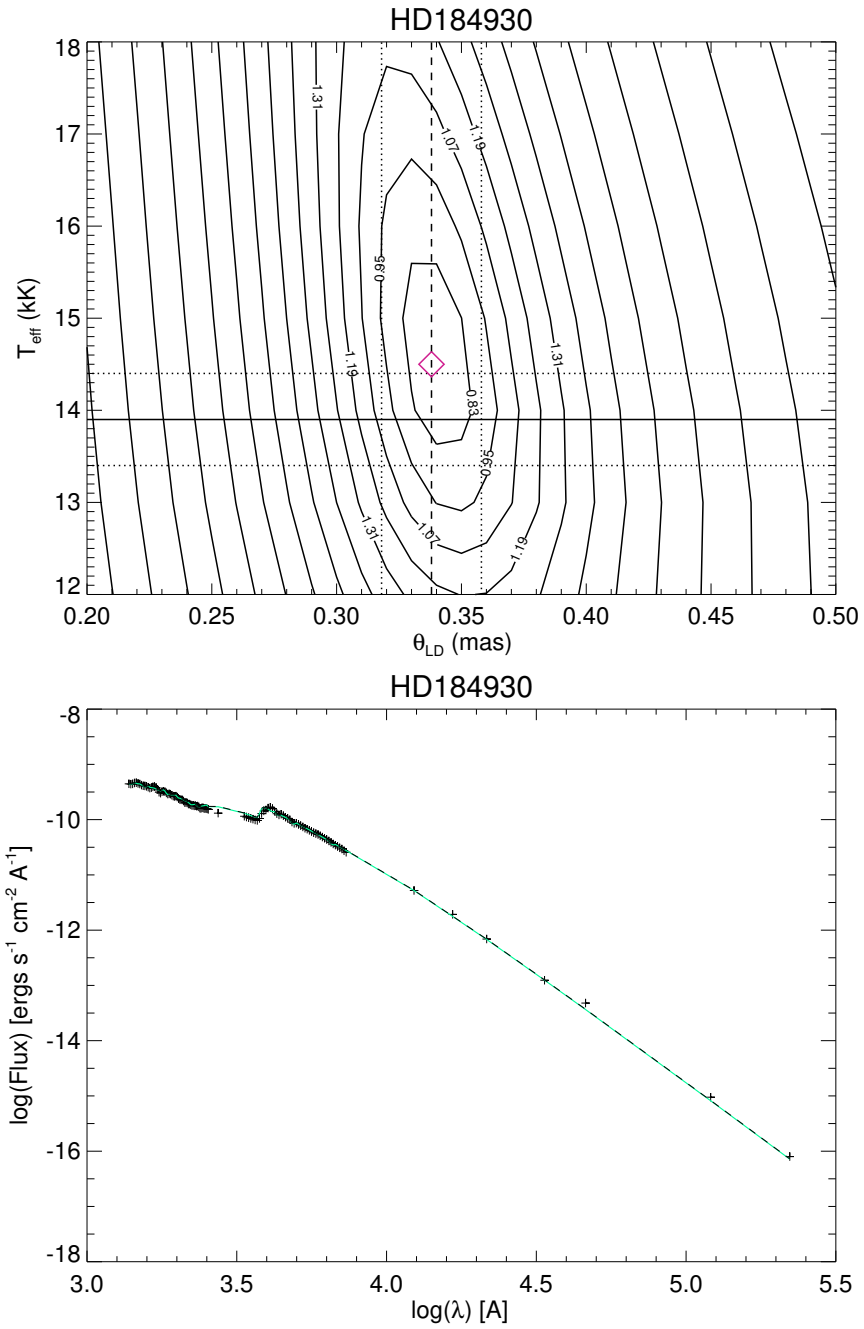
B.18 HD 184930

Figure B.18 Contour (top) and SED (bottom) plots for HD 184930. Fit with the ATLAS9 model.

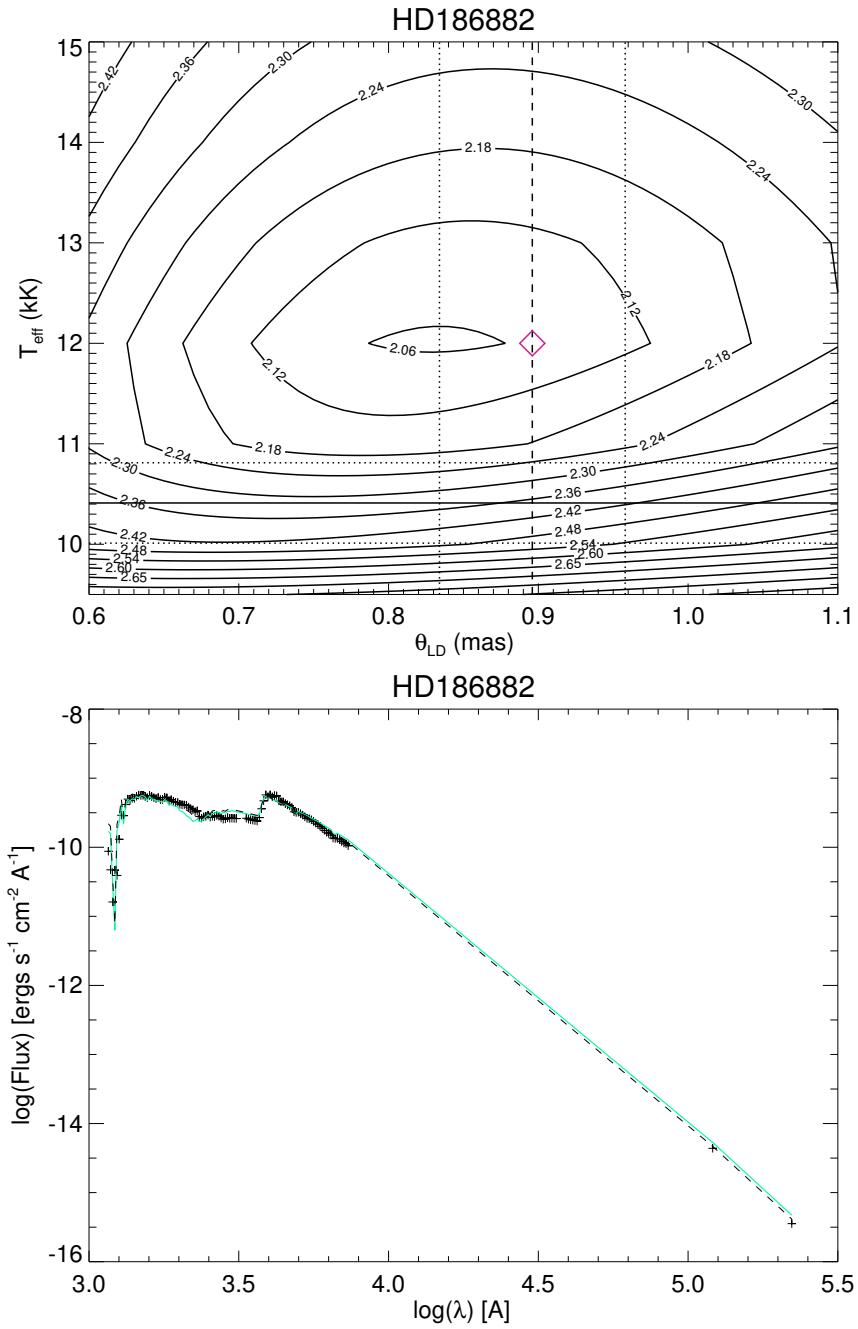
B.19 HD 186882

Figure B.19 Contour (top) and SED (bottom) plots for HD 186882. Fit with the ATLAS9 model.

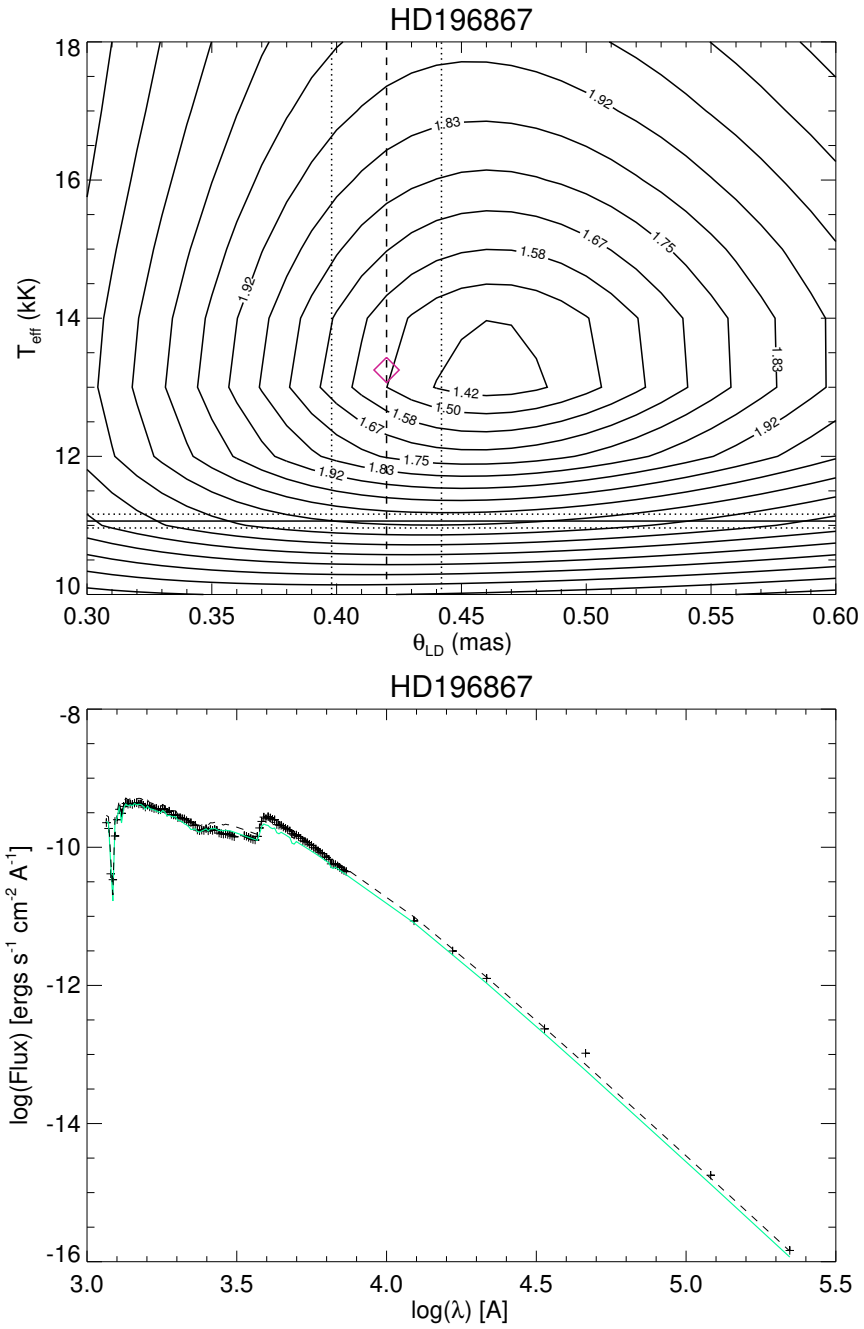
B.20 HD 196867

Figure B.20 Contour (top) and SED (bottom) plots for HD 196867. Fit with the ATLAS9 model.

B.21 HD 198478

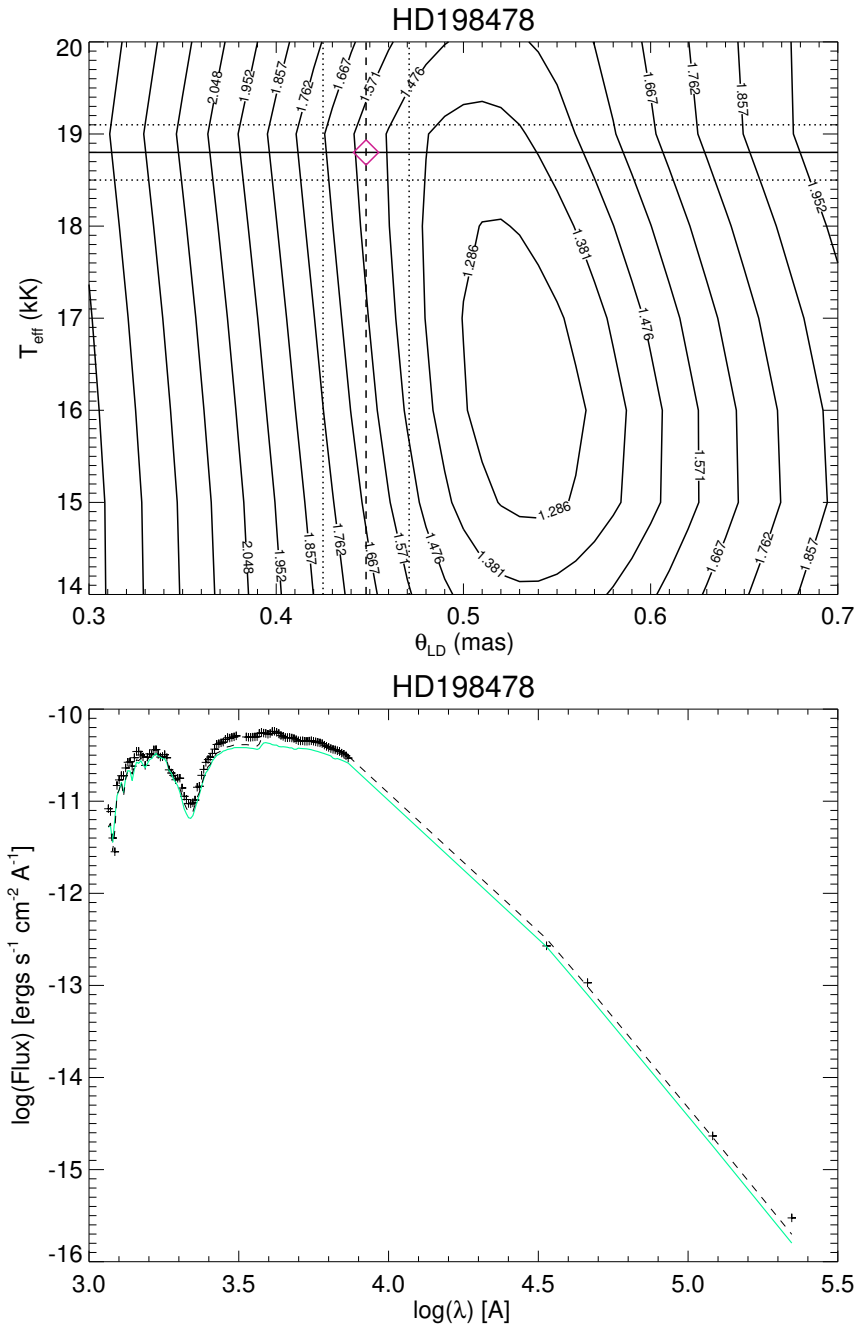


Figure B.21 Contour (top) and SED (bottom) plots for HD 198478. Fit with the ATLAS9 model.

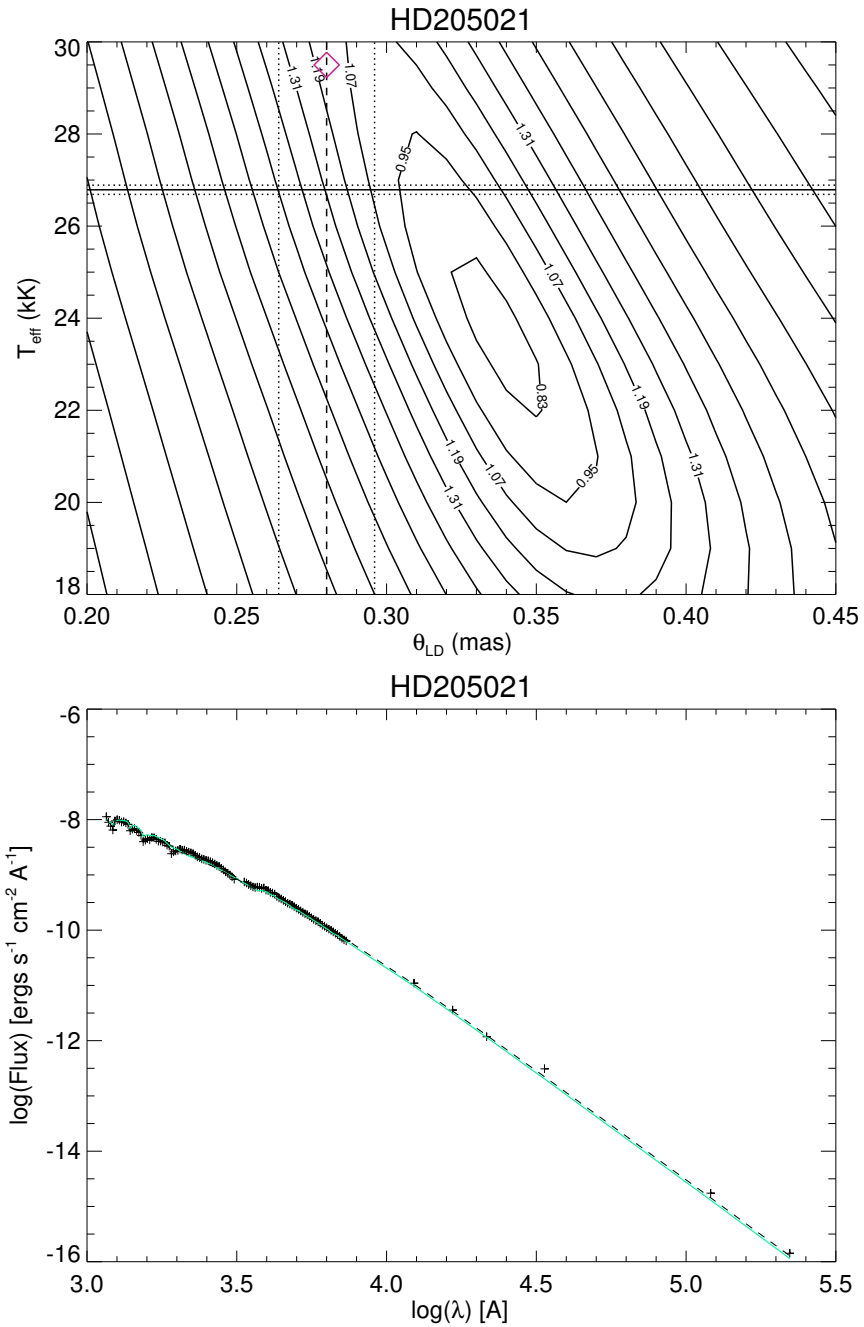
B.22 HD 205021

Figure B.22 Contour (top) and SED (bottom) plots for HD 205021. Fit with the TLUSTY B star model.

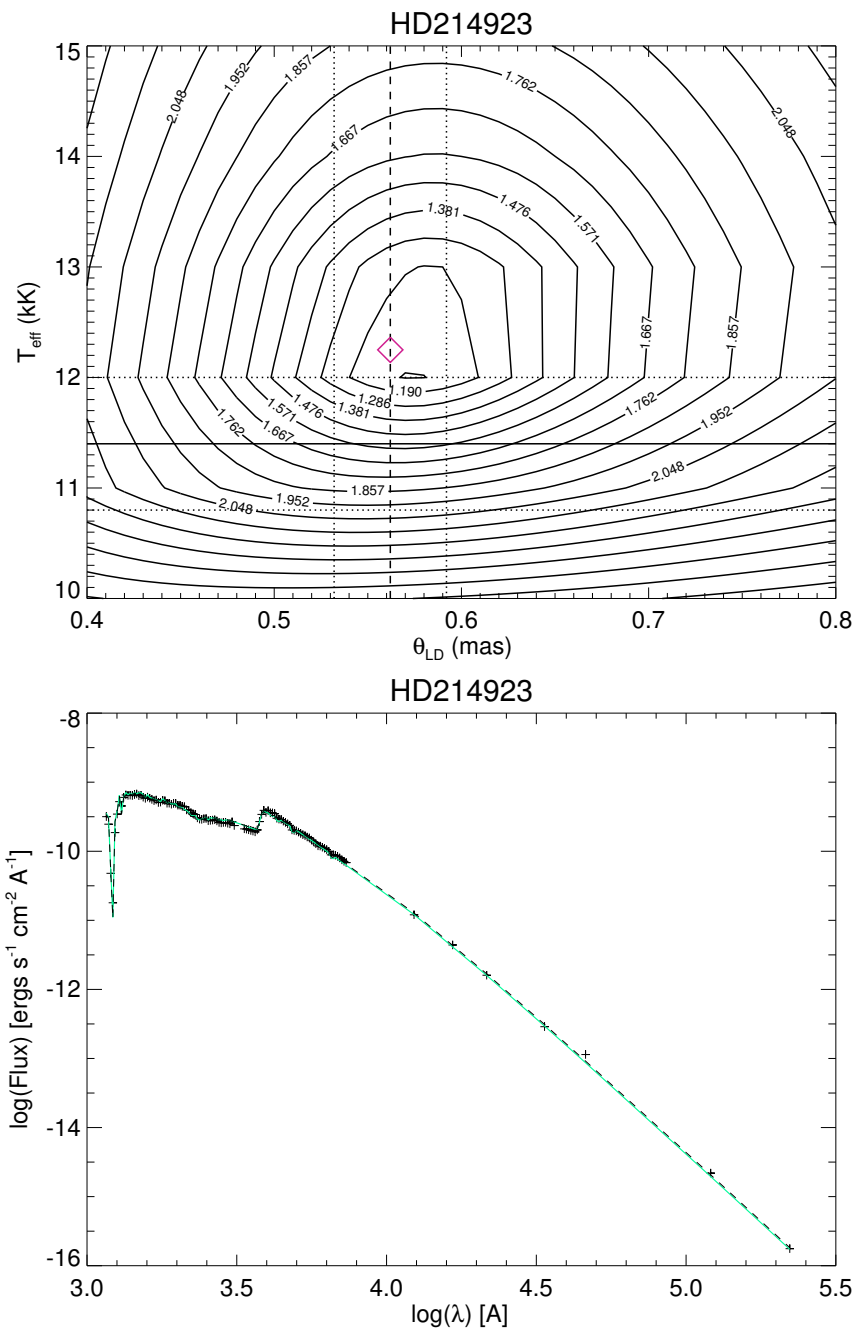
B.23 HD 214923

Figure B.23 Contour (top) and SED (bottom) plots for HD 214923. Fit with the ATLAS9 model.

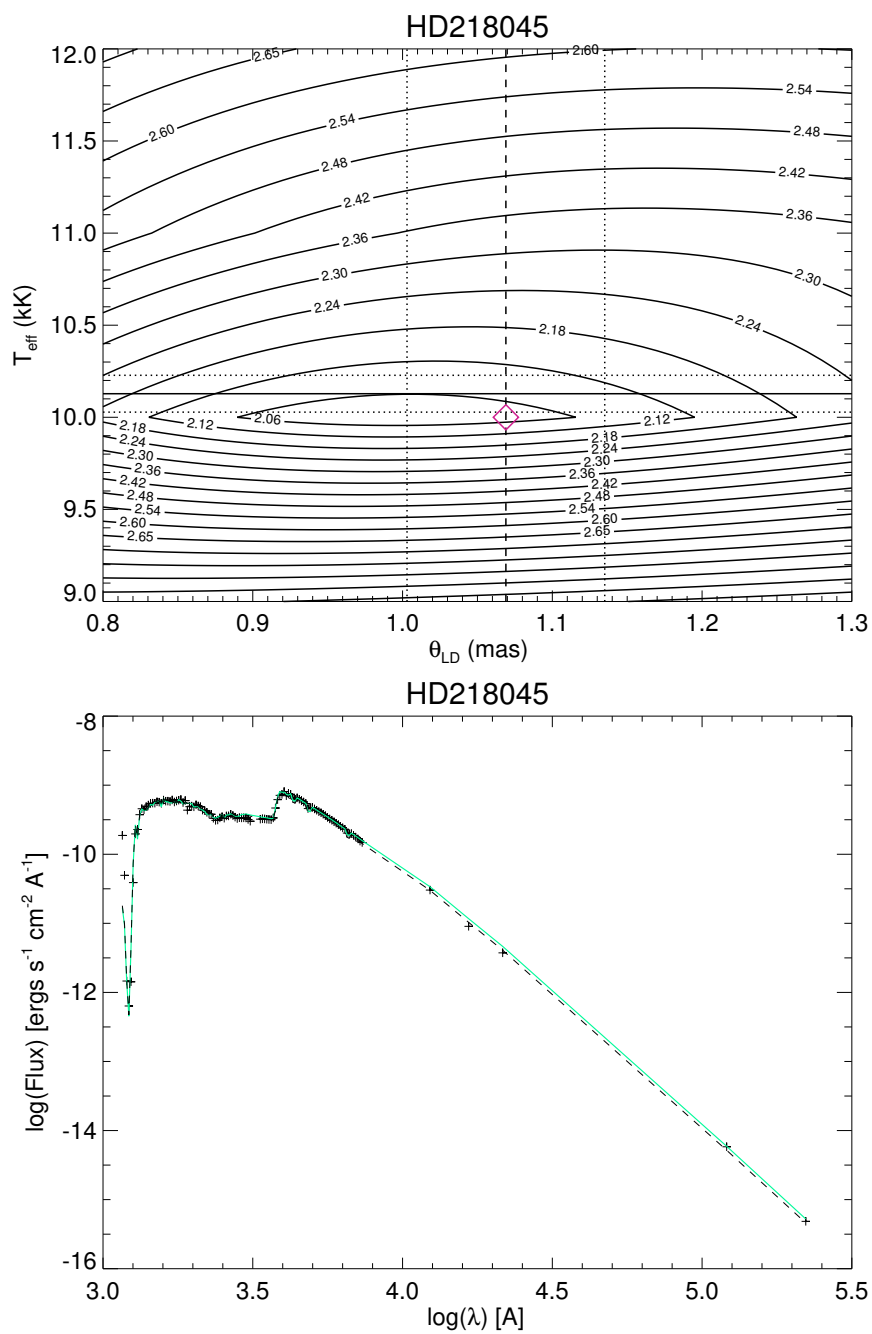
B.24 HD 218045

Figure B.24 Contour (top) and SED (bottom) plots for HD 218045. Fit with the ATLAS9 model.

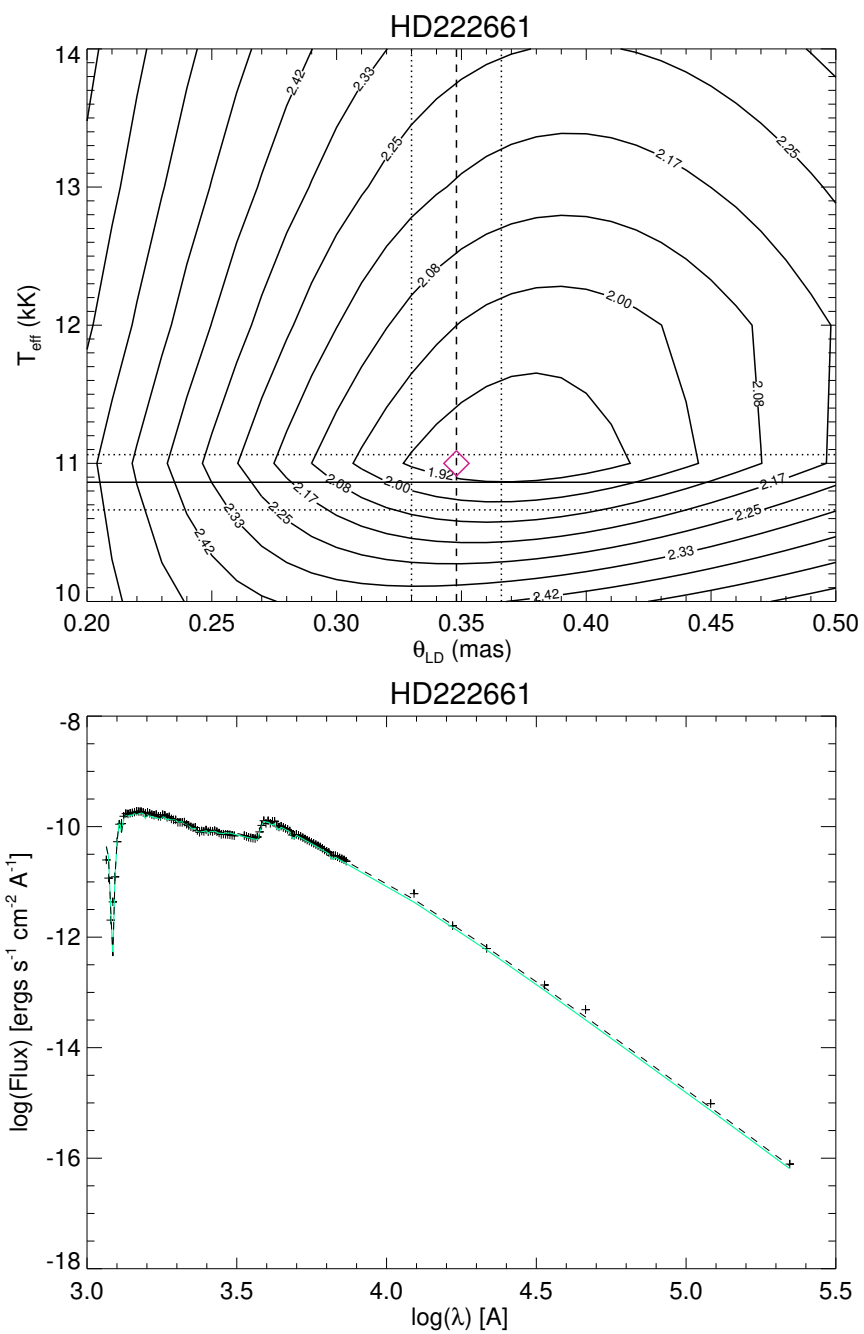
B.25 HD 222661

Figure B.25 Contour (top) and SED (bottom) plots for HD 222661. Fit with the ATLAS9 model.

REFERENCES

- Adelman, S. J., Caliskan, H., Gulliver, A. F., & Teker, A. 2006, *A&A*, 447, 685
- Alekseeva, G. A. et al. 1996, *Baltic Astronomy*, 5, 603
- Ardila, D. R. et al. 2010, *ApJS*, 191, 301
- Armstrong, J. T. et al. 1998, *ApJ*, 496, 550
- Aschenbach, B., Hahn, H.-M., Trümper, J., & Jenkner, H. 1998, *The Invisible Sky*
- Balega, I. I., Balega, Y. Y., Maksimov, A. F., Malogolovets, E. V., Rastegaev, D. A., Shkhagosheva, Z. U., & Weigelt, G. 2007, *Astrophysical Bulletin*, 62, 339
- Bate, M. R. 2009, *MNRAS*, 397, 232
- Blaauw, A. 1961, *Bull. Astron. Inst. Netherlands*, 15, 265
- Bohlin, R. C., Mészáros, S., Fleming, S. W., Gordon, K. D., Koekemoer, A. M., & Kovács, J. 2017, *AJ*, 153, 234
- Born, M., & Wolf, E. 1999, *Principles of optics : electromagnetic theory of propagation, interference and diffraction of light*
- Bouret, J.-C., Donati, J.-F., Martins, F., Escolano, C., Marcolino, W., Lanz, T., & Howarth, I. D. 2008, *MNRAS*, 389, 75
- Boyajian, T. S. et al. 2008, *ApJ*, 683, 424
- Brott, I. et al. 2011, *A&A*, 530, A115
- Burnashev, V. I. 1985, *Abastumanskaia Astrofizicheskaia Observatoriia Byulleten*, 59, 83
- Buss, Jr., R. H., Kruk, J. W., & Ferguson, H. C. 1995, *ApJ*, 454, L55

- Casagrande, L. et al. 2014, MNRAS, 439, 2060
- Castelli, F., & Kurucz, R. L. 2004, ArXiv Astrophysics e-prints
- Cenarro et al. 2001, VizieR Online Data Catalog, 732
- Cenarro, A. J. et al. 2007, MNRAS, 374, 664
- Challouf, M., Nardetto, N., Mourard, D., Aroui, H., & Delaa, O. 2014, in SF2A-2014: Proceedings of the Annual meeting of the French Society of Astronomy and Astrophysics, ed. J. Ballet, F. Martins, F. Bournaud, R. Monier, & C. Reyl e, 471–474
- Che, X. et al. 2011, ApJ, 732, 68
- Chelli, A., Duvert, G., Bourg es, L., Mella, G., Lafrasse, S., Bonneau, D., & Chesneau, O. 2016, A&A, 589, A112
- Choi, J., Dotter, A., Conroy, C., Cantiello, M., Paxton, B., & Johnson, B. D. 2016, ApJ, 823, 102
- Claret, A., & Bloemen, S. 2011, A&A, 529, A75
- Code, A. D., & Meade, M. R. 1979, ApJS, 39, 195
- Conti, P. S., & Alschuler, W. R. 1971, ApJ, 170, 325
- Coud e du Foresto, V. et al. 2003, in Proc. SPIE, Vol. 4838, Interferometry for Optical Astronomy II, ed. W. A. Traub, 280–285
- Cutri, R. M., & et al. 2012, VizieR Online Data Catalog
- Cutri, R. M. et al. 2003, VizieR Online Data Catalog
- de Zeeuw, P. T., Hoogerwerf, R., de Bruijne, J. H. J., Brown, A. G. A., & Blaauw, A. 1999, AJ, 117, 354

- Dotter, A. 2016, *ApJS*, 222, 8
- Dravins, D. 2016, in *Proc. SPIE*, Vol. 9907, *Optical and Infrared Interferometry and Imaging V*, 99070M
- Fitzpatrick, E. L. 1999, *PASP*, 111, 63
- Fu, H.-H., Hartkopf, W. I., Mason, B. D., McAlister, H. A., Dombrowski, E. G., Westin, T., & Franz, O. G. 1997, *AJ*, 114, 1623
- Gaia Collaboration, Brown, A. G. A., Vallenari, A., Prusti, T., de Bruijne, J. H. J., Babusiaux, C., & Bailer-Jones, C. A. L. 2018, *ArXiv e-prints*
- Gies, D. R. et al. 2007, *ApJ*, 654, 527
- Glebocki, R., & Gnacinski, P. 2005, *VizieR Online Data Catalog*, 3244
- Gray, D. F. 2005, *The Observation and Analysis of Stellar Photospheres*
- Gullikson, K., Kraus, A., & Dodson-Robinson, S. 2016, *VizieR Online Data Catalog*, 515
- Habets, G. M. H. J., & Heintze, J. R. W. 1981, *A&AS*, 46, 193
- Hanbury Brown, R. 1956, *Nature*, 178, 1046
- Hanbury Brown, R., Davis, J., Lake, R. J. W., & Thompson, R. J. 1974, *MNRAS*, 167, 475
- Hansen, C. J., Kawaler, S. D., & Trimble, V. 2004, *Stellar interiors : physical principles, structure, and evolution*
- Hartkopf, W. I. et al. 2000, *AJ*, 119, 3084
- Helou, G., & Walker, D. W. 1988, in *Infrared astronomical satellite (IRAS) catalogs and atlases. Volume 7, p.1-265, Vol. 7*
- Henrichs, H. F. et al. 2013, *A&A*, 555, A46

- Herrero, A., Kudritzki, R. P., Vilchez, J. M., Kunze, D., Butler, K., & Haser, S. 1992, *A&A*, 261, 209
- Herrero, A., Puls, J., & Najarro, F. 2002, *A&A*, 396, 949
- Hoogerwerf, R., de Bruijne, J. H. J., & de Zeeuw, P. T. 2000, *ApJ*, 544, L133
- Horch, E., Ninkov, Z., van Altena, W. F., Meyer, R. D., Girard, T. M., & Timothy, J. G. 1999, *AJ*, 117, 548
- Howarth, I. D., & Smith, K. C. 2001, *MNRAS*, 327, 353
- Hubeny, I., & Lanz, T. 1995, *ApJ*, 439, 875
- Hummel, C. A., Rivinius, T., Nieva, M.-F., Stahl, O., van Belle, G., & Zavala, R. T. 2013, *A&A*, 554, A52
- Ireland, M. J. et al. 2008, in *Proc. SPIE*, Vol. 7013, *Optical and Infrared Interferometry*, 701324
- Ishihara, D. et al. 2010, *A&A*, 514
- Jamar, C., Macau-Hercot, D., Monfils, A., Thompson, G. I., Houziaux, L., & Wilson, R., eds. 1976, *ESA Scientific Report*, Vol. 27, *Ultraviolet bright-star spectrophotometric catalogue*.
- Jones, J. et al. 2015, *ApJ*, 813, 58
- Kaplan, S. A., & Pikelner, S. B. 1974, *ARA&A*, 12, 113
- Karovicova, I. et al. 2018, *MNRAS*, 475, L81
- Kharchenko, N. V., Piskunov, A. E., Röser, S., Schilbach, E., & Scholz, R.-D. 2005, *A&A*, 438, 1163
- Kharitonov, A. V., Tereshchenko, V. M., & Knjazeva, L. N. 1988, *The spectrophotometric*

catalogue of stars

Kraus, M. et al. 2015, *A&A*, 581, A75

Krisciunas, K., Suntzeff, N. B., Kelarek, B., Bonar, K., & Stenzel, J. 2017, in *American Astronomical Society Meeting Abstracts*, Vol. 229, American Astronomical Society Meeting Abstracts, 240.31

Kurucz, R. L. 1992, in *IAU Symposium*, Vol. 149, *The Stellar Populations of Galaxies*, ed. B. Barbuy & A. Renzini, 225

Labeyrie, A. 1975, *ApJ*, 196, L71

Lancon, A., & Rocca-Volmerange, B. 1992, *A&AS*, 96, 593

Lanz, T., & Hubeny, I. 2003, *ApJS*, 146, 417

———. 2007, *ApJS*, 169, 83

Lawson, P. R. 1999, in *Bulletin of the American Astronomical Society*, Vol. 31, *American Astronomical Society Meeting Abstracts*, 1406

Le Borgne, J.-F. et al. 2003, *A&A*, 402, 433

Ledrew, G. 2001, *JRASC*, 95, 32

Lyubimkov, L. S., Rachkovskaya, T. M., Rostopchin, S. I., & Lambert, D. L. 2002, *MNRAS*, 333, 9

Lyubimkov, L. S., Rostopchin, S. I., & Lambert, D. L. 2004, *MNRAS*, 351, 745

Maeder, A., & Meynet, G. 2000, *ARA&A*, 38, 143

Maestro, V. et al. 2013, *MNRAS*, 434, 1321

Maestro, V. et al. 2012, in *Proc. SPIE*, Vol. 8445, *Optical and Infrared Interferometry III*,

84450G

Maíz Apellániz, J., Alfaro, E. J., & Sota, A. 2008, ArXiv e-prints

Maíz Apellániz, J., & Barbá, R. H. 2017, ArXiv e-prints

Maíz Apellániz, J. et al. 2014, A&A, 564, A63

Makaganiuk, V. et al. 2011, A&A, 525, A97

Mapelli, M., & Bressan, A. 2013, MNRAS, 430, 3120

Marcolino, W. L. F., Bouret, J.-C., Martins, F., Hillier, D. J., Lanz, T., & Escolano, C.
2009, A&A, 498, 837

Markova, N., Puls, J., Repolust, T., & Markov, H. 2004, A&A, 413, 693

Martins, F., Escolano, C., Wade, G. A., Donati, J. F., Bouret, J. C., & Mimes Collaboration.
2012, A&A, 538, A29

Martins, F. et al. 2015, A&A, 575, A34

Martins, F., Schaerer, D., & Hillier, D. J. 2005, A&A, 436, 1049

Martins, F., Simón-Díaz, S., Barbá, R. H., Gamen, R. C., & Ekström, S. 2017, A&A, 599,
A30

Mason, B. D., Hartkopf, W. I., Gies, D. R., Henry, T. J., & Helsel, J. W. 2009, AJ, 137,
3358

Massa, D., & Fitzpatrick, E. L. 2000, ApJS, 126, 517

McNally, D. 1965, The Observatory, 85, 166

Megier, A., Strobel, A., Galazutdinov, G. A., & Krelowski, J. 2009, A&A, 507, 833

Meynet, G., & Maeder, A. 2003, A&A, 404, 975

- Meynet, G., Mermilliod, J.-C., & Maeder, A. 1993, *A&AS*, 98, 477
- Michelson, A. A., & Pease, F. G. 1921, *ApJ*, 53
- Mokiem, M. R., de Koter, A., Puls, J., Herrero, A., Najarro, F., & Villamariz, M. R. 2005, *A&A*, 441, 711
- Monnier, J. D. 2003, *Reports on Progress in Physics*, 66, 789
- Monnier, J. D., Berger, J.-P., Millan-Gabet, R., & ten Brummelaar, T. A. 2004, in *Proc. SPIE*, Vol. 5491, *New Frontiers in Stellar Interferometry*, ed. W. A. Traub, 1370
- Morales, C. et al. 2001, *ApJ*, 552, 278
- Morrell, N., & Levato, H. 1991, *ApJS*, 75, 965
- Mottram, J. C. et al. 2011, *ApJ*, 730, L33
- Mourard, D. et al. 2009, *A&A*, 508, 1073
- Najarro, F., Hanson, M. M., & Puls, J. 2011, *A&A*, 535, A32
- Neckel, T., Klare, G., & Sarcander, M. 1980, *Bulletin d'Information du Centre de Donnees Stellaires*, 19, 61
- Pan, X., Shao, M., & Kulkarni, S. R. 2004, *Nature*, 427, 326
- Pasinetti Fracassini, L. E., Pastori, L., Covino, S., & Pozzi, A. 2001, *A&A*, 367, 521
- Paxton, B. et al. 2013, *ApJS*, 208, 4
- Petrie, R. M. 1947, *PASP*, 59, 177
- Petrie, R. M., & Ebbighausen, E. G. 1961, *PASP*, 73, 332
- Poeckert, R., Bastien, P., & Landstreet, J. D. 1979, *AJ*, 84, 812
- Prugniel, P., & Soubiran, C. 2001, *A&A*, 369, 1048

- Puls, J. et al. 1996, *A&A*, 305, 171
- Puls, J., Markova, N., Scuderi, S., Stanghellini, C., Taranova, O. G., Burnley, A. W., & Howarth, I. D. 2006, *A&A*, 454, 625
- Puls, J., Urbaneja, M. A., Venero, R., Repolust, T., Springmann, U., Jokuthy, A., & Mokiem, M. R. 2005, *A&A*, 435, 669
- Repolust, T., Puls, J., Hanson, M. M., Kudritzki, R.-P., & Mokiem, M. R. 2005, *A&A*, 440, 261
- Repolust, T., Puls, J., & Herrero, A. 2004, *A&A*, 415, 349
- Roberts, M. S. 1957, *PASP*, 69, 59
- Santolaya-Rey, A. E., Puls, J., & Herrero, A. 1997, *A&A*, 323, 488
- Savage, B. D., Bohlin, R. C., Drake, J. F., & Budich, W. 1977, *ApJ*, 216, 291
- Savage, B. D., Massa, D., Meade, M., & Wesselius, P. R. 1985, *ApJS*, 59, 397
- Schaefer, G. H. et al. 2016, *AJ*, 152, 213
- Scott, N. J., Millan-Gabet, R., Lhomé, E., Ten Brummelaar, T. A., Coudé Du Foresto, V., Sturmann, J., & Sturmann, L. 2013, *Journal of Astronomical Instrumentation*, 2, 1340005
- Shao, M. et al. 1988, *A&A*, 193, 357
- Shull, J. M., & van Steenberg, M. E. 1985, *ApJ*, 294, 599
- Silaj, J., Jones, C. E., Sigut, T. A. A., & Tycner, C. 2014, *ApJ*, 795, 82
- Simón-Díaz, S., Herrero, A., Esteban, C., & Najarro, F. 2006, *A&A*, 448, 351
- Soubiran, C., Le Campion, J.-F., Brouillet, N., & Chemin, L. 2016, *A&A*, 591, A118
- Swihart, S. J., Garcia, E. V., Stassun, K. G., van Belle, G., Mutterspaugh, M. W., & Elias,

- N. 2017, *AJ*, 153, 16
- ten Brummelaar, T., Mason, B. D., McAlister, H. A., Roberts, Jr., L. C., Turner, N. H., Hartkopf, W. I., & Bagnuolo, Jr., W. G. 2000, *AJ*, 119, 2403
- ten Brummelaar, T. A. et al. 2005, *ApJ*, 628, 453
- ten Brummelaar, T. A. et al. 2012, in *Proc. SPIE*, Vol. 8445, *Optical and Infrared Interferometry III*, 84453C
- . 2013, *Journal of Astronomical Instrumentation*, 2, 1340004
- Turner, N. H., ten Brummelaar, T. A., Roberts, L. C., Mason, B. D., Hartkopf, W. I., & Gies, D. R. 2008, *AJ*, 136, 554
- Underhill, A. B., Divan, L., Prevot-Burnichon, M.-L., & Doazan, V. 1979, *MNRAS*, 189, 601
- Valdes, F., Gupta, R., Rose, J. A., Singh, H. P., & Bell, D. J. 2004, *VizieR Online Data Catalog*, 215
- van Leeuwen, F. 2007, *A&A*, 474, 653
- Villamariz, M. R., & Herrero, A. 2005, *A&A*, 442, 263
- Villamariz, M. R., Herrero, A., Becker, S. R., & Butler, K. 2002, *A&A*, 388, 940
- Wade, G. A. 2012, in *Astronomical Society of the Pacific Conference Series*, Vol. 465, *Proceedings of a Scientific Meeting in Honor of Anthony F. J. Moffat*, ed. L. Drissen, C. Robert, N. St-Louis, & A. F. J. Moffat, 33
- Wade, G. A. et al. 2014, in *IAU Symposium*, Vol. 302, *Magnetic Fields throughout Stellar Evolution*, ed. P. Petit, M. Jardine, & H. C. Spruit, 265–269
- Wade, G. A., & MiMeS Collaboration. 2015, in *Astronomical Society of the Pacific Con-*

- ference Series, Vol. 494, Physics and Evolution of Magnetic and Related Stars, ed. Y. Y. Balega, I. I. Romanyuk, & D. O. Kudryavtsev, 30
- Wallander, A. et al. 2004, in Proc. SPIE, Vol. 5496, Advanced Software, Control, and Communication Systems for Astronomy, ed. H. Lewis & G. Raffi, 21–31
- Warren, Jr., W. H., & Hesser, J. E. 1977, ApJS, 34, 115
- Weidner, C., & Vink, J. S. 2010, A&A, 524, A98
- Wheelwright, H. E., Oudmaijer, R. D., & Schnerr, R. S. 2009, A&A, 497, 487
- White, T. R. et al. 2018, MNRAS
- . 2017, MNRAS, 471, 2882
- Wu, Z.-Y., Zhou, X., Ma, J., & Du, C.-H. 2009, MNRAS, 399, 2146
- Zorec, J., Cidale, L., Arias, M. L., Frémat, Y., Muratore, M. F., Torres, A. F., & Martayan, C. 2009, A&A, 501, 297
- Zwahlen, N., North, P., Debernardi, Y., Eyer, L., Galland, F., Groenewegen, M. A. T., & Hummel, C. A. 2004, A&A, 425, L45